

**NON-LINEAR TIME DOMAIN SIMULATION OF MOORED FLOATING
SYSTEMS**

Oguz Yilmaz, B Sc

Thesis submitted for the Degree of Doctor of Philosophy

Department of Naval Architecture and Ocean Engineering
University of Glasgow

October 1992

© Oguz Yilmaz 1992

ProQuest Number: 13815386

All rights reserved

INFORMATION TO ALL USERS

The quality of this reproduction is dependent upon the quality of the copy submitted.

In the unlikely event that the author did not send a complete manuscript and there are missing pages, these will be noted. Also, if material had to be removed, a note will indicate the deletion.



ProQuest 13815386

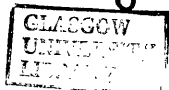
Published by ProQuest LLC (2018). Copyright of the Dissertation is held by the Author.

All rights reserved.

This work is protected against unauthorized copying under Title 17, United States Code
Microform Edition © ProQuest LLC.

ProQuest LLC.
789 East Eisenhower Parkway
P.O. Box 1346
Ann Arbor, MI 48106 – 1346

Thas
9411
copy 1



CONTENTS

	Page
Contents	i
List of Figures	iv
List of Tables	xv
Acknowledgements	xvi
Dedication	xvii
Declaration	xviii
Summary	xix
CHAPTER 1 INTRODUCTION	
1.1 Single Point Mooring Systems	1
1.2 Summary of Previous Work	3
1.3 Objectives of Study	5
1.4 Structure of Thesis	6
CHAPTER 2 MOTION RESPONSE SIMULATION OF MOORED BUOYS	 11
2.1 Introduction	11
2.2 Environmental Loading on Buoys	12
2.2.1 Evaluation of Wave Forces Acting on Buoys	12
2.2.2 Effect of Current and Wind	18
2.3 Evaluation of Mooring Forces	20
2.4 Motion Responses of the Buoy Under Wave Excitation in Frequency Domain	 23
2.5 Time Domain Analysis of Motion Responses of Moored Buoys Under Wave Excitation	 29
2.6 Applications and Comparisons	34
2.7 Conclusions	37

CHAPTER 3	HYDRODYNAMIC FORCES ON TANKERS	62
3.1	Introduction	62
3.2	Formulation of the Diffraction Problem	63
3.3	Velocity Potential of Plane and Scattered Waves	67
3.4	Wave Forces and Moments	69
3.5	Formulation of the Radiation Problem	71
3.6	Calculation of Added Mass and Damping Coefficients	74
3.7	Second Order Mean Forces Acting on the Tanker	76
3.8	Numerical Aspects and Results	78
3.9	Conclusions	80
CHAPTER 4	TIME DOMAIN SIMULATION OF A TANKER-BUOY COUPLED SYSTEM	120
4.1	Introduction	120
4.2	Dynamic Wind Loading and Response	121
4.3	Current Forces	124
4.4	Slowly Varying and Mean Wave Drift Forces in Irregular Waves	129
4.5	Motion Equations of the Tanker-Buoy System in Time and Frequency Domain	133
4.6	Numerical Aspects and Results	138
4.7	Conclusions	140
CHAPTER 5	PARAMETRIC STUDIES	158
5.1	Introduction	158
5.2	Parametric Studies and Discussion of Results	158
5.3	Numerical Aspects	162
CHAPTER 6	EXPERIMENTAL WORK	185
6.1	Introduction	185
6.2	Moored Buoy Tests in Calm Water and in Regular Waves	186
6.2.1	Description of Calibration Procedures	186

6.2.2 Analysis and Comparison of the Measurements	187
6.3 Single Point Moored Tanker-Buoy Experiments	192
6.3.1 Description of Calibration Procedures	192
6.3.2 Analysis and Comparison of the Measurements	193
6.3.3 Observations and Experience from Model Tests	194
6.4 Conclusions	194
CHAPTER 7 CONCLUSIONS	237
7.1 General Conclusions of Thesis	237
7.2 Recommendations for Future Work	242
APPENDIX A Evaluation of Mooring Forces	243
APPENDIX B Elliptical Coordinate System	248
APPENDIX C Some Properties of Mathieu Functions	249
APPENDIX D Derivation of the Incident Wave	
Potential for the Elliptical Cylinder	252
APPENDIX E Blanch's Definition for Radial Functions	255
REFERENCES	257

LIST OF FIGURES

Page

CHAPTER 1

Fig. 1.1	CALM System	8
Fig. 1.2	ELSBM System	8
Fig. 1.3	SPAR	9
Fig. 1.4	SALM	9
Fig. 1.5	Fixed Mooring Tower	10
Fig. 1.6	Articulated Mooring Tower	10

CHAPTER 2

Fig. 2.1	Co-ordinate Systems and Cylindrical and Conical Buoy Geometries	41
Fig. 2.2	A Typical Differential Cable Element	42
Fig. 2.3	Definition of Cable Parameters	42
Fig. 2.4	Horizontal Displacement-Horizontal Displacement	43
Fig. 2.5	Horizontal Displacement-Vertical Displacement	43
Fig. 2.6	Vertical Displacement-Horizontal Displacement	43
Fig. 2.7	Vertical Displacement-Vertical Displacement	43
Fig. 2.8	Top View of a Multi-Cable System	44
Fig. 2.9	Multi-Cable Systems	44
Fig. 2.10	Wave Induced Forces and Resulting Responses of the Cylindrical Buoy	45
Fig. 2.11	Wave Induced Forces and Resulting Responses of the Conical Buoy	46
Fig. 2.12	Motion Response Predictions of the Cylindrical Buoy	47
Fig. 2.13	Motion Response Predictions of the Conical Buoy	48
Fig. 2.14	Stiffness Curves for Linear and Non-linear Cables	49

Fig. 2.15	Motion Response Simulation of a Circular Buoy with Non-linear Cables Wave Height=4 m, Wave Frequency=0.04 rad/sec	50
Fig. 2.15a	Fast Fourier Transformations of the Time Histories Shown in Fig. 2.15	51
Fig. 2.16	Motion Response Simulation of a Circular Buoy with Linear Cables Wave Height=4 m, Wave Frequency=0.04 rad/sec	52
Fig. 2.16a	Fast Fourier Transformations of the Time Histories Shown in Fig. 2.16	53
Fig. 2.17	Motion Response Simulation of a Circular Buoy with Non-linear Cables Wave Height=4 m, Wave Frequency=0.1 rad/sec	54
Fig. 2.17a	Fast Fourier Transformations of the Time Histories Shown in Fig. 2.17	55
Fig. 2.18	Motion Response Simulation of a Circular Buoy with Non-linear Cables Wave Height=4 m, Wave Frequency=0.3 rad/sec	56
Fig. 2.18a	Fast Fourier Transformations of the Time Histories Shown in Fig. 2.18	57
Fig. 2.19	Motion Response Simulation of a Circular Buoy with Non-linear Cables Wave Height=4 m, Wave Frequency=0.5 rad/sec	58
Fig. 2.19a	Fast Fourier Transformations of the Time Histories Shown in Fig. 2.19	59
Fig. 2.20	Motion Response Simulation of a Circular Buoy with Non-linear Cables Wave Height=4 m, Wave Frequency=0.9 rad/sec	60
Fig. 2.20a	Fast Fourier Transformations of the Time Histories Shown in Fig. 2.20	61

CHAPTER 3

Fig. 3.1	Elliptical Cylinder and Real Tanker Hull Comparison	82
Fig. 3.2	Elliptical Coordinates	82
Fig. 3.3	Non-dimensionalised Surge Force Ship Breadth/Ship Length=0.995	83
Fig. 3.4	Non-dimensionalised Surge Force Ship Breadth/Ship Length=0.7	84
Fig. 3.5	Non-dimensionalised Surge Force Ship Breadth/Ship Length=0.5	85
Fig. 3.6	Non-dimensionalised Surge Force Ship Breadth/Ship Length=0.3	86
Fig. 3.7	Non-dimensionalised Surge Force Ship Breadth/Ship Length=0.2	87
Fig. 3.8	Non-dimensionalised Surge Force Ship Breadth/Ship Length=0.15	88
Fig. 3.9	Non-dimensionalised Surge Force Ship Breadth/Ship Length=0.1	89
Fig. 3.10	Non-dimensionalised Surge Force Ship Breadth/Ship Length=0.05	90
Fig. 3.11	Non-dimensionalised Sway Force Ship Breadth/Ship Length=0.995	91
Fig. 3.12	Non-dimensionalised Sway Force Ship Breadth/Ship Length=0.7	92
Fig. 3.13	Non-dimensionalised Sway Force Ship Breadth/Ship Length=0.5	93
Fig. 3.14	Non-dimensionalised Sway Force Ship Breadth/Ship Length=0.3	94
Fig. 3.15	Non-dimensionalised Sway Force Ship Breadth/Ship Length=0.2	95

Fig. 3.16	Non-dimensionalised Sway Force Ship Breadth/Ship Length=0.15	96
Fig. 3.17	Non-dimensionalised Sway Force Ship Breadth/Ship Length=0.1	97
Fig. 3.18	Non-dimensionalised Sway Force Ship Breadth/Ship Length=0.05	98
Fig. 3.19	Non-dimensionalised Yaw Moment Ship Breadth/Ship Length=0.999	99
Fig. 3.20	Non-dimensionalised Yaw Moment Ship Breadth/Ship Length=0.995	100
Fig. 3.21	Non-dimensionalised Yaw Moment Ship Breadth/Ship Length=0.7	101
Fig. 3.22	Non-dimensionalised Yaw Moment Ship Breadth/Ship Length=0.5	102
Fig. 3.23	Non-dimensionalised Yaw Moment Ship Breadth/Ship Length=0.3	103
Fig. 3.24	Non-dimensionalised Yaw Moment Ship Breadth/Ship Length=0.2	104
Fig. 3.25	Non-dimensionalised Yaw Moment Ship Breadth/Ship Length=0.15	105
Fig. 3.26	Non-dimensionalised Yaw Moment Ship Breadth/Ship Length=0.1	106
Fig. 3.27	Non-dimensionalised Yaw Moment Ship Breadth/Ship Length=0.05	107
Fig. 3.28	Sway Force Angle of Incidence=225 Degree	108
Fig. 3.29	Sway Force Angle of Incidence=270 Degree	108
Fig. 3.30	Yaw Moment Angle of Incidence=225 Degree	109

Fig. 3.31	Surge Force Angle of Incidence=225 Degree	109
Fig. 3.32	Surge Force Angle of Incidence=180 Degree	110
Fig. 3.33	Comparison of Surge Force Acting on a Cylinder Ship Breadth/Ship Length=0.995	111
Fig. 3.34	Comparison of Added Mass Coefficient in Surge $a_{11}'=a_{11}/(\rho\pi a^2 b \text{draught})$	112
Fig. 3.35	Comparison of Added Mass Coefficient in Sway $a_{22}'=a_{22}/(\rho\pi a^2 b \text{draught})$	112
Fig. 3.36	Comparison of Added Mass Coefficient in Yaw $a_{66}'=a_{66}/(\rho\pi a^2 b \text{draught}^4 a^2)$	112
Fig. 3.37	Comparison of Damping Coefficient in Surge $b_{11}'=b_{11}/(\rho\pi a^2 b \text{draught}^3 (g/a)^{0.5})$	113
Fig. 3.38	Comparison of Damping Coefficient in Sway $b_{22}'=b_{22}/(\rho\pi a^2 b \text{draught}^3 (g/a)^{0.5})$	113
Fig. 3.39	Comparison of Damping Coefficient in Yaw $b_{66}'=b_{66}/(\rho\pi a^2 b \text{draught}^3 (g/a)^{0.5} a^2)$	113
Fig. 3.40	Comparison of Added Mass Coefficient in Surge $a_{11}'=a_{11}/(\rho\pi a^2 b \text{draught})$	114
Fig. 3.41	Comparison of Added Mass Coefficient in Sway $a_{22}'=a_{22}/(\rho\pi a^2 b \text{draught})$	114
Fig. 3.42	Comparison of Added Mass Coefficient in Yaw $a_{66}'=a_{66}/(\rho\pi a^2 b \text{draught}^4 a^2)$	114
Fig. 3.43	Comparison of Damping Coefficient in Surge $b_{11}'=b_{11}/(\rho\pi a^2 b \text{draught}^3 (g/a)^{0.5})$	115
Fig. 3.44	Comparison of Damping Coefficient in Sway $b_{22}'=b_{22}/(\rho\pi a^2 b \text{draught}^3 (g/a)^{0.5})$	115
Fig. 3.45	Comparison of Damping Coefficient in Yaw $b_{66}'=b_{66}/(\rho\pi a^2 b \text{draught}^3 (g/a)^{0.5} a^2)$	115

Fig. 3.46	Surge Response Angle of Incidence=180 Degree	116
Fig. 3.47	Surge Response Angle of Incidence=225 Degree	116
Fig. 3.48	Sway Response Angle of Incidence=225 Degree	116
Fig. 3.49	Sway Response Angle of Incidence=270 Degree	117
Fig. 3.50	Yaw Response Angle of Incidence=225 Degree	117
Fig. 3.51	Mean Surge Drift Force Angle of Incidence=45 Degree	118
Fig. 3.52	Mean Sway Drift Force Angle of Incidence=45 Degree	118
Fig. 3.53	Mean Surge Drift Force Angle of Incidence=0 Degree	118
Fig. 3.54	Mean Drift Force Acting on a Circular Cylinder Extending from Free Surface to Sea Bottom	119

CHAPTER 4

Fig. 4.1	Wind Spectrums Mean Wind Speed=22 m/sec	141
Fig. 4.2	Wind Force Spectrum Projected Area=472 m ² , Mean Wind Speed=22m/sec	142
Fig. 4.3	Linear Response Spectrum Stiffness Coe.=1200 kN/m, Mass+Added Mass=173154 Ton. Damping Ratio=0.05	143
Fig. 4.4	Wind Velocity Time History Mean Wind Speed=22 m/sec	144

Fig. 4.5	Jonswap Wave Spectrum and Slowly Varying Force Spectrum Significant Wave Height=10 m, Zero Crossing Period=12 sec	145
Fig. 4.6	Linear Response Spectrum Stiffness Coe.=1200 kN/m, Damping Ratio=0.05	146
Fig. 4.7	Time History of Slowly Varying Forces in Irregular Waves	147
Fig. 4.8	Wave Drift Forces for Different Forward Speeds Angle of Incidence=0 Degree	148
Fig. 4.9	Frequency Domain Modelling of the Tanker-Buoy System	149
Fig. 4.10	Experiment Set-up of the Tanker-Buoy System Co-linear Environmental Forces	150
Fig. 4.11	Surge Motion of the Tanker Co-linear Environmental Forces	151
Fig. 4.12	Surge Motion of the Buoy Co-linear Environmental Forces	151
Fig. 4.13	Surge Response of the Tanker Wave Height=8 m, Wind Velocity=20 m/sec Current Velocity=1.5 m/sec	152
Fig. 4.14	Surge Response of the Buoy Wave Height=8 m, Wind Velocity=20 m/sec Current Velocity=1.5 m/sec	152
Fig. 4.15	Approximation to the Retardation Function by Chebyshev Polynoms	153
Fig. 4.16	Approximation to the Retardation Function by Chebyshev Polynoms	154
Fig. 4.17	Approximation to the Retardation Function by Chebyshev Polynoms	155
Fig. 4.18	Comparison Between Static and Dynamic Wind Mean Wind Speed=22 m/sec, Current Speed=1.5 m/sec Co-linear Environmental Forces, Ochi-Shin Wind Spectrum	156
Fig. 4.19	Motion Response and Hawser Tension Predictions Mean Wind Speed=22 m/sec, Current Speed=1.5 m/sec	

Significant Wave Height=10 m, Ochi-Shin Wind Spectrum	
Co-linear Environmental Forces	157

CHAPTER 5

Fig. 5.1	Coupled Buoy-Ship System	172
Fig. 5.2	Time Domain Simulation of the Tanker-Buoy System Pierson Moskowitz Spectrum, Mean Wind Speed=10.3 m/sec	173
Fig. 5.3	Time Domain Simulation of the Tanker-Buoy System Pierson Moskowitz Spectrum, Mean Wind Speed=20.6 m/sec	174
Fig. 5.4	Time Domain Simulation of the Tanker-Buoy System Pierson Moskowitz Spectrum, Mean Wind Speed=25.8 m/sec	175
Fig. 5.5	Time Domain Simulation of the Tanker-Buoy System Ochi-Shin Wind Spectrum, Mean Wind Speed=22 m/sec	176
Fig. 5.6	Time Domain Simulation of the Tanker-Buoy System Davenport Wind Spectrum, Mean Wind Speed=22 m/sec	177
Fig. 5.7	Time Domain Simulation of the Tanker-Buoy System Harris Wind Spectrum, Mean Wind Speed=22 m/sec	178
Fig. 5.8	Time Domain Simulation of the Tanker-Buoy System 4 Legged CALM System	179
Fig. 5.9	Time Domain Simulation of the Tanker-Buoy System Hawser Length=40 m	180
Fig. 5.10	Time Domain Simulation of the Tanker-Buoy System Thruster Force=250 kN	181
Fig. 5.11	Time Domain Simulation of the Tanker-Buoy System Thruster Force=500 kN	182
Fig. 5.12	Time Domain Simulation of the Tanker-Buoy System Thruster Force=750 kN	183
Fig. 5.13	Time Domain Simulation of the Tanker-Buoy System Diameter of the Buoy=20 m, Draft of the Buoy=20 m	184

CHAPTER 6

Fig. 6.1	Motion Response and Cable Tension Measurements of the Conical Buoy	197
Fig. 6.2	Experiment Test Set-up (Mooring Configuration A)	198
Fig. 6.3	Geometrical Characteristics of Conical and Cylindrical Buoys	199
Fig. 6.4	Experimental Set-up for the Coupled Buoy-Ship System	200
Fig. 6.5	Coupled Tanker-Buoy System	201
Fig. 6.6	Experimental Set-up of the Tanker-Buoy System Wave and Current Acting in Different Directions	201
Fig. 6.7	Stiffness Characteristics of Mooring Lines	202
Fig. 6.8	Stiffness Characteristics of Hawser	202
Fig. 6.9	Motion Response Measurements of the Moored Conical Buoy Wave Height=6 m, Wave Frequency=0.702 rad/sec (All values are in full scale)	203
Fig. 6.10	Fast Fourier Transformations of the Time Histories Shown in Fig. 6.9	204
Fig. 6.11	Motion Response Measurements of the Moored Conical Buoy Wave Height=8.84 m, Wave Frequency=0.45 rad/sec (All values are in full scale)	205
Fig. 6.12	Fast Fourier Transformations of the Time Histories Shown in Fig. 6.11	206
Fig. 6.13	Heave Response Measurements of the Moored Conical Buoy	207
Fig. 6.14	Surge Response Measurements of the Moored Conical Buoy	207
Fig. 6.15	Pitch Response Measurements of the Moored Conical Buoy	207
Fig. 6.16	Heave Response Measurements of the Moored Cylindrical Buoy	208
Fig. 6.17	Surge Response Measurements of the Moored Cylindrical Buoy	208
Fig. 6.18	Pitch Response Measurements of the Moored Cylindrical Buoy	208
Fig. 6.19	Heave Response Predictions of the Conical Buoy	209
Fig. 6.20	Heave Response Predictions of the Cylindrical Buoy	210
Fig. 6.21	Surge Response Predictions of the Conical Buoy	209

Fig. 6.22	Surge Response Predictions of the Cylindrical Buoy	210
Fig. 6.23	Pitch Response Predictions of the Conical Buoy	209
Fig. 6.24	Pitch Response Predictions of the Cylindrical Buoy	210
Fig. 6.25	Second-order Surge Response Measurements of the Conical Buoy	211
Fig. 6.26	Steady Surge Response Measurements of the Conical Buoy	211
Fig. 6.27	Second-order Surge Response Measurements of the Cylindrical Buoy	212
Fig. 6.28	Steady Surge Response Measurements of the Cylindrical Buoy	212
Fig. 6.29	Surge Stiffness of the Cylindrical Buoy due to the Surge Motion	213
Fig. 6.30	Natural Frequency Test of the Moored Conical Buoy in Waves Wave Frequency=0.4 rad/sec, Wave Height=5 m (All values are in full scale)	214
Fig. 6.31	Experiment Test Set-up (Mooring Configuration A)	215
Fig. 6.32	Surge Response Measurements of the Conical Buoy Wave Height=5 m	216
Fig. 6.33	Heave Response Measurements of the Conical Buoy Wave Height=5 m	216
Fig. 6.34	Pitch Response Measurements of the Conical Buoy Wave Height=5 m	216
Fig. 6.35	Motion Response Predictions of the Conical Buoy	217
Fig. 6.36	Second-order Surge Measurements of the Conical Buoy Wave Height=5 m	218
Fig. 6.37	Steady Surge Measurements of the Conical Buoy Wave Height=5 m	218
Fig. 6.38	Calculation of Damping Coefficient from the Rate of Decaying Oscillations	219
Fig. 6.39	Damping Coefficients of the Conical Buoy (Mooring Configuration B)	220
Fig. 6.40	Current Effect on the Motion Responses of the Cylindrical Buoy	221
Fig. 6.41	Experimental Test Set-up A	222

Fig. 6.42	Experimental Test Set-up B	222
Fig. 6.43	Natural Frequency Test of the Conical Buoy with Linear Springs	223
Fig. 6.44	Damping Coefficients of the Conical Buoy (Test Set-up A)	224
Fig. 6.45	Damping Coefficients of the Conical Buoy (Test Set-up B)	224
Fig. 6.46	Instrumentation	225
Fig. 6.47	Surge Motion of the Buoy, Co-linear Environmental Forces	226
Fig. 6.48	Surge Motion of the Tanker, Co-linear Environmental Forces	226
Fig. 6.49	Motion Response and Hawser Tension Measurements in Co-linear Current and Wave Wave Frequency=0.4 Hz, Wave Height=4.10 cm Current Force=6 gr	227
Fig. 6.50	Motion Response and Hawser Tension Measurements in Co-linear Current and Wave Wave Frequency=0.5 Hz, Wave Height=3.70 cm Current Force=6 gr	228
Fig. 6.51	Motion Response and Hawser Tension Measurements in Co-linear Current and Wave Wave Frequency=1.4 Hz, Wave Height=3.50 cm Current Force=6 gr	229
Fig. 6.52	Motion Response and Hawser Tension Measurements in Co-linear Current and Wave Wave Frequency=0.8 Hz, Wave Height=5.57 cm Current Force=6 gr	230
Fig. 6.53	Natural Frequency Test of the Tanker-Buoy System in Current Current Force=26 gr	231
Fig. 6.54	Oblique Angle Tests of the Tanker Buoy System	232
Fig. 6.55	Oblique Angle Test, Run No. 11	233
Fig. 6.56	Oblique Angle Test, Run No. 12	234
Fig. 6.57	Oblique Angle Test, Run No. 13	235
Fig. 6.58	Oblique Angle Test, Run No. 14	236

APPENDICES

Fig. A-1	Definition of Cable Parameters	243
----------	--------------------------------	-----

LIST OF TABLES

Table 2.1	Comparison of the Motion Responses of a Moored Cylindrical Buoy with Linear and Non-linear Modelling of Mooring Lines in Regular Waves. Wave Height=4 m	39
Table 2.2	Comparison of the Motion Responses of a Moored Cylindrical Buoy with Linear and Non-linear Modelling of Mooring Lines in Regular Waves. Wave Height=12 m	40
Table 5.1	Effect of Wave Direction	163
Table 5.2	Effect of Wind Direction	163
Table 5.3	Effect of Current Direction	164
Table 5.4	Effect of Current Velocity	164
Table 5.5	Effect of Wind Velocity	165
Table 5.6	Effect of Wave Height	165
Table 5.7	Effect of Sea State	166
Table 5.8	Effect of Wind Spectrum	167
Table 5.9	Effect of Mooring Legs	168
Table 5.10	Effect of Hawser Length	169
Table 5.11	Effect of Thrusters	170
Table 5.12	Effect of Buoy Geometry	171
Table 6.1	Oblique Wave and Current Loading Test Conditions and Results	196

ACKNOWLEDGEMENTS

The author is grateful for the help of the members of the Department of Naval Architecture and Ocean Engineering at the University of Glasgow during the research study reported in the thesis.

The author would like to thank the following;

Professor D. Faulkner, Head of Department, for allowing him to carry out this study and for his continuous encouragement.

Dr. A. Incecik, Superintendent of the Hydrodynamics Laboratory, for supervising this research and for his tireless assistance and encouragement.

Dr. I.H. Helvacioğlu for his stimulating discussions and valuable assistance.

Dr. M. Soylemez for his contribution to the time domain techniques used in the thesis.

Dr. H.S. Chan for allowing him to use his program and for his instructive discussions.

Mr. D. Percival for his assistance during the development of the computer programs.

Mr. R.B. Christison and the staff at the Hydrodynamics Laboratory for their help during the experiments.

Finally, the financial support from the Turkish Ministry of Education is gratefully acknowledged.

DEDICATED TO MY PARENTS

DECLARATION

*Except where reference is made to the work of others,
this thesis is believed to be original*

SUMMARY

This thesis describes the environmental loading and motion response prediction methods of mooring systems.

The first chapter presents existing Single Point Mooring Terminals and gives a summary of previous studies carried out on this subject. The main objectives of the study are also explained. Finally the structure of the thesis is given.

The second chapter is concerned with the motion response prediction of moored buoys. Wave forces acting on the buoy are calculated using Morison's Equation. Catenary equations are utilized to derive cable forces. Two different buoy geometries, cylindrical and conical, are considered in the study. Experimental measurements are compared with time and frequency domain modellings.

In the third chapter, diffraction theory used to derive the wave forces is explained. The tanker is modelled as a vertical elliptical cylinder with a finite draught. Calculated wave forces are compared with Oortmerssen's experiments and with the results of a 3-D program developed by Chan. The water depth effect on wave forces is investigated. Program results for various angles of incidence and for different elliptic cylinders are presented. The second order mean force is calculated using the far-field approach, introduced by Maruo. Also the radiation problem of the tanker which is modelled as an elliptical cylinder is solved. Program results are compared with Oortmerssen's experiments and with Chan's 3-D program results. Program results for different cylinders and for different water depth/draught ratios are presented.

Chapter 4 describes a time domain model used to predict the motion responses of a tanker-buoy system under wave, wind and current loading. Motion equations of the tanker-buoy system are derived by using Cummins' method. Frequency-independent hydrodynamic coefficients and time histories of wave forces in irregular seas are calculated. Experimental measurements are compared with the time domain simulation results.

Chapter 5 presents the results of a series of parametric studies. A computer program developed to predict the motion responses of the coupled tanker-buoy system is run for different parameters, such as; wave, wind and current angle of attacks, wind and

current speed, elasticity of the mooring lines and the hawser line, buoy and tanker geometry, water depth, draught of the ship. Numerical aspects of the program, such as the solution of the differential equations and the evaluation of the convolution integral are discussed.

In chapter 6 a description of model tests performed in regular waves is presented. Two sets of experiments are conducted. The first set of experiments aims to predict the motion responses of conical and cylindrical buoys, the second to predict the motion responses of the tanker-buoy system and the hawser line forces.

In the final chapter general conclusions are drawn and some recommendations for future work are made.

CHAPTER 1

INTRODUCTION

1.1 SINGLE POINT MOORING SYSTEMS

A large number of Single Point Mooring (SPM) systems have been installed in various parts of the world over the past 30 years. As North Sea oil production moves towards a greater dependence on smaller reservoirs, not only in comparatively shallow water on the continental shelf, but also in deeper water off it, there will be a correspondingly greater role for floating production facilities. An example of such a facility is a large tanker moored to a single point. A single point moored tanker weathervanes according to the prevailing weather conditions thus staying on location with a minimum of mooring loads. Single point mooring systems have been installed in various parts of the world and depending on the weather conditions they vary from chain/turret systems to rigid-articulated systems and hybrid-type structures. Economic viability is one reason for this tendency towards SPM systems as they have become alternatives to fixed platforms and subsea pipelines for transportation of oil and gas which becomes an important part of the oil-field development as offshore production activities move into deeper waters. Another noticeable distinction of such systems is that they can endure severe sea and weather conditions. As a result they experience numerous combinations of wave, wind and current. Therefore dynamic analysis of such systems is essential to ensure satisfactory overall performance of these systems.

As single-point mooring systems have increased in size and complexity, a pressing need has arisen for a method of objectively assessing competing designs. A computer-based mathematical model would provide a quick and cost effective means for design assessment. The programs would also provide an independent check on physical model tests of the final design, which would be of use to manufacturers, designers and

certifying authorities. Prediction of the motion responses of moored buoys and mooring forces should be the first step towards the understanding of the dynamic behaviour of the single-point mooring systems under environmental conditions.

Several types of Single Point Mooring systems exist:

1. CALM (Catenary Anchor Leg Mooring)
2. ELSBM (Exposed Location Single Buoy Mooring)
3. SPAR
4. SALM (Single Anchor Leg Mooring)
5. Fixed Mooring Tower
6. Articulated Mooring Tower
7. Yoke Moored Storage

The idea of SPMs is to moor a vessel to a single point and allow it to weathervane under environmental forces to take up the position with minimum mooring loads. All of the SPMs mentioned above have the means to transfer oil to (or from) the tanker through pipelines. Some of the SPM systems are shown in Figs. 1.1-1.6. CALM is the original and the most common system in operation which represents about 80 % of all the existing SPMs. It consists of a simple cylindrical buoy which is designed with a rotating deck and an underwater hose connection for the pipelines. ELSBM is an improved design of CALM systems which solves the fatigue problem of the hoses by increasing the submerged volume of the buoy, thus minimising heaving forces. Another aspect of the ELSBMs is that the loading lines between the buoy and the tanker are raised above the waves to minimise the wave loading. Another version of CALM systems is the SPAR design. The SPAR design has oil storage capacity, unlike other CALM systems. In SALM systems the buoy is moored to a base at the sea bottom by a single anchor leg. There are some advantages of SALM systems over CALM systems; firstly the fluid swivel system is independent of the buoy, thus the hoses attached to the leg are not liable to the forces exerted by the buoy motions, secondly the cargo transfer system of the SALMs is less likely to be affected by collisions. The idea behind the Fixed Mooring Tower is that cargo can be transferred by pipelines thus eliminating the problems related to the loading hoses. Articulated Mooring Towers are preferable to fixed mooring towers

because the structural loads on the articulated tower are much less than the structural load on fixed tower.

1.2 SUMMARY OF PREVIOUS WORK

Several researchers have studied the dynamic response of SPM systems under wave, wind and current loading using numerical simulation and measurement techniques. Haring [1.1] in his paper summarises the full scale measurements which were recorded aboard the 45000 DWT tanker Theotokos at Ekofisk in the North Sea. He concluded in his paper that the maximum tension in the bow hawser was primarily a function of the wave height; that mooring force predictions based on model test data would overestimate full scale measurements under stormy conditions and that measured long period yaw cycles exceeded in magnitude those observed in model tests. Wichers [1.2] studied the dynamic stability and the natural frequencies of the modes of motions of the tanker in the horizontal plane in steady current and wind. It is concluded in the paper that a ship moored to an SPM system can undergo low frequency oscillations in the horizontal plane in wind and current only when the equilibrium position of the ship is unstable. Owen and Linfoot [1.3, 1.4] have presented a mathematical model describing the low frequency motion of an SPM system. It was discussed in the paper that differential equations of motion of SPM systems were mathematically "stiff" and required special treatment. Muga and Freeman [1.5] used an Impulse Response Function technique to model the motions of a single point moored ship in steady wind and current. Wichers [1.6] formulated the motion equations of a Single Point Moored tanker in three degrees of freedom in wind and current. He derived two sets of motion equations, one of them uses the impulse response function technique of Cummins [1.31] to determine the hydrodynamic coefficients while the other one uses constant added mass and damping coefficients. It was concluded in the paper that when there are no sudden changes in motions of tanker both of the motion equations give very close results. Oortmerseen [1.7] studied the time domain analysis of a single point moored ship by using the Impulse Response Function technique. In 1979 Faltinsen et al [1.8] and [1.9] applied seven degrees of freedom linear stability equations to study the slow motions of a tanker moored to a buoy. It was

recommended in the paper that cross mooring between the ship and the buoy and thrusters be used to increase the stability of the system. It was also suggested that transverse current force and yaw moment on the ship for small angles of attack could be obtained by lifting-line theory and Munk moment. Another mathematical model of a ship at a single point mooring was developed by Ractliffe and Clarke [1.10]. In the paper the effect of different parameters on the motions of the tanker are discussed. Selection and design methods of SPM terminals were discussed by Bliault and Stewart [1.11]. In their paper they highlighted the importance of model tests and mathematical models when selecting a SPM terminal. A stability analysis of tankers in single point moorings was carried out by Sørheim [1.12]. Sørheim stated that some general patterns of ship stability in SPM terminals could be given by a single formula assuming zero damping and small motion amplitudes. Molin and Bureau [1.13] presented a simulation model for the dynamic behaviour of single point moored tankers in waves, wind and current. Their model differs from Wichers' [1.6] in the ideal fluid-current force calculation. The "wave damping" was introduced by Wichers [1.14] in formulating the motion equation of a moored tanker in irregular head waves. Wichers stated that the motion equation with low frequency still water damping coefficient overestimated the experimental measurements whereas the inclusion of the wave damping in the motion equation provided a better correlation with the measurements. Wichers and van den Boom [1.15] presented a time domain modelling of combined high and low frequency motions of single point moored tankers. In the paper fluid reactive forces were taken into account by convolution integrals and first and second order wave forces were evaluated using impulse response techniques. Low frequency fluid reactive forces were experimentally determined in the paper for a range of relative current speeds, yaw velocities, loading conditions and water depths, then results were expressed in terms of Fourier series. Their formulations were also compared with the formulations given by Gerritsma et al [1.16], which consider three contributions to the overall flow: 1) ideal flow forces 2) forces due to viscous cross flow 3) lift forces generated by viscosity. A model to account for hull-propeller-rudder interactions was introduced by Oltmann and Sharma [1.17]. Later the same model was used by Jiang and Schellin [1.18], [1.19], [1.20] and [1.21] to carry out the stability analysis and motion simulation of a single point moored tanker. The stability of SPM

systems was also studied by Papoulias [1.22] and Bernitsas [1.23] and [1.24]. Wichers [1.25] and [1.26] presented recent developments in computer simulations of single point moored vessels. He carried out simulation calculations for two models. The first model was based on a 1-DOF system in which wave drift damping and viscous surge damping were examined in current and still water. The second model was on a 3-DOF system when Wichers compared his formulations of equations of motion with those given by Molin [1.13] and Obokata [1.27]. A semi empirical method with the use of experimental data to calculate the wave drift and viscous damping forces was also presented by Wichers [1.28]. Aghamohammadi and Thompson [1.29] carried out some experiments to investigate the large amplitude fish-tailing instabilities of a single point moored tanker. Effects of dynamic wind, current and waves on the stability of a single point moored tanker were investigated by de Kat and Wichers [1.30].

1.3 OBJECTIVES OF STUDY

As explained in the first section dynamic analysis of Single Point Mooring systems is necessary at the initial design stage of these systems.

The overall aim of this research is to study the environmental loading and motion response of moored objects such as moored buoys and Single Point Mooring Systems and to provide the designer with the tools that could be used at the design of these systems. In analysing the moored systems particular attention is given to the time domain simulation techniques. Wave forces acting on moored buoys are derived by using Morison's equation and time and frequency domain simulation techniques are utilized to analyse the motion characteristics of moored buoys. A vertical cylinder of elliptical cross sections is used to model the tanker in a CALM system. Hydrodynamic coefficients and wave forces obtained from the solution of diffraction and radiation problems of the elliptical cylinder are used in the time domain simulations. By modelling the tanker as an elliptical cylinder it is also possible to produce the wave forces at each time step without the need of creating a database since the wave forces on an elliptical cylinder is obtained semi analytically by using the Mathieu functions. Effect of dynamic wind and random

waves are also incorporated in the study. At each stage of the study prediction methods are validated by experiments.

1.4 STRUCTURE OF THESIS

The study starts with the motion response simulation of moored buoys. Chapter 2 is thus devoted to the motion response prediction of moored buoys. Wave forces acting on the buoy are calculated using Morison's Equation. Catenary equations are utilized to derive cable forces. Two different buoy geometries, cylindrical and conical, are considered in the study. Experimental measurements are compared with time and frequency domain modellings. In chapter 3, diffraction theory used to derive the wave forces is explained. The tanker is modelled as a vertical elliptical cylinder with a finite draught. Calculated wave forces are compared with Oortmerssen's experiments and with the results of a 3-D program developed by Chan. The water depth effect on wave forces is investigated. Program results for various angles of incidence and for different elliptic cylinders are presented. The second order mean force is calculated using the far-field approach, introduced by Maruo. Also the radiation problem of the tanker which is modelled as an elliptical cylinder is solved. Program results are compared with Oortmerssen's experiments and with Chan's 3-D program results. Program results for different cylinders and for different water depth/draught ratiou are presented. Chapter 4 describes a time domain model used to predict the motion responses of a tanker-buoy system under wave, wind and current loading. Motion equations of the tanker-buoy system are derived by using Cummins' method. Frequency-independent hydrodynamic coefficients and time histories of wave forces in irregular seas are calculated. Experimental measurements are compared with the time domain simulation results. In Chapter 5 the results of a series of parametric studies are presented. A computer program developed to predict the motion responses of the coupled tanker-buoy system is run for different parameters, such as; wave, wind and current angle of attacks, wind and current speed, elasticity of the mooring lines and the hawser line, buoy's and tanker's geometry, water depth, draught of the ship. Numerical aspects of the program, such as; solution of the differential equations, evaluation of the convolution integral are discussed. Chapter 6

describes the model tests performed in regular waves. Two sets of experiments are conducted. The first set of experiments aims to predict the motion responses of conical and cylindrical buoys, the second to predict the motion responses of the tanker-buoy system and the hawser line forces. Finally some conclusions are drawn in Chapter 7.

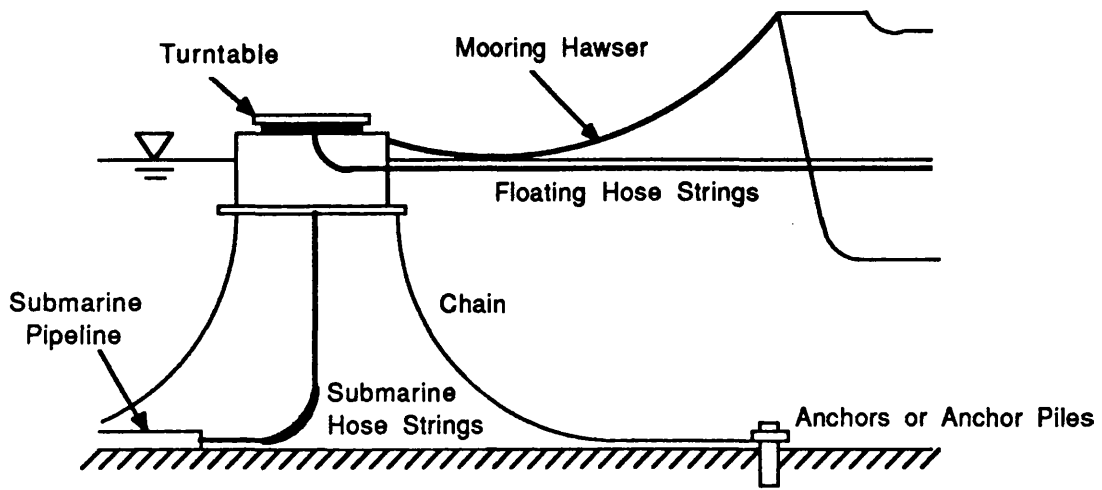


Fig. 1.1 CALM System

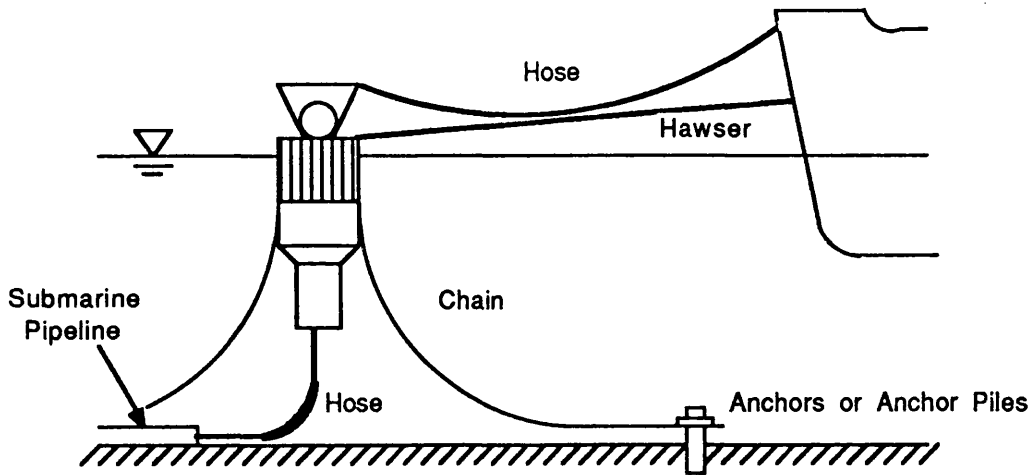


Fig. 1.2 ELSBM System

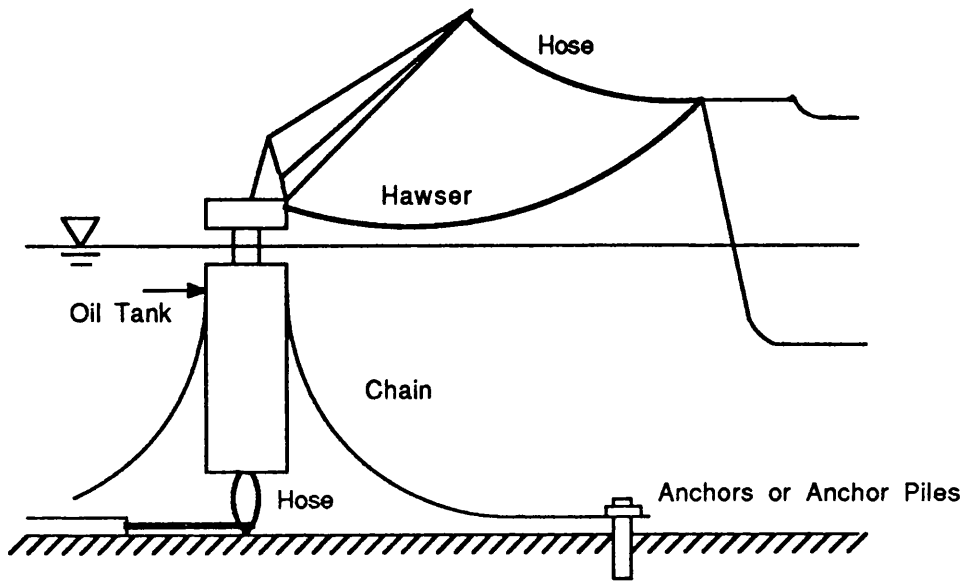


Fig. 1.3 SPAR

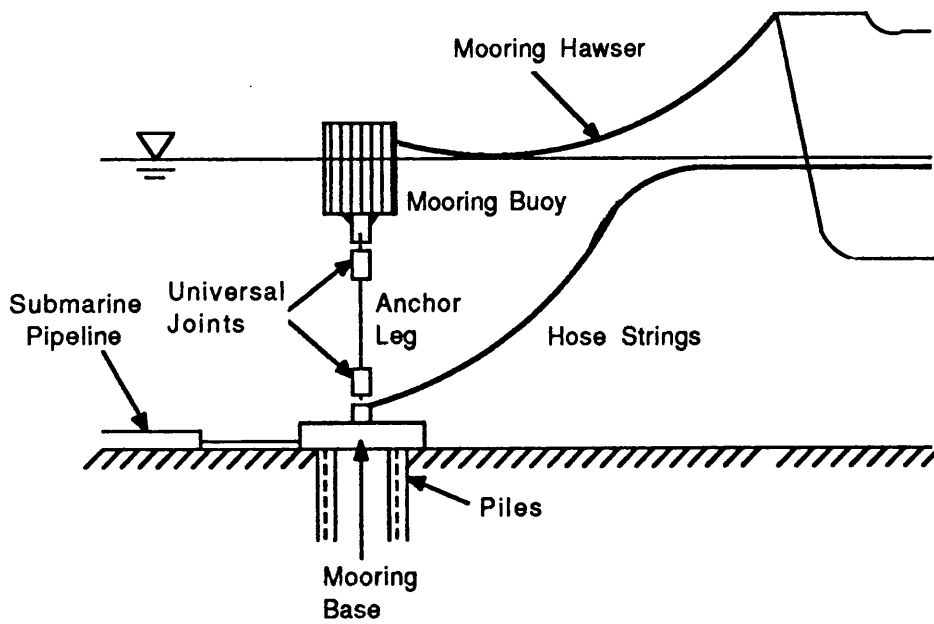


Fig. 1.4 SALM

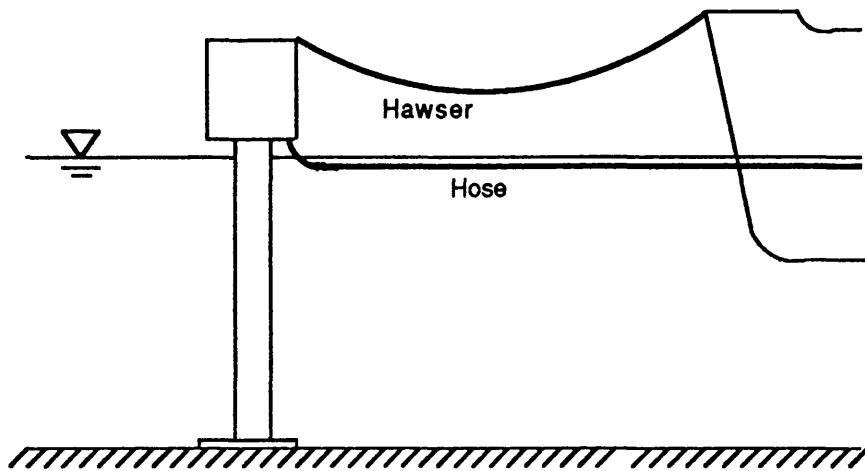


Fig. 1.5 Fixed Mooring Tower

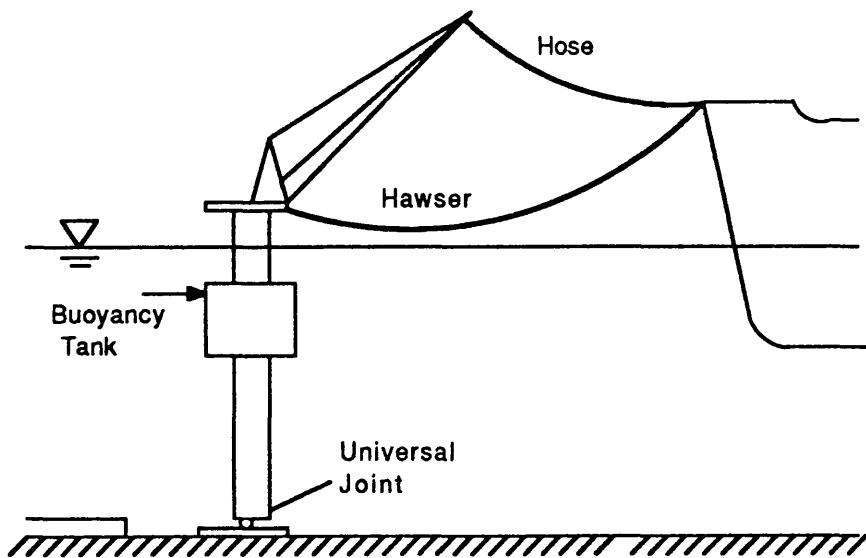


Fig. 1.6 Articulated Mooring Tower

CHAPTER 2

MOTION RESPONSE SIMULATION OF MOORED BUOYS

2.1 INTRODUCTION

In this chapter the motion response of moored buoys under environmental loading is predicted through time and frequency domain modelling and model tests. In the following sections of the chapter firstly wave forces acting on the buoy are predicted using Morison's Equation, secondly mooring forces are evaluated by making use of the catenary equations, lastly frequency and time domain simulation techniques are presented and compared with measurements. In the study two different buoy geometries, a circular cylinder and a right truncated circular cone (frustum), are considered.

The motion response prediction of moored buoys has been the subject of several investigations. Berteaux in his book entitled Buoy Engineering [2.1], presented a detailed study of the dynamics of buoys and mooring lines. Remery and Kokkeel [2.2] presented approximate methods to calculate the hydrodynamic loads acting on a cylindrical buoy and compared the estimated results with the results of exact computer calculations and with the results of model tests. It is claimed in the paper that approximations are accurate enough for comparison of the behaviour of different buoys. Arai and his colleagues [2.3], studied the motion of a CALM system. In their paper a design method for the mooring systems is given. In his paper (1977), Koterayama [2.4] carried out theoretical and experimental studies of a moored floating cylinder and dynamic tension of mooring lines in waves. He proposed an approximate method to calculate the dynamic tensions, in which inertia and hydrodynamic forces acting on the chain are taken into account. Harichandran [2.5] developed a tangent stiffness technique for the static analysis of a multi leg cable buoy system, in which an approximate method of accounting for the current drag forces is presented. In his thesis (1982), Tsiniyoglou [2.6] derived a time

domain model for moored buoys and applied cable mass modelling to the dynamic analysis of mooring lines. Nakajima [2.7], in his paper (1986), introduced a time domain simulation technique for moored buoys and also discussed numerical simulations of deep sea mooring lines. The lumped mass method was used in the paper for the dynamic analysis of mooring lines. In the present study time and frequency domain modelling of the motion responses of conical and cylindrical buoys will be presented. The equations in this chapter later will be used in formulating the motion equations of the tanker-buoy coupled system which features in chapter 5.

2.2 ENVIRONMENTAL LOADING ON BUOYS

2.2.1 Evaluation of Wave Forces Acting on the Buoy

In formulating the forces acting on a buoy placed in a wave field of monochromatic regular waves, the potential flow and Airy small amplitude wave theories are used. In formulating the motion equations of the moored buoy in frequency domain, buoy motion responses are assumed to be small enough so that the equations of motion of the buoy are linear. Morison's equation [2.8] is utilized in deriving the wave forces acting on the buoy. It has been proved by many researchers that Morison's equation is adequate for the calculation of wave forces on relatively small diameter cylinders provided that the diameter of the cylinder is less than one-fifth of the wave length [2.9]. As an alternative to the circular cylinder buoy geometry, a truncated circular cone (frustum) buoy form is considered to derive wave excitation forces and moments. In formulating the vertical forces, both dynamic pressure and wave acceleration induced forces acting on the bottom of the cylindrical and the conical buoy as well as the vertical component of the dynamic pressure and wave acceleration forces acting on the sides of the conical buoy are taken into account. In formulating the wave forces acting on the buoy a 2-Dimensional model was used. In the following, heave and surge forces and pitching moment formulations are derived for the conical buoy geometry.

Reference Systems

In formulating the wave induced force and moment equations, two right-handed rectangular co-ordinate systems were chosen. The first co-ordinate system which is referred to as the wave reference system [Oxyz] , was used to define wave kinematic equations , i.e. wave particular velocity and accelerations and dynamic wave pressure. The second co-ordinate system which is referred to as the structure co-ordinate system [GXYZ] was chosen to calculate wave excitation forces and moments as well as non-linear hydrostatic and mooring forces. The centre of gravity of the buoy was selected as the origin of the structure co-ordinate system which oscillates as the buoy moves in waves. The definition of the reference systems is illustrated in Fig. 2.1.

Heave Forces

The dynamic wave pressure and wave particle accelerations give rise to the major part of the heave force. In the following, vertical pressure and acceleration forces are calculated on a frustum geometry which is examined as an alternative configuration for the design of mooring buoys.

Total Heave Force:

$$F_{TH} = F_{AB} + F_{PB} + F_{PSy} \quad (2.1)$$

where F_{AB} is the acceleration force at the bottom of the frustum.

F_{PB} and F_{PSy} are the pressure forces at the bottom and the side of the frustum respectively.

Pressure force at the bottom of the frustum:

$$dF_{PB} = 0.5\rho gH_w \exp(-Hk)\cos(kR \cos\theta - \omega t)rdrd\theta$$

$$F_{PB} = 0.5\rho gH_w \exp(-Hk) \int_0^{2\pi} \int_0^R \cos(kR \cos\theta - \omega t)rdrd\theta \quad (2.2)$$

where k is the wave number

ρ is the water density

g is the gravity acceleration

H_w is the wave height

H is the draft of the frustum

R is the largest radius of the frustum

ω is the wave frequency

t is the time

Acceleration force at the bottom of the frustum:

$$F_{AB} = \frac{4}{3}\rho R^3(-0.5H_w\omega^2 \cos\omega t \exp(-Hk)) \quad (2.3)$$

where $\frac{4}{3}\rho R^3$ is added mass coefficient (k_M)

Additional forces due to dynamic wave pressure acting on the side of the frustum are also included in the heave force calculations. The side forces act in opposite direction to the forces at the bottom of the frustum and have a reducing effect on the total heave force.

Pressure force acting on the side of the frustum in y direction:

$$F_{PSy} = 0.5 \rho g H_w \sin\phi \int_{-H}^0 \int_0^{2\pi} \exp kz \cos(kR(z)\cos\theta - \omega t) R(z) d\theta dz \quad (2.4)$$

$$R(z) = r - \frac{R-r}{H} z \quad (2.5)$$

where $R(z)$ is the geometric definition of the frustum slope

r is the radius of the frustum on the water surface

The pressure and acceleration force equations can be expressed by taking into account the motions of the frustum as follows:

$$F_{PB} = 0.5 \rho g H_w \int_0^{2\pi R} \int_0^R \exp[k(-\beta_{31}r \cos\theta - \beta_{33}Z_G + x_1 - H + Z_G)] \cos[k(\beta_{11}r \cos\theta + \beta_{13}Z_G + x_2) - \omega t] r dr d\theta \quad (2.6)$$

$$F_{AB} = \frac{4}{3} \rho r^3 (-0.5 H_w \omega^2 \exp[k(\beta_{33}(-Z_G) + x_1 - H + Z_G)]) \cos[k(\beta_{13}Z_G + x_2) - \omega t] \quad (2.7)$$

$$F_{PSy} = 0.5 \rho g H_w \sin \phi \int_{-H+Z_G}^{Z_G} \int_0^{2\pi} \exp[k(-\beta_{31}R(Z) \cos\theta - \beta_{33}Z + x_1 - H + Z_G)] \cos[k(\beta_{11}R(Z) \cos\theta + \beta_{13}Z + x_2) - \omega t] R(Z) d\theta dZ \quad (2.8)$$

where x_1 is the heave motion, x_2 is the surge motion

Surge Forces

The pressure, acceleration and drift components of the surge force are calculated as follows:

Total Surge Force:

$$F_{TS} = F_{AH} + F_{DH} + F_{PH} \quad (2.9)$$

Acceleration force:

$$F_{AH} = \rho k_M \int_{-H}^0 \int_0^{2\pi} A_s u'_x d\theta dz \quad (2.10)$$

where k_M is added mass coefficient

$$A_s = R(z) d\theta dz$$

$$F_{AH} = 0.5 \rho k_M H_w \omega^2 \int_{-H}^0 \int_0^{2\pi} \exp kz \sin(-\omega t) R(z) d\theta dz \quad (2.11)$$

where A_s is the projection area

u'_x is the acceleration of the water particle in the x direction

Drift force acting in x direction:

$$F_{DH} = 0.5 \rho \int_{-H}^0 C_D u_x |u_x| 2R(z) dz \quad (2.12)$$

$$F_{DH} = 0.5 \rho C_D (0.5 H_w \omega)^2 \cos(-\omega t) |\cos(-\omega t)| \int_{-H}^0 2 \exp(2kz) R(z) dz \quad (2.13)$$

where C_D is the drag coefficient

u_x is the velocity of the water particle in the x direction

Pressure force acting in x direction:

$$F_{PH} = 0.5 \rho g H_w \cos \phi \int_{-H}^0 \int_0^{2\pi} \exp kz \cos(kR(z) \cos \theta - \omega t) R(z) d\theta dz \quad (2.14)$$

The surge force expression written above can also be expressed by taking into account the motions of the frustum as follows:

$$F_{AH} = 0.5 \rho k_M H_w \omega^2 \int_{-(H-Z_G)}^{Z_G} \exp[k(-\beta_{33}Z - H + Z_G + x_1)] \sin[k(\beta_{13}Z + x_2) - \omega t] R(Z)^2 \pi dZ \quad (2.15)$$

$$F_{DH} = \frac{1}{4} \rho C_D (H_w \omega)^2 \int_{-(H-Z_0)}^{Z_0} R(Z) \exp[2k(-\beta_{33}Z - H + Z_G + x_1)] \cos[k(\beta_{13}Z + x_2) - \omega t] \left| \cos[k(\beta_{13}Z + x_2) - \omega t] \right| dZ \quad (2.16)$$

Pitch moments due to Heave forces

Pitch moment due to pressure force acting at the bottom of the frustum:

lever = $R \cos \theta$

$$M_{PB} = 0.5 \rho g H_w \int_0^{2\pi R} \int_0^{2\pi} \exp(-\beta_{31}r \cos \theta - \beta_{33}Z_G + x_1 - H + Z_G) \cos[k(\beta_{11}r \cos \theta + \beta_{13}Z_G + x_2) - \omega t] r \cos \theta r dr d\theta \quad (2.17)$$

Pitch moment due to pressure force acting on the side of the frustum:

lever = $R(z) \cos \theta$

$$M_{PS} = \sin(\phi) 0.5 \rho g H_w \int_{H-Z_0}^{Z_0} \int_0^{2\pi} \exp[k(-\beta_{31}R(Z) \cos \theta - \beta_{33}Z + x_1 - H + Z_G)] \cos[k(\beta_{11}R(Z) \cos \theta + \beta_{13}Z + x_2) - \omega t] R(Z) \cos \theta R(Z) d\theta dZ \quad (2.18)$$

Pitch moment due to Surge forces

Pitch moment due to the wave acceleration force:

lever = $Z_G + x_1$

$$M_{AS} = 0.5 \rho \cos^2 \phi H_w \omega^2 \int_{-(H-Z_0)}^{Z_0} \exp[k(-\beta_{33}Z - H + Z_G + x_1)] \sin[k(\beta_{13}Z + x_2) - \omega t] (Z_G + x_1) R^2(Z) \pi dZ \quad (2.19)$$

Pitch moment due to the drift force:

lever = Z

$$M_{DS} = \frac{1}{4} \rho C_D (H_w \omega)^2 \int_{-(H-Z_0)}^{Z_0} R(Z) \exp[2k(-\beta_{33}Z - H + Z_0 + x_1)] \cos[k(\beta_{13}Z + x_2) - \omega t] \cos[k(\beta_{13}Z + x_2) - \omega t] Z dZ \quad (2.20)$$

Pitch moment due to pressure force acting on the side of the frustum is calculated as follows:

lever= Z

$$M_{PSH} = \iint F_{PH} Z \quad (2.21)$$

2.2.2 Effect of Current and Wind

2.2.2.1 Current Forces

Currents often have a velocity profile that decays very slowly with depth. Current can be expected to have an influence over the whole immersed length of the structure. The presence of current has several effects that need to be taken into account in force calculations.

Firstly, current affects the water particle velocities of the surface waves. The drag force on a member is proportional to the square of wave particle velocities, and current with a low velocity may have a significant effect, particularly at large depths. This effect is very important for slender members, since the Morison equation used to calculate the forces on such members is modified both through the velocities and the coefficient C_D . The inertia force is not modified in this way, as it is assumed to be proportional to the water particle accelerations.

$$F_D = \frac{1}{2} \rho C_D A_p (V_x + V_c \cos \alpha) \left[(V_x + V_c \cos \alpha)^2 + V_c^2 \sin^2 \alpha \right]^{1/2} \quad (2.22)$$

where C_D is the drag coefficient

V_x is the water particle velocity due to waves in the x direction

V_c is the steady uniform horizontal current velocity

α is the angle between the direction of current and x direction

A_p is the projection area

Secondly, current will also modify the surface wave field by altering the wave amplitude, the velocity of wave propagation and the wave length.

$$\omega' = \omega - V_c k \cos \alpha \quad (2.23)$$

where ω' is the modified frequency

ω is the frequency due to waves

k is the wave number, equal to $2\pi / \lambda$

λ is the wave length

The effects of vortex shedding will not be considered here.

2.2.2.2 Wind Forces

Calculation of wind forces on structures is a very difficult task so empirical formulas have to be used. The wind flow is largely determined by the Reynolds number and the wind forces are calculated using a Morison type equation. Only the drag term of the Morison equation is important, because of the relatively low density and high compressibility of the air. Vortex shedding may occur causing vibration transverse to the flow direction. We may write the wind pressure at a point as:

$$P(t) = \frac{1}{2} \rho_a C_d V^2(t) \quad (2.24)$$

where $P(t)$ is the time-dependent pressure

ρ_a is the density of air

C_d is a drag coefficient that depends on the geometrical shape

$V(t)$ is the time-dependent wind velocity

Mean pressure is obtained by neglecting the fluctuating component of the velocity and pressure,

$$\bar{P} = \frac{1}{2} \rho_a C_d \bar{V}^2 \quad (2.25)$$

where \bar{V} is the mean velocity
and the wind force is expressed as:

$$F_{\text{wind}} = \frac{1}{2} \rho_a C_d \bar{V}^2 A_p \quad (2.26)$$

where A_p is the projected area of the buoy, exposed to the wind

2.3 EVALUATION OF MOORING FORCES

The mooring line is required to provide a holding force and at the same time it is subjected to environmental excitation. As a result the mooring line assumes various configurations changing with time. Since the cable cannot handle compression and, as explained below, a negative tension usually results in unsatisfactory mooring behaviour, a successful design must guarantee positive tensions at all times.

In order to guarantee positive tensions sufficiently large mean forces must be applied which in turn imply larger cable diameter and high cost. It must be noted that mooring lines are used to offset steady forces, while oscillatory forces usually deteriorate their performance especially when they are close to the natural frequencies of the line. Since most oscillatory forces are caused by the waves one must make sure that the floating vessel and mooring system will perform satisfactorily given the specific environmental conditions.

In most cases a mooring line assumes a slowly changing mean position around which it performs oscillations. A significant simplification results since we can separate a static solution referring to the slowly changing position, and a dynamic solution referring to the deviations from the static solution. As mentioned above the static solution is of primary interest since it provides the holding forces. The dynamics of a mooring line are mathematically a very difficult problem and computer solutions using some numerical scheme are not trivial. The numerical stability of the solution is not guaranteed and usually depends on the parameters of the system.

Catenary Solution: In the case of a heavy chain with significant sag, the effects of extensibility are negligible and the weight is the principal load, if the current has a small to moderate velocity.

A typical differential cable element is shown in the Fig.2.2. The static equilibrium equations are:

$$y' = \frac{dy}{dx} = \sinh \left[\frac{wx}{T_0} + \sinh^{-1}(\tan \theta_s) \right] \quad (2.27)$$

$$l = \frac{T_0}{w} \left[\sinh \left(\frac{wx}{T_0} + \sinh^{-1}(\tan \theta_s) \right) - \tan \theta_s \right] \quad (2.28)$$

$$y = \frac{T_0}{w} \left[\cosh \left(\frac{wx}{T_0} + \sinh^{-1}(\tan \theta_s) \right) - \cosh(\sinh^{-1}(\tan \theta_s)) \right] \quad (2.29)$$

If $\theta_s = 0$ then ;

$$y' = \frac{dy}{dx} = \sinh \left(\frac{wx}{T_0} \right) \quad (2.30)$$

$$l = \frac{T_0}{w} \left[\sinh \left(\frac{wx}{T_0} \right) \right] \quad (2.31)$$

$$y = \frac{T_0}{w} \left[\cosh\left(\frac{wx}{T_0}\right) - 1 \right] \quad (2.32)$$

and the vertical tension on the line is,

$$T_z = wl \quad (2.33)$$

In Appendix A, a solution algorithm based on the method by Orgill et al [2.10] is given. However, the formulas could be used in a more practical way. From Fig. 2.3 the horizontal distance X_T between the anchor and the attachment point of the mooring line on the vessel could be written as follows,

$$X_T = l - l_s + x_s \quad (2.34)$$

By using Equation (2.31) and (2.32) the following relation between h and l_s can be written,

$$l_s^2 = h^2 + 2ha \quad (2.35)$$

By using Equation (2.35) to express l_s and Equation (2.32) to express x_s , the relation between X_T and T_0 can be written as,

$$X_T = l - h \left(1 + 2 \frac{a}{h} \right)^{\frac{1}{2}} + a \cosh^{-1} \left(1 + \frac{h}{a} \right) \quad (2.36)$$

where

$$a = \frac{T_0}{w} \quad (2.37)$$

By using Equation (2.36) and (2.33) horizontal force-horizontal displacement and vertical force-horizontal displacement are plotted in Figs. 2.4 and 2.5. Also horizontal force-vertical displacement and vertical force-vertical displacement are calculated by keeping X_T constant in Equation (2.36) (Figs. 2.6 and 2.7).

The procedure outlined for one cable could be generalized for multi-cable systems (Fig. 2.8 and 2.9). Horizontal and vertical forces and yaw and pitch moments can be written as follows,

$$\begin{aligned}
 F_x^M &= \sum_{i=1}^n T_{0i} \cos \phi_i \\
 F_z^M &= \sum_{i=1}^n T_{zi} \\
 F_\phi^M &= \sum_{i=1}^n T_{0i} (x_i \sin \phi_i - y_i \cos \phi_i) \\
 F_\theta^M &= \sum_{i=1}^n (T_{0i} z_i + T_{zi} x_i)
 \end{aligned} \tag{2.38}$$

2.4. MOTION RESPONSES OF THE BUOY UNDER WAVE EXCITATION IN FREQUENCY DOMAIN

Heave, surge and pitch motion equations of the cylindrical and conical buoy were solved in the frequency domain.

Heave Response of the cylindrical buoy: A differential equation representing the heave motion of the cylindrical buoy can be written as:

$$A_z \ddot{z} + c_z \dot{z} + k_z z = F_v \tag{2.39}$$

where $A_z = \text{Mass} + \text{Added mass in heave}$

$$= \rho g R^2 H + \frac{4}{3} \rho R^3 \quad (2.40)$$

c_z is the damping coefficient

k_z is the restoring term

$$= \rho g A_w + k_m = \rho g \pi R^2 + k_m \quad (2.41)$$

F_v is the vertical force and consists of in-phase out-phase components.

$$F_v = A \sin \omega t + B \cos \omega t \quad (2.42)$$

Where $A = 0$, $B = 0.5 \rho g H_w e^{-Hk} \pi R^2 + \frac{4}{3} \rho R^3 (-0.5 H_w \omega^2 e^{-Hk}) +$

$$+ 0.5 \rho g H_w \int_{-H}^0 \int_0^{2\pi} e^{kz} \cos(kR(z) - \omega t) R(z) d\theta dz$$

Solution of the differential equation will be in the following form,

$$z = Z_1 \sin \omega t + Z_2 \cos \omega t \quad (2.43)$$

If Equation (2.43) is substituted in (2.39), coefficients of the solution are obtained

as:

$$Z_1 = \frac{A'(\omega_n^2 - \omega^2) + 2\xi\omega_n\omega B'}{(\omega_n^2 - \omega^2)^2 + (2\xi\omega_n\omega)^2} \text{ and } Z_2 = \frac{B'(\omega_n^2 - \omega^2) + 2\xi\omega_n\omega A'}{(\omega_n^2 - \omega^2)^2 + (2\xi\omega_n\omega)^2} \quad (2.44)$$

where $A' = A / A_z$, $B' = B / A_z$, $\omega_n^2 = k_z / A_z$ and $2\xi\omega_n = c_z / A_z$

ω_n is the natural frequency of the system

ξ is a dimensionless quantity called viscous damping factor

$$\xi = \frac{c_z}{c_{cr}} \quad (2.45)$$

where c_{cr} is the critical damping coefficient $c_{cr} = 2A_z\omega_n = \frac{2k_z}{\omega_n}$

Heave Response of the conical buoy: A differential equation representing the heave motion of the frustum will be similar to Equation (2.39). However, the added mass of the frustum will be calculated as follows:

$$A_z = \frac{1}{3}\pi H(r^2 + rR + R^2) + \frac{4}{3}\rho R^3 + \frac{4}{3}\rho R_E^3 \sin^2 \alpha \quad (2.46)$$

$$R_E = \sqrt{\frac{S}{\pi}} \quad (2.47)$$

where S is the lateral surface area of the frustum.

$$S = \pi(r + R)\sqrt{H^2 + (R - r)^2} \quad (2.48)$$

$$\sin \alpha = \frac{R - r}{\sqrt{(R - r)^2 + H^2}} \quad (2.49)$$

Due to the geometrical configuration of the frustum, stiffness term in the motion equation will be non-linear. However In order to solve the differential equation in the frequency domain, we assume that the stiffness term linearly changes with the heave motion. The solution of the differential equation will be equal to the expressions (2.43) and (2.44) except for the added mass term.

Surge Response of the cylindrical buoy: It is represented by a differential equation as follows:

$$A_x \ddot{x} + c_x \dot{x} + k_x x = F_H \quad (2.50)$$

where $A_x = \text{Mass} + \text{Added mass for surge}$

$$= \frac{1}{4} C_M \rho \pi D^2 H \quad (2.51)$$

D is the diameter of the cylinder

c_x is the damping coefficient

k_x is the restoring term due to the mooring lines

F_H is the horizontal force consisting in-phase and out-phase components

$$F_H = A \sin \omega t + B \cos \omega t \quad (2.52)$$

A and B in Equation 2.52 are as follows:

$$A = 0.5 \rho k H_w \omega^2 \int_{-H}^0 \int_0^{2\pi} e^{kz} R(z) d\theta dz$$

$$B = 0.5 \rho C_D (0.5 H_w \omega)^2 |\cos(\omega t)| \int_{-H}^0 2 e^{2kz} R(z) dz +$$

$$+ 0.5 \rho g H_w \cos \phi \int_{-H}^0 \int_0^{2\pi} e^{kz} R(z) d\theta dz$$

$\cos(\omega t)|\cos(\omega t)|$ term in the above equation can be linearized by representing this term in Fourier series. If the first term of the Fourier series only is taken into account, then the nonlinear term can be expressed as follows:

$$\cos(\omega t)|\cos(\omega t)| \approx \frac{8}{3\pi} \cos(\omega t)$$

The solution of the differential Equation (2.50) is similar to the solution of Equation (2.39).

Surge Response of the conical buoy: A differential equation representing the surge motion of the frustum will be similar to the Equation (2.50). However, the added mass of the frustum will be calculated as follows:

$$A_x = \frac{1}{3} \pi H C_M (r^2 + rR + R^2) \quad (2.53)$$

Solution of the differential equation will be equal to the expressions (2.43) and (2.44) except for the added mass term.

Pitch Response of the cylindrical buoy: A differential equation representing the heave motion of the cylindrical buoy can be written as:

$$I_p \ddot{\theta} + c_p \dot{\theta} + k_p \theta = M_p \quad (2.54)$$

where I_p = Moment of Inertia of mass and added mass

$$I_p = I_v + I_{avm}$$

$$I_v = \frac{1}{12} m(l^2 + 3R^2) \quad (2.55)$$

$$I_{avm} = \int_{-Z_G}^{H-Z_G} \pi R^2 \rho z^2 dz \quad (2.56)$$

$$= \frac{1}{3} \pi \rho R^2 [(H - Z_G)^3 + Z_G^3]$$

$$I_p = \frac{1}{12} m(l^2 + 3R^2) + \frac{1}{3} \pi \rho R^2 [(H - Z_G)^3 + Z_G^3] \quad (2.57)$$

c_p is the damping coefficient

k_p is the restoring term

M_p is the pitching moment

$$k_p = \rho g m G M \quad (2.58)$$

where m is the mass of the cylinder

$G M$ is the metacentric height

Differential equation (2.54) could be solved in a similar way to the others.

Pitch Response of the conical buoy: A differential equation representing the pitch motion of the frustum will be similar to Equation (2.54). However, the moment of inertia and added mass, and restoring term of the frustum will be calculated as follows.

Moment of inertia of mass and added mass will be calculated first,

$$I_v = \frac{1}{36} m \left[9(R^2 + r^2) + \frac{2l^2}{(R^2 + r^2)^2} (R^2 + 4Rr + r^2) \right] \quad (2.59)$$

$$m = \rho \pi t (R + r) [l^2 + (R - r)^2]^{\frac{1}{2}} \quad (2.60)$$

l is the whole height of the frustum

t is the thickness

$$I_{avm} = \int_{-Z_G}^{H-Z_G} \rho \pi R^2(Z) z^2 dz \quad (2.61)$$

$$= \rho \pi \left[r^2 \left(\frac{(H - Z_G)^3}{3} + \frac{Z_G^3}{3} \right) + 2r \frac{R - r}{H} \left(-\frac{(H - Z_G)^4}{4} + \frac{Z_G^4}{4} \right) \right]$$

$$+ \frac{(R - r)^2}{H^2} \left(\frac{(H - Z_G)^5}{5} + \frac{Z_G^5}{5} \right) \right] \quad (2.62)$$

Restoring force due to the under water geometry is calculated as follows:

$$k_p = \rho g \nabla GM \quad (2.63)$$

where GM is the metacentric height = KB + BM - KG

$$KB = \frac{H(R + 2r)}{3(R + r)} \quad (2.64)$$

$$KG = \frac{l(R + 2r')}{3(R + r')} \quad (2.65)$$

r' is the smallest radius of the frustum

$$BM = H \frac{r^2}{4} \quad (2.66)$$

2.5 TIME DOMAIN ANALYSIS OF MOTION RESPONSES OF MOORED BUOYS UNDER WAVE EXCITATION

In this section coupled heave, surge and pitch motion equations are derived and solved in the time domain. Nonlinear restoring terms due to variations in the under water geometry of the buoy and due to variations in the geometry of cables are introduced. All differential equations are derived and solved for the conical buoy. In order to simulate the motion of the cylindrical buoy, maximum and minimum diameters of the conical buoy are chosen equal to each other.

Heave Response : A differential equation representing the heave motion of the buoy can be written as:

$$A_z \ddot{z} + b_{zz} \dot{z} + \frac{1}{2} \rho C_{Dy} A_w \dot{z} |\dot{z}| + \rho g \frac{\pi}{3} \left(\frac{R-r}{H} \right)^2 z^3 + \rho g \frac{\pi}{3} \left(-3r \frac{R-r}{H} \right) z^2 + \rho g \frac{\pi}{3} (3r^2) z + F_w(z, x) = F_v(z, x, \theta) \quad (2.67)$$

Firstly, the heave restoring force due to variation in the under water geometry will be introduced. Let us assume that the frustum is displaced upwards from its stable position in calm water. The volume emerged from the water will give rise to the restoring force.

$$\text{Vol} = \frac{\pi}{3} z \left[\left(\frac{R-r}{H} \right)^2 z^2 - 3r \frac{R-r}{H} z + 3r^2 \right] \quad (2.68)$$

$$\text{Force} = \rho g \frac{\pi}{3} \left(\frac{R-r}{H} \right)^2 z^3 + \rho g \frac{\pi}{3} \left(-3r \frac{R-r}{H} \right) z^2 + \rho g \frac{\pi}{3} (3r^2) z \quad (2.69)$$

Secondly, restoring forces due to changes in the geometry of cables will be introduced. Mooring forces were calculated in section 2.3. The vertical mooring force will be the restoring force for the buoy in heave motions and it depends on both the vertical and horizontal motions of the buoy. In order to express the relation between vertical mooring force and vertical(horizontal) displacement, a curve fitting method (weighted least-squares polynomials) was used. This method determines least-squares polynomial approximations of degrees 0,1,...,K to the set of data points with weights. Each polynomial is represented in Chebyshev-series form with normalized argument. This argument lies in the range -1 to +1 and is related to the original variable by the linear transformation. This curve-fitting routine ,E02ADF, can be found in the NAG Fortran library, Mark 12. In order to use the vertical mooring forces in time domain simulation, depending on both vertical and horizontal displacement of the buoy, a set of data was created by using the least-squares polynomial(Chebyshev-series form) approximations.

Thirdly, potential damping will be introduced. it will be observed that the damping causes a loss of kinetic energy of the structure's motion that corresponds to the energy of the outgoing waves. This consideration has led to the idea that the damping due to outgoing waves should be related to the excitation force on the structure due to incoming waves [2.11].

$$b_{zz}(\omega) = 2\pi c_f \left(\frac{F_v(\omega)}{\frac{H_w}{2}} \right)^2 \quad (2.70)$$

$$c_f = \frac{\omega^3 \cosh^2(kh)}{4\pi\rho g^3 kh \tanh\left(kh \left[1 + \frac{\sin(2kh)}{2kh}\right]\right)} \quad (2.71)$$

where k is the wave number and h is the water depth

Lastly, viscous damping is calculated as follows:

$$c_z = \frac{1}{2}\rho C_{Dz} A_w \dot{z}|\dot{z}| \quad (2.72)$$

where A_w is the waterplane area $A_w = \pi r^2$

C_{Dz} is the drag coefficient in heave

$F_v(z, x)$ is the restoring force due to the cables in heave motion

Mass and added mass term, A_z , will be calculated according to expression (2.46)

Surge Response : A differential equation representing the surge motion of the buoy can be written as:

$$A_x \ddot{x} + b_{xx} \dot{x} + c_x + F_{in}(z, x) = F_h(z, x, \theta) \quad (2.73)$$

Mass and added mass term, A_x , will be equal to expression (2.53). Viscous damping in surge is calculated as follows:

$$c_x = \frac{1}{2} \rho C_{Dx} \int_{-Z_0}^{H-Z_0} 2R(Z) (\dot{x} + Z\dot{\theta}) |\dot{x} + Z\dot{\theta}| dZ \quad (2.74)$$

where $\dot{\theta}$ is the angular velocity for pitch motion

\dot{x} is the velocity in the horizontal direction

C_{Dx} is the drag coefficient in surge

In order to calculate the mooring stiffness due to the horizontal excursion of the buoy, firstly a force-excursion curve is obtained for one cable by Chebyshev curve-fitting approximation. These results are, then extended for all mooring lines. In the last step data for force-excursion curves for all mooring lines and for different drafts are generated. $F_{ah}(z, x)$ is the restoring force due to the cables for surge.

Potential damping coefficient for surge is calculated as follows,

$$b_{xx}(\omega) = \pi c_f \left(\frac{F_H(\omega)}{\frac{H_w}{2}} \right)^2 \quad (2.75)$$

Pitch Response: A differential equation representing the pitch motion of the buoy can be written as:

$$(I_v + I_{svm})\ddot{\theta} + M_D\dot{\theta} + b_{\theta\theta}\dot{\theta} + mGM\sin\theta + k_{ps} = M_p \quad (2.76)$$

The moment of inertia of mass and added mass are equal to expressions (2.59) and (2.60) respectively and viscous damping is calculated as follows:

$$dM_D = \frac{1}{2} \rho C_{Dx} (\theta\omega z)^2 z A_p \quad (2.77)$$

where A_p is the projected area, $A_p = R(z)dz$

$$M_D = \int_{y=Z_0}^{H-Z_0} \frac{1}{2} \rho C_{Dx} \theta^2 \omega^2 z^3 \left(r - \frac{R-r}{H} z \right) dz \quad (2.78)$$

$$M_D = \rho C_{Dx} \theta^2 \omega^2 \left[\frac{r}{4} ((H-Z_G)^4 - Z_G^4) - \frac{R-r}{5H} ((H-Z_G)^5 + Z_G^5) \right] \quad (2.79)$$

Potential damping is calculated as follows:

$$b_{\theta\theta}(\omega) = \pi c_f \left(\frac{M_p(\omega)}{\frac{H_w}{2}} \right)^2 \quad (2.80)$$

Restoring force due to the under water geometry is equal to expression (2.63). GM is the metacentric height = KB + BM - KG. KB, KG and BM are equal to expressions (2.64), (2.65) and (2.66) respectively.

Solution of the motion equations: In order to solve heave, surge and pitch motion equations, a variable-order variable-step Adams differential equation solver was used. This method integrates a system of first-order ordinary differential equations over a range with suitable initial conditions. Firstly, this system of ordinary differential equations was written in first-order form. Therefore instead of having three second-order differential equations, we have six first-order differential equations. Starting from initial values of the dependent variables (solution) at a given point, the numerical solution is obtained by a step-by-step calculation which gives approximate values of the variables at finite intervals over the required range. The system adjusts the step-length automatically to meet specified accuracy tolerances. This routine ,D02CBF, can be found in NAG Fortran Library, Mark 12.

2.6 APPLICATIONS AND COMPARISONS

In order to solve the motion equations for cylindrical buoy in the frequency domain, a program ,HYD, was written. This program calculates wave excitation forces and motion equations in heave, surge and pitch. Dimensions of cylinder, wave height, damping coefficient, drag coefficient, mass coefficient, density of sea water, gravity acceleration and frequency (independent variable) are the input data for this program. Another program ,HYDCON, performs the same calculations for a conical buoy. The only differences in the input data are the dimensions of the conical buoy. In order to calculate the pressure force on the side of the frustum, a two dimensional integral was evaluated by using an adaptive deterministic routine ,D01FCF, NAG Fortran Library, Mark 12. HYDCON also uses a function subroutine ,FS, in which the integrand has been written.

HYDCOT9 and HYDCOT10 were written to calculate the motion responses in the time domain for a frustum and a cylinder respectively. These programs calculate wave excitation forces and motion equations in heave, surge and pitch. In addition to the data used in the frequency domain calculations, metacentric height, vertical distance between the centre of gravity and the reference system and mooring forces as a function of both vertical and horizontal excursion of the upper end of the cable are the input data for these programs. In order to calculate the two and one dimensional integrals in force and moment calculations, NAG Fortran Library routines D01FCF and D01DAF were used respectively. Some function subroutines, FS1, FS, FS2, FS3, FSTS, FS1P, FSP, FS2P, FST, FSPD, were used to supply the integrands for integral evaluating routines. Subroutine FCN was used to evaluate the first-order differential equations. Subroutine OUT was used to obtain access to intermediate values of the computed solution, at successive points. Functions CXX, XYH1, SINT, YY, CXY, XYH2, IUOK, PMDS were used to interpolate the mooring forces in the intermediate points, regarding both horizontal and vertical excursions of the attachment point.

STIFF9 was written to produce the force-excursion data to be used in the program HYDCOT9 and HYDCOT10. This program firstly produces the force-excursion data for one cable and then computes weighted least-squares polynomial approximations to this set of data. In order to perform this curve-fitting, the routine ,E02ADF-NAG Fortran Library-Mark12, was used. Secondly, force-excursion data were produced for all cables and different positions of the buoy.

Programs HYD and HYDCON were run to produce wave exciting forces and moments and motion responses for the cylinder and the frustum. Wave exciting forces and moments and the resulting responses for the cylinder and the frustum are shown in Figs. 2.10 and 2.11 respectively.

In order to investigate the effects of non-linearities and of coupling between the different modes of motion, motion equations were solved in the frequency domain by calculating wave and rigid-body motion induced forces and moments on the buoys at the still water level and thus ignoring the non-linearities and coupling. Comparisons between the results obtained from the time domain simulations and those obtained from the frequency domain are shown in Figs. 2.12 and 2.13.

The heave response curves given in Figs 2.12 and 2.13 show that non-linear time domain predictions correlate better with measurements than linear frequency domain predictions. This may be explained by the fact that the non-linear time domain approach models the stiffness characteristics due to hydrostatic and mooring lines more accurately and therefore a significant difference occurs between the results obtained from the two methods in the frequency region where motion responses are controlled by the restoring forces.

Surge response curves show a significant shift at the maximum response values corresponding to the natural surge frequency region. This can be attributed to the different surge stiffness modelling employed in the linear frequency as against the non-linear time domain prediction method. However both prediction methods yield significantly higher

results than experimental measurements. This may be due to the inertia coefficients used in the wave force formulations being higher than they actually should be.

As with surge responses, predicted pitch response values are higher than the measured experimental pitch responses and the difference may also be due to the high wave force coefficients used in the predictions.

In order to investigate the effect of the linear and nonlinear modelling of the mooring lines and the effect of the wave height on motion responses of a moored buoy, computer program 'HYDCOT9' which simulates motions of a moored buoy was used. Catenary equations were used in modelling the nonlinear cables (Fig. 2.14). Table 2.1 shows a comparison of linear and nonlinear cables. It is clearly seen from the table that the motion equations with nonlinear cable modelling give bigger motion response values than the linear cable modelling. The difference is especially clear around the natural frequency region of surge and pitch motions. Another noticeable difference between the models is that the surge natural frequency of the nonlinear cable modelling is higher than the linear cable modelling. The reason for this is that the equation of motion for nonlinear modelling resembles Duffing's equation in which the stiffness term consists of a linear and a cubic term. It is the presence of the cubic term that causes the increase in natural frequency (Sincock [2.13]).

With an increase in the wave height from 4 m to 12 m the difference in motion responses between the linear and nonlinear cable modellings widens (Table 2.1 and 2.2) (from %5 to %10). Examples of simulations and a corresponding F.F.T. analysis are presented in Figs. 2.15-2.20. As is seen from a comparison of Figs. 2.15 and 2.16, the nonlinear cable simulation includes superharmonic motion together with the usual, dominant oscillations at wave frequency. Superharmonic response occur at 0.095 rad/sec which is the natural frequency of the surge motion. Pitch response in Fig. 2.17 exhibits superharmonic response at a frequency of 0.31, very close to the pitch natural frequency, 0.27. Surge response in the same figure is increasing steadily up to 300 secs. It is interesting to note that in Figs. 2.18, 2.19 and 2.20 there are superharmonics in heave

and surge responses at twice the wave frequency. Subharmonic responses are also noticeable in high frequencies (Figs. 2.19 and 2.20). Some of these subharmonics correspond to the natural frequencies of heave, surge and pitch motions and occur at fractions of the wave frequency. This behaviour with sub and superharmonics is a characteristic of nonlinear systems which are distinct from the response of linear systems.

2.7 CONCLUSIONS

A calculation procedure to predict the non-linear coupled large amplitude motions of a conical and a cylindrical buoy was presented. Comparisons of the motion response predictions with measurements show an acceptable degree of correlation.

The formulations which took into account the non-linearities in hydrodynamic and restoring forces gave larger response values than those derived in the frequency domain with linearity assumptions.

Comparisons between the motion performance of the conical buoy and that of the cylindrical buoy indicate that the heave and pitch motions of the conical buoy are significantly less than those of the cylindrical buoy. Although the heave response amplitude values are similar to each other for conical and cylindrical buoy forms since the heave response amplitude curve of the cylindrical buoy has a wider band than that of the conical form spectral analysis gives much more significant motion response values for the cylindrical buoy. When a Pierson-Moskowitz spectrum with the wind speed of 22 m/sec was applied to predict the heave and pitch motion response values of the conical and cylindrical buoys, significant heave motion response amplitudes of 4.13 and 4.09 m and pitch response values of 8.37 and 2.42 degree were obtained for the cylinder and frustum forms respectively. It may therefore be concluded that a conical form gives a better motion performance than does a cylindrical buoy.

Simulation with the nonlinear cable modelling gives bigger motion response values than the simulation with linear cable modelling. Also the natural frequencies of the buoy shift towards higher frequencies with nonlinear cable modelling.

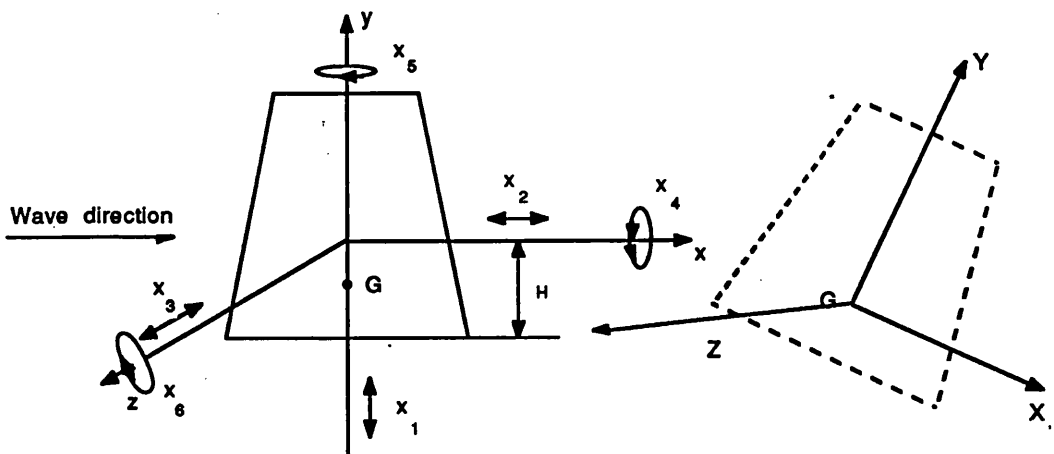
As wave height increases, the difference in motion responses between linear and nonlinear cable modelling widens (from %5 to 10%). After the F.F.T. analysis of the motion responses obtained from the nonlinear time domain predictions were carried out, together with the oscillations at wave frequency, some superharmonic motions at twice the wave frequency and subharmonics at fractions of the wave frequency were detected.

FREQUENCY [RAD/SEC]	SURGE (m)		PITCH (deg)		HEAVE (m)	
	LINEAR	NON-LINEAR	LINEAR	NON-LINEAR	LINEAR	NON-LINEAR
0.018	0.528	0.068	0.002	0.007	1.811	1.811
0.040	5.594	0.429	0.017	0.043	1.977	1.976
0.100	2.366	12.361	0.117	1.665	1.973	1.972
0.200	2.048	2.571	0.787	0.931	2.005	2.006
0.273	1.939	2.169	2.715	2.842	2.033	2.035
0.300	1.942	2.134	2.440	2.508	2.042	2.045
0.400	1.750	1.846	1.142	1.130	2.233	2.236
0.500	1.417	1.465	0.791	0.775	2.834	2.846
0.560	1.125	1.158	0.657	0.644	2.773	2.792
0.600	0.945	0.969	0.588	0.579	1.949	1.957
0.700	0.598	0.609	0.452	0.450	0.521	0.520
0.800	0.364	0.368	0.322	0.322	0.122	0.122
0.900	0.229	0.231	0.206	0.207	0.004	0.004

Table 2.1: Comparison of the motion responses of a moored cylindrical buoy with linear and non-linear modelling of mooring lines in regular waves. Wave Height=4 m

FREQUENCY [RAD/SEC]	SURGE (m)		PITCH (deg)		HEAVE (m)	
	LINEAR	NON-LINEAR	LINEAR	NON-LINEAR	LINEAR	NON-LINEAR
0.020	2.186	0.269	0.017	0.029	5.850	5.771
0.100	7.100	16.369	0.350	2.699	5.920	5.904
0.200	6.121	7.849	2.362	2.888	6.012	6.027
0.273	5.103	5.533	8.145	11.318	5.995	5.911
0.300	5.879	7.111	7.321	9.345	5.979	5.985
0.400	5.170	5.750	3.426	3.311	6.592	6.568
0.500	4.093	4.589	2.374	2.199	8.174	8.392
0.540	3.332	4.023	2.114	1.896	8.540	8.080
0.600	2.740	2.973	1.764	1.679	5.690	5.954
0.700	1.770	1.825	1.357	1.348	1.568	1.568
0.800	1.092	1.104	0.965	0.965	0.365	0.364
0.900	0.683	0.692	0.618	0.620	0.010	0.011

Table 2.2: Comparison of the motion responses of a moored cylindrical buoy with linear and non-linear modelling of mooring lines in regular waves. Wave Height=12 m



$$\begin{bmatrix} x \\ y \\ z \end{bmatrix} = \begin{bmatrix} \beta_{11} & \beta_{12} & \beta_{13} \\ \beta_{21} & \beta_{22} & \beta_{23} \\ \beta_{31} & \beta_{32} & \beta_{33} \end{bmatrix} \begin{bmatrix} X \\ Y \\ Z \end{bmatrix} + \begin{bmatrix} X_G \\ Y_G \\ Z_G \end{bmatrix}$$

$$\beta_{11} = \cos(x_6) \quad , \quad \beta_{12} = -\sin(x_6) \quad , \quad \beta_{13} = 0$$

$$\beta_{21} = \sin(x_6) \quad , \quad \beta_{22} = \cos(x_6) \quad , \quad \beta_{23} = 0$$

$$\beta_{31} = 0 \quad , \quad \beta_{32} = 0 \quad , \quad \beta_{33} = 1$$

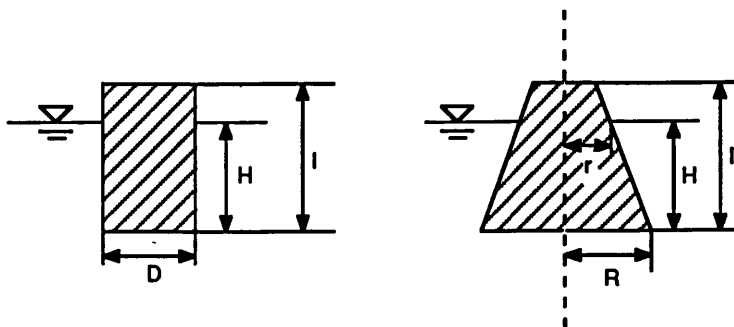


Fig. 2.1 Co-ordinate Systems and Cylindrical and Conical Buoy Geometries

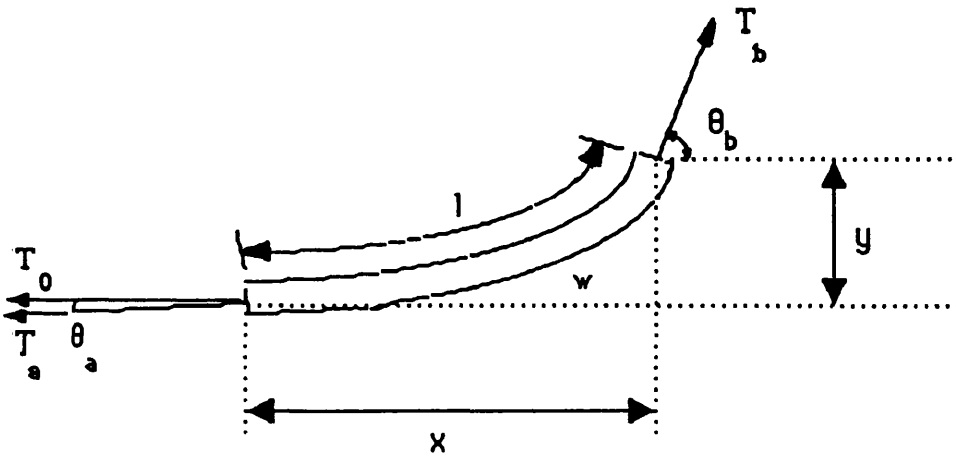


Fig. 2.2 A Typical Differential Cable Element

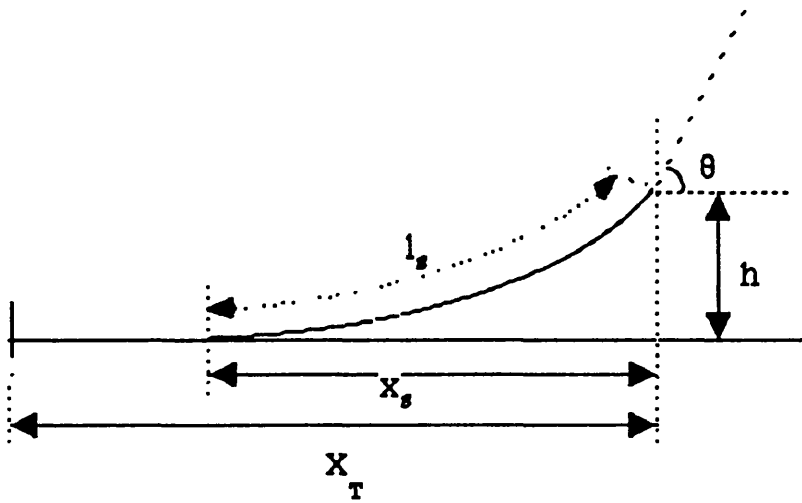


Fig. 2.3 Definition of Cable Parameters

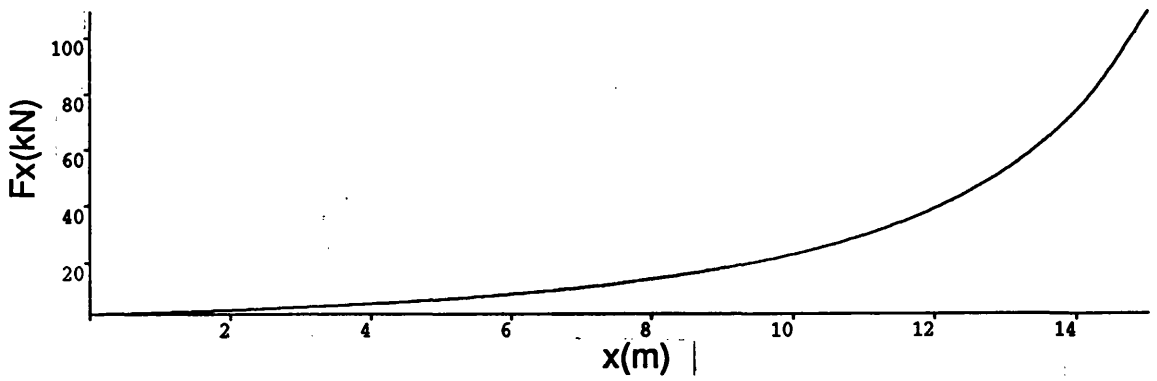


Fig. 2.4 Horizontal Displacement-Horizontal Force

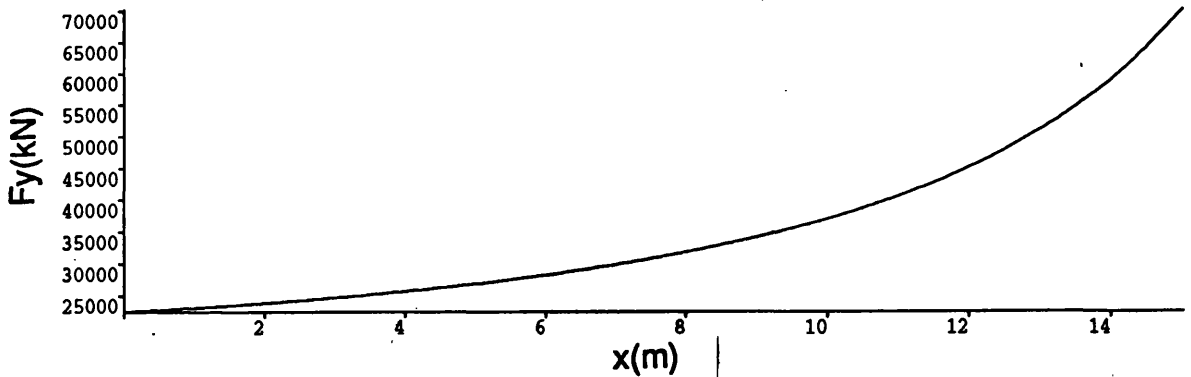


Fig. 2.5 Horizontal Displacement-Vertical Force

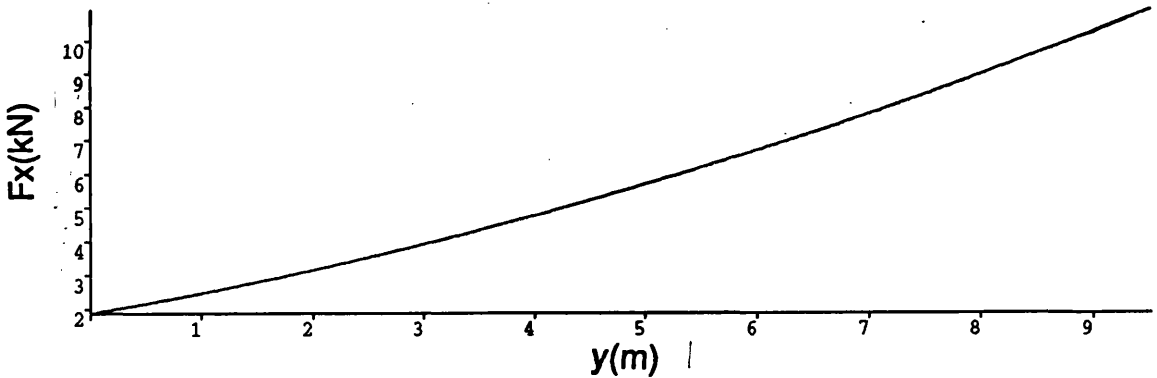


Fig. 2.6 Vertical Displacement-Horizontal Force

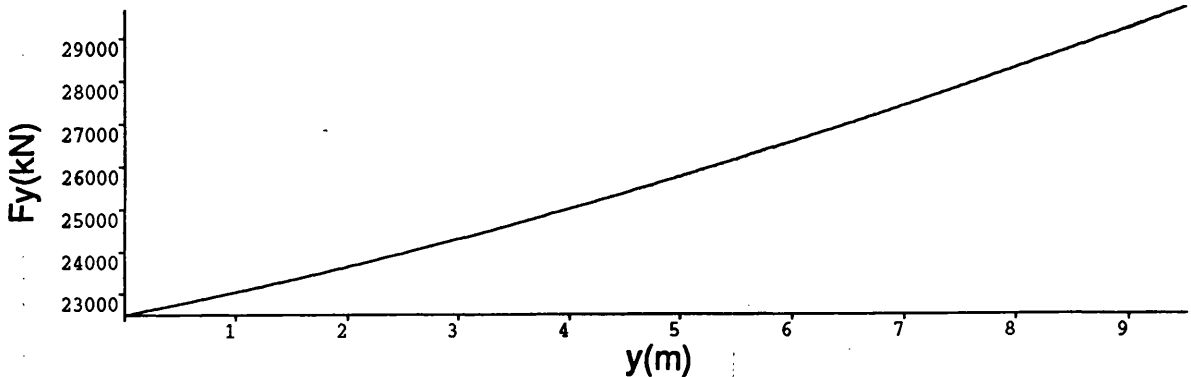


Fig. 2.7 Vertical Displacement-Vertical Force

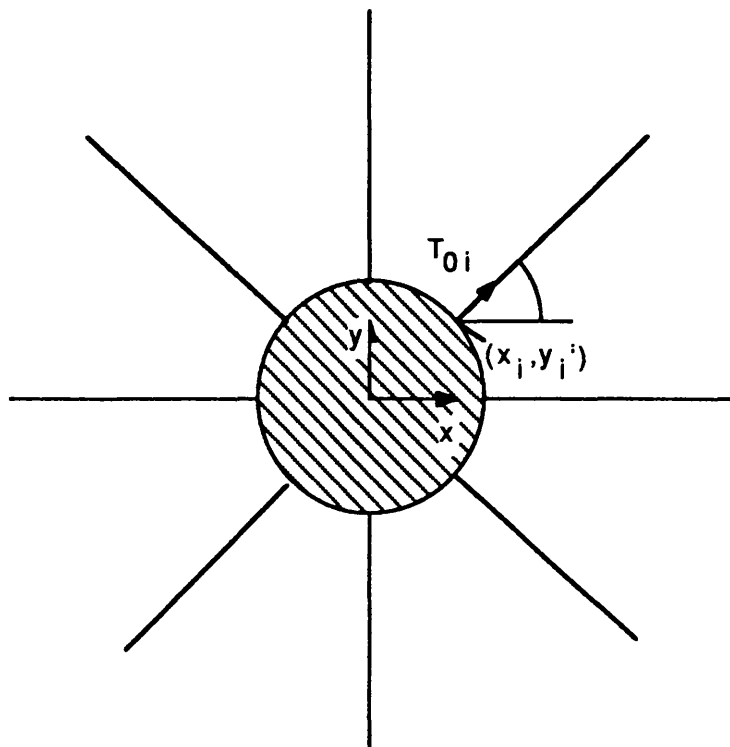


Fig. 2.8 Top View of a Multi-Cable System

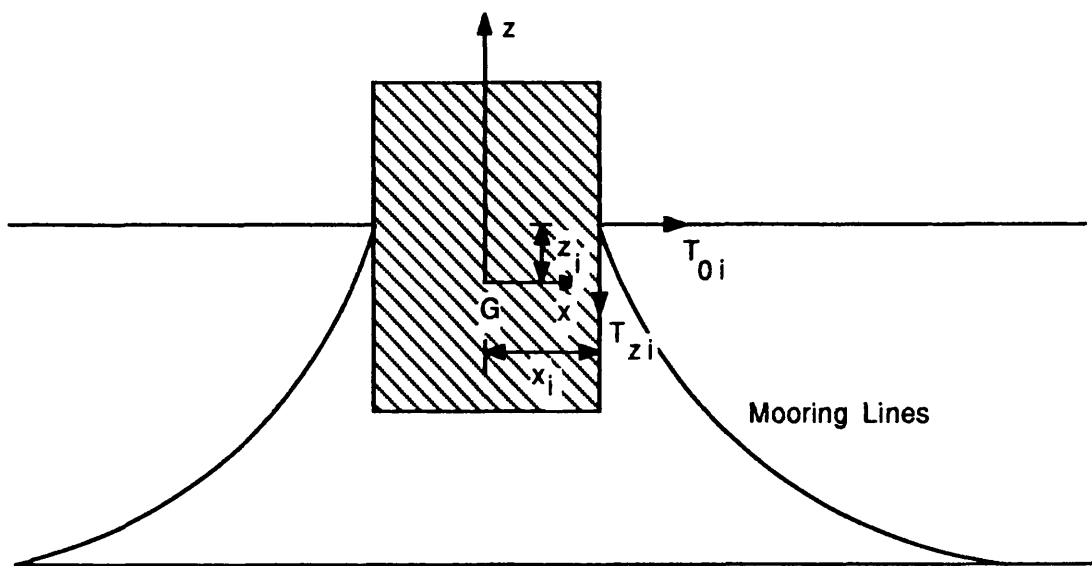


Fig. 2.9 Multi-Cable Systems

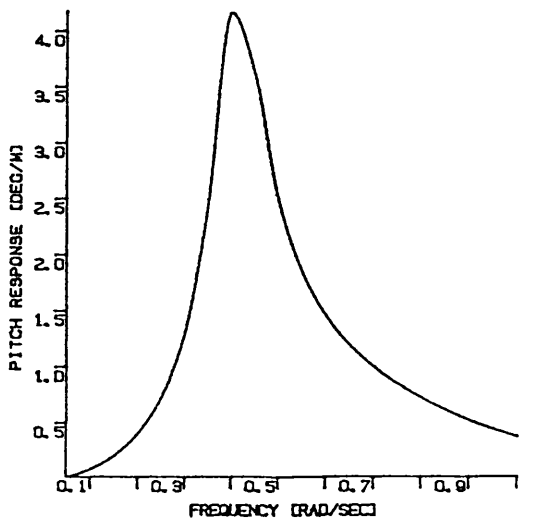
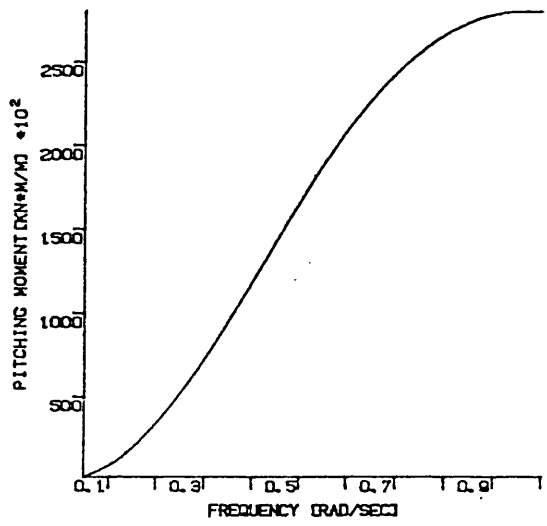
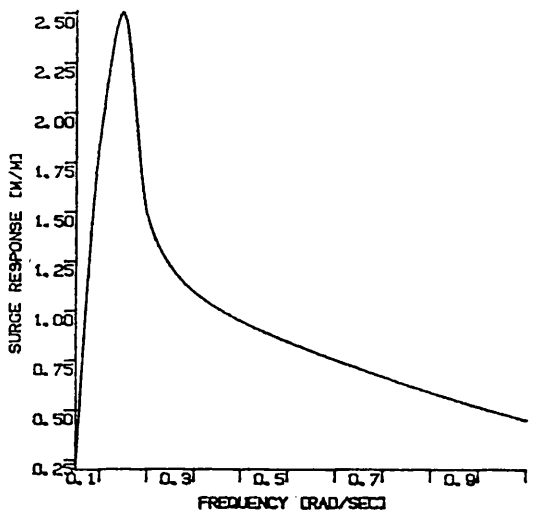
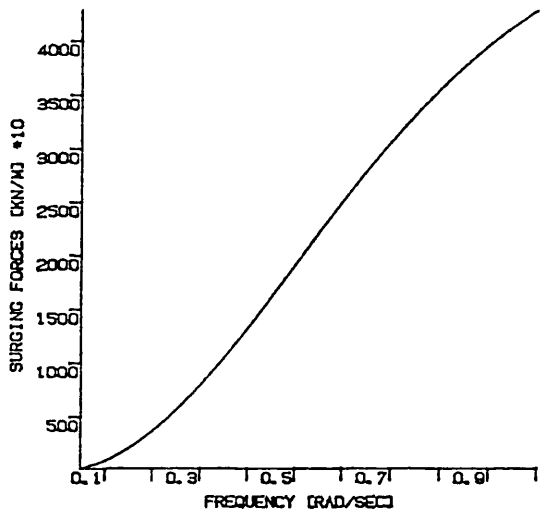
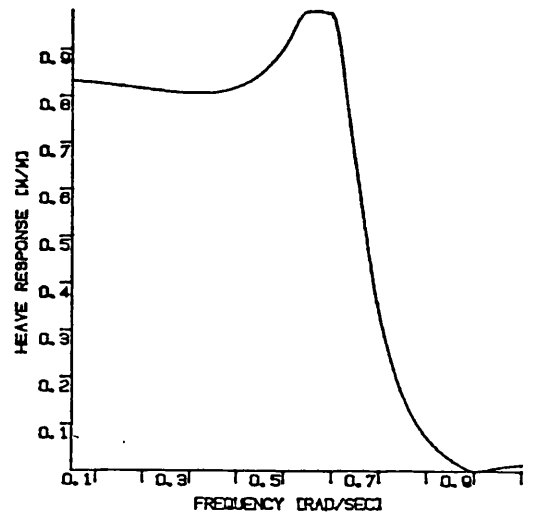
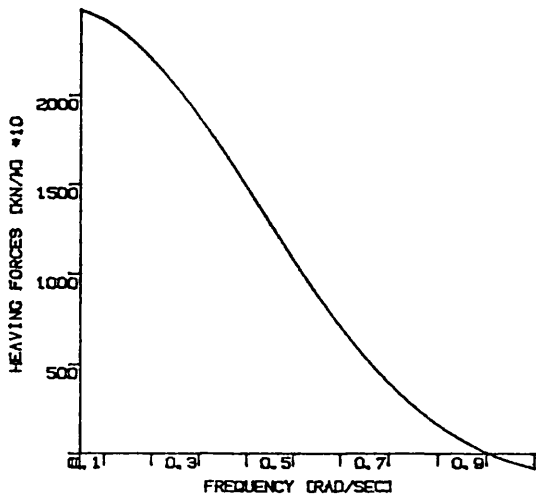


Fig. 2.10 Wave Induced Forces and Resulting Responses of the Cylindrical Buoy

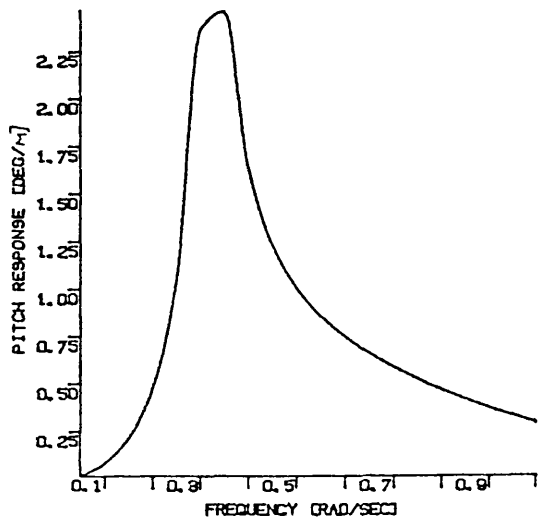
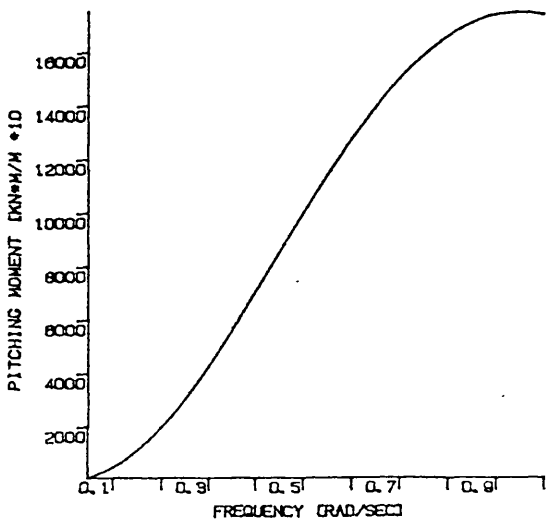
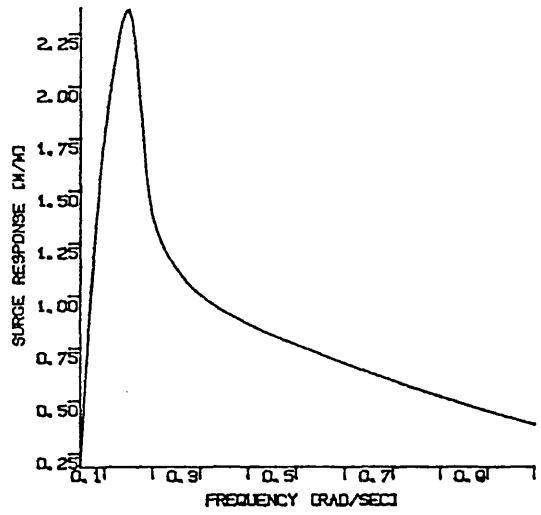
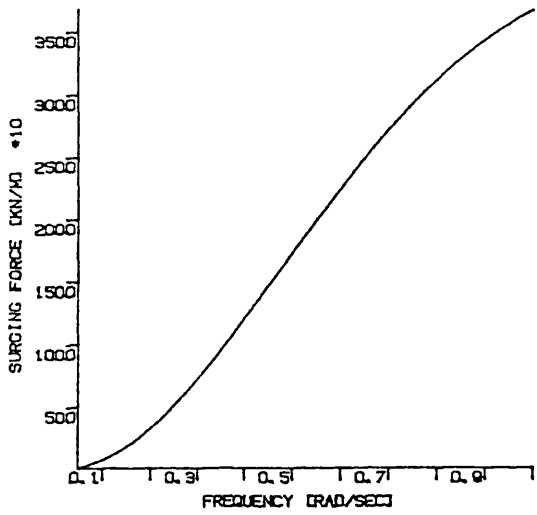
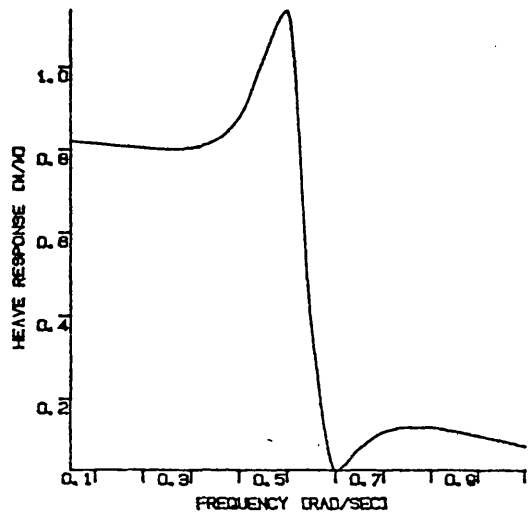
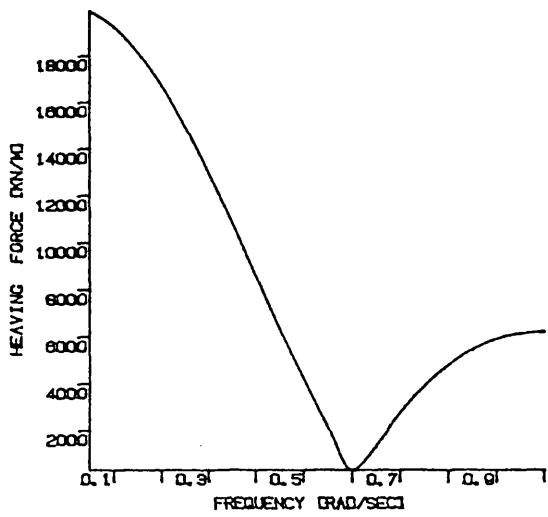


Fig. 2.11 Wave Induced Forces and Resulting Responses of the Conical Buoy

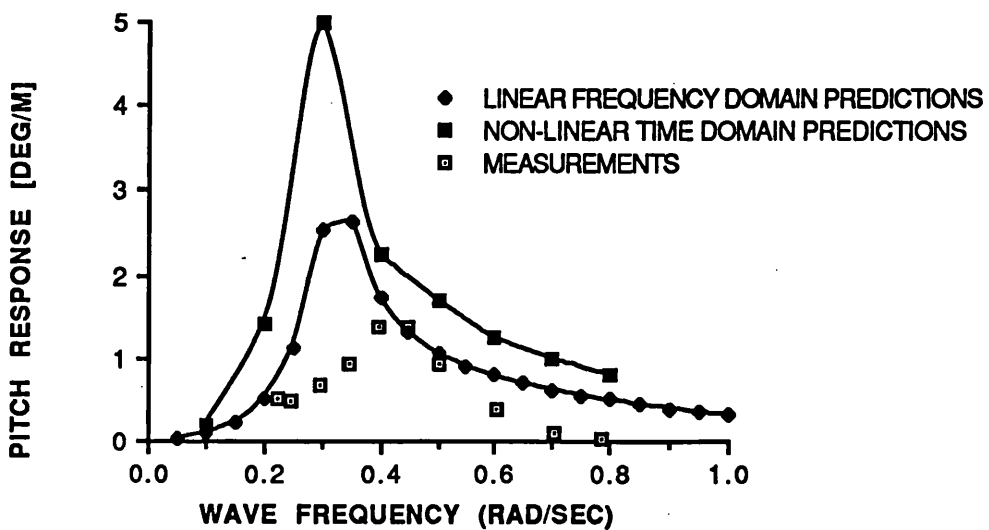
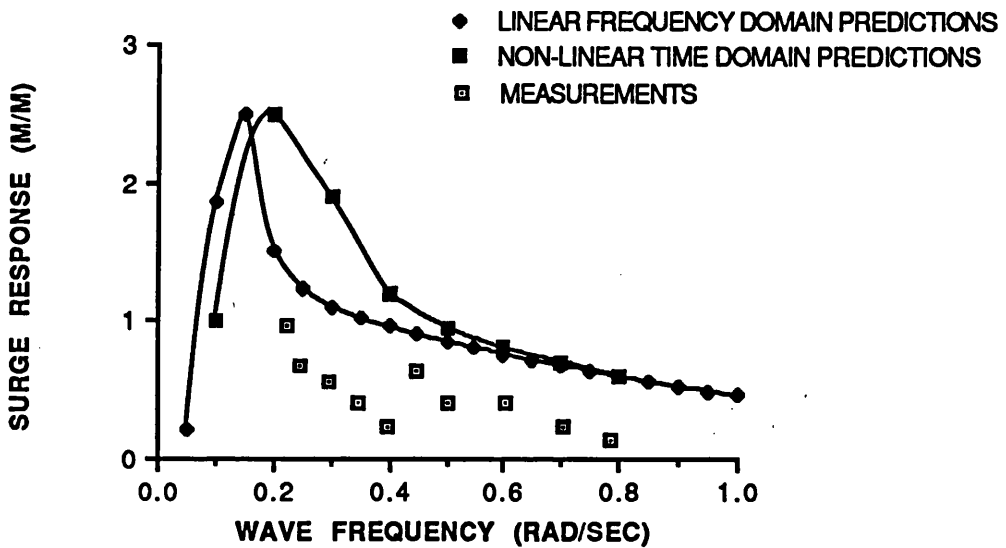
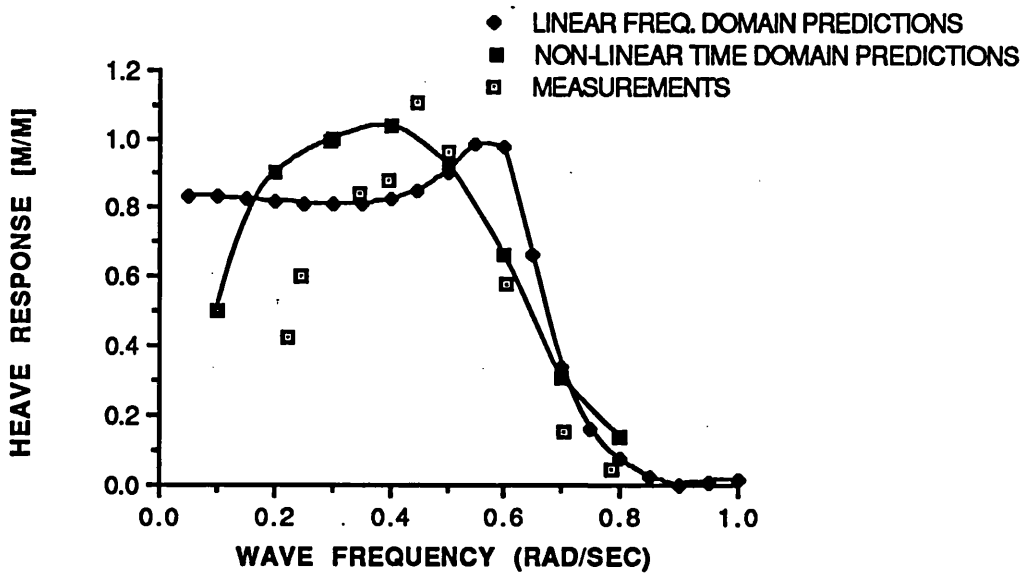


Fig. 2.12 Motion Response Predictions of the Cylindrical Buoy
 Cylindrical Buoy Geometry is shown in Fig. 6.3

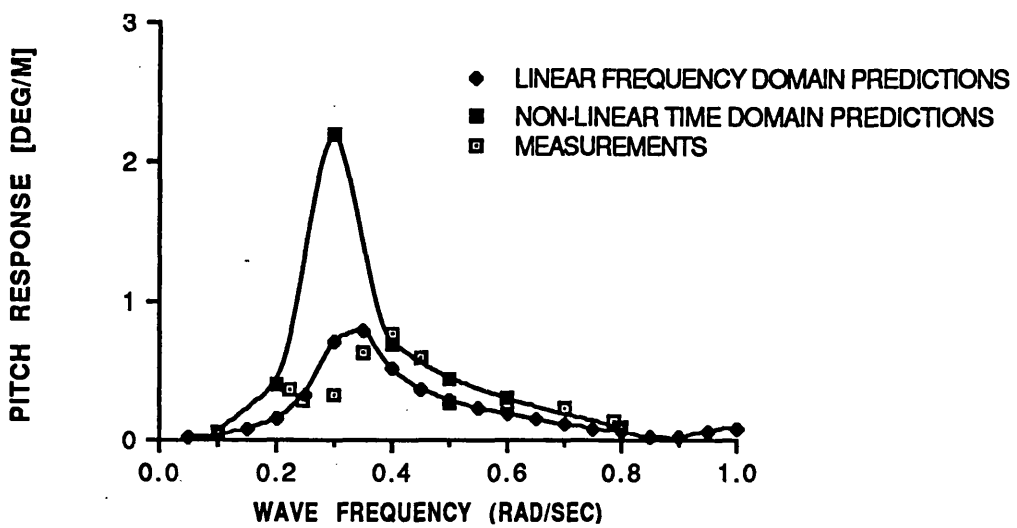
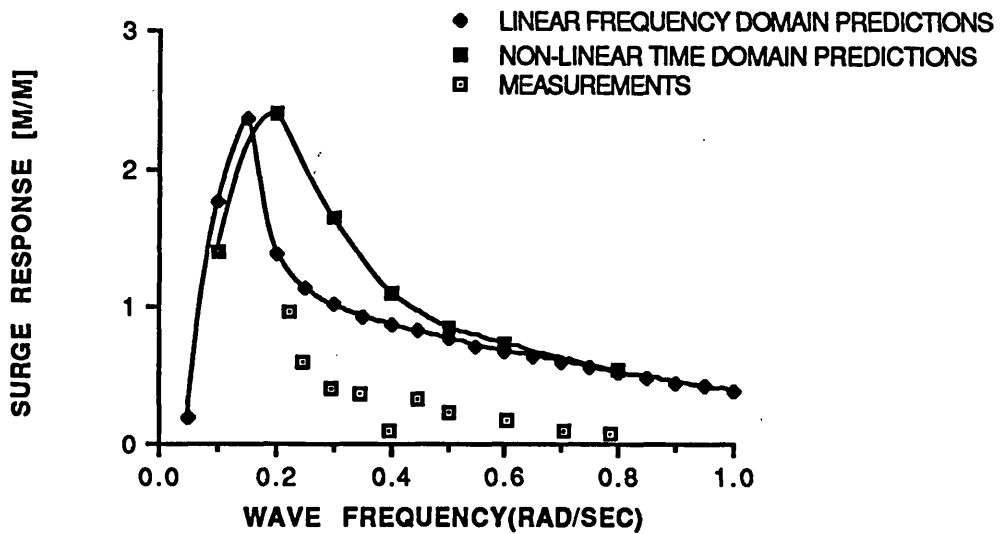
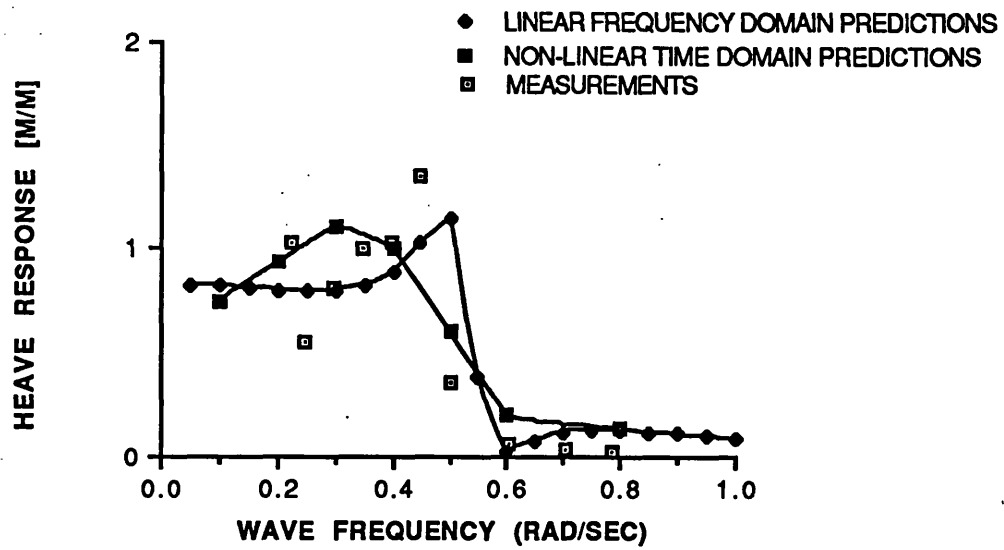


Fig. 2.13 Motion Response Predictions of the Conical Buoy
 Conical Buoy Geometry is shown in Fig. 6.3

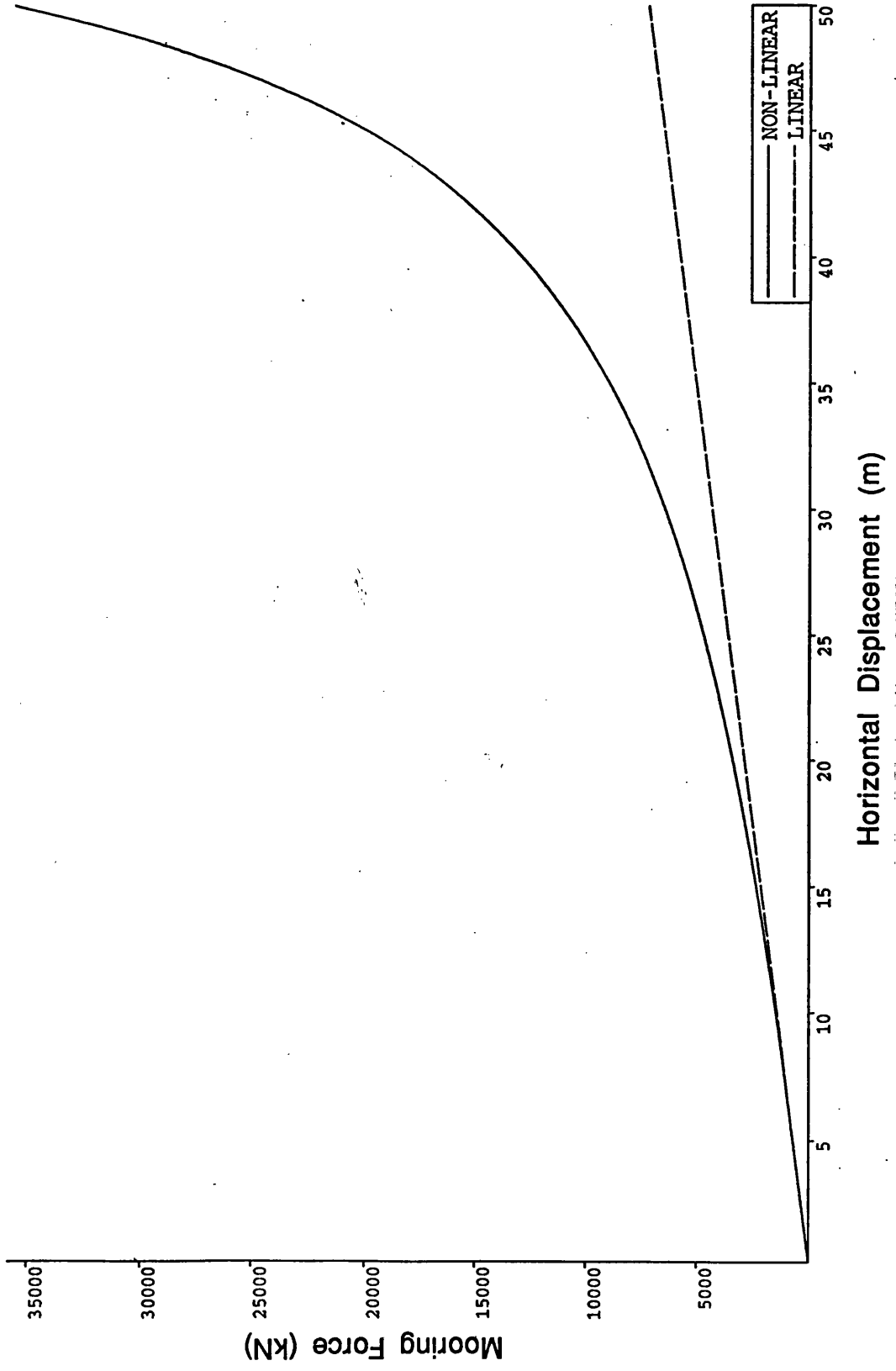


Fig. 2.14 Stiffness Curves for Linear and Non-linear Cables

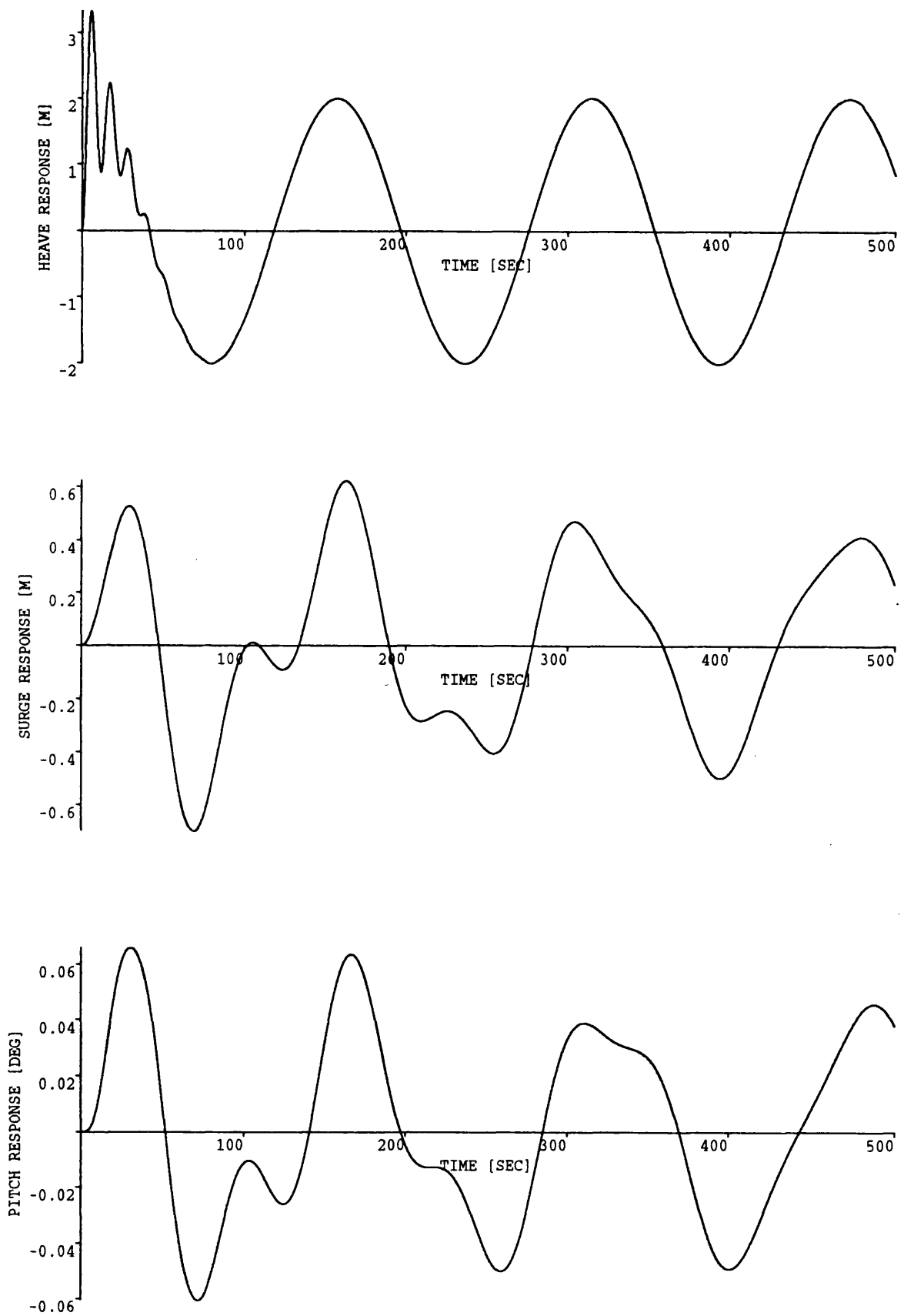


Fig. 2.15 Motion Response Simulation of a Circular Buoy with Non-linear Cables
 Wave Height=4 m, Wave Frequency=0.04 rad/sec

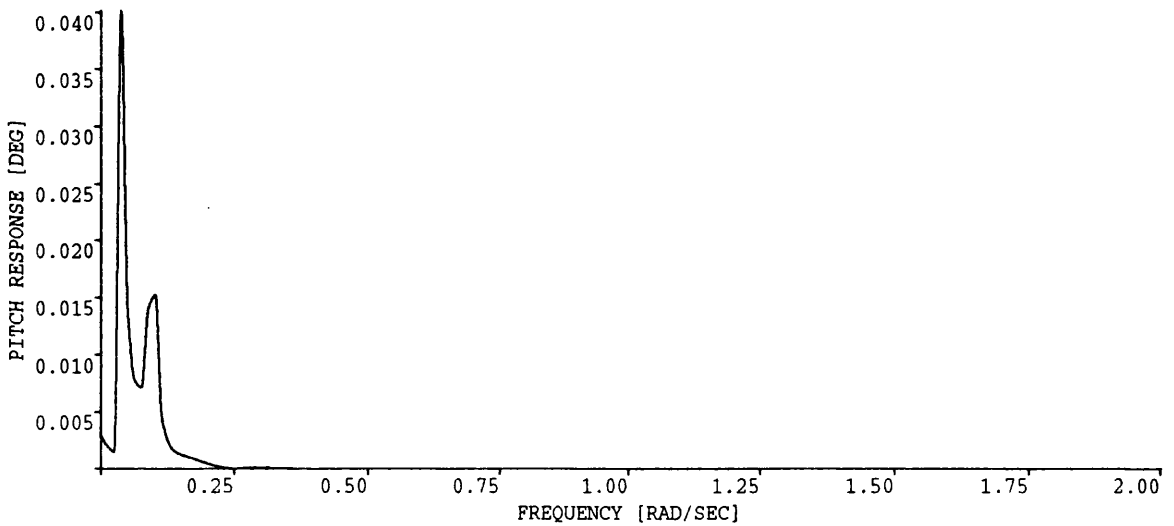
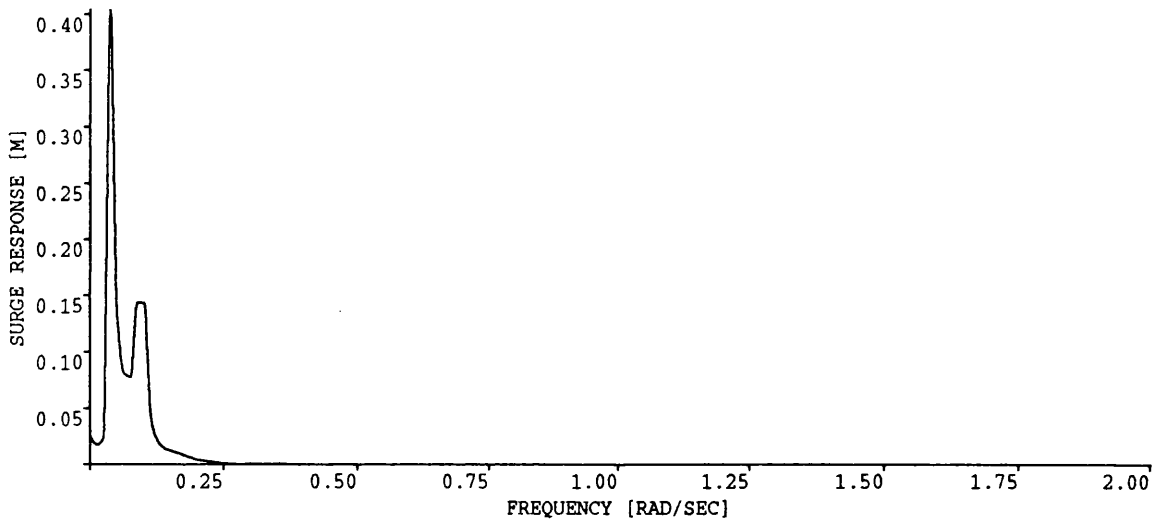
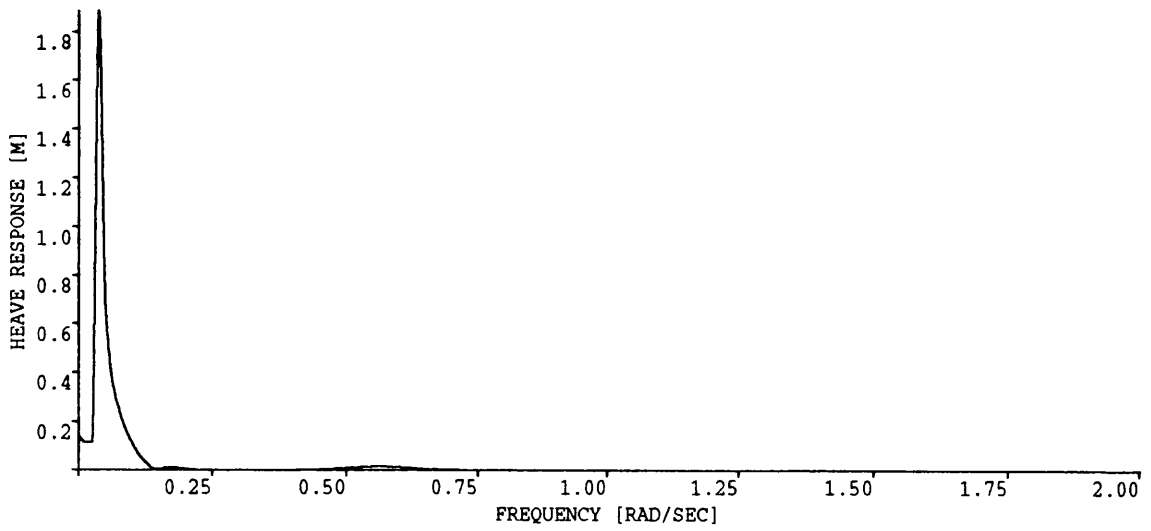


Fig. 2.15a Fast Fourier Transformations of the Time Histories Shown in Fig. 2.15

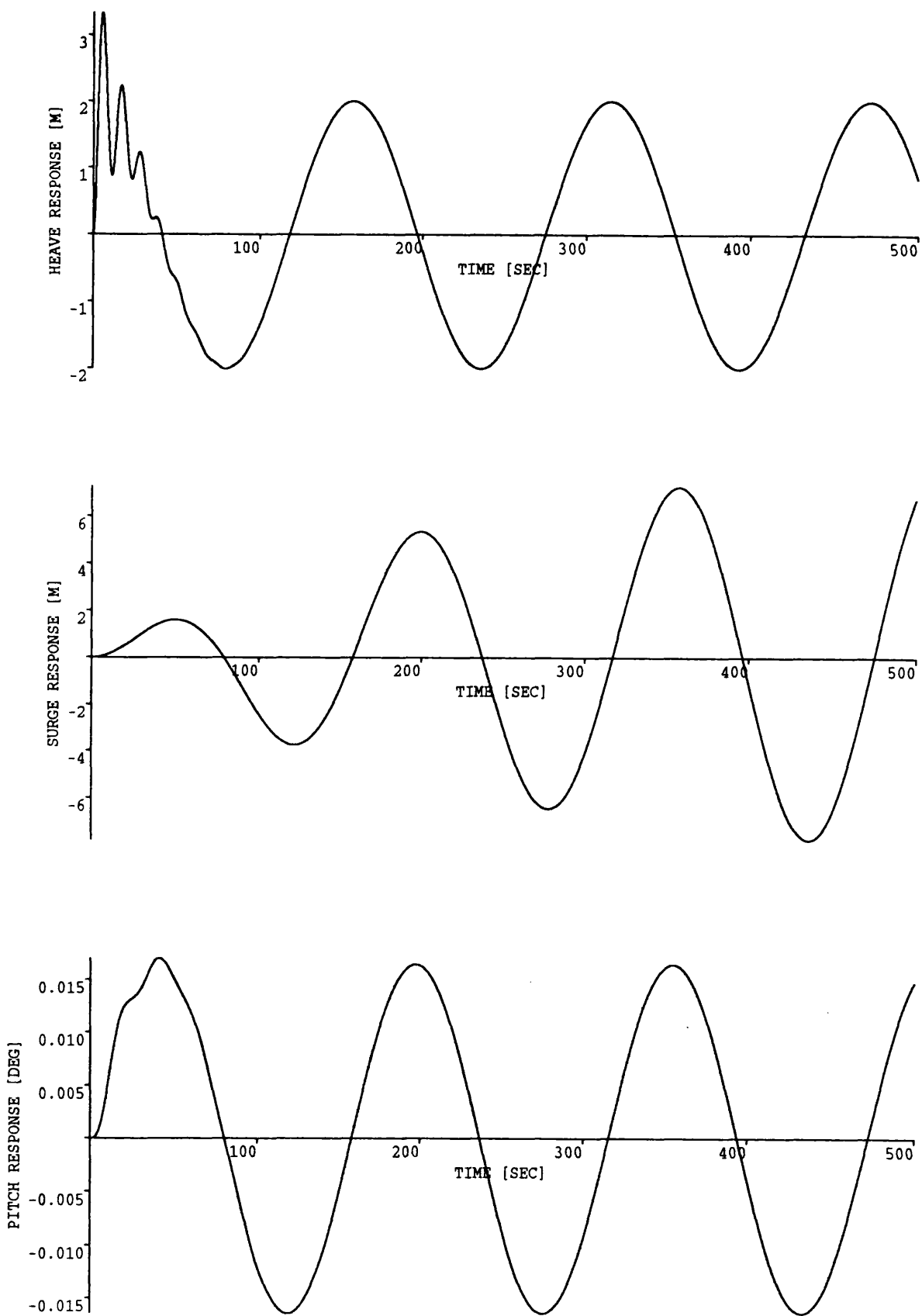


Fig. 2.16 Motion Response Simulation of a Circular Buoy with Linear Cables
 Wave Height=4 m, Wave Frequency=0.04 rad/sec

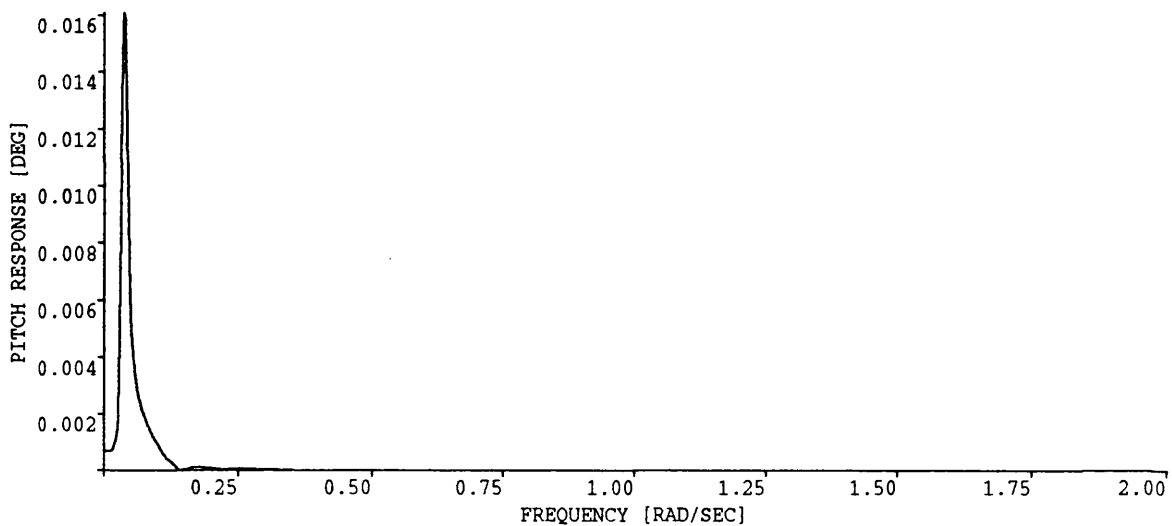
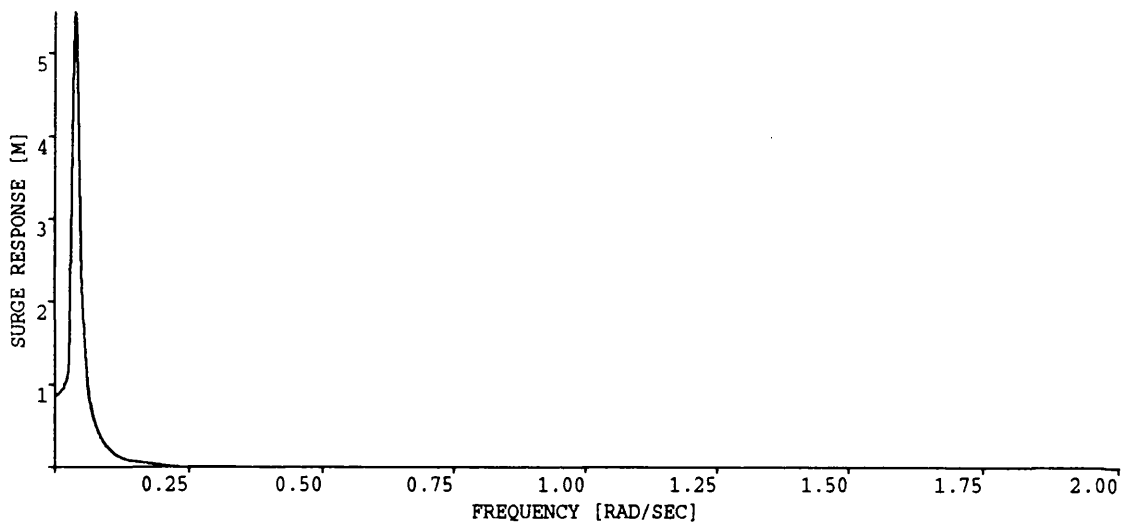
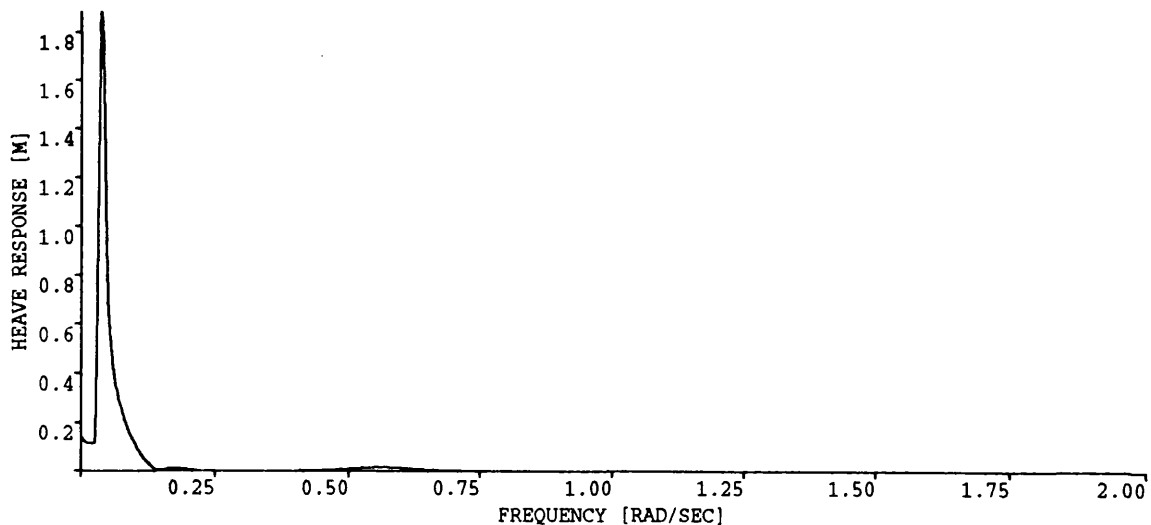


Fig. 2.16a Fast Fourier Transformations of the Time Histories Shown in Fig. 2.16

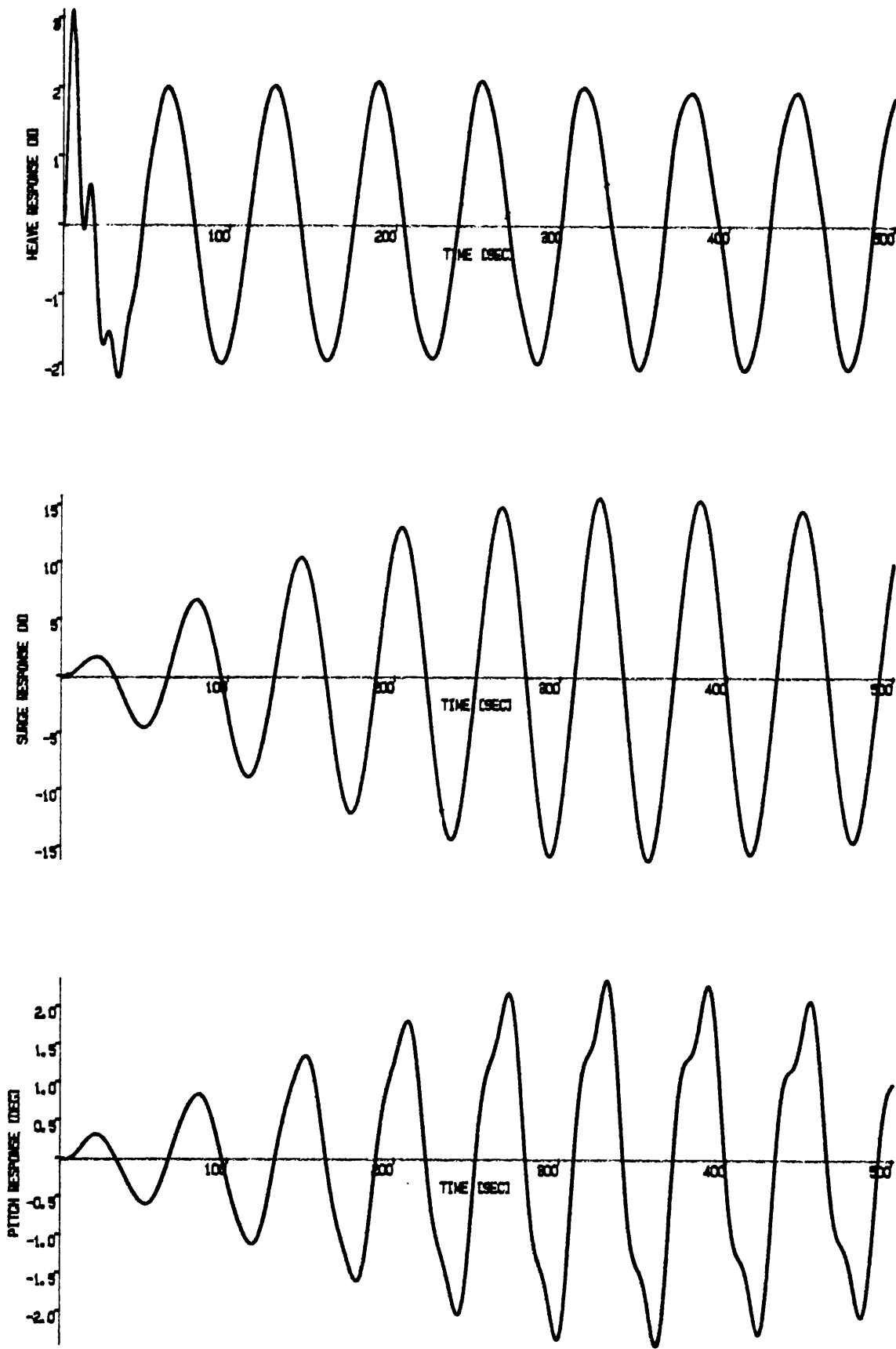


Fig. 2.17 Motion Response Simulation of a Circular Buoy with Non-linear Cables
 Wave Height=4 m, Wave Frequency=0.1 rad/sec

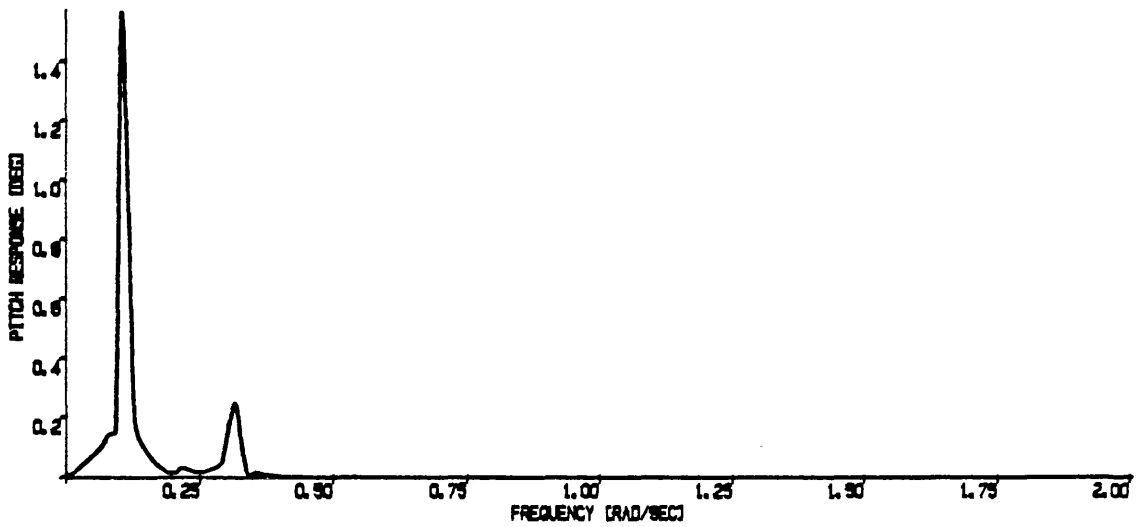
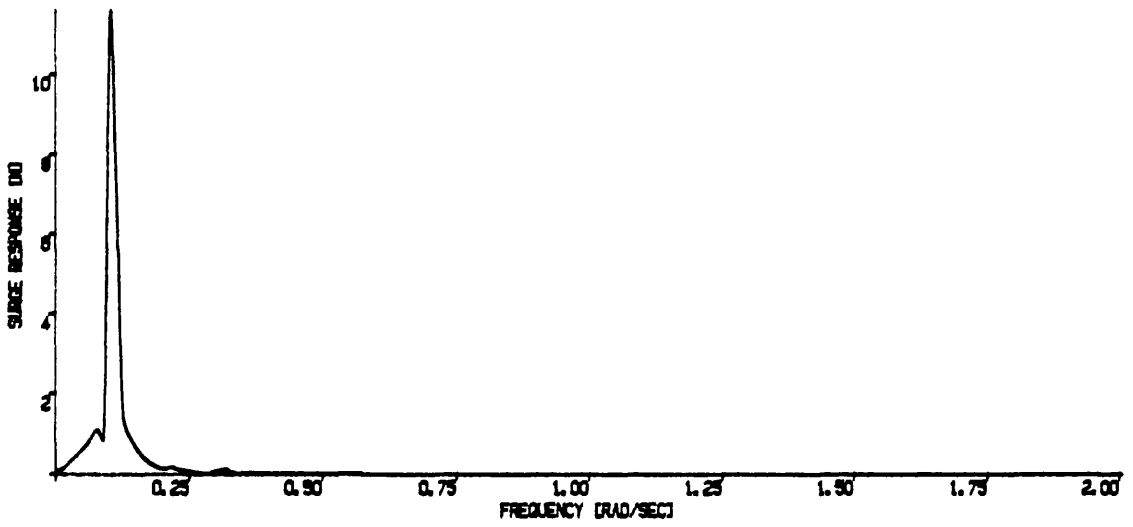
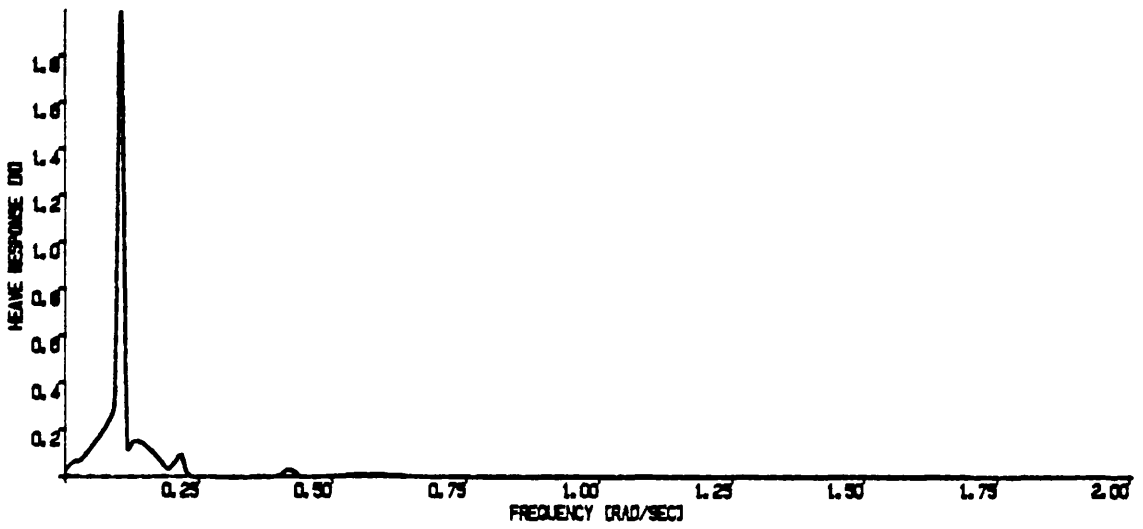


Fig. 2.17a Fast Fourier Transformations of the Time Histories Shown in Fig. 2.17

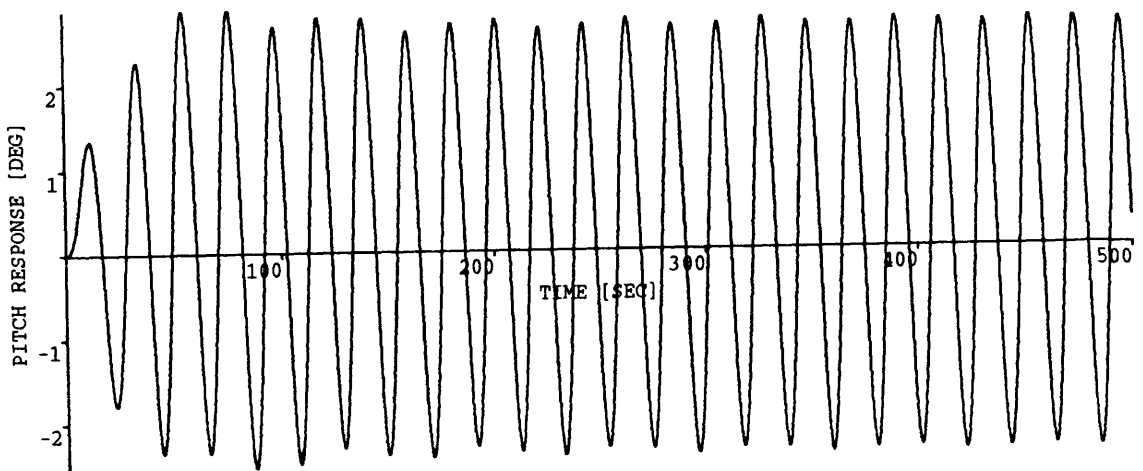
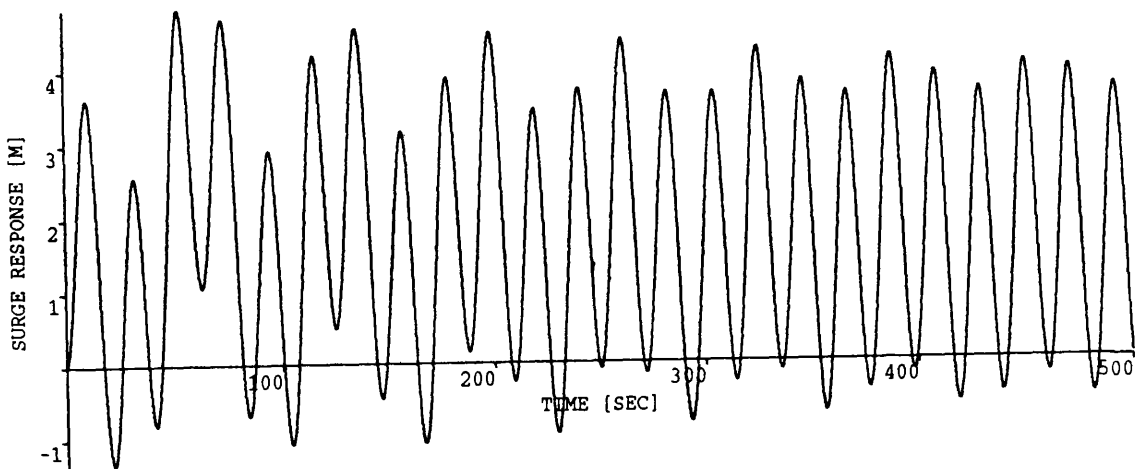
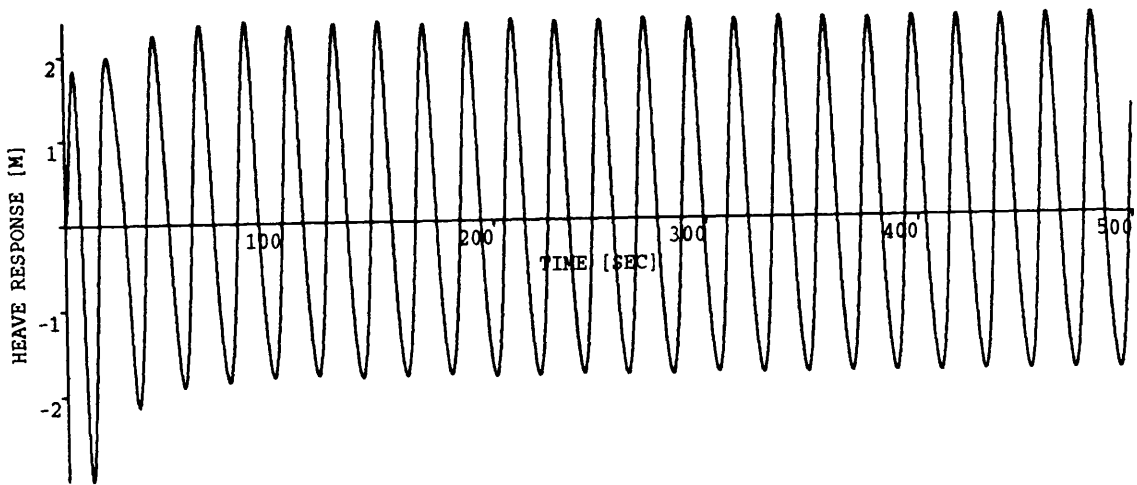


Fig. 2.18 Motion Response Simulation of a Circular Buoy with Non-linear Cables
 Wave Height=4 m, Wave Frequency=0.3 rad/sec

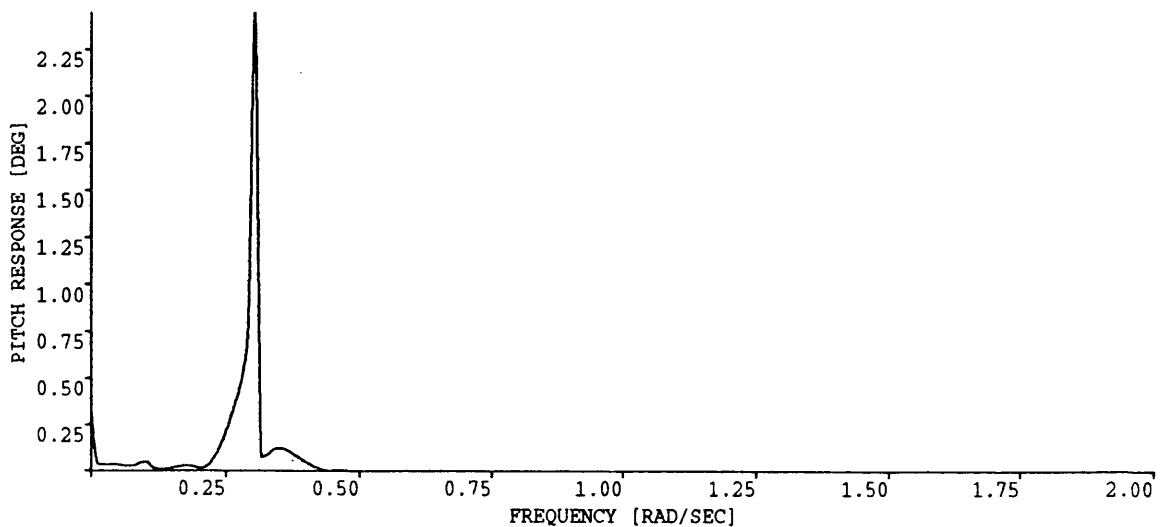
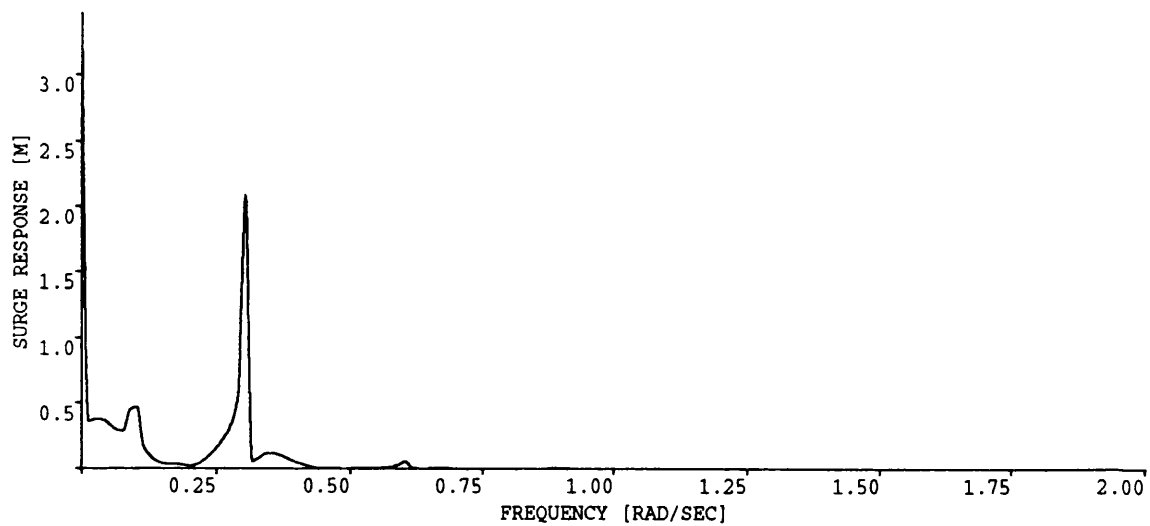
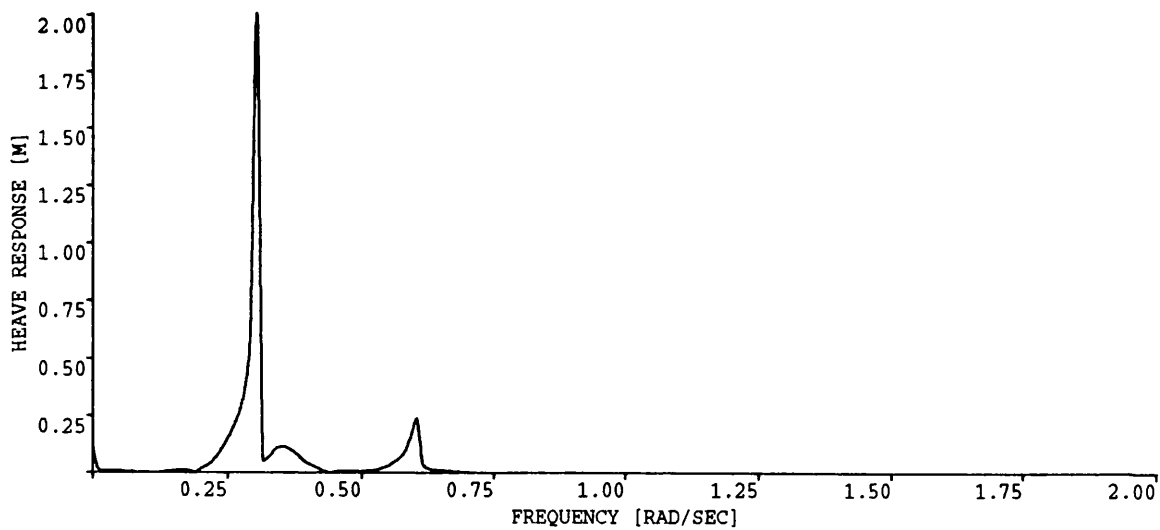


Fig. 2.18a Fast Fourier Transformations of the Time Histories Shown in Fig. 2.18

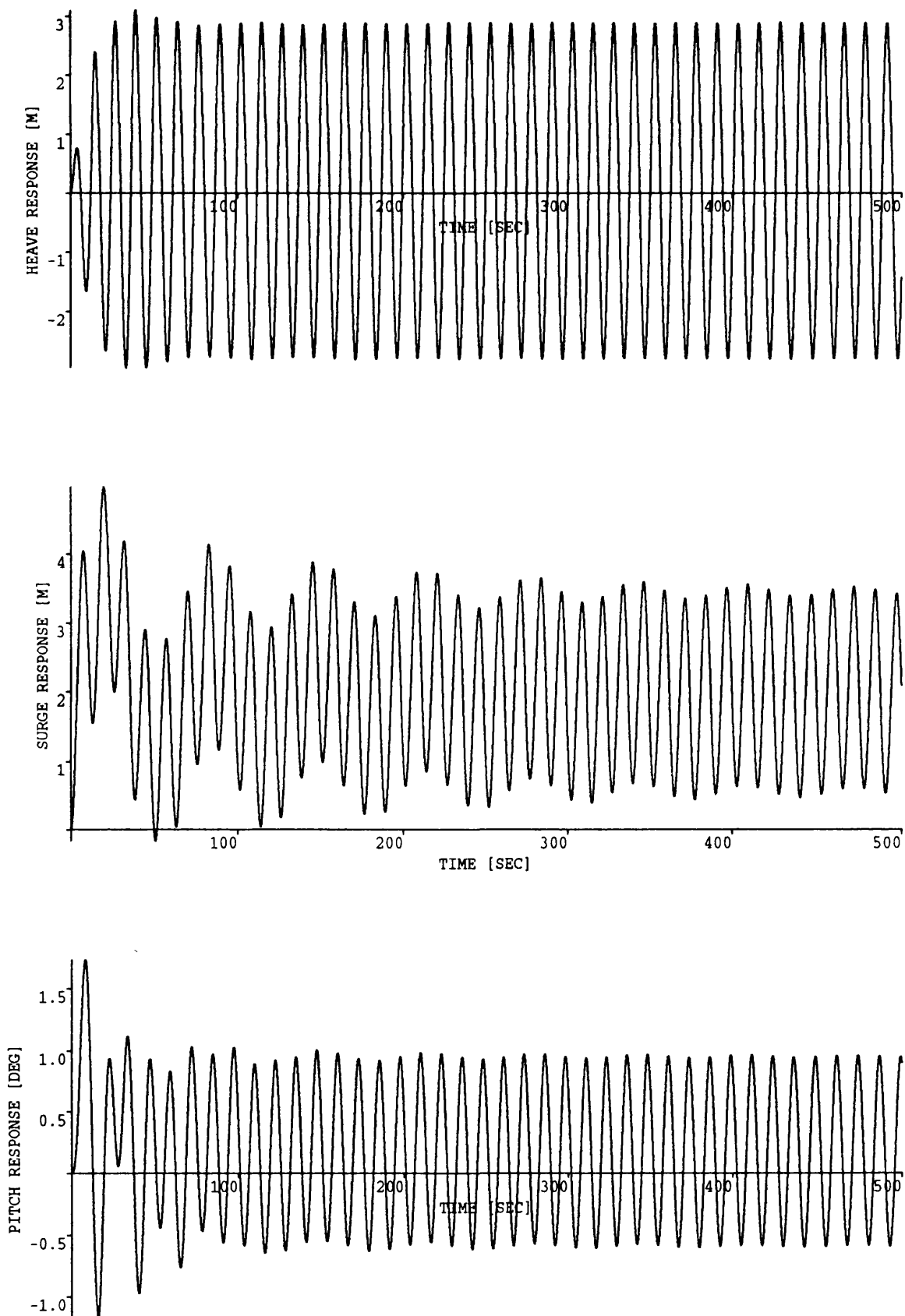


Fig. 2.19 Motion Response Simulation of a Circular Buoy with Non-linear Cables
 Wave Height=4 m, Wave Frequency=0.5 rad/sec

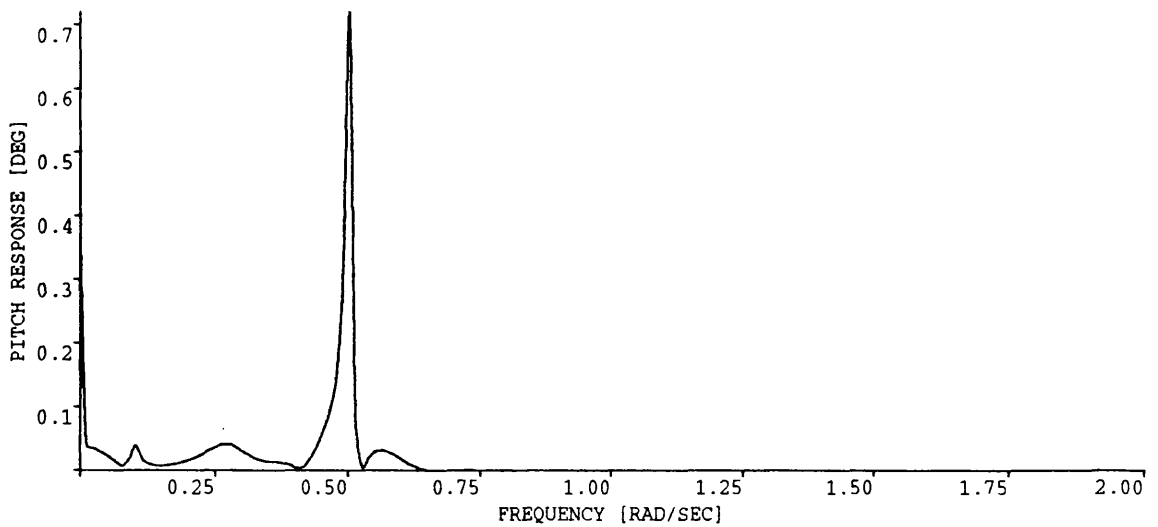
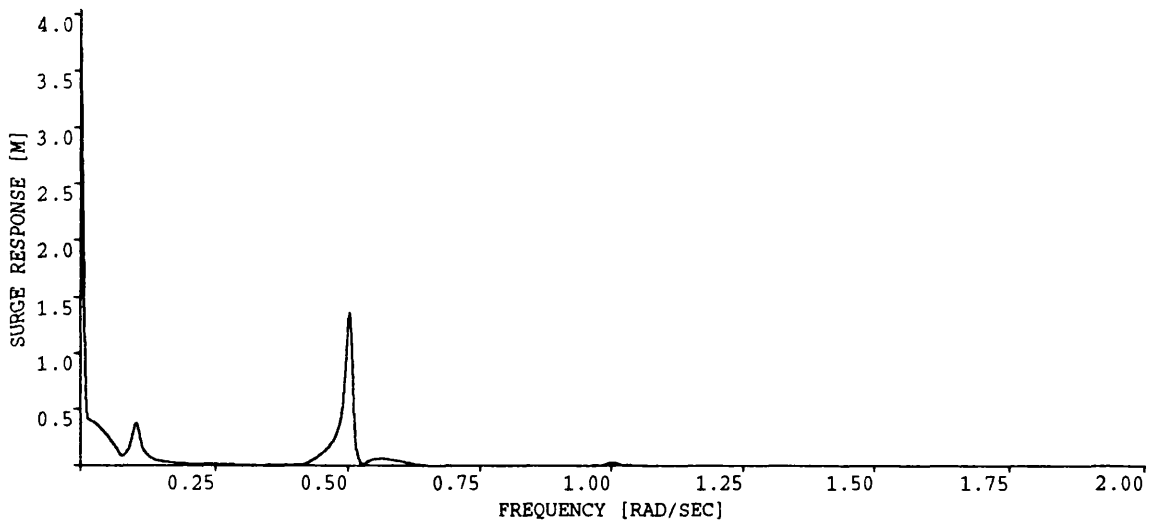
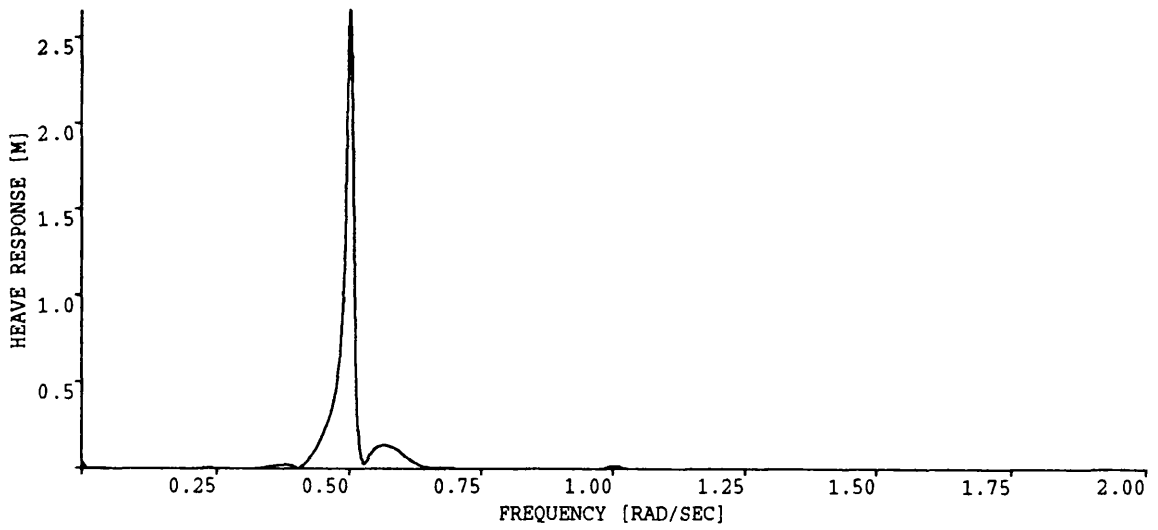


Fig. 2.19a Fast Fourier Transformations of the Time Histories Shown in Fig. 2.19

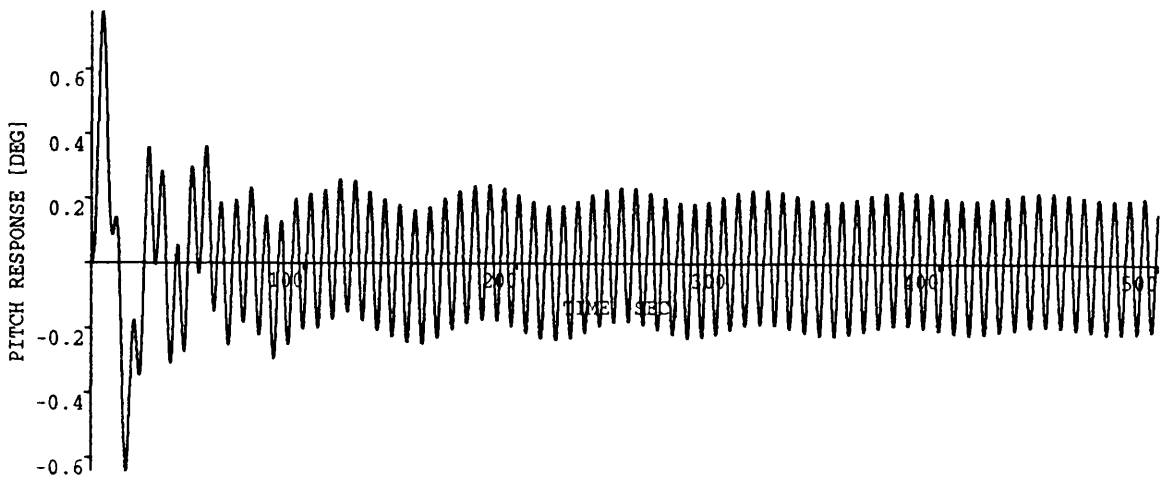
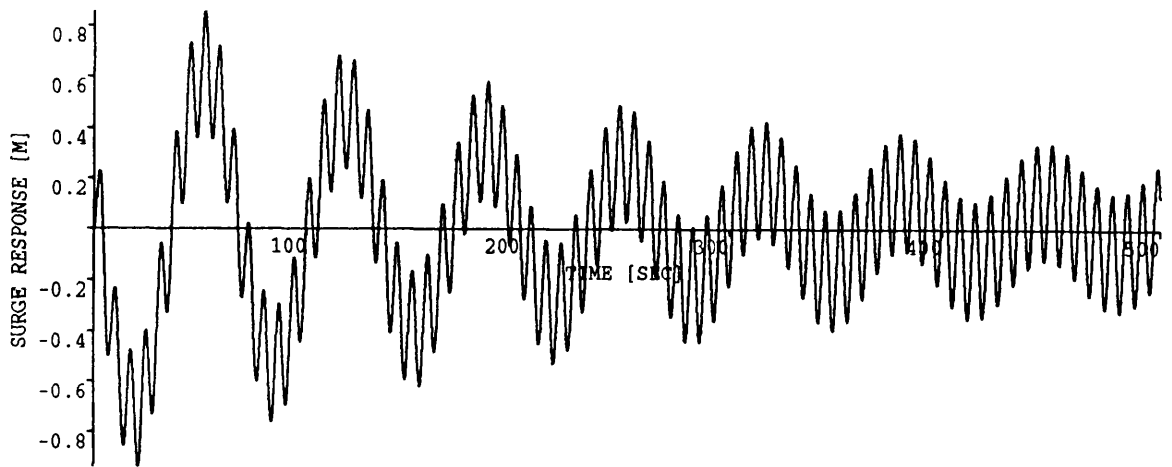
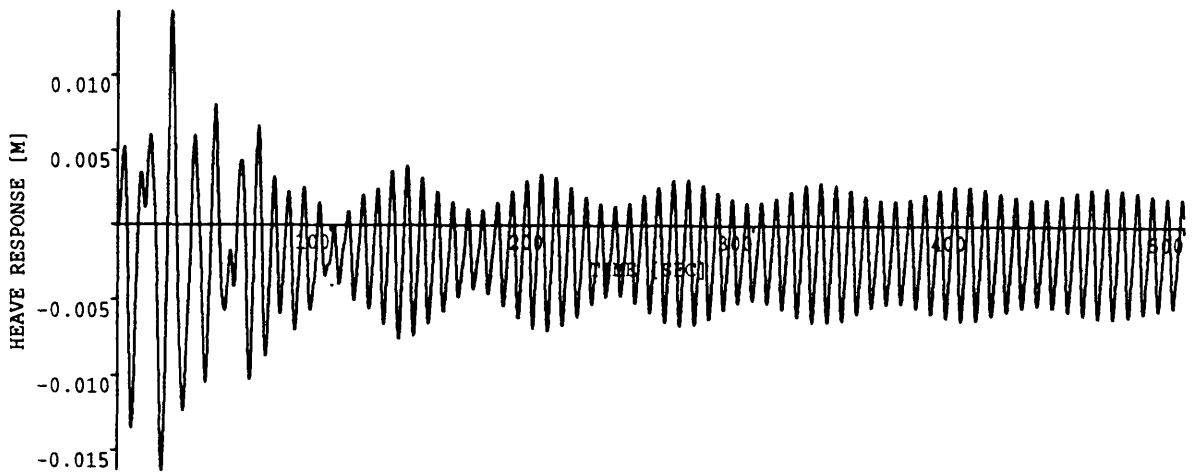


Fig. 2.20 Motion Response Simulation of a Circular Buoy with Non-linear Cables
 Wave Height=4 m, Wave Frequency=0.9 rad/sec

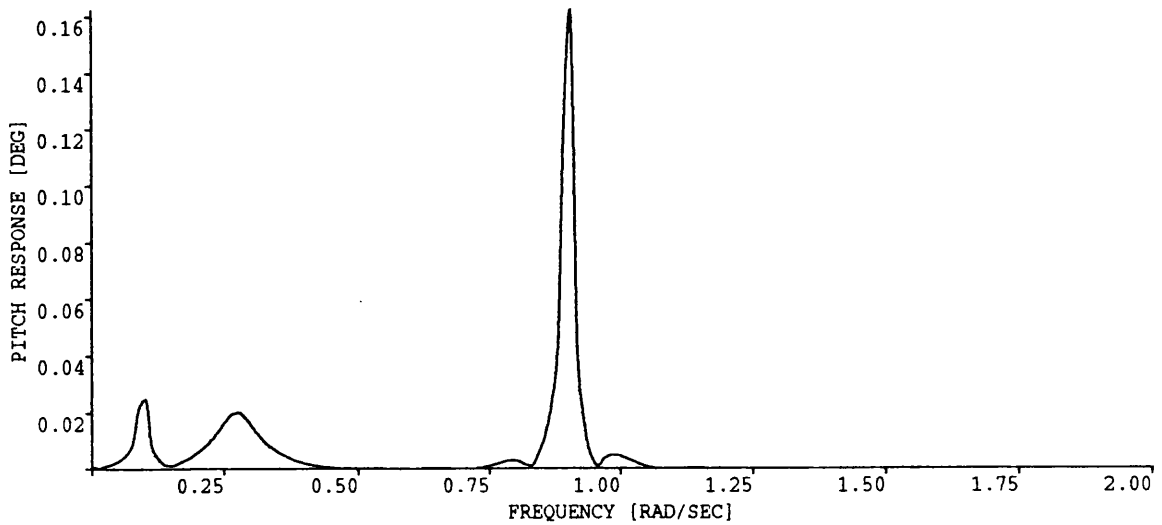
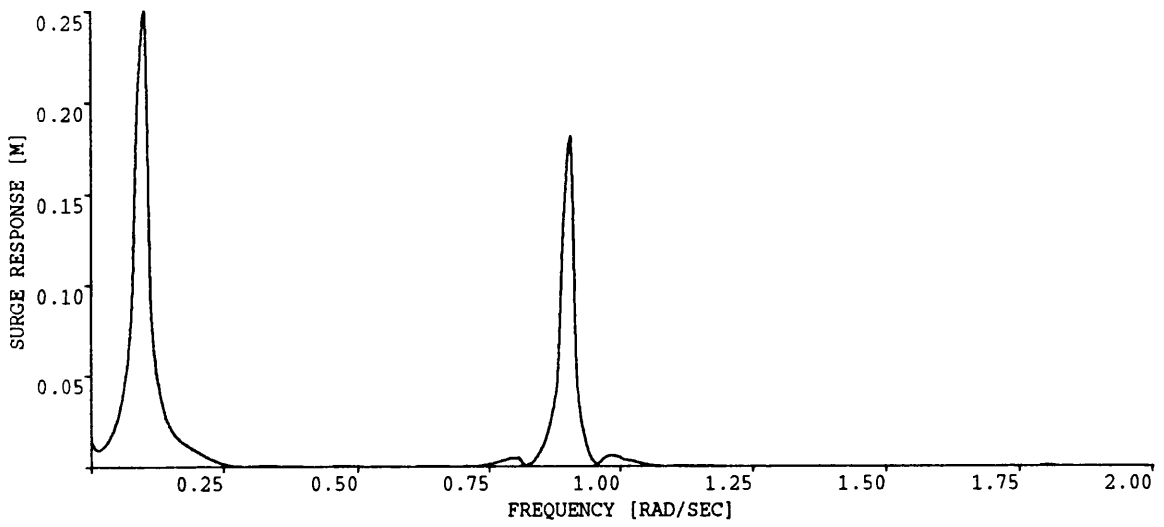
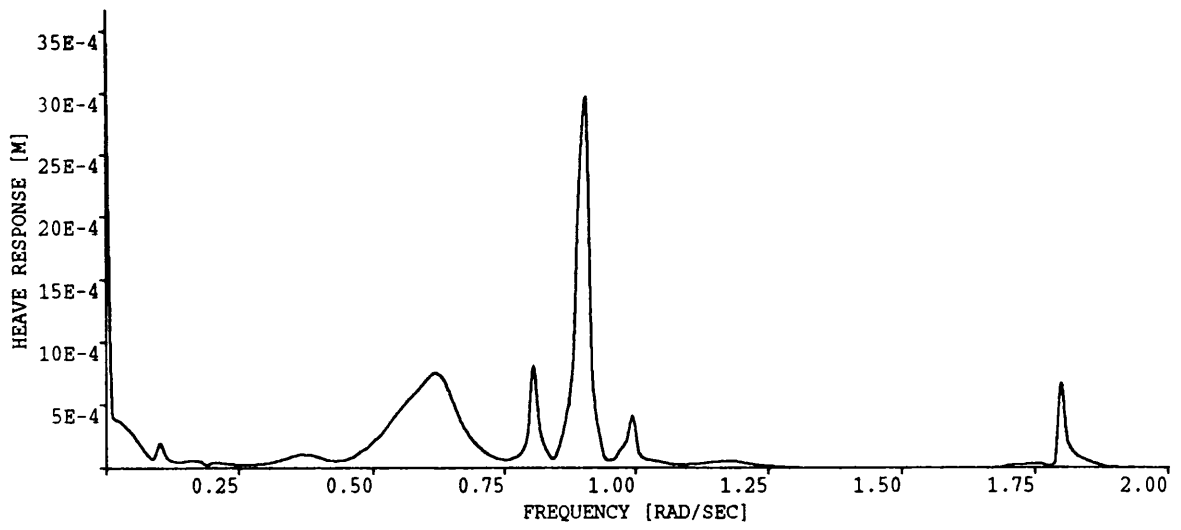


Fig. 2.20a Fast Fourier Transformations of the Time Histories Shown in Fig. 2.20

CHAPTER 3

HYDRODYNAMIC FORCES ON TANKERS

3.1 INTRODUCTION

The interaction of gravity waves and structures is rather complicated in many aspects: such as the non-linear effects of waves, viscous and turbulent effects on the drag, irregular geometry of structures, large amplitude motions of the structures,...etc. This chapter describes a theoretical method for predicting the wave and motion induced forces on a large tanker by modelling the tanker as a prismatic elliptic cylinder. The prismatic elliptic cylinder form is not a common shape for the tankers but it is a fairly good approximation for tankers utilised as offshore production and storage platforms (Fig. 3.1). Although it is always possible to solve the problem by using one of the commercial programs which utilize the Green's function method, this requires a powerful computer, skilful and experienced users and involves a high cost.

Diffraction wave potential from an infinite cylinder of elliptic cross section was solved by McLachlan (1951) [3.1] for sound waves. Later the same method was applied to the problem of diffraction of water waves about a stationary ship by Goda and Yoshimura (1972) [3.2] and Muga and Fong (1976) [3.3]. Chen and Mei (1973) [3.4] solved the problem in shallow water of constant depth.

The mathematical solution of the problem follows the usual pattern of separation of variables in elliptical coordinates, which leads to the *Mathieu equation* [3.5]. Although this problem of elliptic cylinders has been well-known for many decades, understanding of numerical aspects has been rather limited due to the lack of sufficient tables and due to the complexities of the Mathieu functions. In 1969 a complete algorithm was published

by Clemm [3.6] for all coefficients, characteristic values and various solutions and their first derivatives of both the Mathieu functions and the Modified Mathieu functions.

In this chapter wave forces and added mass and damping coefficients are calculated by using the elliptical cylinder approach and compared with Oortmerssen's experiments [3.7] and with the results of a computer program based on three-dimensional source distribution technique and developed by Chan [3.8]. Water depth effect on the wave forces is also investigated. Program results for various angles of incidence and for different elliptic cylinders are presented. In the last section of the chapter second order mean forces acting on the elliptical cylinder are evaluated by using the far-field approach, introduced by Maruo [3.9].

Second order mean forces acting on the floating bodies have attracted considerable attention for the last 30 years due to their role in causing large amplitude slowly varying oscillations on moored floating structures. There are two methods to predict the drift forces; the near field method developed by Pinkster [3.10] and the far field method developed by Maruo. In this study, the far field (wave momentum) method which uses momentum relations to express the drift forces and moment in terms of the far field disturbance of the ship is employed to predict the drift forces because with this method it is possible to obtain the drift forces in a more compact form than with the near field equations. Moreover the near field method requires rigorous calculations around the body surface. Since diffraction and radiation potentials are already known, it seems logical to employ the far field method to obtain analytical expressions for the drift forces. Maruo in 1960 originated this method. Later Newman [3.11] developed the method to predict the drift moment about the vertical axis.

3.2 FORMULATION OF THE DIFFRACTION PROBLEM

The geometry is depicted in Fig. 3.2 The fluid is assumed inviscid, incompressible and the motion is irrotational, thus a velocity potential may be introduced,

$$\phi(x, y, z) = \phi(x, y, z)_{\text{incident}} + \phi(x, y, z)_{\text{scattered}} \quad (3.1)$$

The fluid motion is governed by the Laplace equation,

$$\frac{\partial^2 \phi}{\partial x^2} + \frac{\partial^2 \phi}{\partial y^2} + \frac{\partial^2 \phi}{\partial z^2} = 0 \quad (3.2)$$

The boundary conditions are:

$$\frac{\partial \xi}{\partial t} = \left(\frac{\partial \phi}{\partial z} \right)_{z=0} \quad \text{at water surface} \quad (3.3)$$

$$\xi = -\frac{1}{g} \left(\frac{\partial \phi e^{i\omega t}}{\partial t} \right)_{z=0} \quad \text{at water surface} \quad (3.4)$$

$$\left(\frac{\partial \phi}{\partial z} \right)_{z=-d} = 0 \quad \text{at sea floor} \quad (3.5)$$

$$\left(\frac{\partial \phi}{\partial n} \right)_s = 0 \quad \text{at hull surface} \quad (3.6)$$

$$\phi \rightarrow 0 \quad \text{at infinity} \quad (3.7)$$

where d is the water depth

ξ is the free surface elevation

By using the linear shallow water theory, velocity potential can be rewritten as follows:

$$\phi(x, y, z)e^{i\omega t} = \phi(x, y) \cosh k(d + z) \quad (3.8)$$

where $k = \frac{2\pi}{\lambda}$ and $\omega = \frac{2\pi}{T}$

The dispersion relation exists between the values ω , k and h ,

$$\omega^2 = gk \tanh kh \quad (3.9)$$

where k is the wave number

λ is the wave length

ω is the wave frequency

T is the wave period

By the substitution of Eq. (3.7) into Eq. (3.2), the Helmholtz equation can be written as follows:

$$\frac{\partial^2 \phi}{\partial x^2} + \frac{\partial^2 \phi}{\partial y^2} + k^2 \phi = 0 \quad (3.10)$$

The Helmholtz equation in elliptical coordinates is written as follows,

$$J \left(\frac{\partial^2 \phi}{\partial \zeta^2} + \frac{\partial^2 \phi}{\partial \eta^2} \right) + k^2 \phi = 0 \quad (3.11)$$

where J is the jacobian of the coordinate transformation from cartesian to elliptical coordinate systems and is given by:

$$J = \frac{8}{(2h)^2 (\cosh 2\zeta - \cos 2\eta)} \quad (3.12)$$

(ζ, η) is the elliptical coordinate system

h is the interfocal distance of the ellipse

Transformation between the elliptical and rectangular coordinates is given in Appendix B.

By using Equation (3.11), Equation (3.10) can be rewritten as follows:

$$\frac{\partial^2 \phi}{\partial \zeta^2} + \frac{\partial^2 \phi}{\partial \eta^2} + 2k_1^2 (\cosh 2\zeta - \cos 2\eta) \phi = 0 \quad (3.13)$$

where k_1 is the combined parameter of elliptic interfocal distance and wave number

Separation of variables could be used to solve Equation (3.12),

$$\phi(\zeta, \eta) = R(\zeta)Q(\eta) \quad (3.14)$$

when the separation of variables is applied, Equation (3.12) becomes:

$$\frac{\delta^2 R}{R \delta \zeta^2} + 2k_1 \cosh 2\zeta = -\frac{\delta^2 Q}{Q \delta \eta^2} + 2k_1^2 \cos 2\eta = A \quad (3.15)$$

where A is the separation constant from which the following two equations can be obtained:

$$\frac{\delta^2 Q}{\delta \eta^2} + (A - 2k_1^2 \cos 2\eta)Q = 0 \quad (3.16)$$

$$\frac{\delta^2 R}{\delta \zeta^2} + (A - 2k_1^2 \cosh 2\zeta)R = 0 \quad (3.17)$$

Equations (3.15) and (3.16) are known as the Mathieu and the Modified Mathieu differential equation respectively. These equations have been solved by Mclachlan [3.1] for incident and scattered waves. We will follow this solution, leaving the details to Appendix D.

3.3 VELOCITY POTENTIAL OF PLANE AND SCATTERED WAVES

When the plane waves approach the elliptic cylinder as shown in Fig. 3.2, the velocity potential of waves is represented by,

$$\phi_1 = 2 \phi_0 e^{-i\omega t} \phi_1 \quad (3.18)$$

$$\phi_0 = \frac{gH_{in}}{2\omega} \frac{\cosh(k(d+z))}{\cosh(kd)} \quad (3.19)$$

where H_{in} is the wave height

$$\begin{aligned} \phi_1 = \sum_{n=0}^{\infty} & \left[\frac{1}{P_{2n}} Ce_{2n}(\zeta) ce_{2n}(\eta) ce_{2n}(\theta) + \right. \\ & \frac{1}{s_{2n+2}} Se_{2n+2}(\zeta) se_{2n+2}(\eta) se_{2n+2}(\theta) + \\ & i \left\{ \frac{1}{P_{2n+1}} Ce_{2n+1}(\zeta) ce_{2n+1}(\eta) ce_{2n+1}(\theta) + \right. \\ & \left. \left. \frac{1}{s_{2n+1}} Se_{2n+1}(\zeta) se_{2n+1}(\eta) se_{2n+1}(\theta) \right\} \right] \quad (3.20) \end{aligned}$$

The $ce_n(\eta)$ and $se_n(\eta)$ are the solutions of Equation (3.16) and are known as even and odd radial functions, respectively. The functions $Ce_n(\zeta)$ and $Se_n(\zeta)$ are the solutions of Equation (3.17) and correspond to $ce_n(\eta)$ and $se_n(\eta)$ respectively. Detailed information about Mathieu functions is given in Appendix C. The terms p_n and s_n are constants expressible in terms of Mathieu functions and are given in Appendix D.

For the scattered wave,

$$\phi_2 = \phi_0 e^{-i\omega t} \phi_D \quad (3.21)$$

$$\begin{aligned}
\phi_D = & \sum_{n=0}^{\infty} [C_{2n} \text{Me}_{2n}^{(2)}(\zeta) \text{ce}_{2n}(\eta) \text{ce}_{2n}(\theta) + \\
& C_{2n+1} \text{Me}_{2n+1}^{(2)}(\zeta) \text{ce}_{2n+1}(\eta) \text{ce}_{2n+1}(\theta) + \\
& S_{2n+1} \text{Ne}_{2n+1}^{(2)}(\zeta) \text{se}_{2n+1}(\eta) \text{se}_{2n+1}(\theta) + \\
& S_{2n+2} \text{Ne}_{2n+2}^{(2)}(\zeta) \text{se}_{2n+2}(\eta) \text{se}_{2n+2}(\theta)] \quad (3.22)
\end{aligned}$$

The functions $\text{Me}_n^{(2)}(\zeta)$ and $\text{Ne}_n^{(2)}(\zeta)$ are the other solutions of Equation (3.17) and correspond to the second kind of Hankel functions. The constants C_n and S_n are determined by applying the boundary condition on the elliptical cylinder. This boundary condition implies that the sum of the normal velocities of the incident and scattered waves shall vanish at the boundary of the elliptical cylinder. If u_{n1} is the normal velocity of the incident wave and u_{n2} that of the scattered wave, we have

$$u_{n1} + u_{n2} = -\left(\frac{\partial\phi_1}{\partial n} + \frac{\partial\phi_2}{\partial n}\right)_{\zeta=\zeta_0} = 0 \quad (3.23)$$

n indicating the direction of the normal. Since $\partial n = l_1 \partial \zeta$ (l_1 is given in Appendix B), the boundary condition may be written as

$$\left(\frac{\partial\phi_1}{\partial\zeta} + \frac{\partial\phi_2}{\partial\zeta}\right)_{\zeta=\zeta_0} = 0$$

Using this condition and equating the sum of the derivatives of functions of the same kind and order to zero, for $\zeta = \zeta_0$ we have

$$C_{2n} = -\frac{2\phi_0 \text{Ce}'_{2n}(\zeta_0)}{P_{2n} \text{Me}_{2n}^{(2)'}(\zeta_0)}, \quad C_{2n+1} = -\frac{2i\phi_0 \text{Ce}'_{2n+1}(\zeta_0)}{P_{2n+1} \text{Me}_{2n+1}^{(2)'}(\zeta_0)}$$

$$S_{2n+1} = -\frac{2i\phi_0 Se'_{2n+1}(\zeta_0)}{s_{2n+1} Ne_{2n+1}^{(2)'(\zeta_0)}, \quad S_{2n+2} = -\frac{2\phi_0 Se'_{2n+2}(\zeta_0)}{s_{2n+2} Ne_{2n+2}^{(2)'(\zeta_0)},$$

Total potential is obtained from Equations (3.18) and (3.21)

$$\begin{aligned} \phi &= \phi_1 + \phi_2 \\ &= \phi_0 e^{-i\omega t} \sum_{n=0}^{\infty} \left[\frac{2}{P_{2n}} ce_{2n}(\eta) ce_{2n}(\theta) \left(Ce_{2n}(\zeta) - Me_{2n}^{(2)}(\zeta) \frac{Ce'_{2n}(\zeta_0)}{Me_{2n}^{(2)'(\zeta_0)}} \right) + \right. \\ &\quad \frac{2}{s_{2n+2}} se_{2n+2}(\eta) se_{2n+2}(\theta) \left(Se_{2n+2}(\zeta) - Ne_{2n+2}^{(2)}(\zeta) \frac{Se'_{2n+2}(\zeta_0)}{Ne_{2n+2}^{(2)'(\zeta_0)}} \right) + \\ &\quad i \left\{ \frac{2}{s_{2n+1}} se_{2n+1}(\eta) se_{2n+1}(\theta) \left(Se_{2n+1}(\zeta) - Ne_{2n+1}^{(2)}(\zeta) \frac{Se'_{2n+1}(\zeta_0)}{Ne_{2n+1}^{(2)'(\zeta_0)}} \right) + \right. \\ &\quad \left. \left. \frac{2}{P_{2n+1}} ce_{2n+1}(\eta) ce_{2n+1}(\theta) \left(Ce_{2n+1}(\zeta) - Me_{2n+1}^{(2)}(\zeta) \frac{Ce'_{2n+1}(\zeta_0)}{Me_{2n+1}^{(2)'(\zeta_0)}} \right) \right\} \right] \quad (3.24) \end{aligned}$$

3.4 WAVE FORCES AND MOMENTS

Wave forces are obtained by integrating the pressure around the cylinder. The pressure on the cylinder is derived from Bernoulli's equation. Since we are considering only the linearized problem the pressure becomes,

$$P = -\rho \frac{\partial \phi}{\partial t} \quad (3.25)$$

Surge, sway forces and yaw moment can be obtained by integrating the pressure over the surface. If the elliptic coordinates are used,

$$F_x = - \int_0^{2\pi} \int_{-\delta}^0 P h \sinh \zeta_0 \cos \eta \, dz \, d\eta \quad (3.26)$$

$$F_x = -i\rho\omega \frac{gH_{in}}{2\omega} e^{-i\omega t} \int_0^{2\pi} \int_{-\delta}^0 \frac{\cosh k(d+z)}{\cosh kd} dz$$

$$\left[\sum_{n=0}^{\infty} \left[\frac{2}{P_{2n}} ce_{2n}(\eta) ce_{2n}(\theta) \left(Ce_{2n}(\zeta) - Me_{2n}^{(2)}(\zeta) \frac{Ce'_{2n}(\zeta_0)}{Me_{2n}^{(2)'}(\zeta_0)} \right) + \right. \right.$$

$$\frac{2}{s_{2n+2}} se_{2n+2}(\eta) se_{2n+2}(\theta) \left(Se_{2n+2}(\zeta) - Ne_{2n+2}^{(2)}(\zeta) \frac{Se'_{2n+2}(\zeta_0)}{Ne_{2n+2}^{(2)'}(\zeta_0)} \right) +$$

$$i \left\{ \frac{2}{s_{2n+1}} se_{2n+1}(\eta) se_{2n+1}(\theta) \left(Se_{2n+1}(\zeta) - Ne_{2n+1}^{(2)}(\zeta) \frac{Se'_{2n+1}(\zeta_0)}{Ne_{2n+1}^{(2)'}(\zeta_0)} \right) + \right.$$

$$\left. \left. \frac{2}{P_{2n+1}} ce_{2n+1}(\eta) ce_{2n+1}(\theta) \left(Ce_{2n+1}(\zeta) - Me_{2n+1}^{(2)}(\zeta) \frac{Ce'_{2n+1}(\zeta_0)}{Me_{2n+1}^{(2)'}(\zeta_0)} \right) \right] \right] h \sinh \zeta_0 \cos \eta d\eta \quad (3.27)$$

If this integral is calculated and simplified, we have

$$F_x = \frac{1}{k} \rho g \pi e^{-i\omega t} H_{in} h \sinh \zeta_0 \frac{\sinh kd - \sinh k(d-\delta)}{\cosh kd}$$

$$\sum_{n=0}^{\infty} \frac{1}{P_{2n+1}} A_1^{(2n+1)} ce_{2n+1}(\theta) \left[Ce_{2n+1}(\zeta_0) - Me_{2n+1}^{(2)}(\zeta_0) \frac{Ce'_{2n+1}(\zeta_0)}{Me_{2n+1}^{(2)'}(\zeta_0)} \right] \quad (3.28)$$

where δ is the draft of the ship

A_m^n, B_m^n are the coefficients used in the calculation of Mathieu functions

P_m is the Mathieu constant coefficient

Sway force and yaw moment are calculated in a similar way

$$F_y = - \int_0^{2\pi} \int_{-\delta}^0 P h \cosh \zeta_0 \sin \eta dz d\eta$$

$$F_y = \frac{1}{k} \rho g \pi e^{-i\omega t} H_{in} h \cosh \zeta_0 \frac{\sinh kd - \sinh k(d - \delta)}{\cosh kd}$$

$$\sum_{n=0}^{\infty} \frac{2}{s_{2n+1}} B_1^{(2n+1)} se_{2n+1}(\theta) [Se_{2n+1}(\zeta_0) - Ne_{2n+1}^{(2)}(\zeta_0) \frac{Se'_{2n+1}(\zeta_0)}{Ne_{2n+1}^{(2)'}}(\zeta_0)] \quad (3.29)$$

Yaw moment can be written as follows,

$$M_z = - \int_0^{2\pi} \int_{-\delta}^0 P [h^2 \sin \eta \cos \eta (\sinh \zeta_0^2 + \cosh \zeta_0^2)] d\eta dz$$

$$M_z = - \frac{i}{k} \rho g \pi e^{-i\omega t} H_{in} h^2 \frac{\sinh kd - \sinh k(d - \delta)}{\cosh kd}$$

$$\sum_{n=0}^{\infty} \frac{1}{s_{2n+2}} B_2^{(2n+2)} se_{2n+2}(\theta) [Se_{2n+2}(\zeta_0) - Ne_{2n+2}^{(2)}(\zeta_0) \frac{Se'_{2n+2}(\zeta_0)}{Ne_{2n+2}^{(2)'}}(\zeta_0)] \quad (3.30)$$

Integrations used in calculating the wave forces are given in Appendix C.

3.5 FORMULATION OF THE RADIATION PROBLEM

The geometry is depicted in Fig. 3.2. The fluid is assumed inviscid, incompressible and the motion is irrotational. The fluid motion is governed by the Laplace equation,

$$\frac{\partial^2 \phi_R}{\partial x^2} + \frac{\partial^2 \phi_R}{\partial y^2} + \frac{\partial^2 \phi_R}{\partial z^2} = 0 \quad (3.31)$$

The boundary conditions are:

$$\frac{\partial \xi}{\partial t} = \left(\frac{\partial \phi_R}{\partial z} \right)_{z=0} \quad \text{at water surface} \quad (3.32)$$

$$\frac{\partial \phi_R}{\partial z} - \frac{\omega^2}{g} \phi_R = 0, \quad z = 0 \quad \text{at water surface} \quad (3.33)$$

$$\left(\frac{\partial \phi_R}{\partial z}\right)_{z=-d} = 0 \quad \text{at sea floor} \quad (3.34)$$

$$\phi_R \rightarrow 0 \text{ as } \xi \rightarrow \infty \quad \text{at infinity} \quad (3.35)$$

Solution of Equation (3.31) in elliptical coordinates together with the boundary conditions gives the radiation potential.

$$\begin{aligned} \phi_R = \frac{\cosh k(d+z)}{\cosh kd} \sum_{n=0}^{\infty} [& c_{2n} Mc_{2n}^{(3)}(\zeta) ce_{2n}(\eta) + \\ & c_{2n+1} Mc_{2n+1}^{(3)}(\zeta) ce_{2n+1}(\eta) + \\ & s_{2n+1} Ms_{2n+1}^{(3)}(\zeta) se_{2n+1}(\eta) + \\ & s_{2n+2} Ms_{2n+2}^{(3)}(\zeta) se_{2n+2}(\eta)] \end{aligned} \quad (3.36)$$

where Mc_m and Ms_m are radial Mathieu functions.

Constant coefficients c_m and s_m are determined using the boundary conditions on the body.

The body boundary conditions:

$$\left. \frac{\partial \phi_R}{\partial \xi} \right|_{\xi_0} = V_x h \sinh \xi_0 \cos \eta \quad \text{in the surge direction} \quad (3.37)$$

$$\left. \frac{\partial \phi_R}{\partial \xi} \right|_{\xi_0} = V_y h \cosh \xi_0 \sin \eta \quad \text{in the sway direction} \quad (3.38)$$

$$\left. \frac{\partial \phi_R}{\partial \xi} \right|_{\xi_0} = \frac{h}{2} \Omega_z \sin 2\eta \quad \text{in the yaw direction} \quad (3.39)$$

where h is the interfocal distance of the ellipse: $h = \sqrt{a^2 - b^2}$

V_x and V_y are the velocities in the surge and sway directions. Ω_z is the angular velocity in the yaw direction.

In order to obtain the coefficients c_m and s_m , boundary conditions (3.37), (3.38) and (3.39) are applied to Eq. 3.36 in turn. Then we obtain the coefficients

$$c_{2n=0} \quad (3.40)$$

$$c_{2n+1} = \frac{h \sinh \xi_0 A_1^{(2n+1)}}{N_k M c_{2n+1}^{(3)}(\xi_0, q)} \int_{-\delta}^0 V_x \cosh k(z+d) dz \quad (3.41)$$

$$s_{2n+1} = \frac{h \cosh \xi_0 B_1^{(2n+1)}}{N_k M s_{2n+1}^{(3)}(\xi_0, q)} \int_{-\delta}^0 V_y \cosh k(z+d) dz \quad (3.42)$$

$$s_{2n+2} = \frac{1/2 h^2 B_2^{(2n+2)}}{N_k M s_{2n+2}^{(3)}(\xi_0, q)} \int_{-\delta}^0 \Omega_z \cosh k(z+d) dz \quad (3.43)$$

$$N_k = \frac{\sinh 2kd}{4k} + \frac{\delta}{2} - \frac{\sinh(2k(d-\delta))}{4k}$$

3.6 CALCULATION OF ADDED MASS AND DAMPING COEFFICIENTS

Added mass and damping coefficients are determined by integrating the radiation potential around the cylinder.

$$m_{ij} = \rho \int_A \text{Re}[\phi_j] n_i dA \quad (3.44)$$

$$c_{ij} = \omega \rho \int_A \text{Im}[\phi_j] n_i dA \quad (3.45)$$

Damping coefficient in the surge direction is calculated as follows:

$$c_{11} = \omega \rho \int_{-\delta}^0 \int_0^{2\pi} \text{Im}[\phi_1] h \sinh \xi_0 \cos \eta d\eta dz$$

$$c_{11} = 2\rho\omega^2 \frac{(b/2)^2}{k^2 N_k} (\sinh kd - \sinh k(d - \delta))^2$$

$$\sum_{n=0}^{\infty} \frac{(A_1^{(2n+1)})^2}{(Mc_{2n+1}^{(1)}(\xi_0, q))^2 + (Mc_{2n+1}^{(2)}(\xi_0, q))^2} \quad (3.46)$$

Damping coefficient in the sway direction:

$$c_{22} = \omega \rho \int_{-\delta}^0 \int_0^{2\pi} \text{Im}[\phi_2] h \cosh \xi_0 \sin \eta d\eta dz$$

$$c_{22} = 2\rho\omega^2 \frac{(a/2)^2}{k^2 N_k} (\sinh kd - \sinh k(d - \delta))^2$$

$$\sum_{n=0}^{\infty} \frac{(B_1^{(2n+1)})^2}{(Ms_{2n+1}^{(1)}(\xi_0, q))^2 + (Ms_{2n+1}^{(2)}(\xi_0, q))^2} \quad (3.47)$$

Damping coefficient in the yaw direction:

$$c_{66} = \omega \rho \int_{-\delta}^0 \int_0^{2\pi} \text{Im}[\phi_6] h^2 \cos \eta \sin \eta \, d\eta \, dz$$

$$c_{66} = 2\rho \omega^2 \frac{1/2 h^4}{k^2 N_k} (\sinh kd - \sinh k(d - \delta))^2$$

$$\sum_{n=0}^{\infty} \frac{(B_2^{(2n+2)})^2}{(Ms_{2n+2}^{(1)'(\xi_0, q)})^2 + (Ms_{2n+2}^{(2)'(\xi_0, q)})^2} \quad (3.48)$$

Added mass coefficient in the surge direction:

$$m_{11} = \rho \int_{-\delta}^0 \int_0^{2\pi} \text{Re}[\phi_2] h \sinh \xi_0 \cos \eta \, d\eta \, dz$$

$$m_{11} = \rho \pi \frac{(b/2)^2}{k^2 N_k} (\sinh kd - \sinh k(d - \delta))^2$$

$$\sum_{n=0}^{\infty} (A_1^{(2n+1)})^2 \frac{Mc_{2n+1}^{(1)'(\xi_0)} Mc_{2n+1}^{(2)'(\xi_0)} + Mc_{2n+1}^{(2)'(\xi_0)} Mc_{2n+1}^{(1)'(\xi_0)}}{(Mc_{2n+1}^{(1)'(\xi_0)})^2 + (Mc_{2n+1}^{(2)'(\xi_0)})^2} \quad (3.49)$$

Added mass coefficient in the sway direction:

$$m_{22} = \rho \int_{-\delta}^0 \int_0^{2\pi} \text{Re}[\phi_3] h \cosh \xi_0 \sin \eta \, d\eta \, dz$$

$$m_{22} = \rho \pi \frac{(a/2)^2}{k^2 N_k} (\sinh kd - \sinh k(d - \delta))^2$$

$$\sum_{n=0}^{\infty} (B_1^{(2n+1)})^2 \frac{Ms_{2n+1}^{(1)'(\xi_0)} Ms_{2n+1}^{(1)'(\xi_0)} + Ms_{2n+1}^{(2)'(\xi_0)} Ms_{2n+1}^{(2)'(\xi_0)}}{(Ms_{2n+1}^{(1)'(\xi_0)})^2 + (Ms_{2n+1}^{(2)'(\xi_0)})^2} \quad (3.50)$$

Added mass coefficient in the yaw direction:

$$m_{66} = \rho \int_{-\delta}^0 \int_0^{2\pi} \text{Re}[\phi_6] h^2 \cos \eta \sin \eta \, d\eta \, dz$$

$$m_{66} = \rho \pi \frac{1/2 h^4}{k^2 N_k} (\sinh kd - \sinh k(d - \delta))^2$$

$$\sum_{n=0}^{\infty} (B_2^{(2n+2)})^2 \frac{Ms_{2n+2}^{(1)}(\xi_0) Ms_{2n+2}^{(1)'}(\xi_0) + Ms_{2n+2}^{(2)}(\xi_0) Ms_{2n+2}^{(2)'}(\xi_0)}{(Ms_{2n+2}^{(1)'}(\xi_0))^2 + (Ms_{2n+2}^{(2)'}(\xi_0))^2} \quad (3.51)$$

3.7 SECOND ORDER MEAN FORCES ACTING ON THE TANKER

According to Newman [3.11], the Kochin function is expressed as follows,

$$K(\theta) = \iint_{S_B} \left(\frac{\partial \phi_B}{\partial n} - \phi_B \frac{\partial}{\partial n} \right) e^{(kz + ikx \cos \theta + ikys \sin \theta)} \, dS \quad (3.52)$$

where ϕ_B = Diffraction+Radiation potential

S_B = Wetted surface area of the ship

θ = Polar angle

Surge and sway forces and yaw moment are derived by using the Kochin function,

$$\bar{F}_x = \frac{\rho k^2}{8\pi} \int_0^{2\pi} |K(\theta)|^2 (\cos \theta + \cos \theta_1) \, d\theta \quad (3.53)$$

$$\bar{F}_y = \frac{\rho k^2}{8\pi} \int_0^{2\pi} |K(\theta)|^2 (\sin \theta + \sin \theta_1) \, d\theta \quad (3.54)$$

$$\bar{M}_z = -\frac{\rho k}{8\pi} \int_0^{2\pi} K^*(\theta) K'(\theta) d\theta - \frac{1}{2k} \rho \omega A_I \operatorname{Re} K'(\pi + \theta_I) \quad (3.55)$$

where θ_I is the wave incidence

k is the wave number

A_I is the wave amplitude

K' is the derivative of the Kochin function

K^* is the conjugate of the Kochin function

Diffraction potential for an elliptical cylinder is written as follows [3.12];

$$\begin{aligned} \phi_D = \frac{2A_I g}{\omega} e^{kz} \sum_{n=0}^{\infty} (-1)^{n+1} \{ & [a_{2n} \operatorname{Mc}_{2n}^{(3)}(\zeta)] \operatorname{ce}_{2n}(\eta) \operatorname{ce}_{2n}(\theta) + \\ & i [a_{2n+1} \operatorname{Mc}_{2n+1}^{(3)}(\zeta)] \operatorname{ce}_{2n+1}(\eta) \operatorname{ce}_{2n+1}(\theta) + \\ & i [b_{2n+1} \operatorname{Ms}_{2n+1}^{(3)}(\zeta)] \operatorname{se}_{2n+1}(\eta) \operatorname{se}_{2n+1}(\theta) - \\ & [b_{2n+2} \operatorname{Ms}_{2n+2}^{(3)}(\zeta)] \operatorname{se}_{2n+2}(\eta) \operatorname{se}_{2n+2}(\theta) \} \end{aligned} \quad (3.56)$$

where

$$a_m(\xi_0) = \frac{\operatorname{Mc}_m^{(1)'(\xi_0)}}{\operatorname{Mc}_m^{(3)'(\xi_0)}} \quad b_m(\xi_0) = \frac{\operatorname{Ms}_m^{(1)'(\xi_0)}}{\operatorname{Ms}_m^{(3)'(\xi_0)}}$$

The Kochin function for the elliptical cylinder is derived by substituting ϕ_D in Eq. 3.1,

$$\begin{aligned} K(\theta) = \frac{4i A_I g}{k \omega} (1 - e^{-2k\delta}) \sum_{n=0}^{\infty} [& -a_{2n} \operatorname{ce}_{2n}(\theta) \operatorname{ce}_{2n}(\theta_I) - b_{2n+2} \operatorname{se}_{2n+2}(\theta) \operatorname{se}_{2n+2}(\theta_I) \\ & + a_{2n+1} \operatorname{ce}_{2n+1}(\theta) \operatorname{ce}_{2n+1}(\theta_I) + b_{2n+1} \operatorname{se}_{2n+1}(\theta) \operatorname{se}_{2n+1}(\theta_I)] \end{aligned} \quad (3.57)$$

Krokstad tried to tackle the same problem [3.13]. But his work contained some errors. His expression for the kochin function is as follows,

$$K(\theta) = \frac{4i}{k} \sum_{n=0}^{\infty} [a_n ce_n(\theta) ce_n(\theta_1) + b_{n+1} se_{n+1}(\theta) se_{n+1}(\theta_1)] \quad (3.58)$$

By substituting Eq. 3.58 into Eqs. 3.53, 3.54 and 3.55 wave forces and moments could be integrated numerically.

3.8 NUMERICAL ASPECTS AND RESULTS

The Theoretical solution of a problem is not sufficient for most engineering requirements. Quantative results are needed.

Tabulated values for periodic Mathieu functions by Ince [3.14] and radial Mathieu functions by Blanch and Clemm [3.15] are insufficient for the calculations needed for the solution of this problem. Published algorithm by Clemm [3.6] has been used to carry out the calculations. Tolerance used in this algorithm was 1.0e-14. Higher tolerances cause divergence in the solutions. The calculation of Mathieu functions for very high frequencies is difficult because of the very large parametric value, q . For instance, for 5 rad/sec the parametric value becomes 38078,56. Results of the algorithm have been checked with Ince's tabulated values and they agree well with each other. However, in this algorithm a different kind of definition for radial Mathieu functions was used. So all the force terms derived in the previous section were expressed again using the new definitions. These new definitions and force terms are given in Appendix E. Ince's normalization has been used in the calculations. The series used in the force calculations converge very fast even for high q values.

Non-dimensionalised surge and sway forces and yaw moment for shiplike bodies with beam-to-length ratio (b/a) ranging from 0.005 to 0.995 and with angle of incidence ranging from 0 to 90 degrees are presented in Figs. 3.3 to 3.27. In these graphs, a/l in the

horizontal axes correspond to the ship length/wave length ratio. Results of the elliptical cylinder approach are compared with Oortmerssen's experimental results [3.7] which have been performed for a tanker whose dimensions are 310 x 47.2 x 18.9 m.

The results given in Figs. 3.28 and 3.29 show good agreement for the sway forces as the waves approach with angles of incidence of 225 and 270 degrees . Fig. 3.30 show a good agreement between the predictions and measurements for the wave incidence angle of 225 degrees. Fig. 3.31 shows also a good correlation between the measurements and predictions for the wave incidence of angle 225. Agreement is not so good in the surge force with the angle of incidence 180 degrees (Fig. 3.32). One possible reason for that is the aft-forward symmetry exhibited by the elliptic cylinder. Comparisons show that the method described in this report for the calculation of wave forces and moments is capable of handling the shallow water effect since in the Oortmerssen's experiments water depth/draft ratio was 1.2.

The limiting geometry of the elliptical cylinder is a circular cylinder when length/beam ratio approaches unity. This provides an excellent check on the correctness of the programming. Results for the circular cylinder obtained from the limiting case of the elliptic cylinder are compared with the results obtained from the exact formula for circular cylinders [3.16, 3.17 and 3.18]. This comparison shows excellent agreement (See Fig. 3.33). The exact formula used for the cylinder is taken from Ref. 3.18.

$$F_x = \int_{-\delta}^0 \frac{2\rho g H_w e^{ky}}{k} \frac{\cos(\omega t - \theta)}{\sqrt{J_1'^2(kR) + Y_1'^2(kR)}} dy$$

where $\theta = \arctan\left(\frac{Y_1'(kR)}{J_1'(kR)}\right)$

and $J_1'(kR) = J_0(kR) - \frac{1}{(kR)} J_1(kR)$

$$Y_1'(kR) = Y_0(kR) - \frac{1}{(kR)} Y_1(kR)$$

$J_m(kR)$ and $Y_m(kR)$ are the Bessel functions of the first and second kinds.

Non-dimensionalised hydrodynamics coefficients are also compared with Oortmerssen's experimental data (Figs. 3.34-3.39). Comparisons show reasonable agreement except the surge damping coefficient (Fig. 3.37). The discrepancy in Fig. 3.37 may be due to the very small values of surge damping which are very difficult to measure. The difference between the tanker form and the elliptical cylinder form may be a reason for the discrepancies seen in the low frequencies in the comparisons. The results of the elliptical approach are also compared with a 3-D program based on oscillating source distribution technique [3.8] (Figs 3.40-3.45). Agreement is generally good. Discrepancies in the low frequencies are due to the fact that the elliptical approach does not take into account the effect of underwater clearance.

Motion transfer functions for surge, sway and yaw motions are compared with Oortmerssen's experimental results (Figs. 3.46-3.50). Agreement is generally good except the yaw motion response (Fig. 3.50). The discrepancy shown in the yaw motion comparison is due to the discrepancies in the yaw added mass and damping predictions (Figs. 3.36 and 3.39).

3.9 CONCLUSIONS

The theory described to calculate the wave and motion induced forces on tankers provides an alternative method of predicting the wave forces and moments on tankers. CPU time for the calculation of wave forces is about 15 minutes for three angles of wave incidence and for 80 wave frequencies at each wave incidence angle in VAX. It is quite fast compared to the programs which utilize the Green's function method. The combination of reasonable accuracy and low computational cost makes it a good alternative to other numerical methods. This method could be used for the time domain analysis of the tankers and single-point moored systems.

Mean drift forces acting on the elliptical cylinder are compared with Chan's 3-D program (Fig. 3.51, 3.52 and 3.53). There are large discrepancies between the elliptical cylinder approach and the 3-D program. This is because the flow under the cylinder was not modelled in the theory. Results of the elliptical cylinder approach are also compared with the Havelock's method [3.19] for the limiting case of circular cylinder extending from sea surface to sea bottom and agreement is quite good (Fig. 3.54).

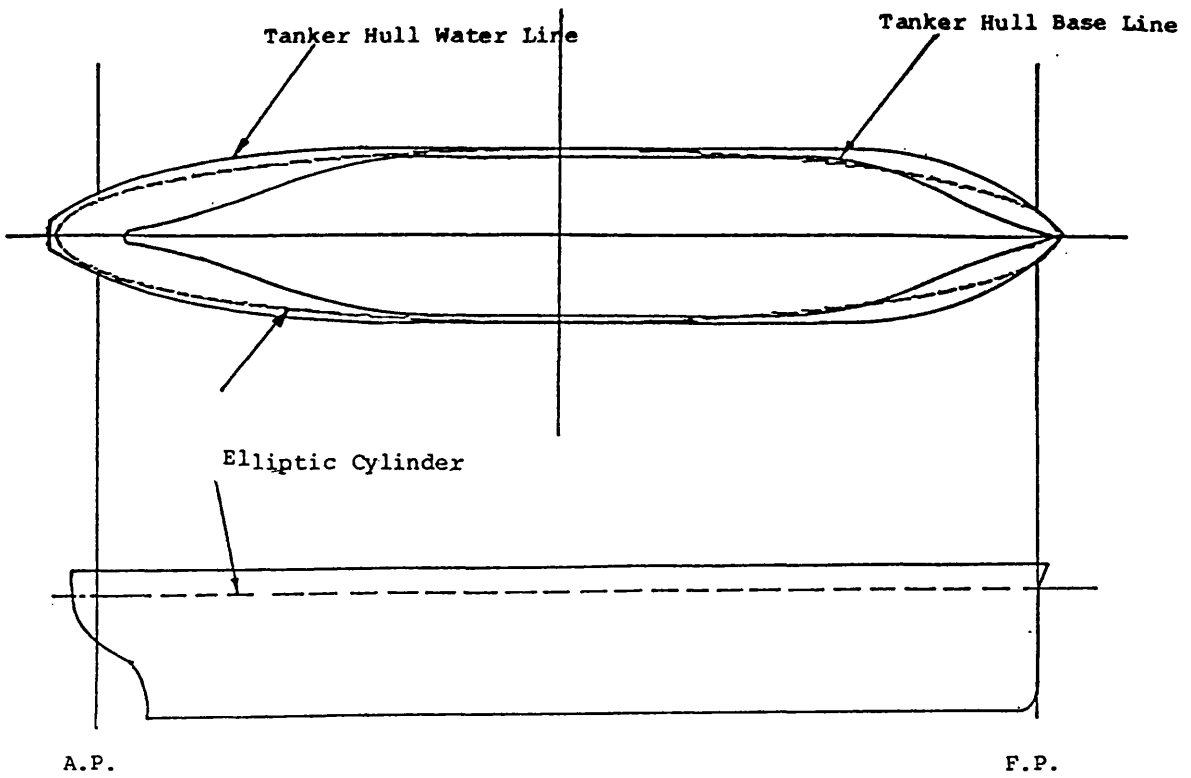


Fig. 3.1 Elliptical Cylinder and Real Tanker Hull Comparison

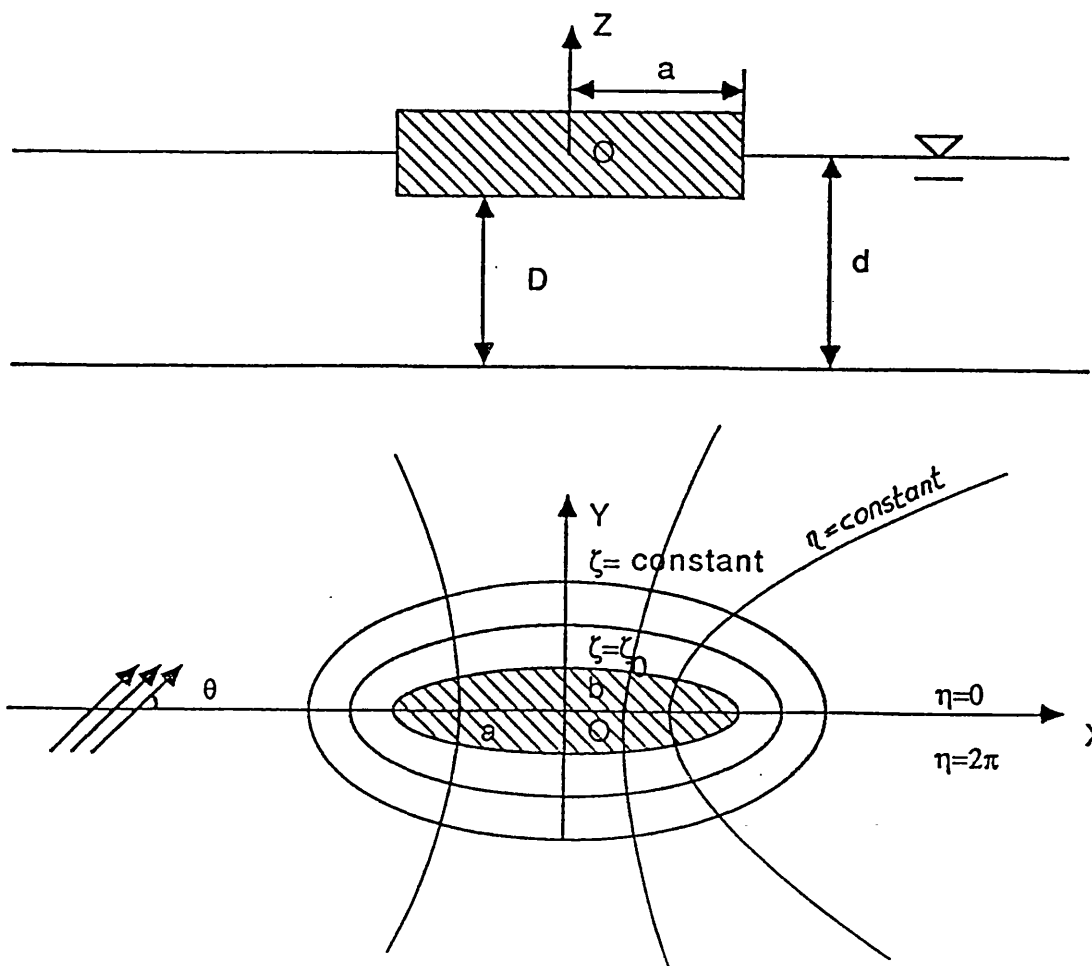


Fig. 3.2 Elliptical Co-ordinates

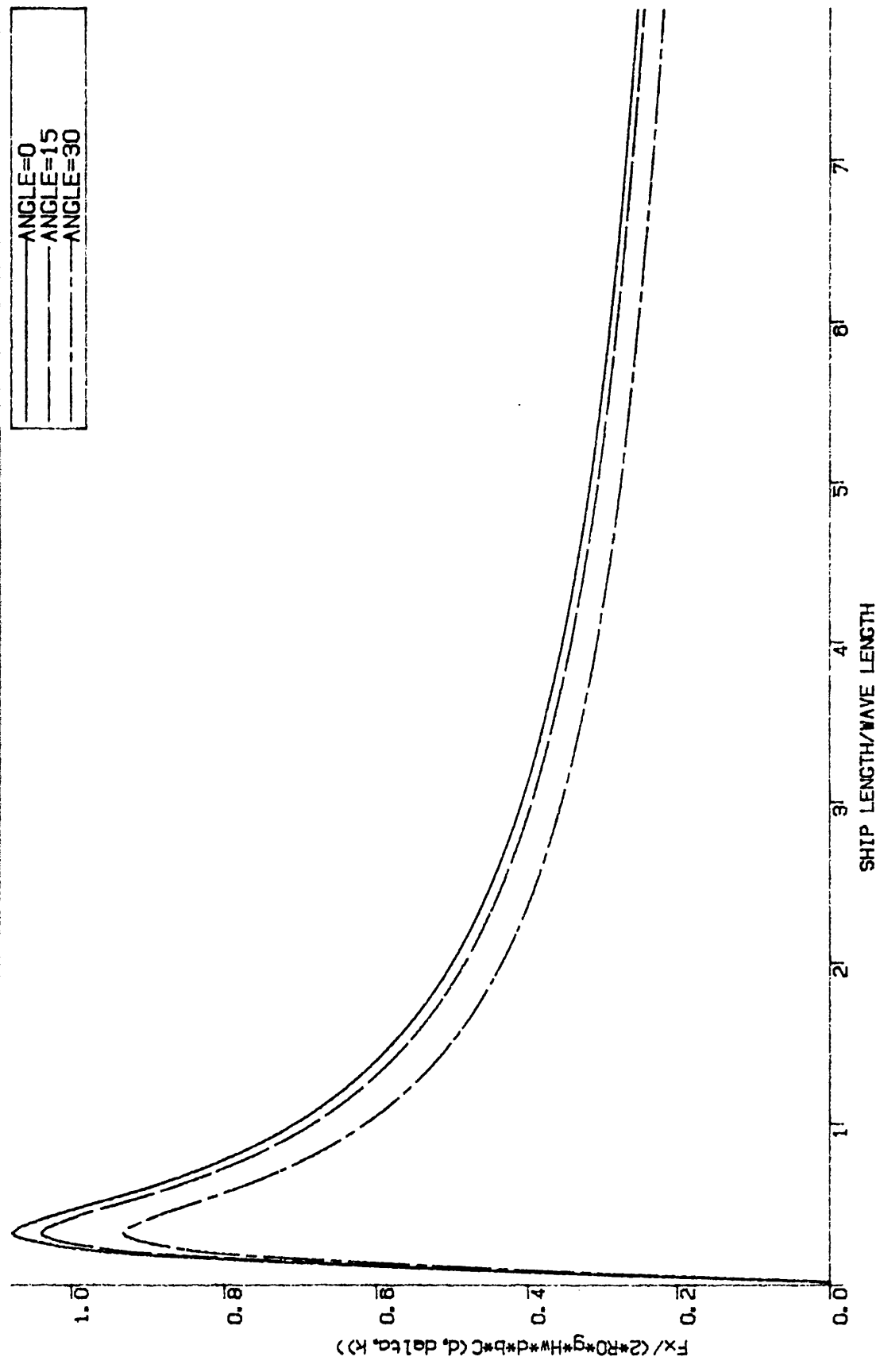


Fig. 3.3 Non-dimensionalised Surge Force
Ship Breadth/Ship Length=0.995

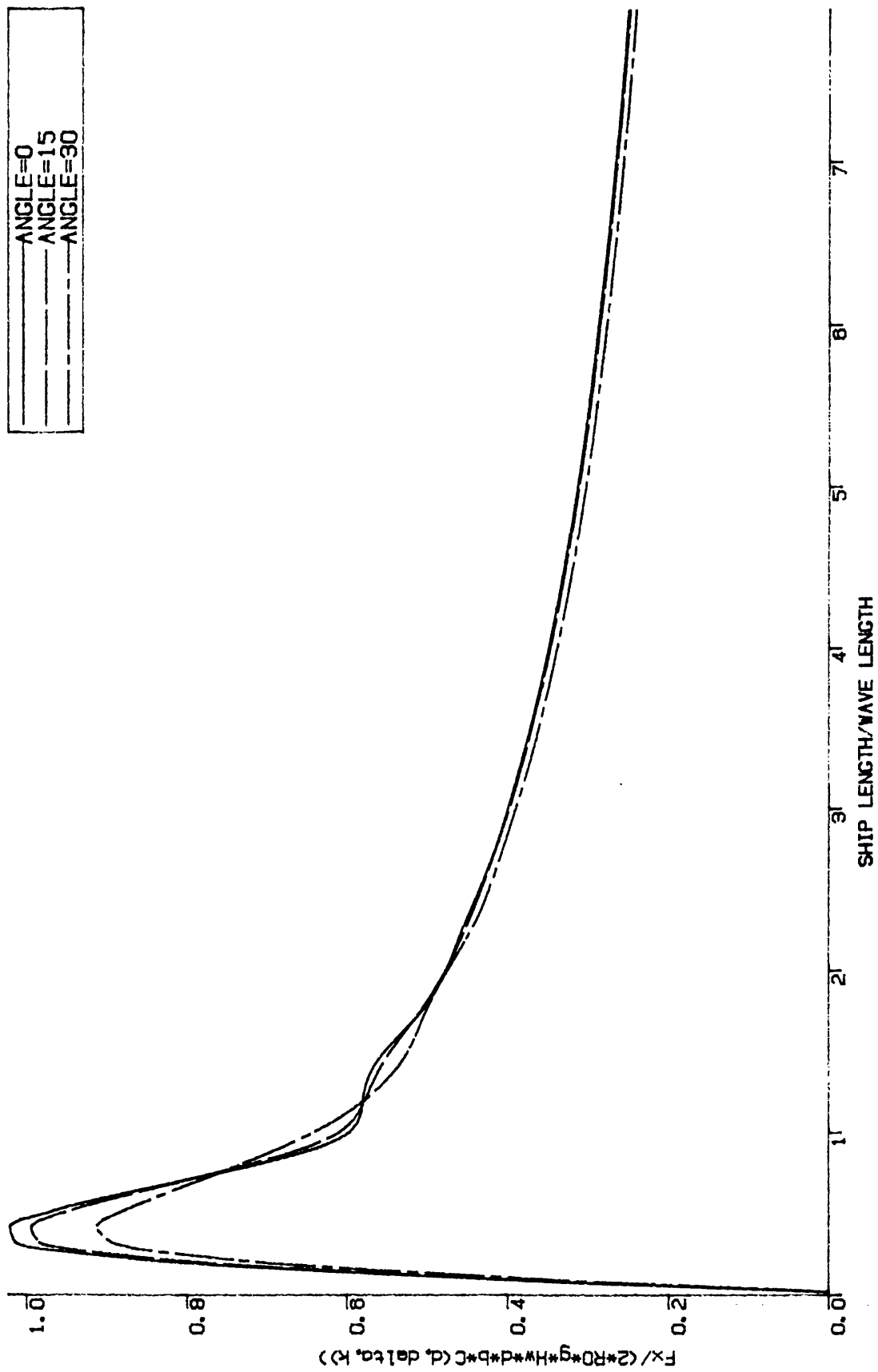


Fig. 3.4 Non-dimensionalised Surge Force
Ship Breadth/Ship Length=0.7

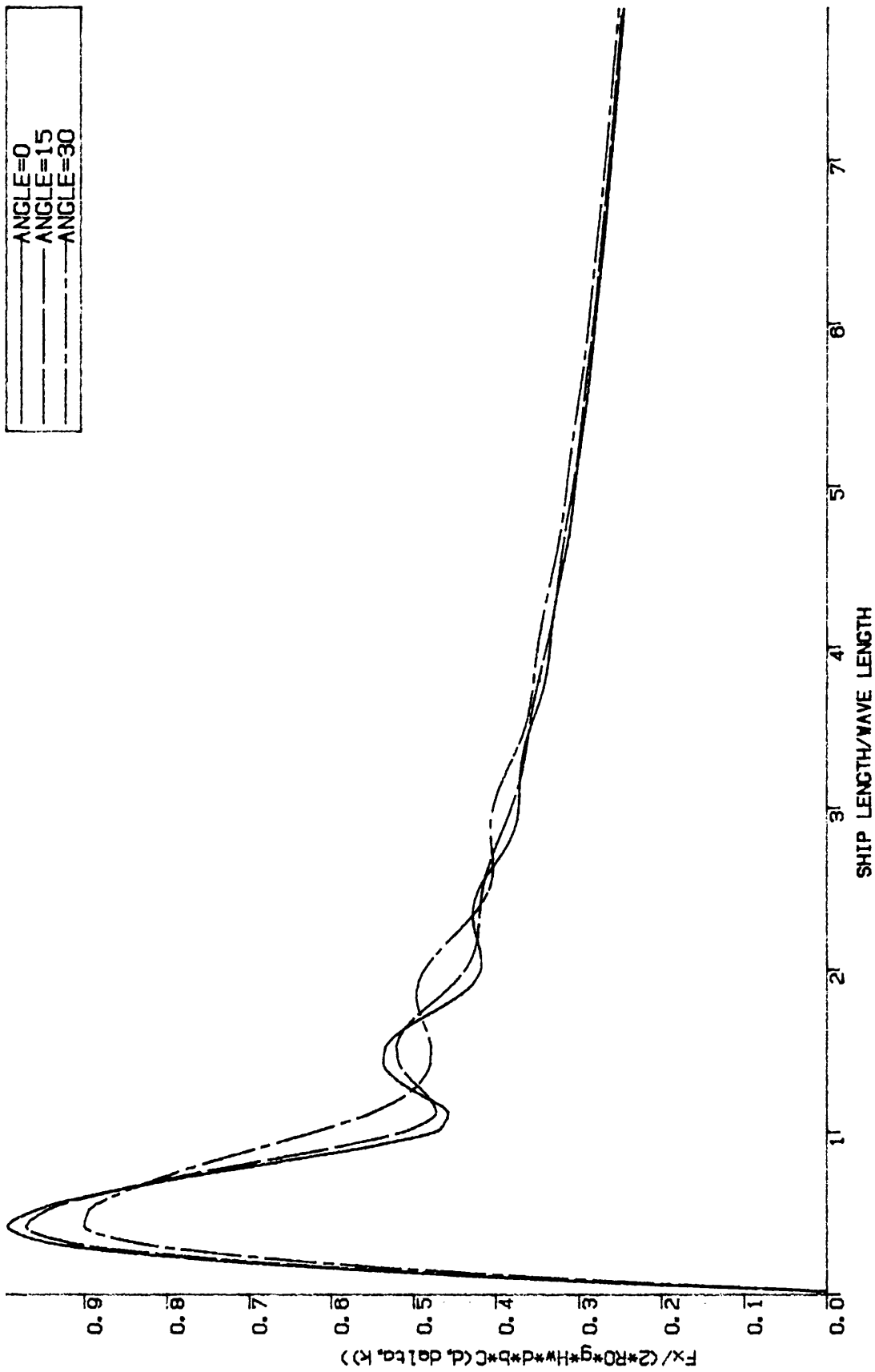


Fig. 3.5 Non-dimensionalised Surge Force
Ship Breadth/Ship Length=0.5

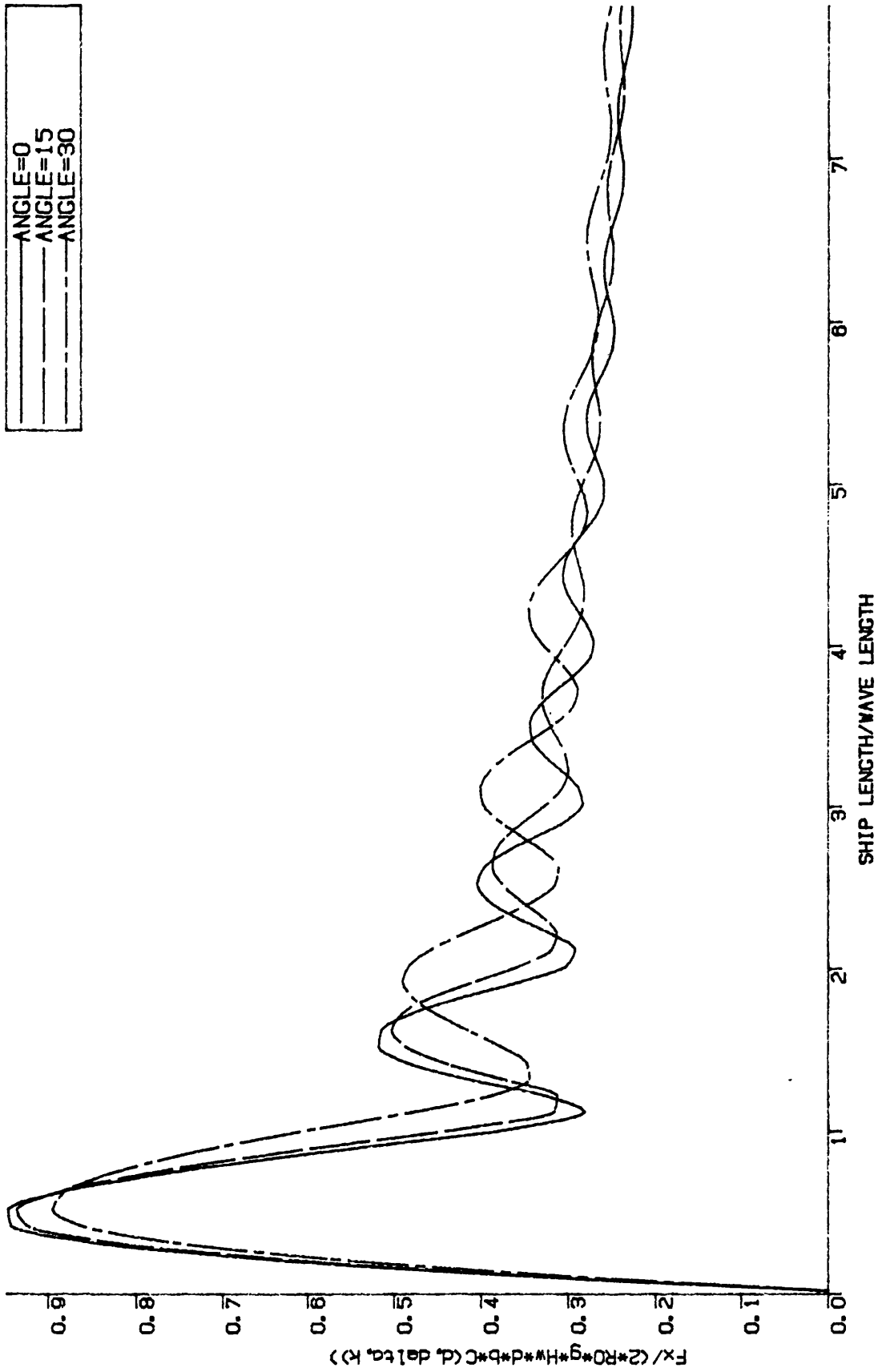


Fig. 3.6 Non-dimensionalised Surge Force
Ship Breadth/Ship Length=0.3

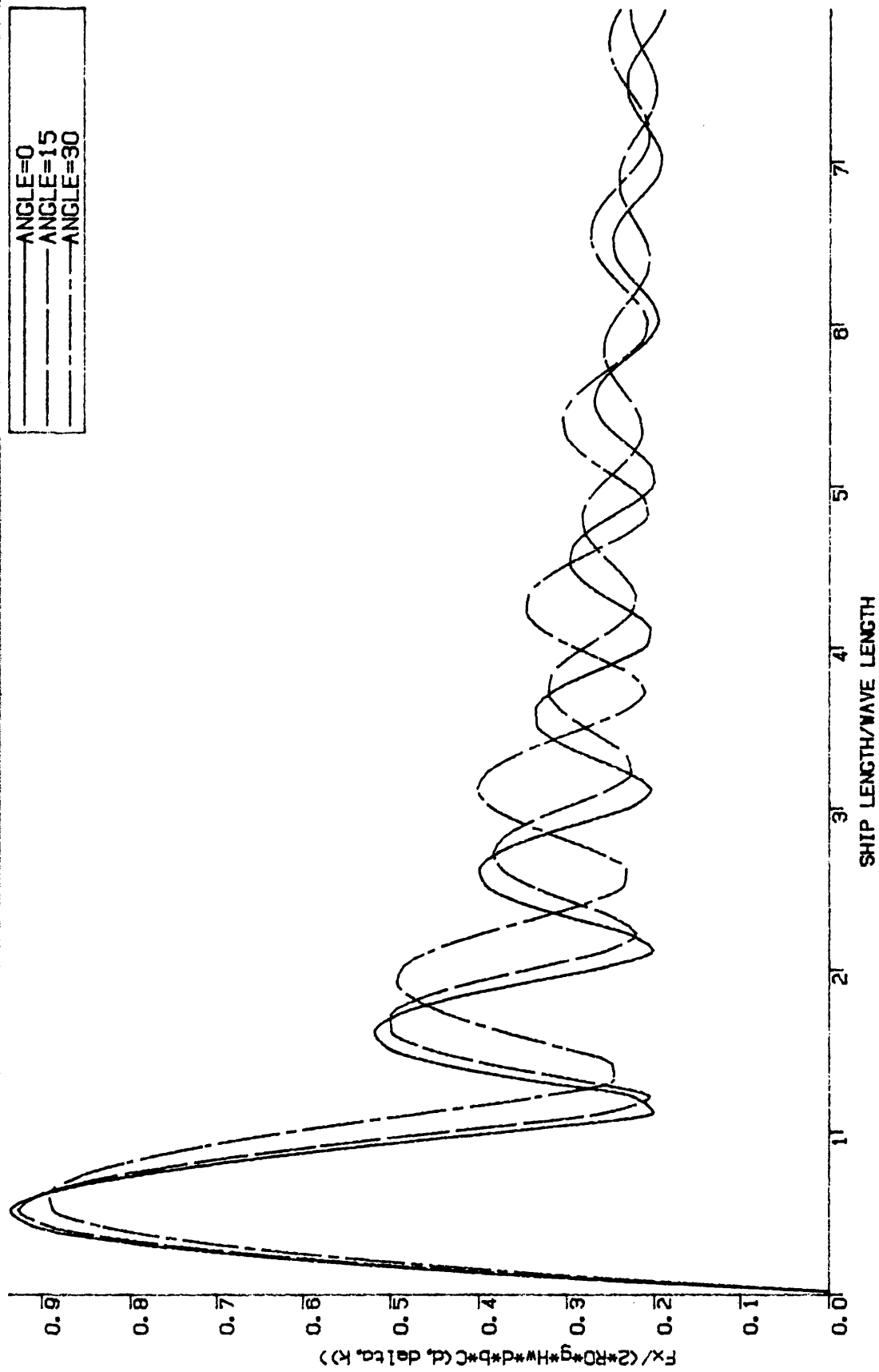


Fig. 3.7 Non-dimensionalised Surge Force
Ship Breadth/Ship Length=0.2

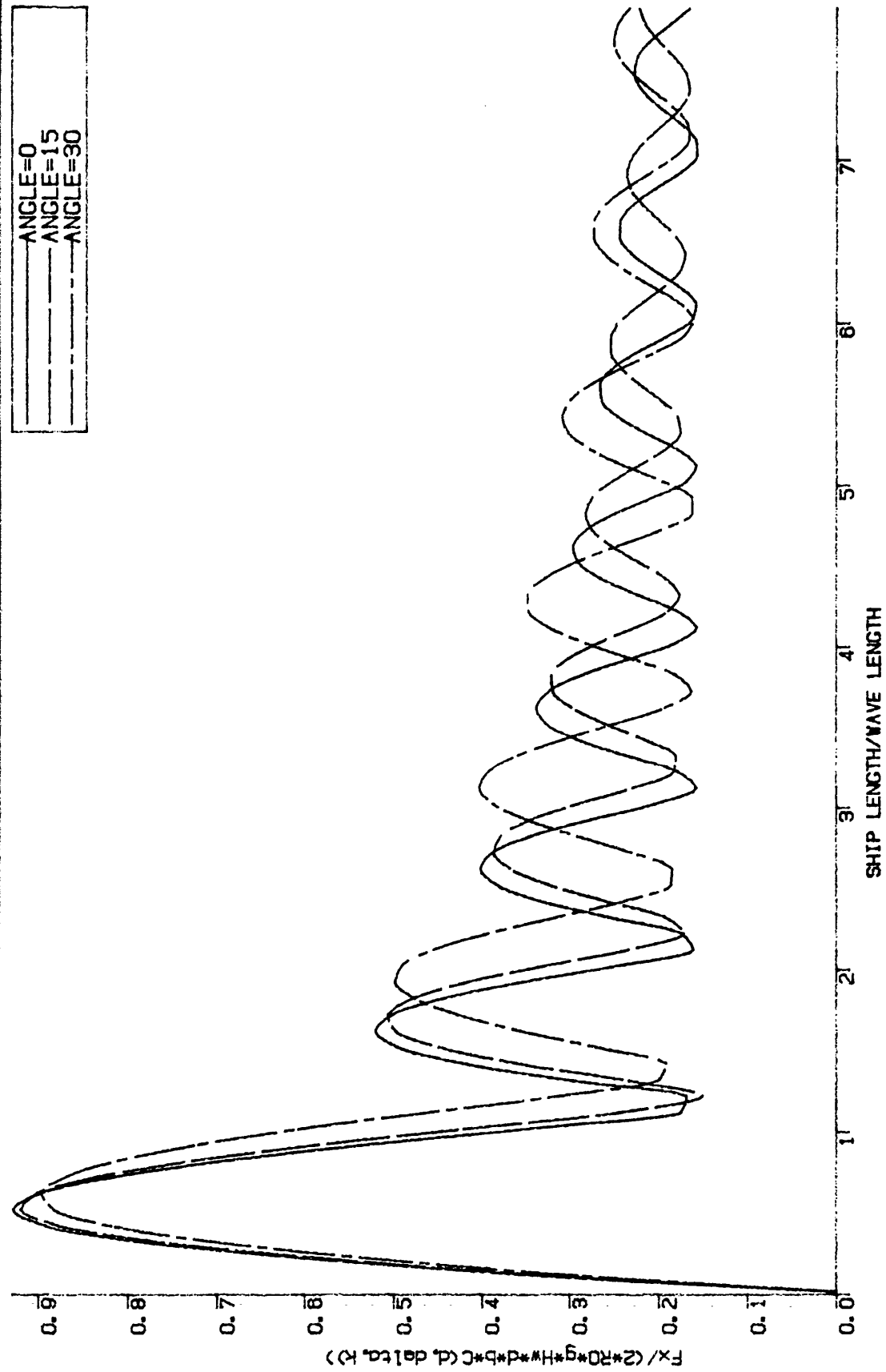


Fig. 3.8 Non-dimensionalised Surge Force
 Ship Breadth/Ship Length=0.15

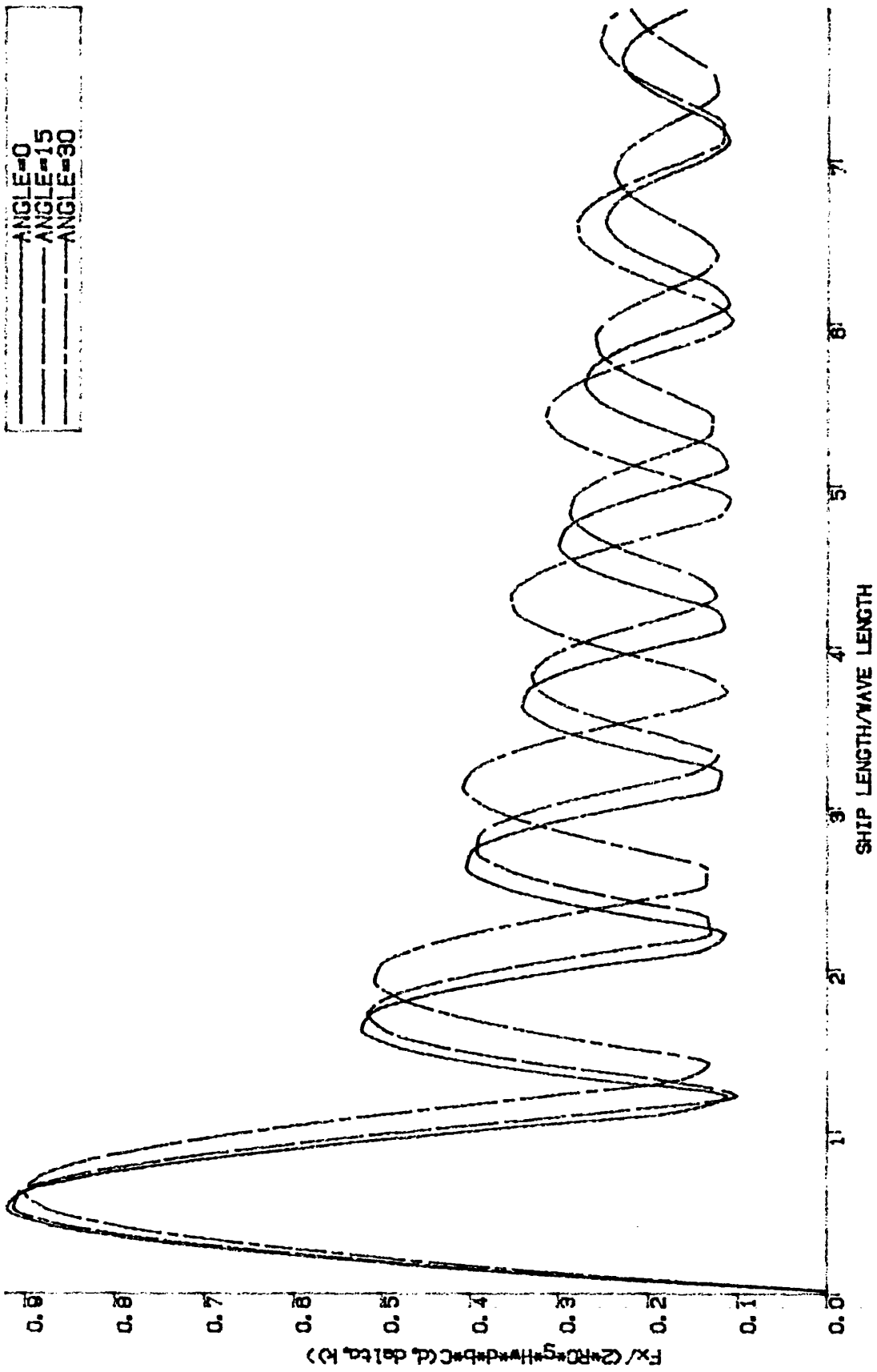
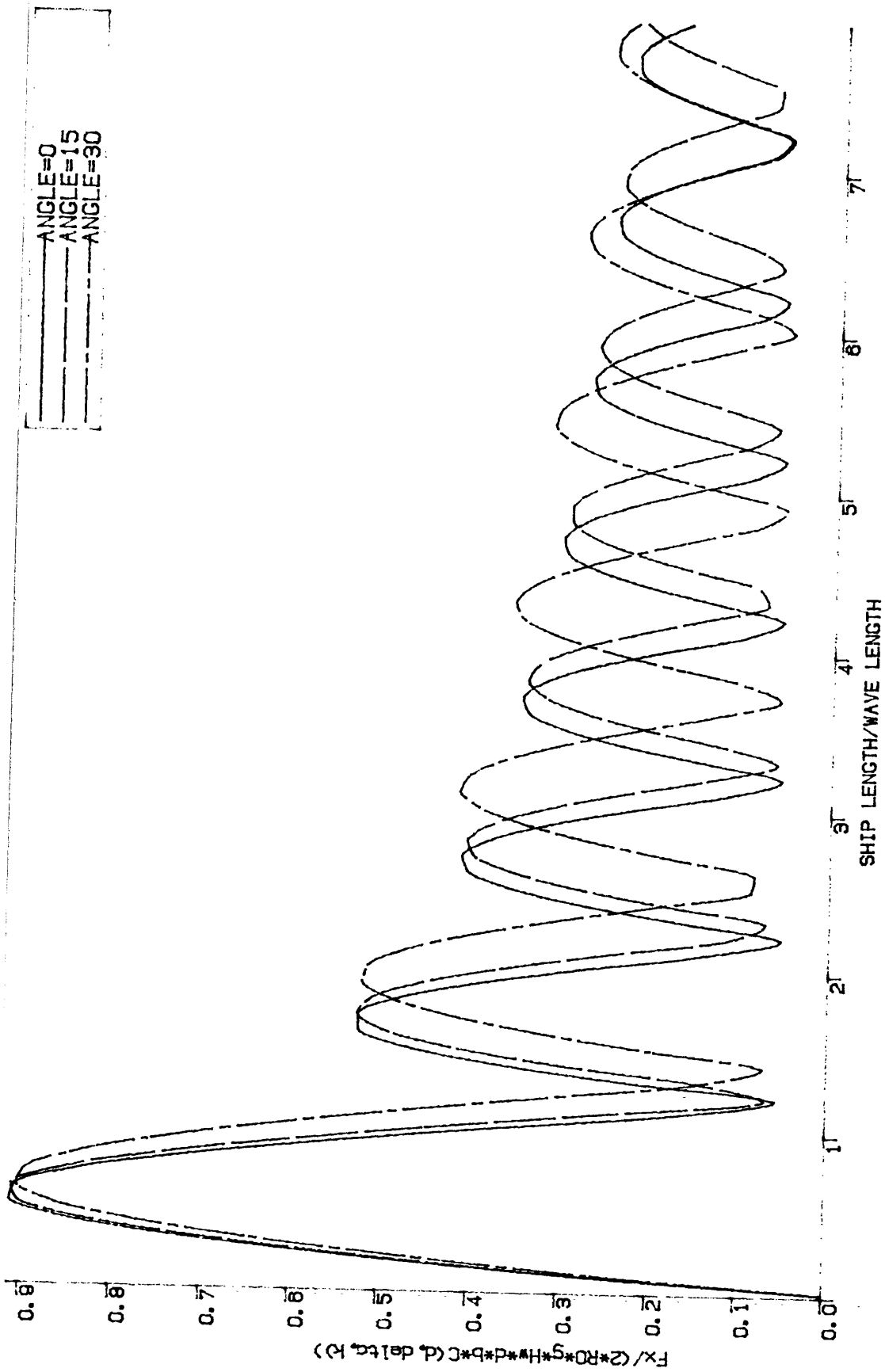


Fig. 3.9 Non-dimensionalised Surge Force
Ship Breadth/Ship Length=0.1



— ANGLE=0
 - - ANGLE=15
 - . ANGLE=30

Fig. 3.10 Non-dimensionalised Surge Force
 Ship Breadth/Ship Length=0.05

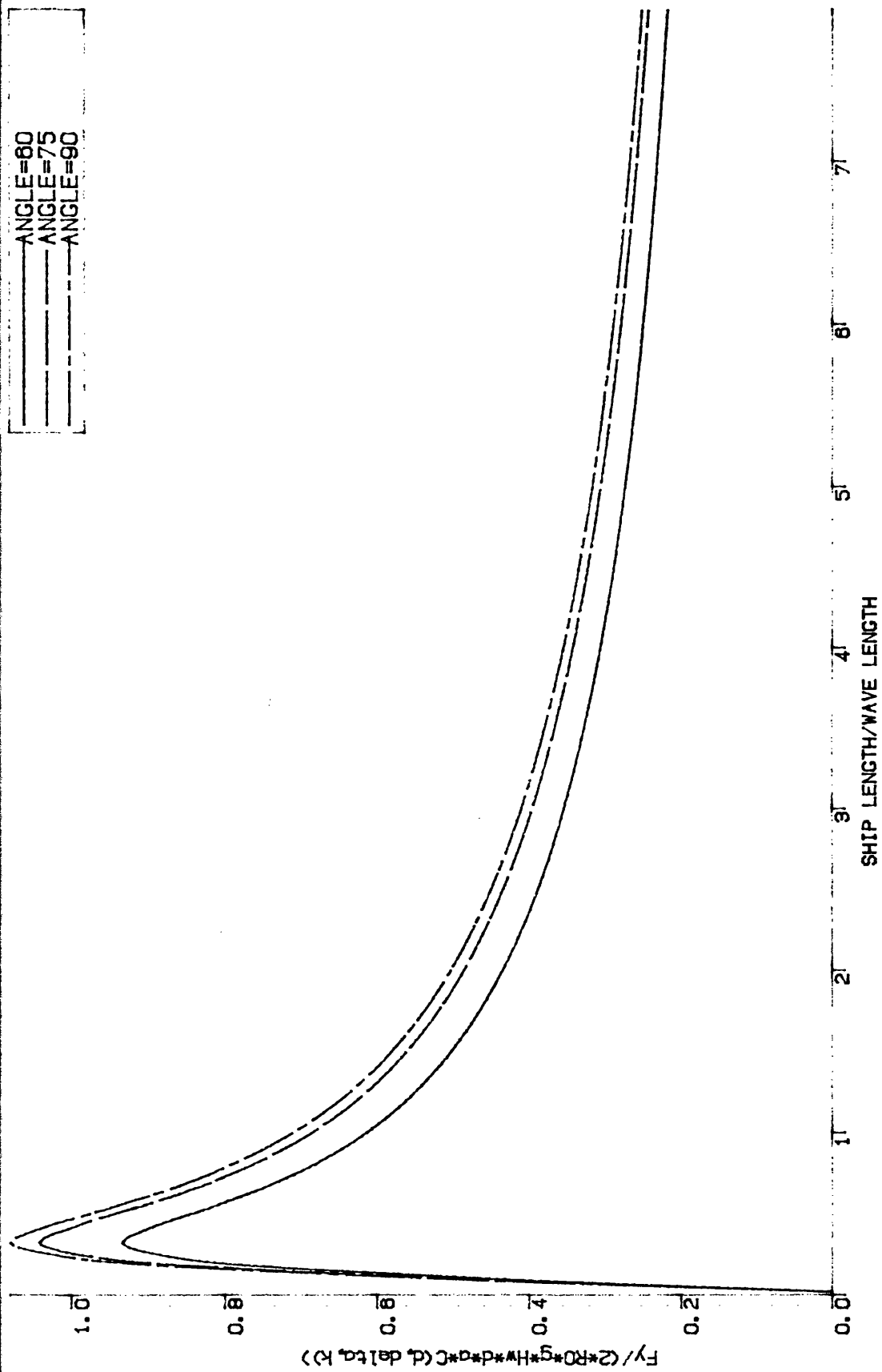


Fig. 3.11 Non-dimensionalised Sway Force
Ship Breadth/Ship Length=0.995

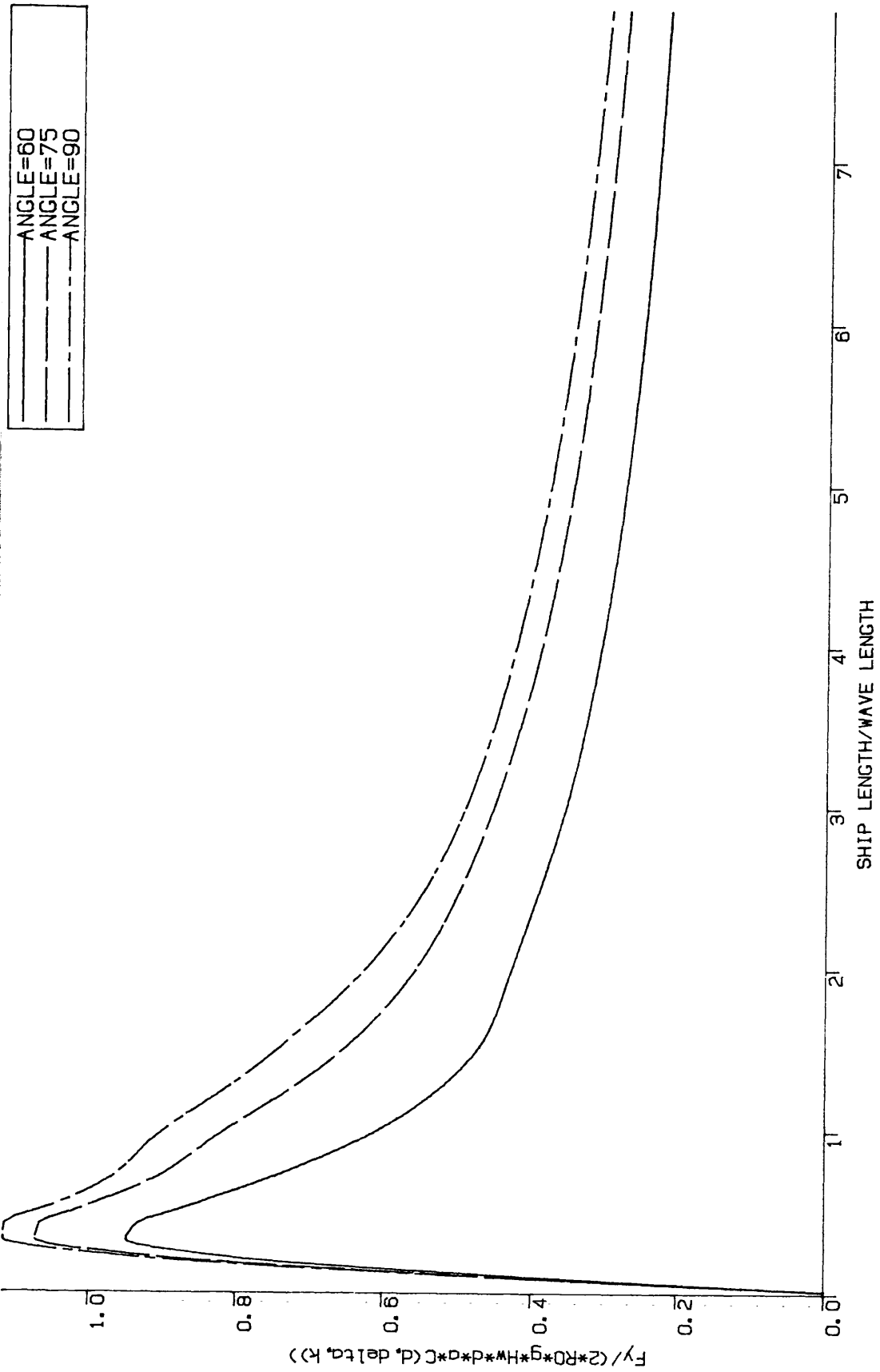


Fig. 3.12 Non-dimensionalised Sway Force
Ship Breadth/Ship Length=0.7

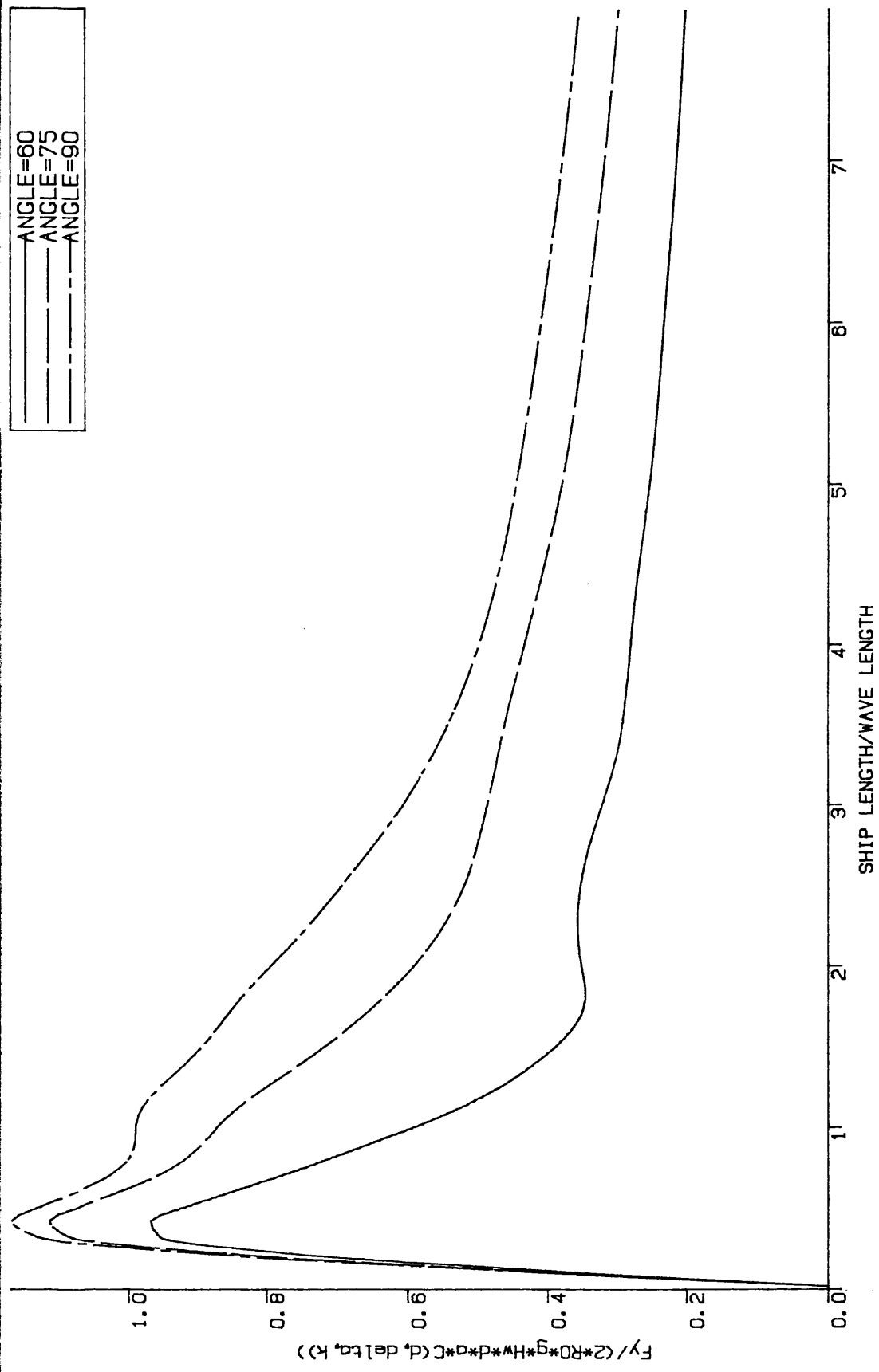


Fig. 3.13 Non-dimensionalised Sway Force
 Ship Breadth/Ship Length=0.5

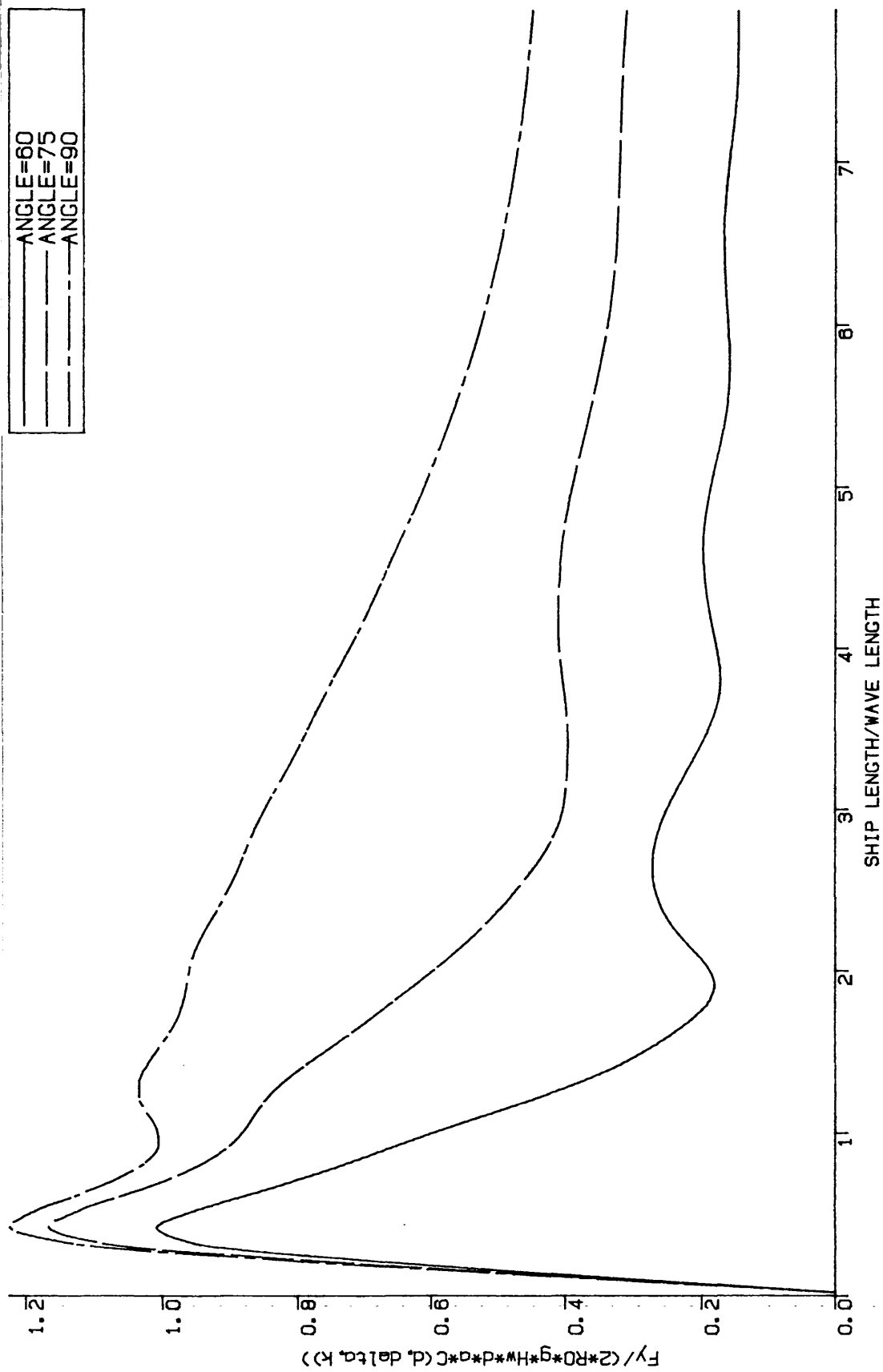


Fig. 3.14 Non-dimensionalised Sway Force
Ship Breadth/Ship Length=0.3

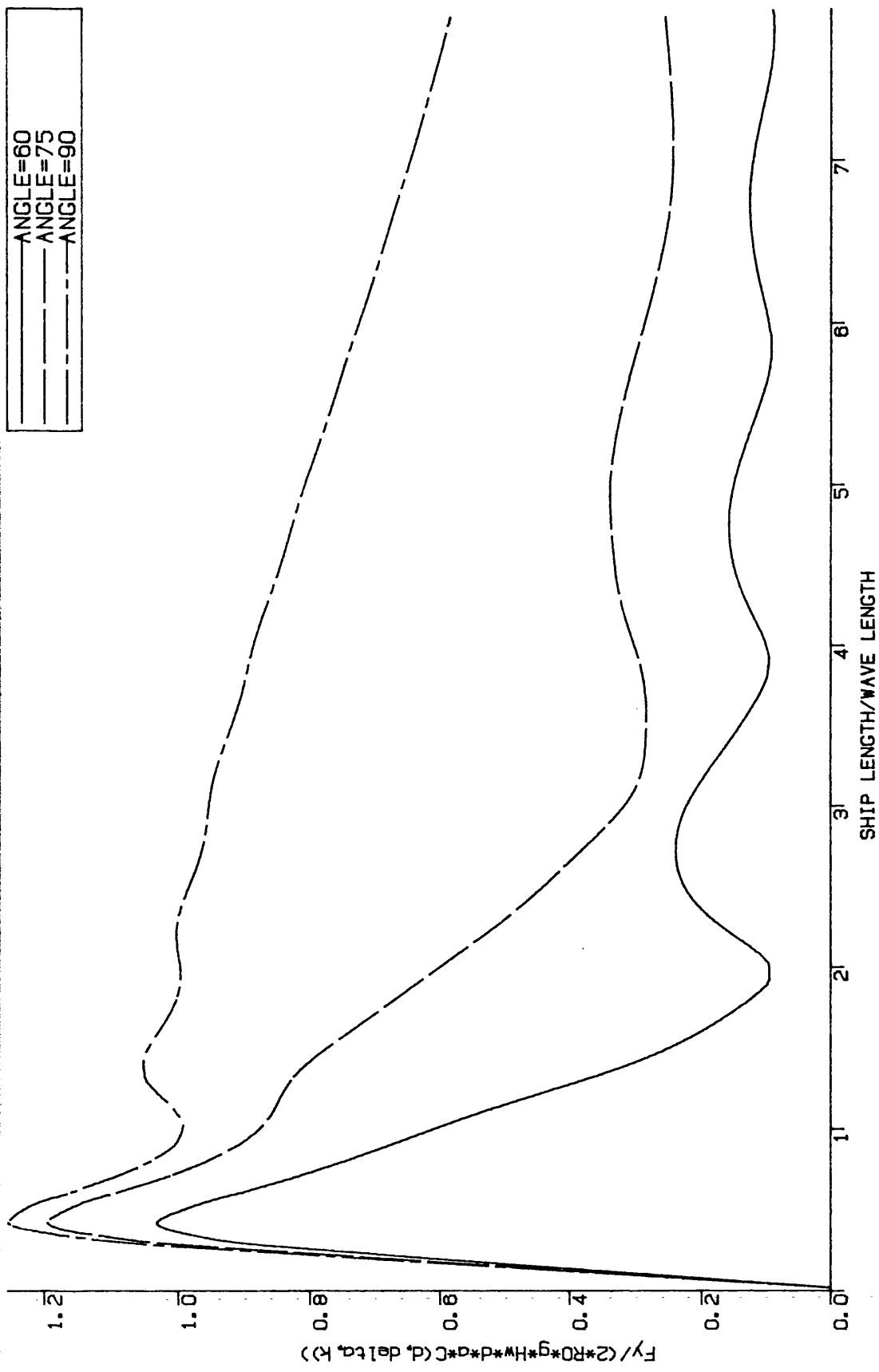


Fig. 3.15 Non-dimensionalised Sway Force
Ship Breadth/Ship Length=0.2

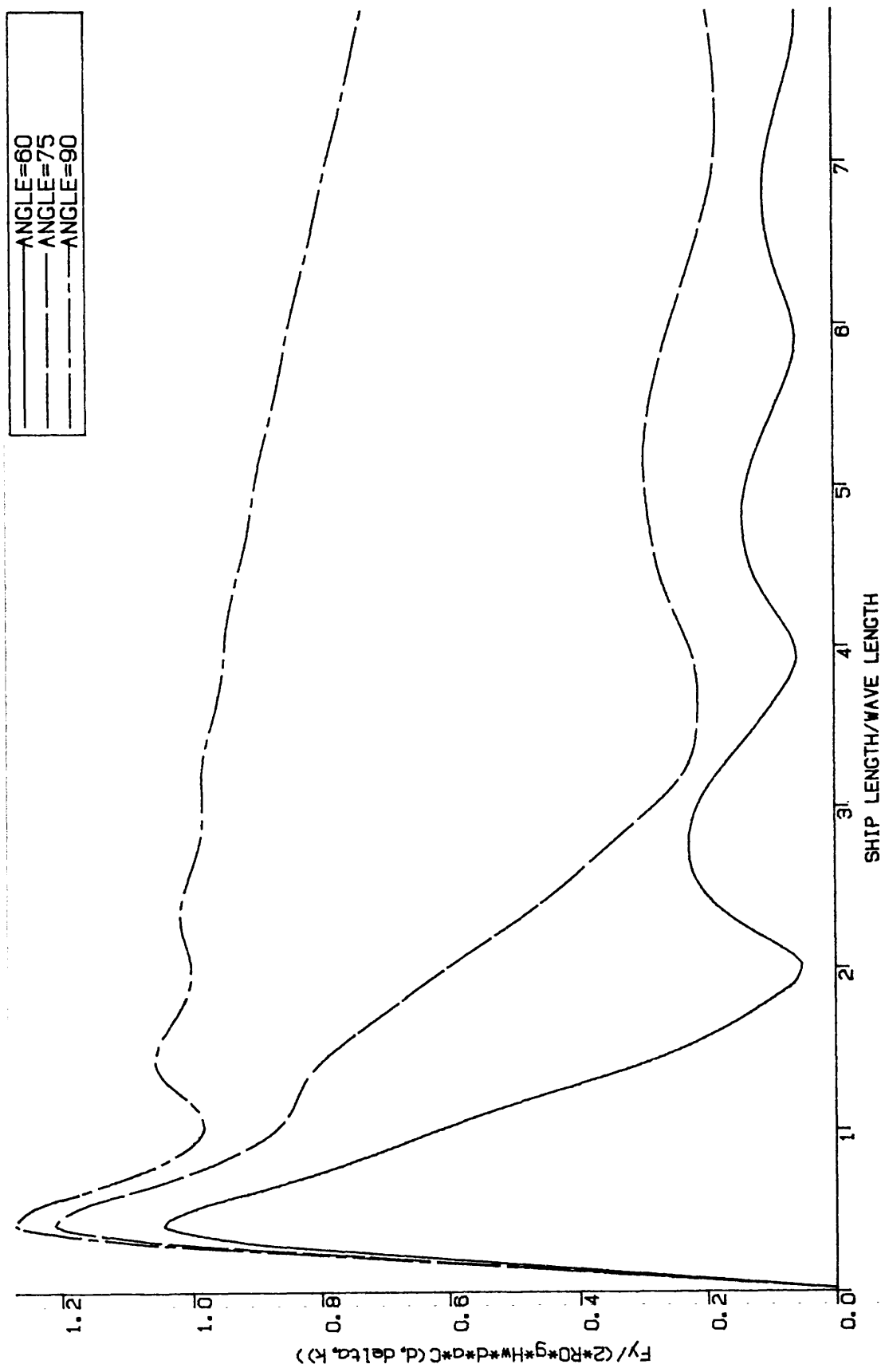


Fig. 3.16 Non-dimensionalised Sway Force
Ship Breadth/Ship Length=0.15

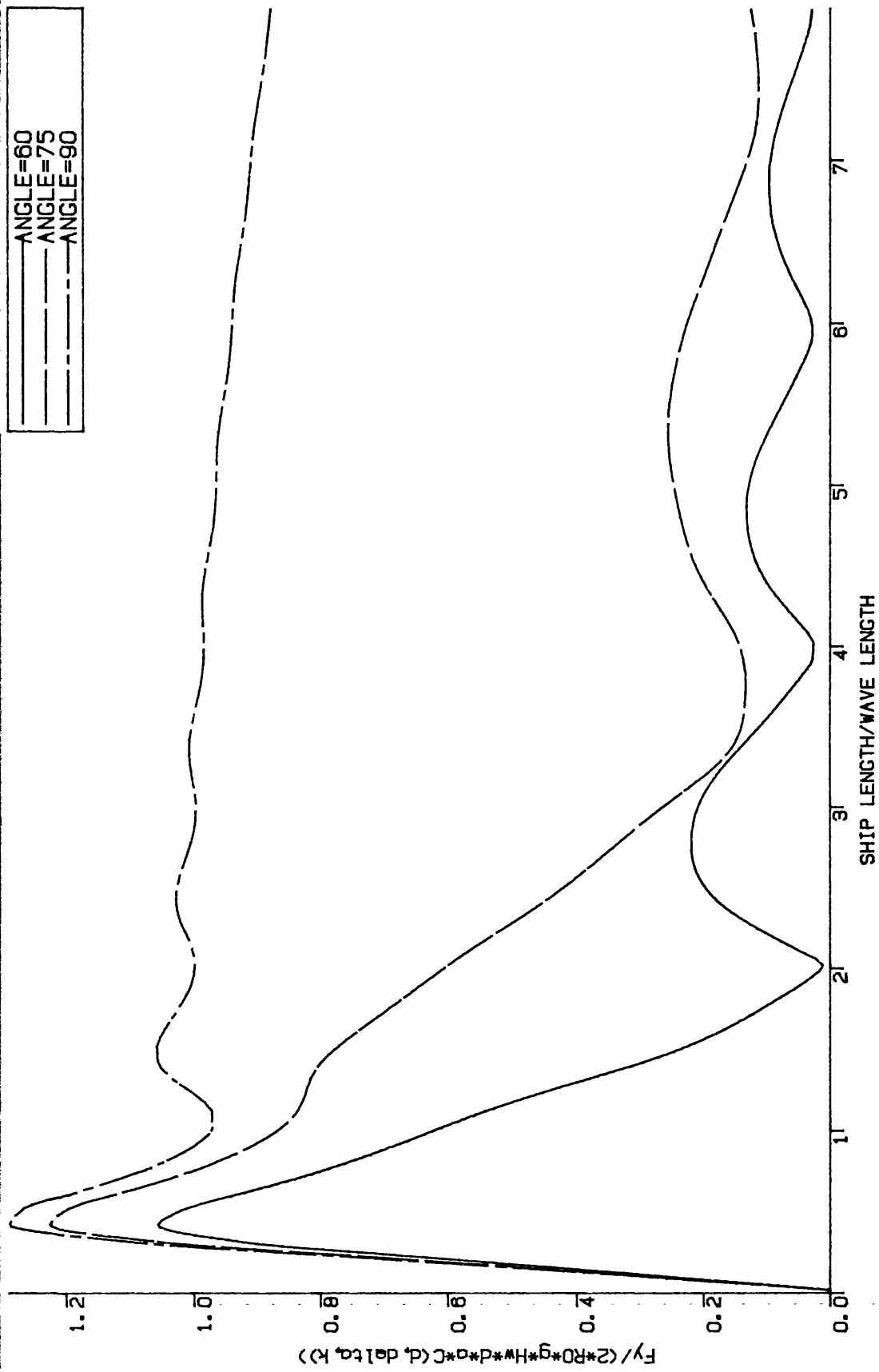


Fig. 3.17 Non-dimensionalised Sway Force
Ship Breadth/Ship Length=0.1

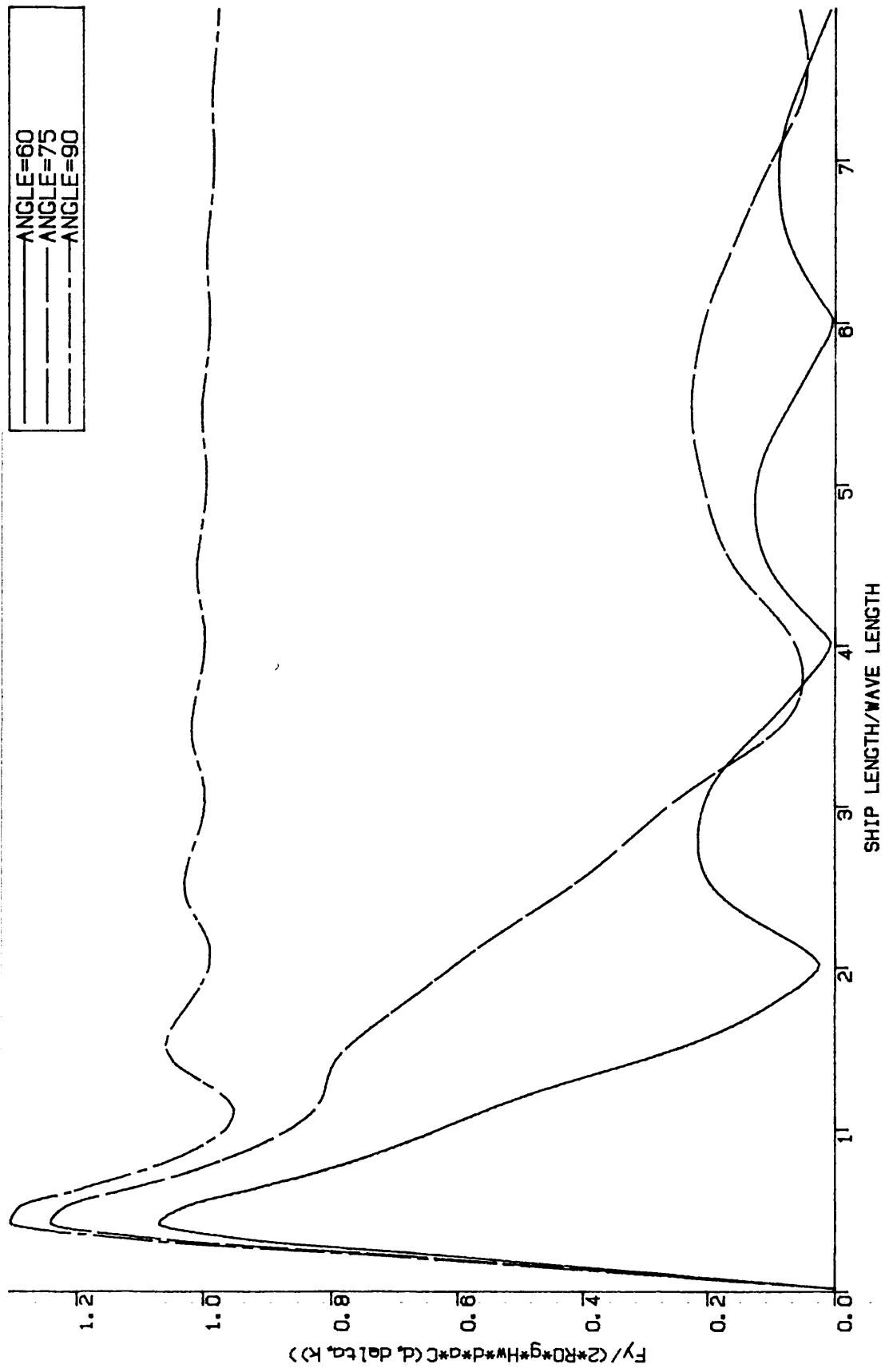


Fig. 3.18 Non-dimensionalised Sway Force
Ship Breadth/Ship Length=0.05

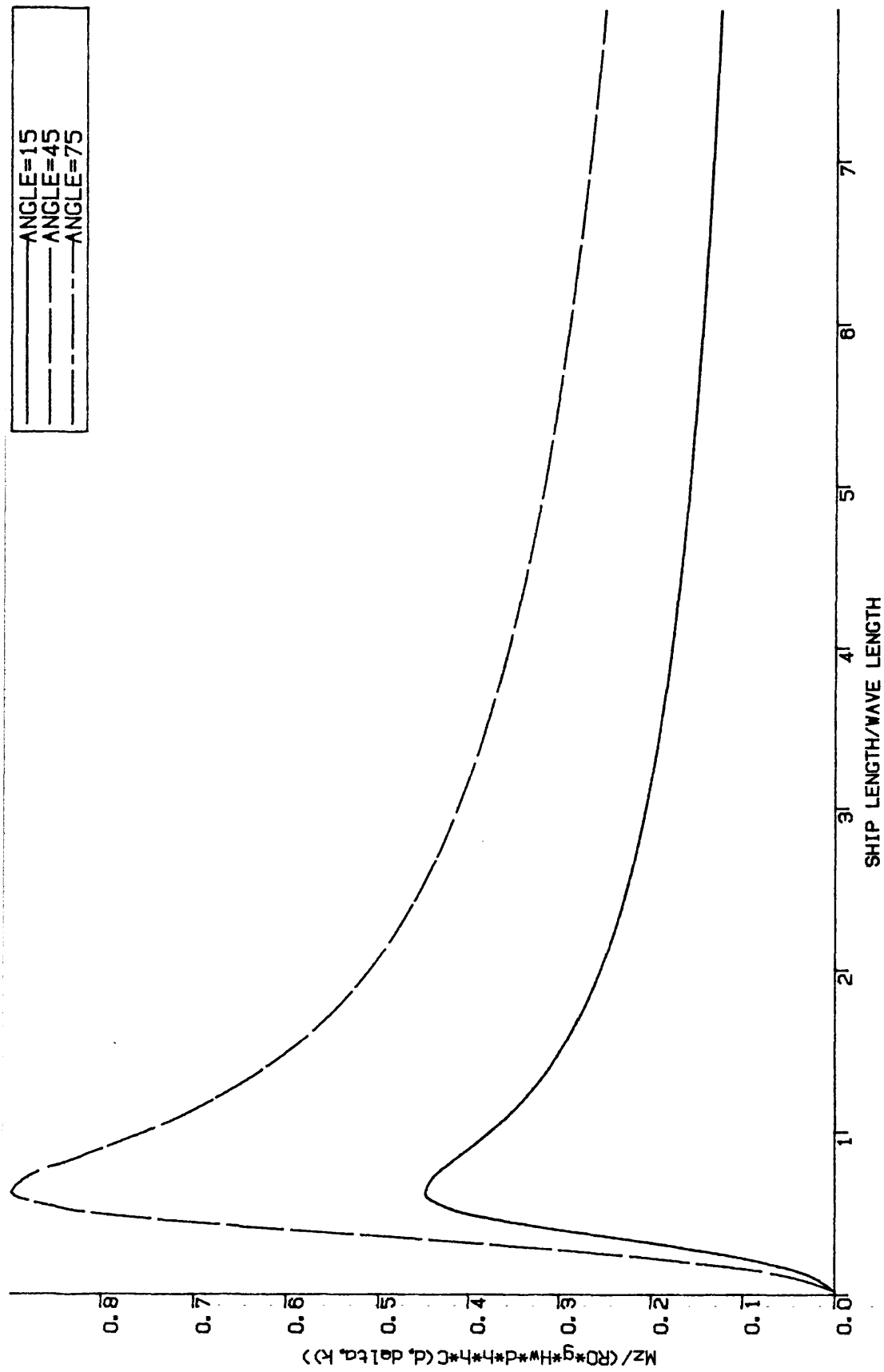


Fig. 3.19 Non-dimensionalised Yaw Moment
Ship Breadth/Ship Length=0.999

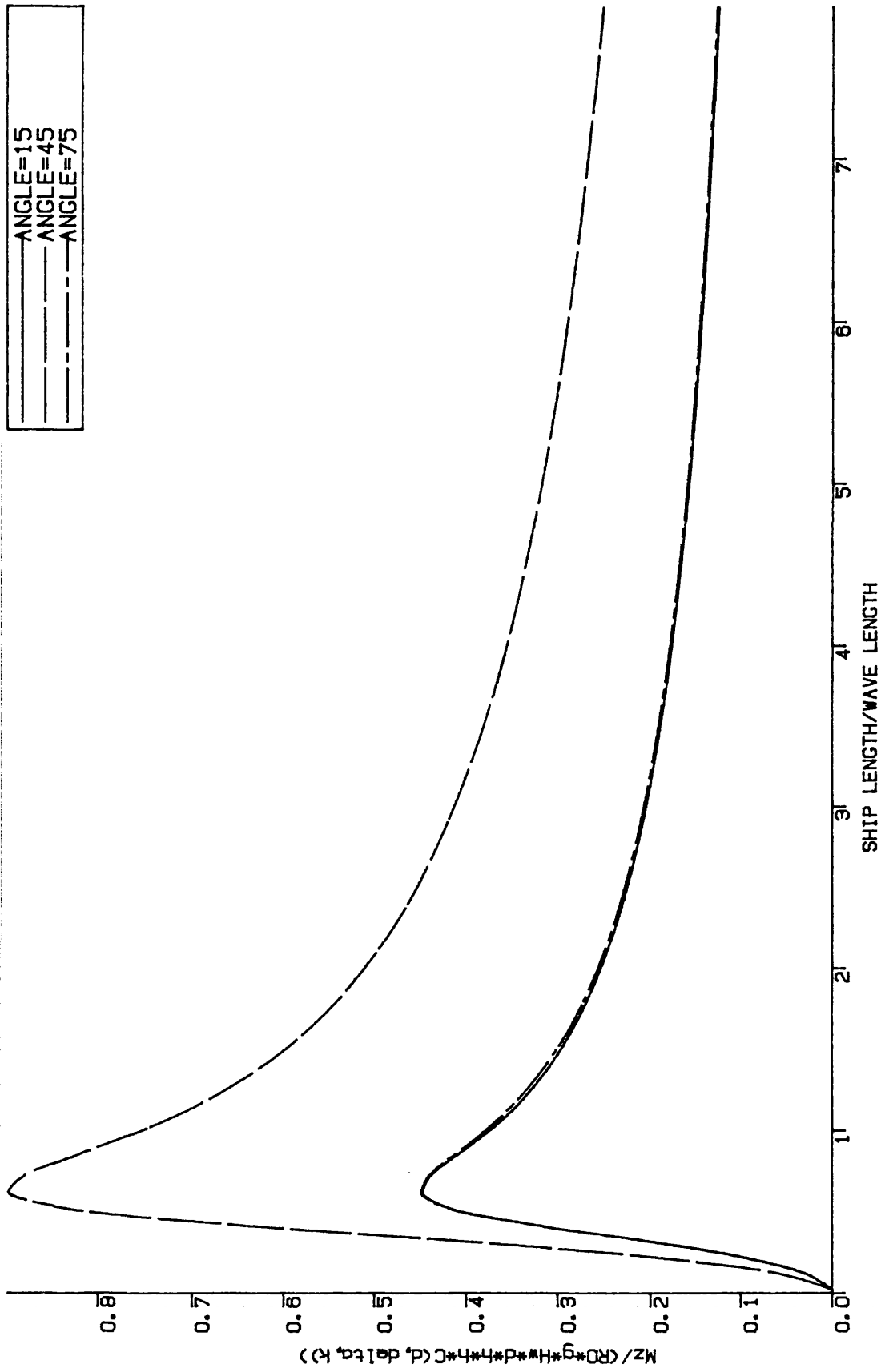


Fig. 3.20 Non-dimensionalised Yaw Moment
Ship Breadth/Ship Length=0.995

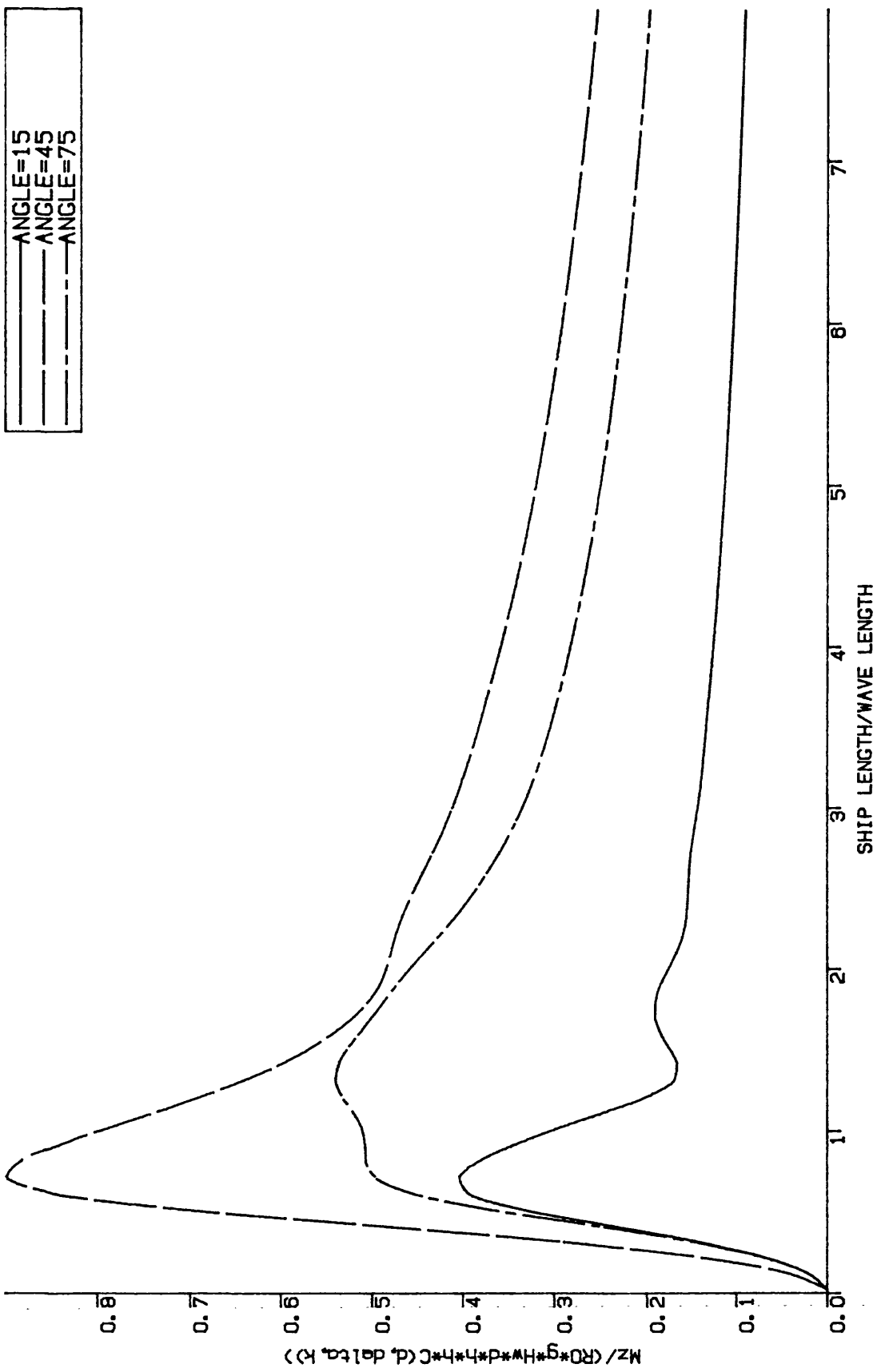


Fig. 3.21 Non-dimensionalised Yaw Moment
Ship Breadth/Ship Length=0.7

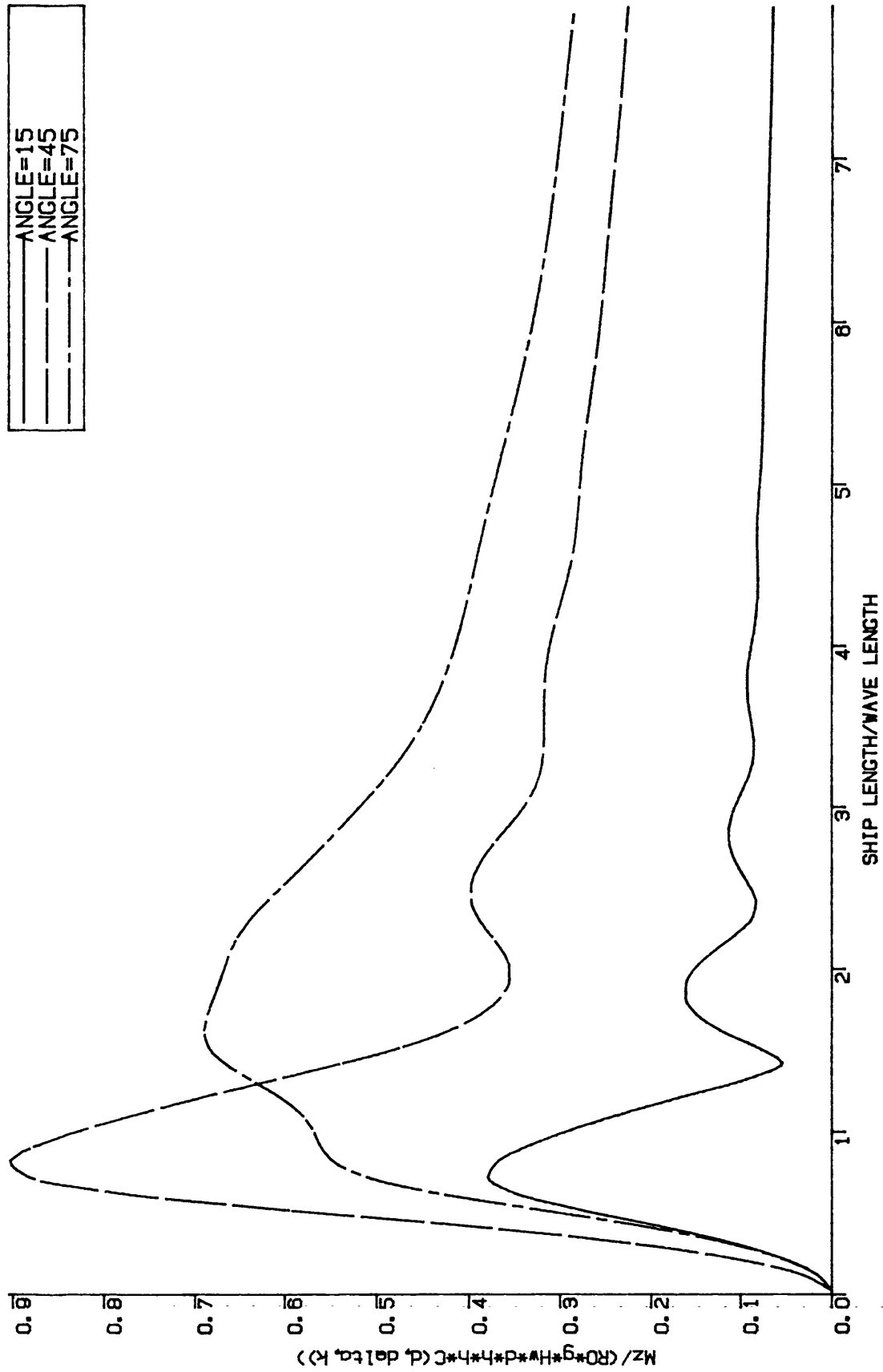


Fig. 3.22 Non-dimensionalised Yaw Moment
 Ship Breadth/Ship Length=0.5

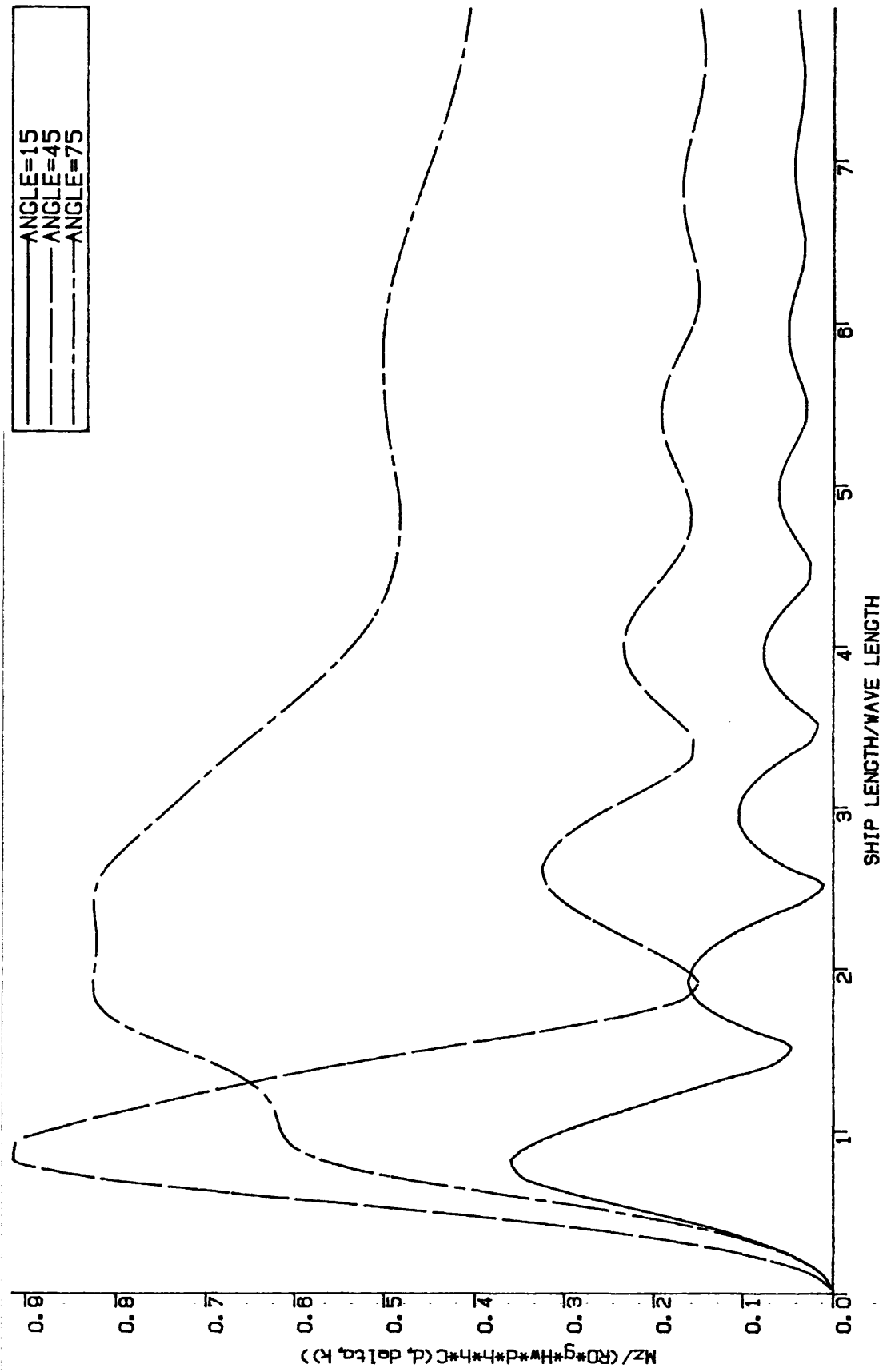


Fig. 3.23 Non-dimensionalised Yaw Moment
 Ship Breadth/Ship Length=0.3

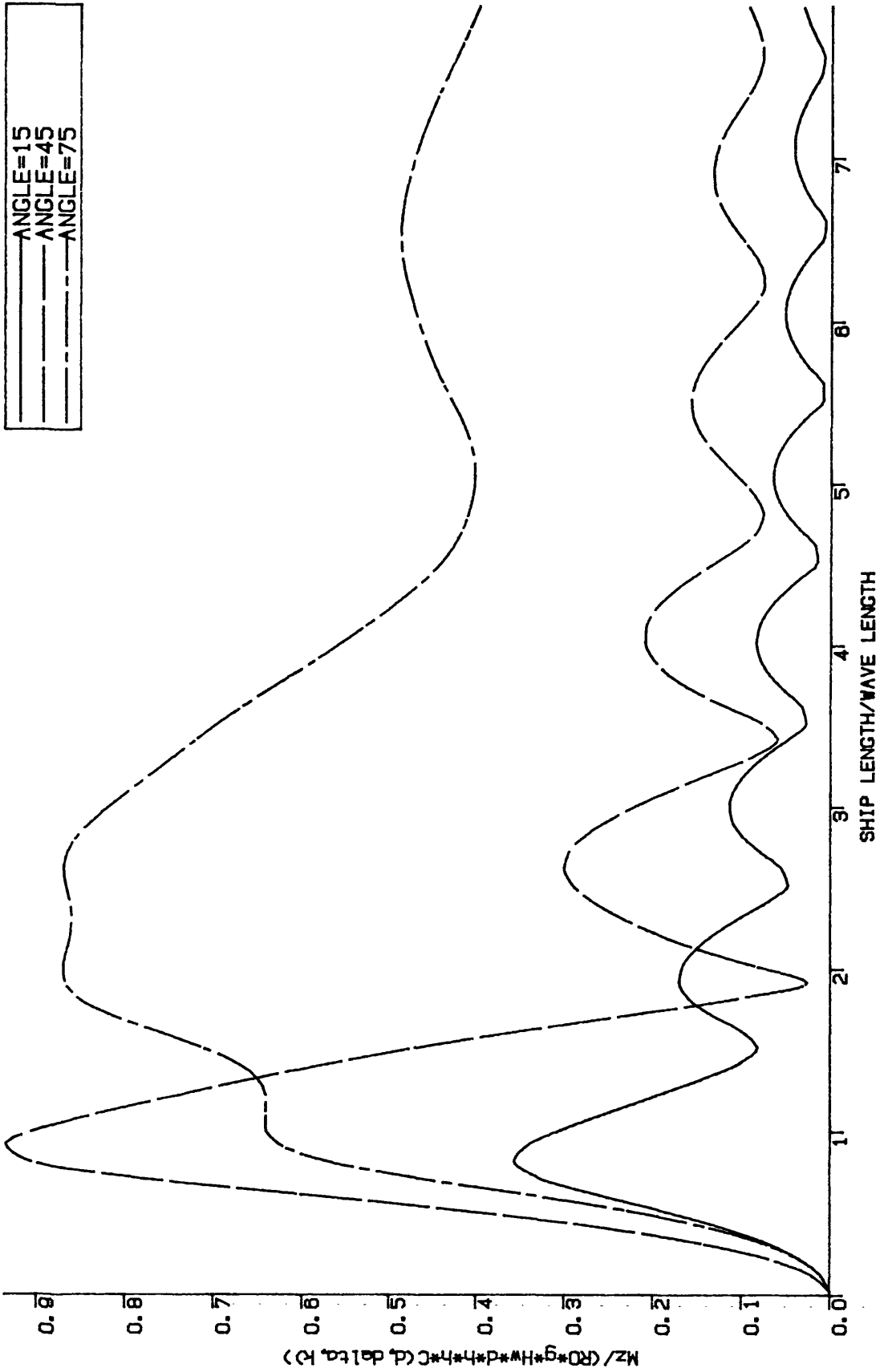


Fig. 3.24 Non-dimensionalised Yaw Moment
Ship Breadth/Ship Length=0.2

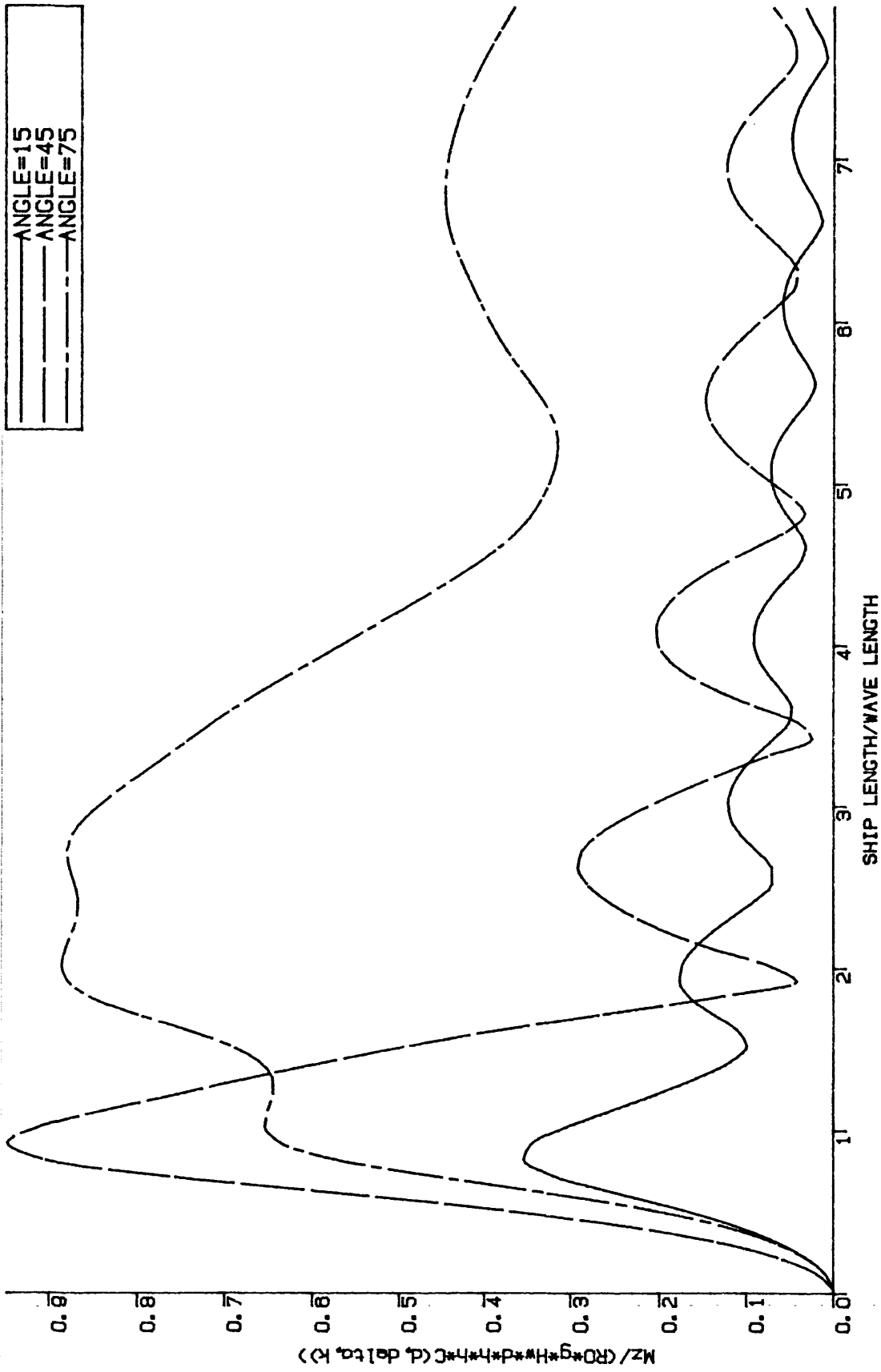


Fig. 3.25 Non-dimensionalised Yaw Moment
 Ship Breadth/Ship Length=0.15

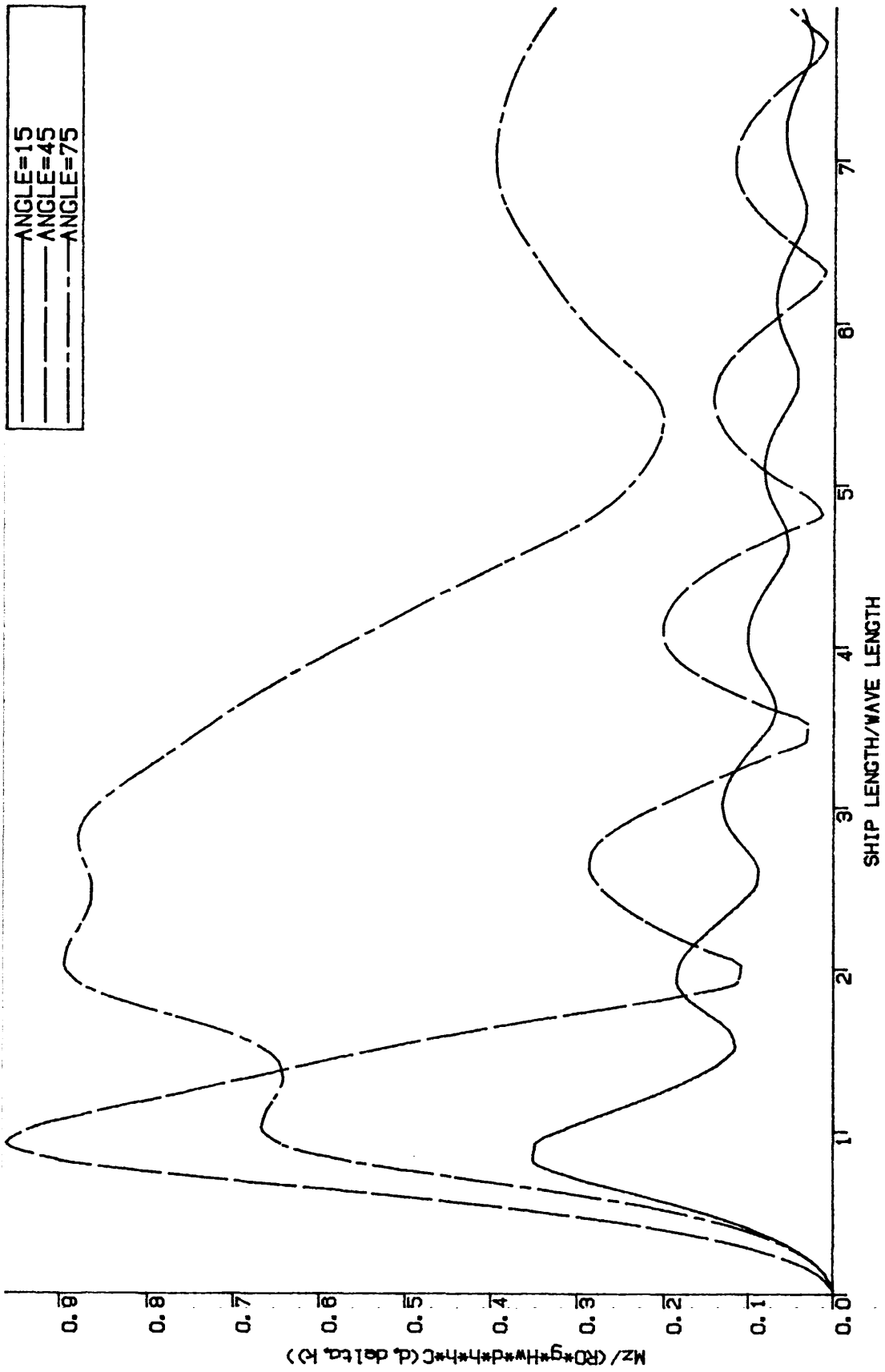


Fig. 3.26 Non-dimensionalised Yaw Moment
 Ship Breadth/Ship Length=0.1

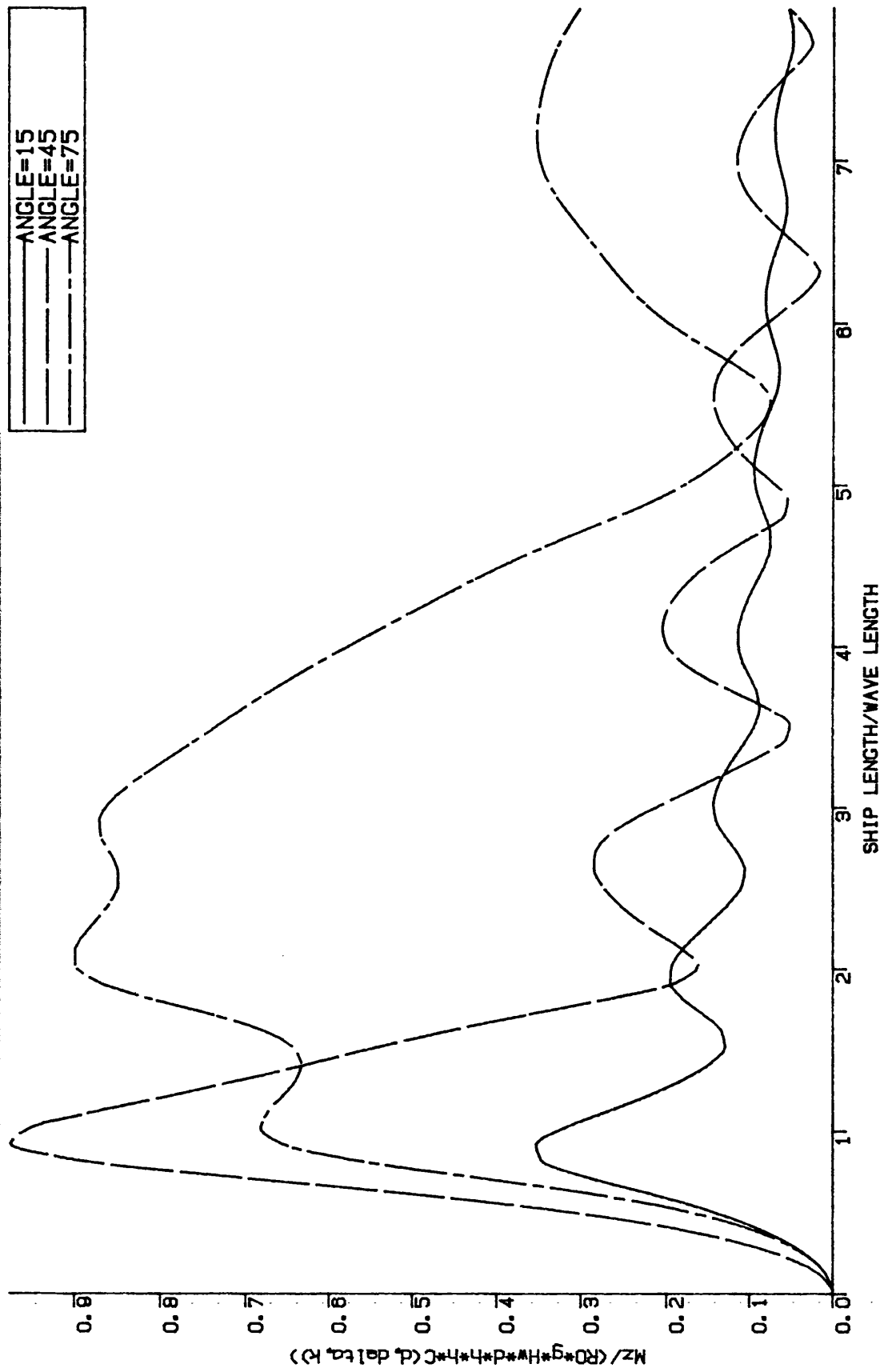


Fig. 3.27 Non-dimensionalised Yaw Moment
Ship Breadth/Ship Length=0.05

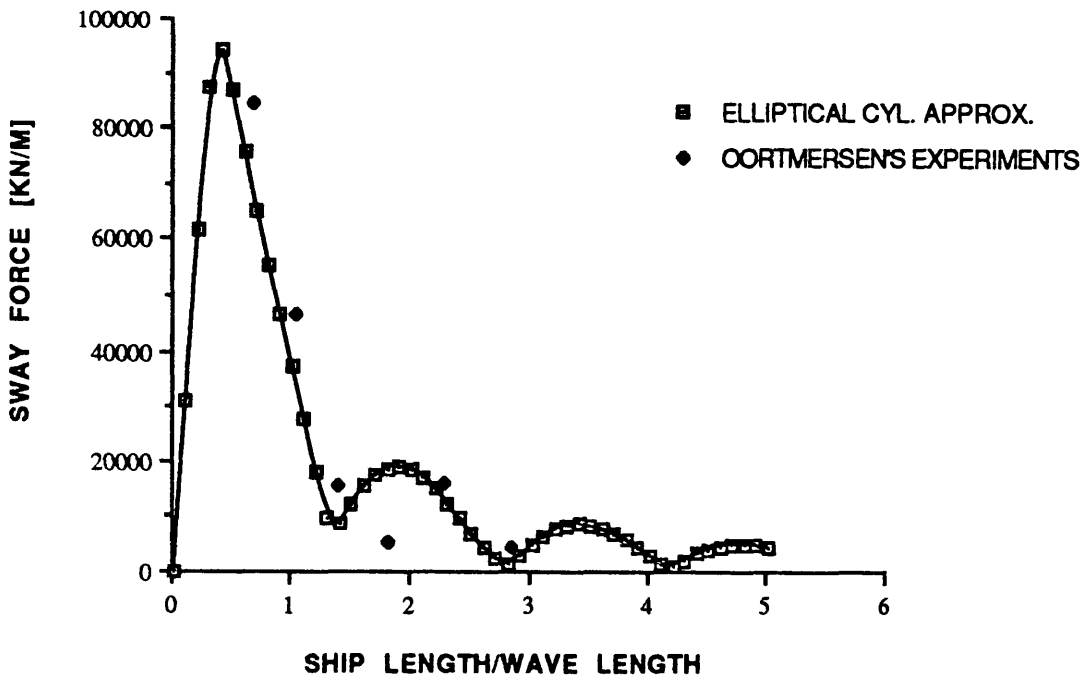


Fig. 3.28 Sway Force
Angle of Incidence=225 Degree

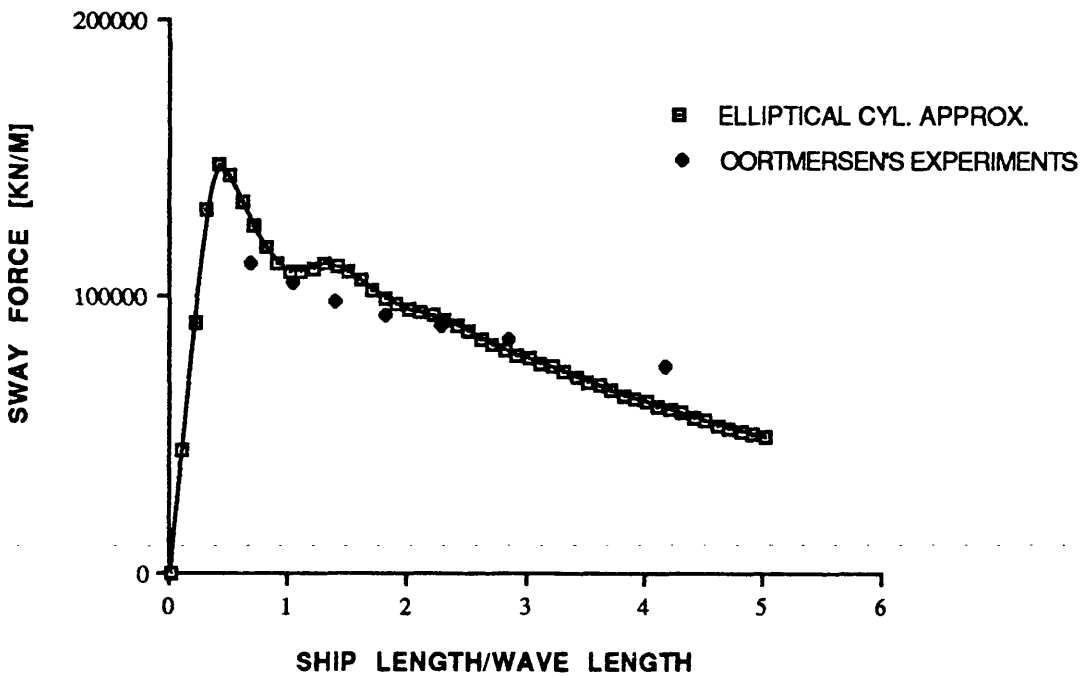


Fig. 3.29 Sway Force
Angle of Incidence=270Degree

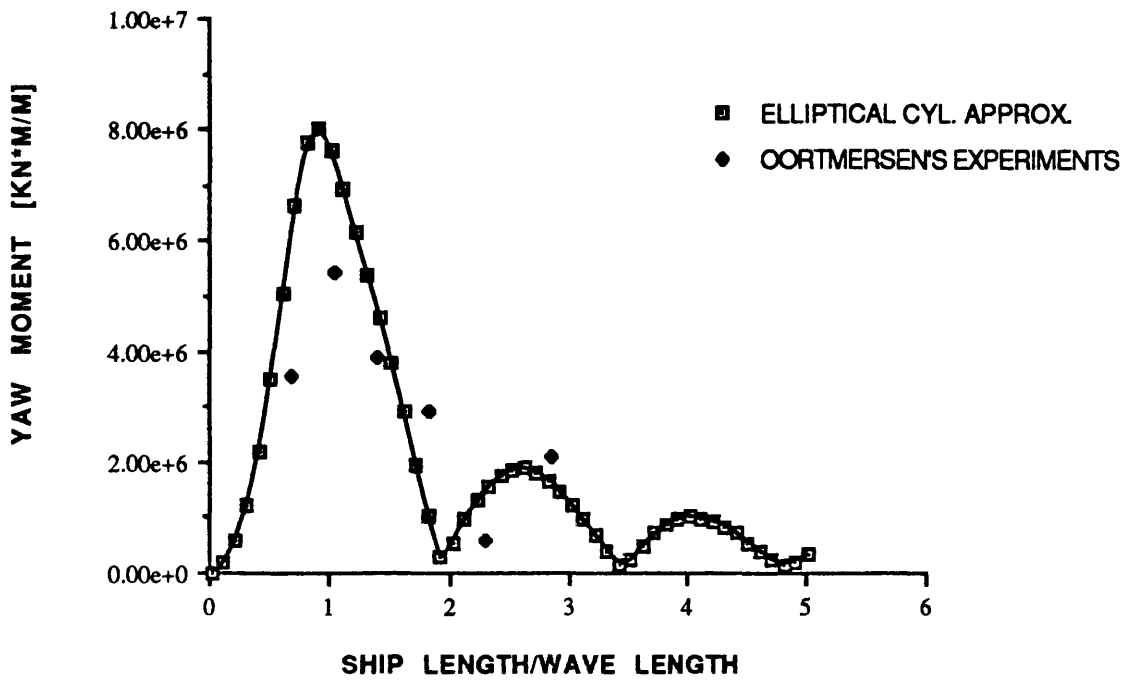


Fig. 3.30 Yaw Moment
 Angle of Incidence=225 Degree

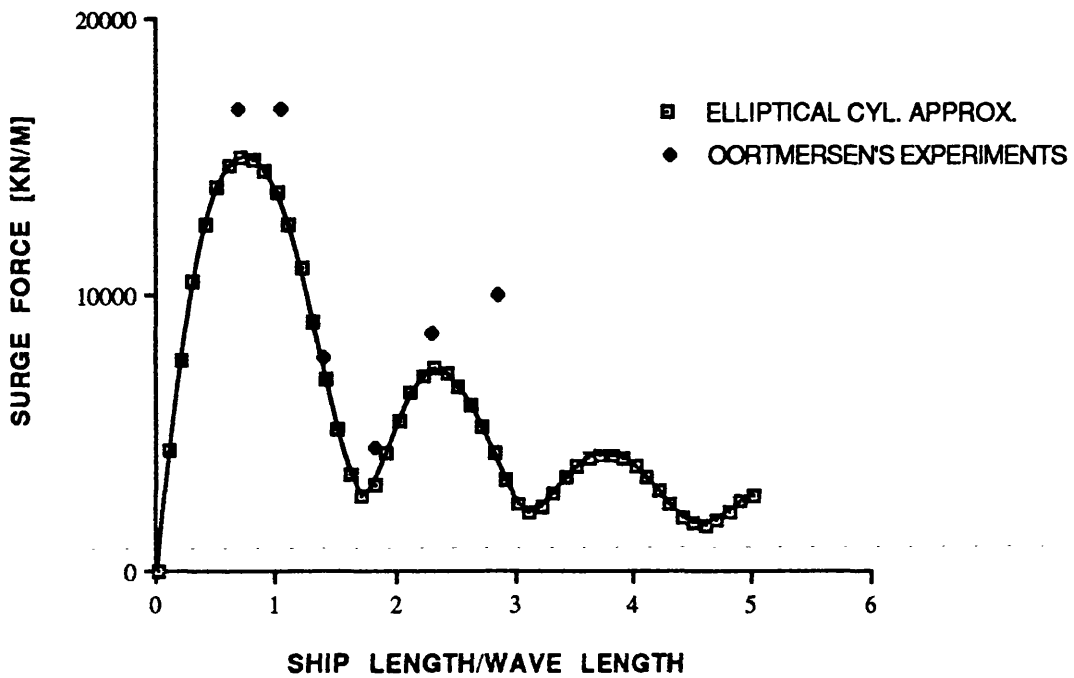


Fig. 3.31 Surge Force
 Angle of Incidence=225 Degree

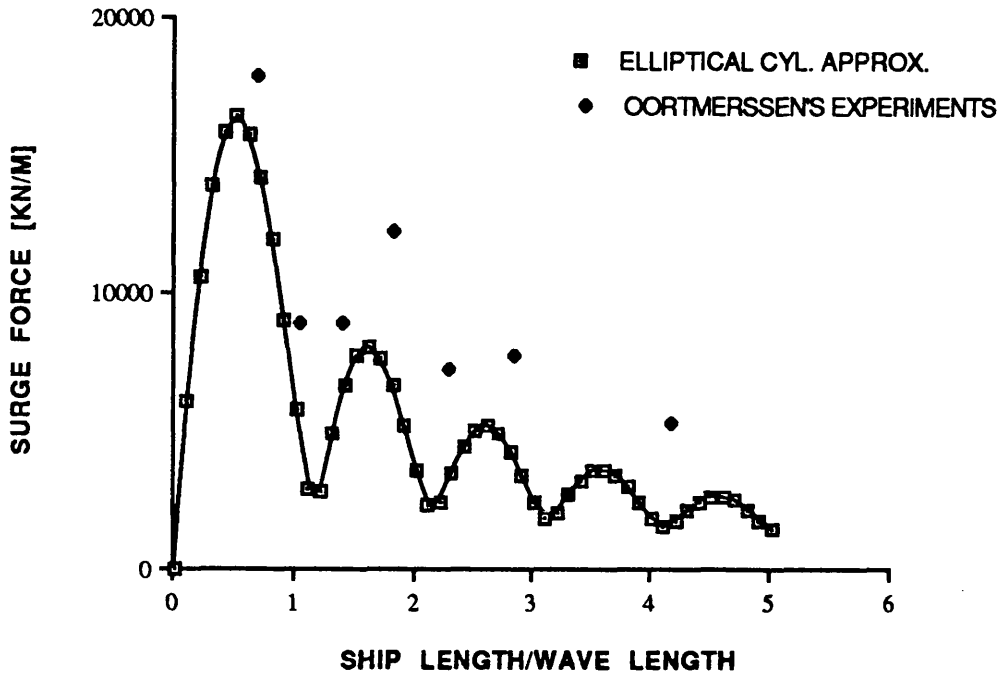


Fig. 3.32 Surge Force
Angle of Incidence=180 Degree

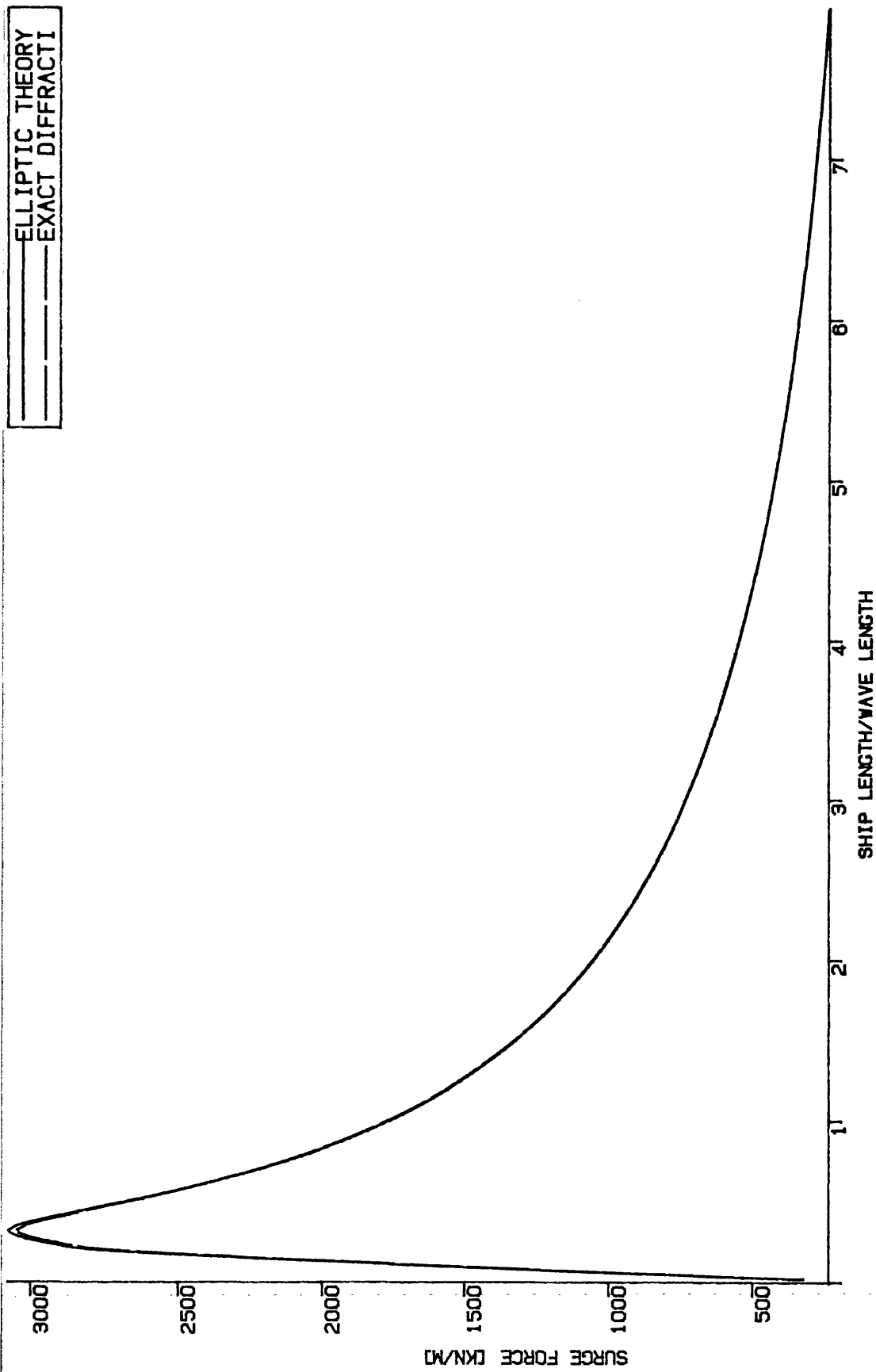
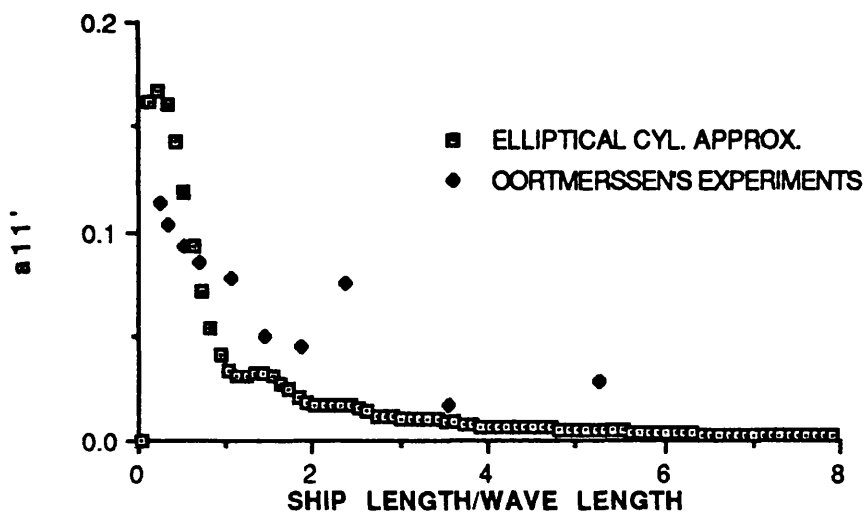
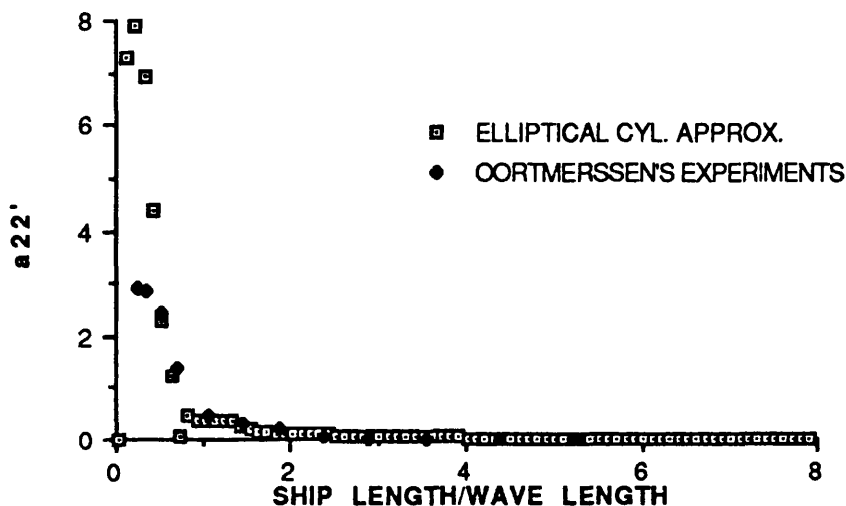


Fig. 3.33 Comparison of Surge Force Acting on a Cylinder
Ship Breadth/Ship Length=0.995



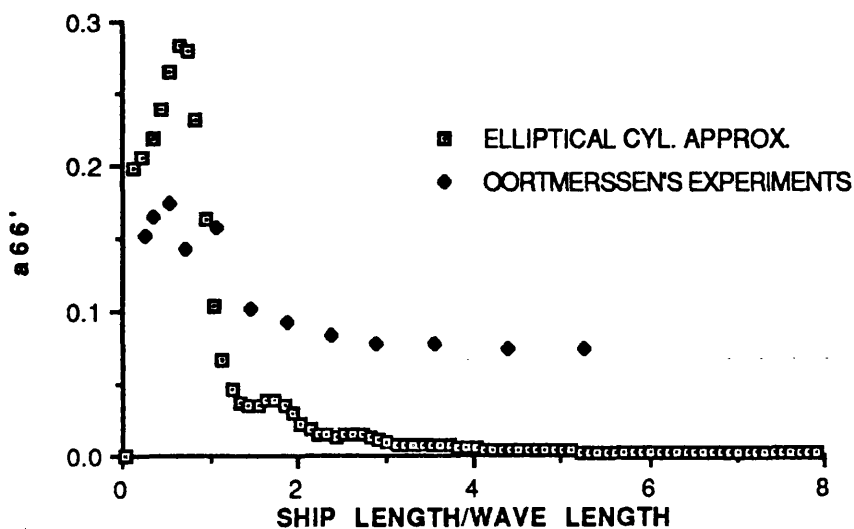
$$a_{11}' = a_{11} / (\rho \pi a b \text{draught})$$

Fig. 3.34 Comparison of Added Mass Coefficient in Surge



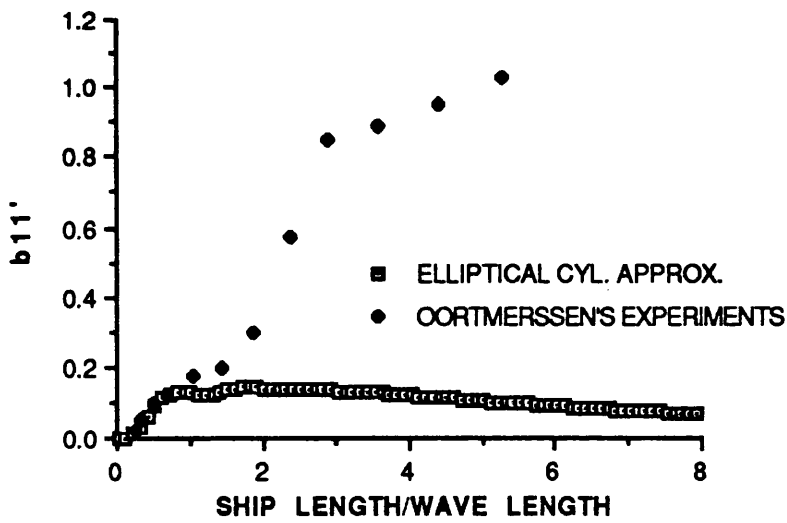
$$a_{22}' = a_{22} / (\rho \pi a b \text{draught})$$

Fig. 3.35 Comparison of Added Mass Coefficient in Sway



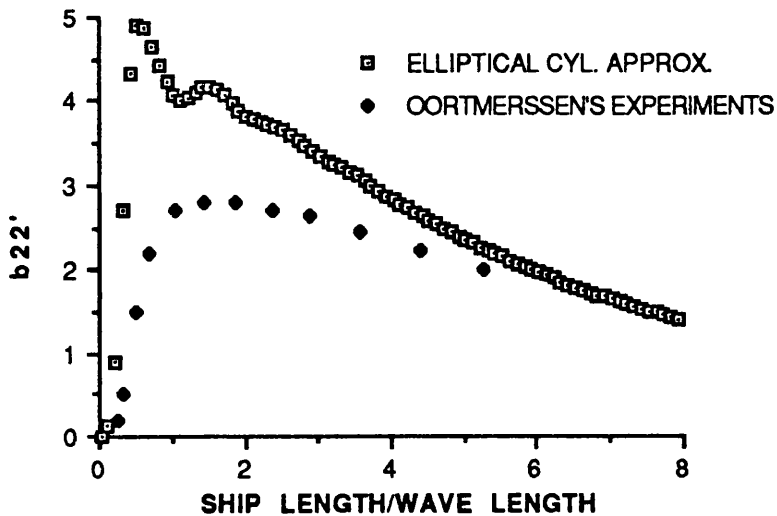
$$a_{66}' = a_{66} / (\rho \pi a b \text{draught}^4 a^2)$$

Fig. 3.36 Comparison of Added Mass Moment of Inertia in Yaw



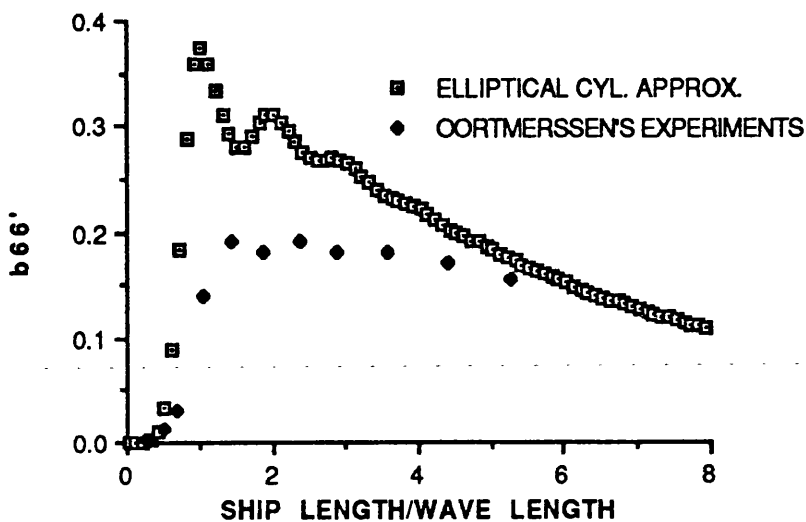
$$b_{11}' = b_{11} / (\rho \omega \pi a^2 b \text{draught} (g/a)^{0.5})$$

Fig. 3.37 Comparison of Damping Coefficient in Surge



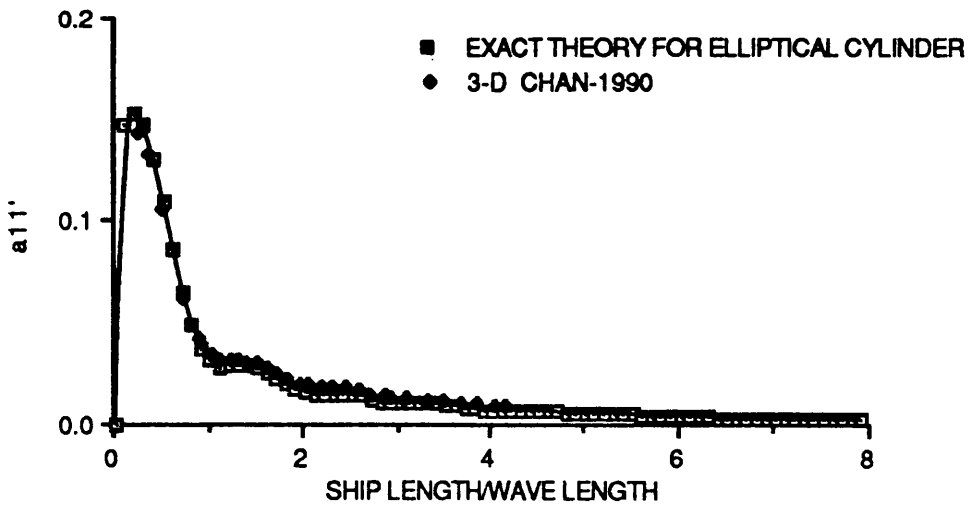
$$b_{22}' = b_{22} / (\rho \omega \pi a^2 b \text{draught} (g/a)^{0.5})$$

Fig. 3.38 Comparison of Damping Coefficient in Sway



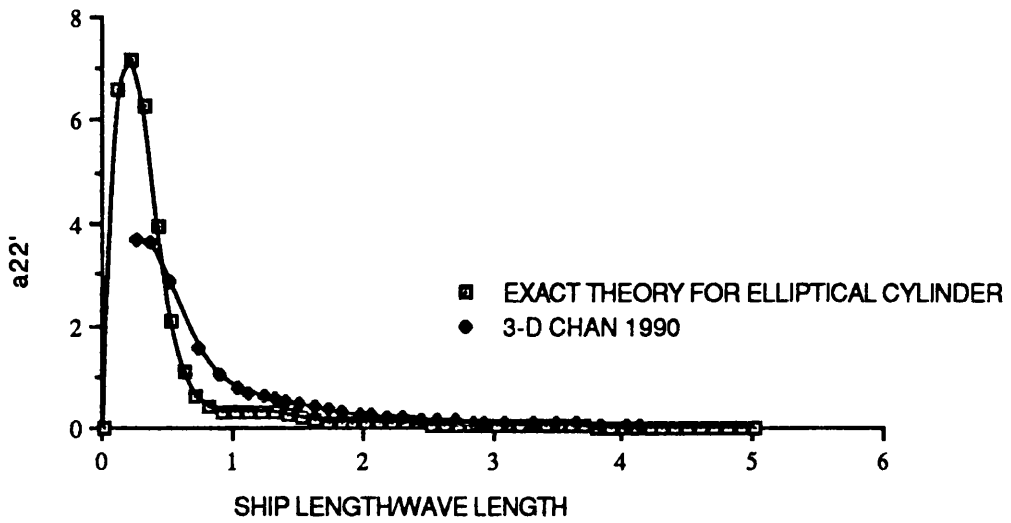
$$b_{66}' = b_{66} / (\rho \omega \pi a^2 b \text{draught} (g/a)^{0.5} 4 a^2)$$

Fig. 3.39 Comparison of Damping Coefficient in Yaw



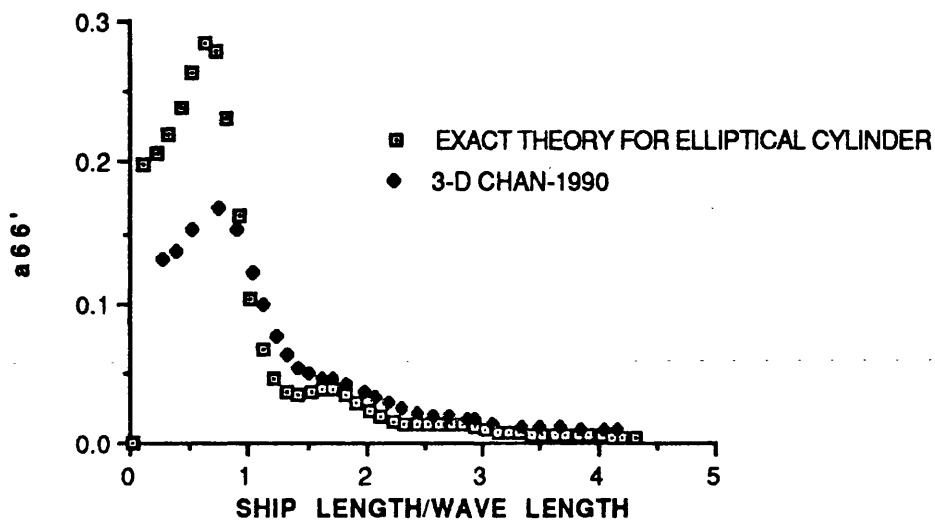
$$a_{11}' = a_{11} / (\rho \cdot \pi \cdot a \cdot b \cdot \text{draft})$$

Fig. 3.40 Comparison of Added Mass Coefficient in Surge



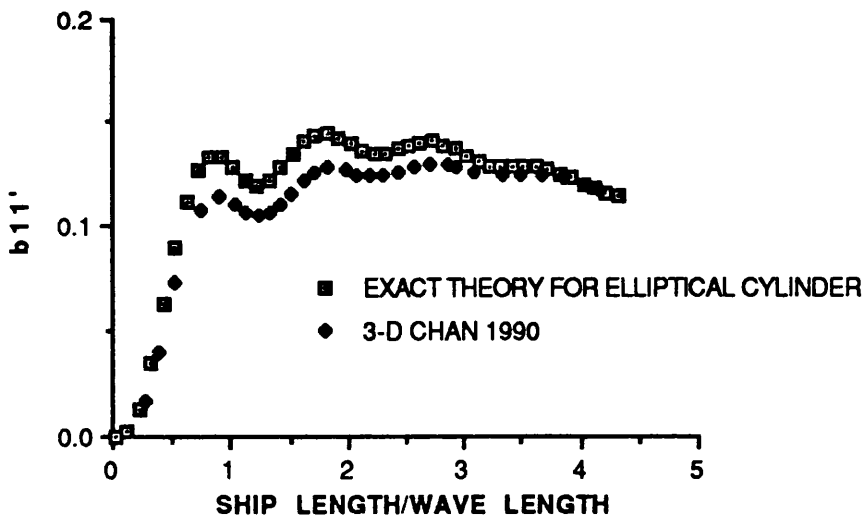
$$a_{22}' = a_{22} / (\rho \cdot \pi \cdot a \cdot b \cdot \text{draft})$$

Fig. 3.41 Comparison of Added Mass Coefficient in Sway



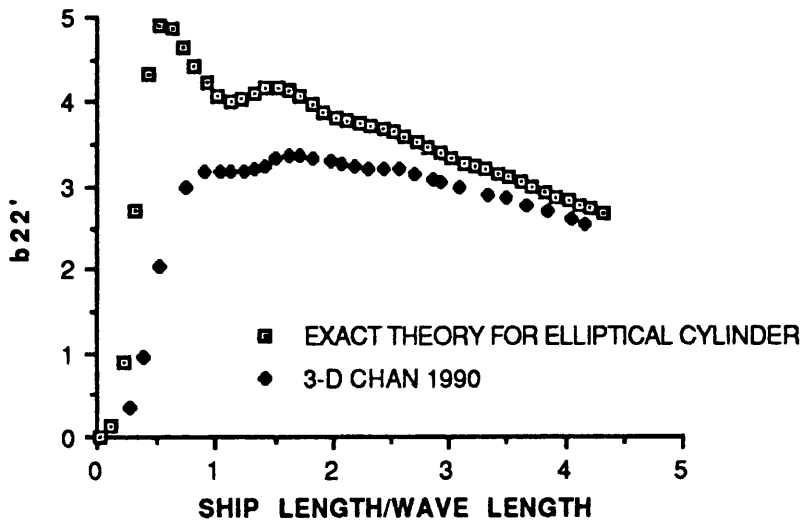
$$a_{66}' = a_{66} / (\rho \cdot \pi \cdot a \cdot b \cdot \text{draught}^4 \cdot a^2)$$

Fig. 3.42 Comparison of Added Mass Moment of Inertia in Yaw



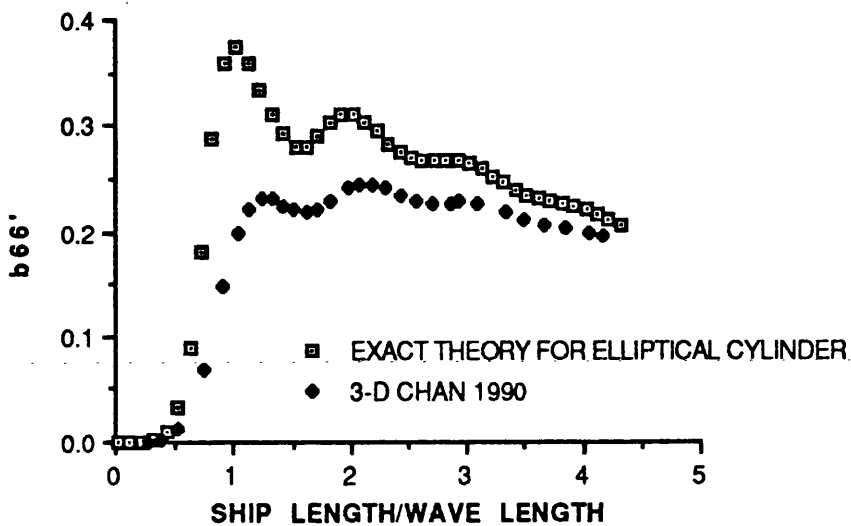
$$b_{11}' = b_{11} / (\rho \pi a b \text{draught} (g/a)^{0.5})$$

Fig. 3.43 Comparison of Damping Coefficient in Surge



$$b_{22}' = b_{22} / (\rho \pi a b \text{draught} (g/a)^{0.5})$$

Fig. 3.44 Comparison of Damping Coefficient in Sway



$$b_{66}' = b_{66} / (\rho \pi a b \text{draught} (g/a)^{0.5} 4 a^3)$$

Fig. 3.45 Comparison of Damping Coefficient in Yaw

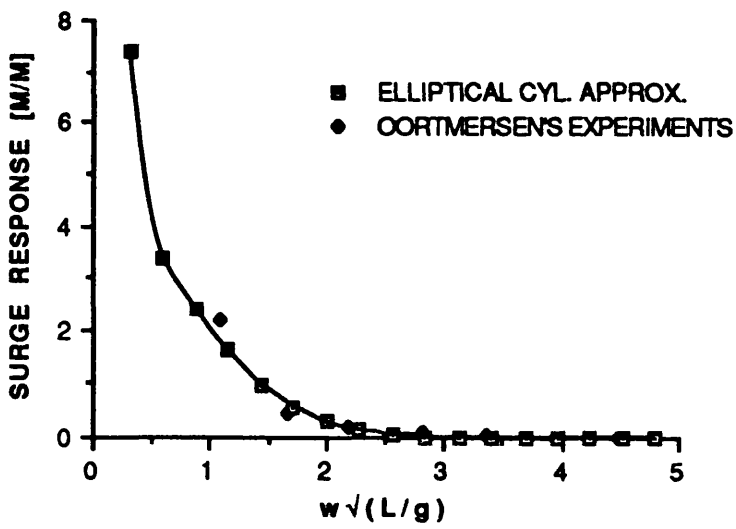


Fig. 3.46 Surge Response
 Angle of Incidence=180 Degree

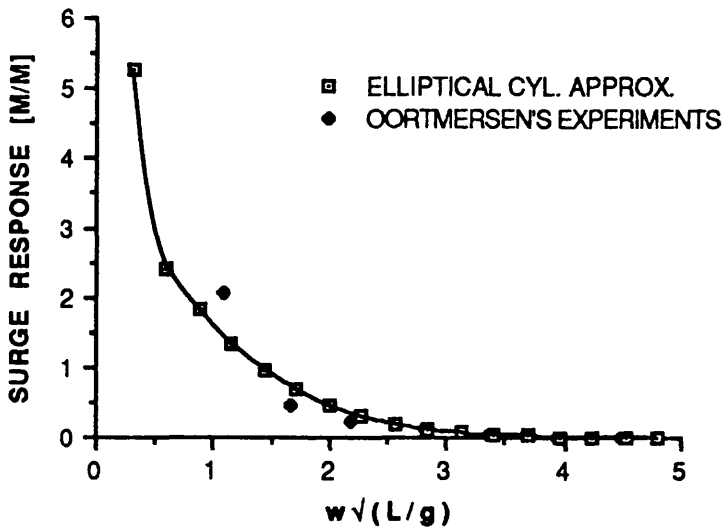


Fig. 3.47 Surge Response
 Angle of Incidence=225 Degree

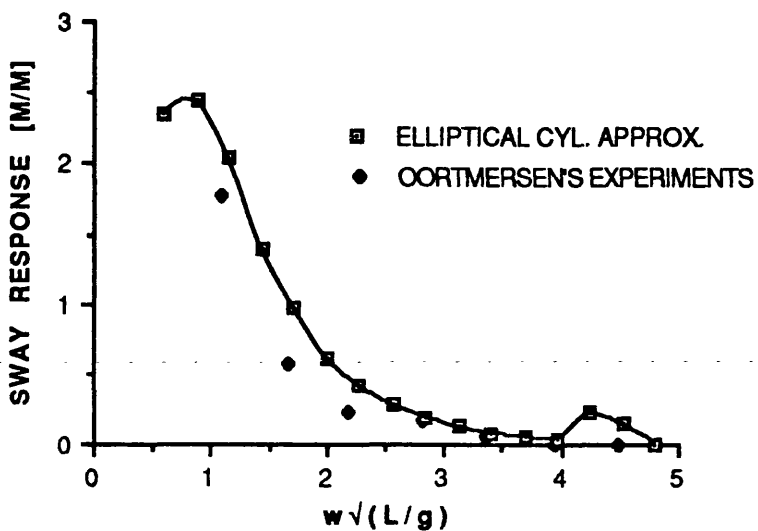


Fig. 3.48 Sway Response
 Angle of Incidence=225 Degree

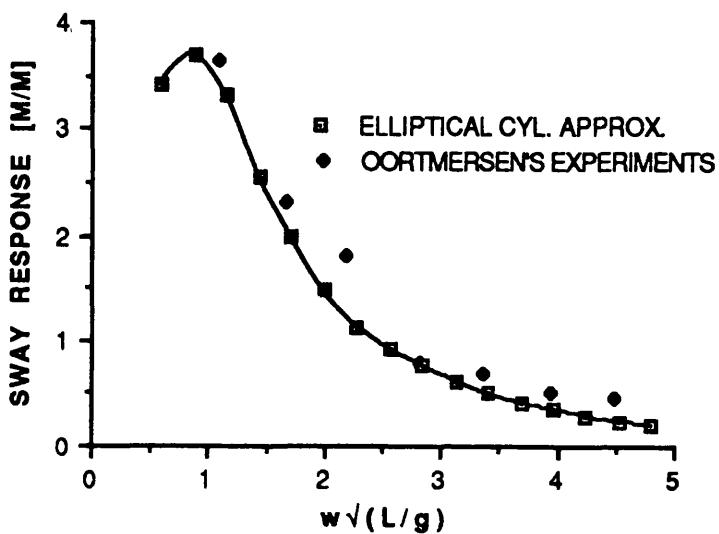


Fig. 3.49 Sway Response
 Angle of Incidence=270 Degree

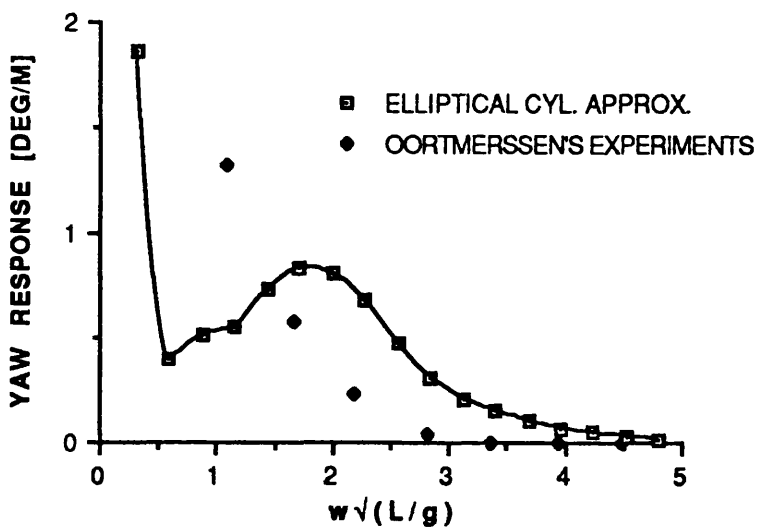


Fig. 3.50 Yaw Response
 Angle of Incidence=225 Degree

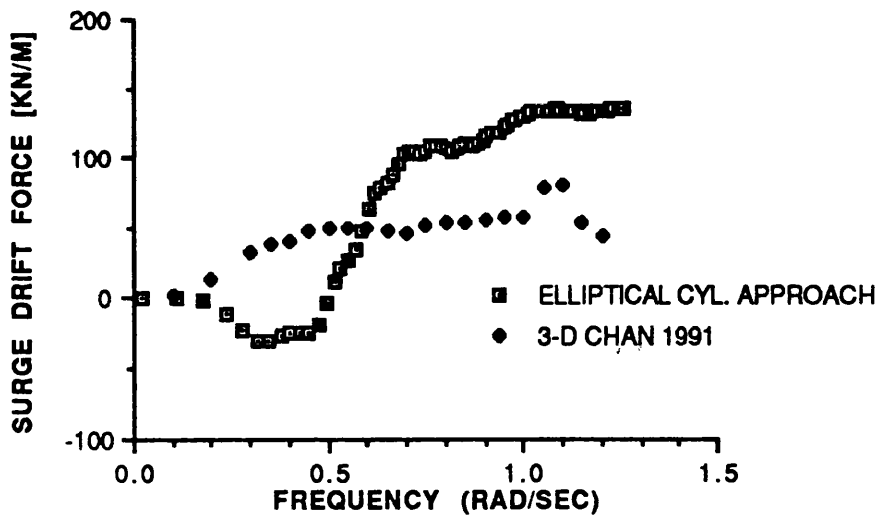


Fig. 3.51 Mean Surge Drift Force
Angle of Incidence=45 Degree

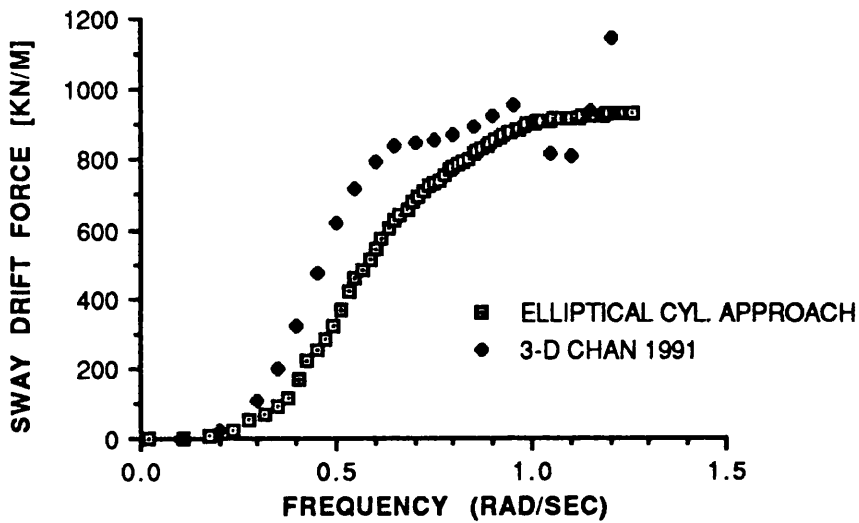


Fig. 3.52 Mean Sway Drift Force
Angle of Incidence=45 Degree

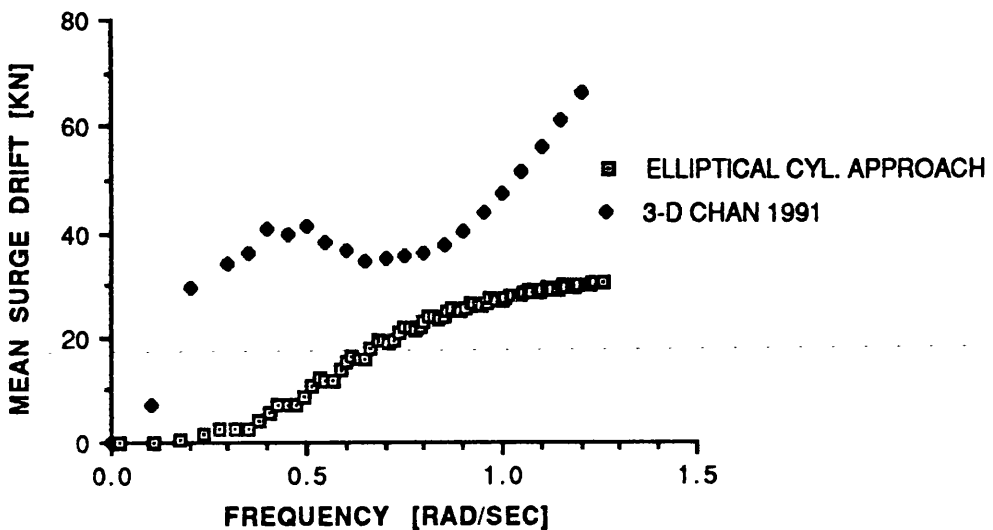


Fig. 3.53 Mean Surge Drift Force
Angle of Incidence=0 Degree

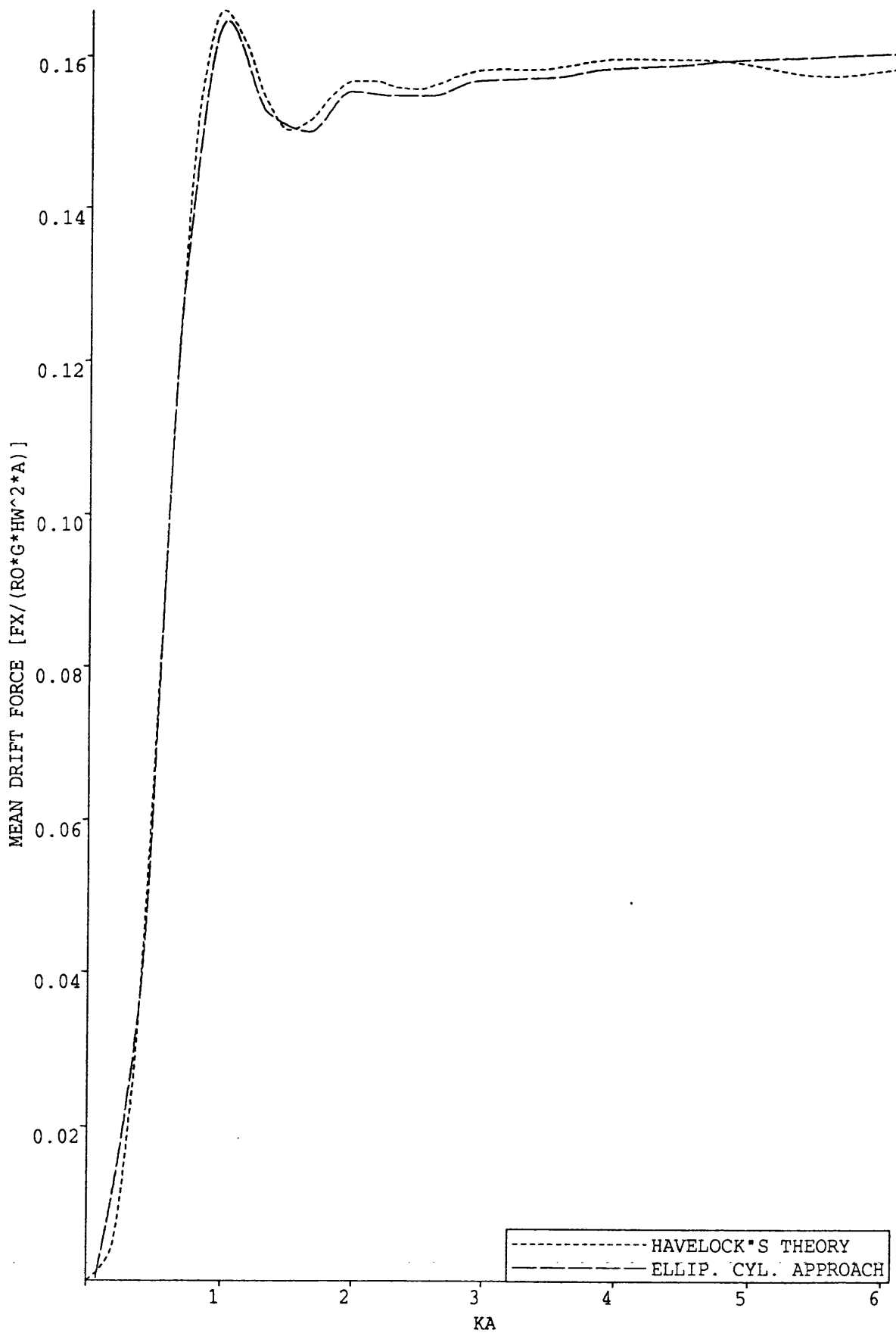


Fig. 3.54 Mean Drift Force Acting on a Circular Cylinder Extending from Free Surface to Sea Bottom

CHAPTER 4

TIME DOMAIN SIMULATION OF A TANKER-BUOY COUPLED SYSTEM

4.1 INTRODUCTION

In this chapter a time domain model is used to predict the motion responses of a tanker-buoy system under wave, wind and current loading. Motion equations of the tanker-buoy system are derived by using Cummins' method. Frequency-independent hydrodynamic coefficients and time histories of wave forces in irregular seas are calculated. Experimental measurements are compared with the time domain simulation results. Effects of random waves and gusting wind are also included in this chapter.

When a floating structure is moored to a single point, be it fixed, floating or an anchor, the vessel exhibits motions due to steady wave, wind and current forces as well as first and second-order wave, dynamic wind and variable current forces. The development of prediction methods for first-order wave excitation forces and resulting motions of floating structures have been the subject of several investigations over the last two decades. The prediction methods developed provide a good degree of accuracy for floating vessel motions [4.1, 4.2 and 4.3]. Prediction methods for second-order wave drift forces and moments and resulting slowly varying motion responses of floating structures have also been successfully developed in Refs. 4.4, 4.5 and 4.6. In Reference 4.7, de Kat and Wichers have illustrated through numerical simulations the dynamic behaviour of a ballasted and fully loaded tanker due to unsteady current loading.

4.2 DYNAMIC WIND LOADING AND RESPONSE

Calculation of wind forces is a difficult task. Most of the time experimental data and/or empirical formulas have to be used.

Wind is usually treated as a time invariant environmental effect. But fluctuations of the wind velocity acting on the superstructures may have a large effect on the response of the offshore structures. Wind velocity is expressed by the following formula in which wind shear is characterised by a power law expression [4.9],

$$\frac{\bar{V}_{t(z)}}{\bar{V}_{1h(10)}} = \alpha \left(\frac{z}{10} \right)^\beta \quad (4.1)$$

where $\bar{V}_{t(z)}$ is wind speed at z at an averaged t seconds

$\bar{V}_{1h(10)}$ is wind speed at 10 m at an averaged 1 hour

α is the gust factor (=1)

β is the power law exponent(=0.16 suggested by Davenport [4.10].)

Drag force due to wind loading is expressed by the following formula;

$$F_w(t) = \frac{1}{2} \rho_a C_D A_p V^2(t) \quad (4.2)$$

where ρ_a is air density (= 0.0012 t / m³), C_D is drag coefficient

A_p is projection area, $V(t)$ is time dependent wind velocity

By writing $V(t) = \bar{V} + v(t)$, mean and dynamic wind forces are obtained as follows,

$$F_w^M(t) = \frac{1}{2} \rho_a C_D A_p \bar{V}^2 \quad (4.3)$$

$$F_w^D(t) = \rho_a C_D A_p \bar{V} v(t) \quad (4.4)$$

Fluctuations in wind velocity could be modelled by a spectrum. Three of the most commonly used spectrums are as follows;

Harris Spectrum [4.11] is described by

$$S_w(f) = \frac{4\kappa\tilde{f}\bar{V}_{10}^2}{f(2 + \tilde{f}^2)^{5/6}} \quad (4.5)$$

where $\tilde{f} = 1200f / \bar{V}_{10}$; f is frequency; κ is drag coefficient ($=0.005$)

Davenport spectral formulation [4.12] is given by

$$S_w(f) = \frac{4\kappa\tilde{f}\bar{V}_{10}^2}{f(2 + \tilde{f}^2)^{4/3}} \quad (4.6)$$

Ochi and Shin [4.13] suggested a spectral formulation based on wind speed measurements carried out at sea. It has the following formulation,

$$S(f_*) = \begin{cases} 583 f_* & \text{for } 0 \leq f_* \leq 0.003 \\ \frac{420 f_*^{0.70}}{(1 + f_*^{0.35})^{11.5}} & \text{for } 0.003 \leq f_* \leq 0.1 \\ \frac{838 f_*}{(1 + f_*^{0.35})^{11.5}} & \text{for } f_* \geq 0.1 \end{cases} \quad (4.7)$$

where f_* is dimensionless frequency

$$f_* = f z / \bar{V}_z \quad (4.8)$$

$S(f_*)$ is dimensionless spectral density

$$S(f_*) = f S(f) / v_*^2 \quad (4.9)$$

f is frequency in cps; z is height above sea level in metres; \bar{V}_z is mean wind speed at height z in m/sec; $S(f)$ is spectral density function in m^2 / sec ; v_* is shear velocity in m/sec.

Mean wind speed, \bar{V}_z , and friction velocity, v_* , are defined in the following formulas,

$$\bar{V}_z = \bar{V}_{10} + 2.5 v_* \ln(z / 10) \quad (4.10)$$

$$v_* = \sqrt{C_{10}} \bar{V}_{10} \quad (4.11)$$

where \bar{V}_{10} = mean wind speed at 10 m height in m/sec,

C_{10} = surface drag coefficient [4.13].

For the sake of comparison the Harris, Davenport and Ochi-Shin spectra are plotted in Fig.4.1.

The wind force spectrum is given by

$$S_{wf}(f) = S_w(f) H^2 A_a^2 \quad (4.12)$$

where A_a is aerodynamic admittance function

$$A_a = 1 / (1 + (f \sqrt{A_p}) / \bar{V})^4 \quad (4.13)$$

A_p is projection area

H is wind force transfer function and given by

$$H = \frac{F_w^D}{v(t)} \quad (4.14)$$

The response spectrum of a linear system to wind loading is

$$S_{wr}(f) = S_{wf}(f)Q^2 / k^2 \quad (4.15)$$

where k is stiffness coefficient; Q is magnification factor given by

$$Q = \frac{1}{\sqrt{(1-r^2)^2 + (2\zeta r)^2}} \text{ and } r = \frac{\omega}{\omega_n} \quad (4.16)$$

ζ is damping ratio and ω_n is natural frequency

Wind force and linear response spectra are produced for a ship whose dimensions are 310.0x47.2x14.0 (Figs. 4.2 and 4.3).

Time dependent wind velocity is obtained by the sum of sines approach with a random phase distribution (Fig. 4.4),

$$V(t) = \bar{V} + \sum_{n=0}^{\infty} \sqrt{2 S_w(\omega_n) \bar{V} \omega} \cos(\omega_n t + \epsilon_n) \quad (4.17)$$

4.3 CURRENT FORCES

As with the wind forces, empirical formulas have to be used in calculating the current forces.

The longitudinal current force is formulated according to the ITTC friction resistance formula as follows;

$$F_x^c = \left[\frac{0.075}{(\log_{10} Re - 2)^2} \right] \frac{1}{2} \rho S (V_c \cos \alpha - V_{sx}) | (V_c \cos \alpha - V_{sx}) | \quad (4.18)$$

where S is the wetted surface area of the ship, V_c is the current velocity, V_{sx} ship velocity in the x direction at the centre of the gravity of the ship, α is the instantaneous angle between the current direction and the x -axis of the ship and

$$Re = \frac{|(V_c \cos \alpha - V_{sx})| L_s}{\nu}$$

where ν is the kinematic viscosity coefficient for sea water

The transverse current force and current yaw moment are formulated following the cross-flow principle as given in Faltinsen et al in Ref. 4.14. According to the cross flow principle the flow separates due to cross flow past the ship, the longitudinal current components do not influence the transverse forces on a cross section, and the transverse force on a cross section is due mainly to separated flow effects on the pressure distribution around the ship.

$$F_y^c = \frac{1}{2} \rho \int C_D(x) T(x) V_{RC} |V_{RC}| dx \quad (4.19)$$

$$F_\theta^c = \frac{1}{2} \rho \int C_D(x) T(x) V_{RC} |V_{RC}| x dx + \frac{1}{2} V_c^2 (a_{22} - a_{11}) \sin 2(\alpha - \theta) \quad (4.20)$$

where $C_D(x)$ is the drag coefficient for cross-flow past an infinitely long cylinder with a cross sectional area equal to the sum of the ship cross section at longitudinal coordinate x and its image above the free surface; a_{11} , a_{22} are added mass coefficients in surge and sway respectively ; $T(x)$ is the sectional draught and

$$V_{RC} = V_c \sin \alpha - V_{sy} - \dot{\theta} x \quad (4.21)$$

where V_{sy} is the ship velocity in the y direction at the centre of gravity of the ship, $\dot{\theta}$ is the rotational velocity of the ship about the z axis and x is the x coordinate of any point along the ship length.

Last term in eq. 4.20 is known as Munk moment and can be derived from non-separated potential theory [4.14].

Current and ideal fluid forces could be expressed in another way, as was adopted by Wichers [4.6], Molin[4.15]. In this approach current forces and moments are represented as a combination of the ideal fluid forces and "real" forces based on semi-empirical mathematical models including quasi-steady and dynamic current components. Ideal flow forces are given by Norbinn [4.16] as follows,

$$\begin{aligned}
 F_{xid} &= -a_{xx}\dot{u} + a_{yy}v\dot{\theta} + a_{y\theta}\dot{\theta}^2 \\
 F_{yid} &= -a_{yy}\dot{v} - a_{xx}u\dot{\theta} - a_{y\theta}\ddot{\theta} \\
 F_{\theta id} &= -a_{\theta\theta}\ddot{\theta} - (a_{yy} - a_{xx})uv - a_{y\theta}(\dot{v} + u\dot{\theta})
 \end{aligned}
 \tag{4.22}$$

and the relative velocity components are given as follows

$$\begin{aligned}
 u &= \dot{x} - V_c \cos(\alpha - \theta) \\
 v &= \dot{y} - V_c \sin(\alpha - \theta)
 \end{aligned}
 \tag{4.23}$$

The relative acceleration components are

$$\begin{aligned}
 \dot{u} &= \ddot{x} - V_c\dot{\theta}\sin(\alpha - \theta) \\
 \dot{v} &= \ddot{y} + V_c\dot{\theta}\cos(\alpha - \theta)
 \end{aligned}
 \tag{4.24}$$

If equations 4.23 and 4.24 are substituted into equation 4.22, we obtain

$$\begin{aligned}
 F_{xid} &= -a_{xx}\ddot{x} - (a_{yy} - a_{xx})V_c \sin(\alpha - \theta)\dot{\theta} + a_{yy}\dot{y}\dot{\theta} + a_{y\theta}\dot{\theta}^2 \\
 F_{yid} &= -a_{yy}\ddot{y} - (a_{yy} - a_{xx})V_c \cos(\alpha - \theta)\dot{\theta} - a_{xx}\dot{x}\dot{\theta} - a_{y\theta}\ddot{\theta} \\
 F_{\theta id} &= -a_{\theta\theta}\ddot{\theta} - (a_{yy} - a_{xx})uv - a_{\theta y}\dot{x}\dot{\theta} - a_{\theta y}\ddot{y}
 \end{aligned} \tag{4.25}$$

According to Wichers, Munk moment in equation 4.25 can be replaced by the steady current moment components and the equation can be rewritten as follows to include the viscous forces,

$$\begin{aligned}
 F_{xid} &= -a_{xx}\ddot{x} + a_{yy}\dot{y}\dot{\theta} + F_{xstat} + F_{xdyn} \\
 F_{yid} &= -a_{yy}\ddot{y} - a_{y\theta}\ddot{\theta} - a_{xx}\dot{x}\dot{\theta} + F_{ystat} + F_{ydyn} \\
 F_{\theta id} &= -a_{\theta\theta}\ddot{\theta} - a_{\theta y}\ddot{y} + F_{\theta stat} + F_{\theta dyn}
 \end{aligned} \tag{4.26}$$

where

$$\begin{aligned}
 F_{xstat} &= 0.5\rho L_s TC_{xc}(\alpha_{cr})V_{cr}^2 \\
 F_{ystat} &= 0.5\rho L_s TC_{yc}(\alpha_{cr})V_{cr}^2 \\
 F_{\theta stat} &= 0.5\rho L_s^2 TC_{\theta c}(\alpha_{cr})V_{cr}^2
 \end{aligned} \tag{4.27}$$

F_{stat} is the quasi-steady current force and moment components according to the relative current concept.

where C_{xc} is the resistance coefficient in longitudinal direction

C_{yc} is the resistance coefficient in transverse direction

$C_{\theta c}$ is the resistance coefficient in transverse direction

$$V_{cr} = (u^2 + v^2)^{0.5}$$

$$\alpha_{cr} = \arctan(-v / -u)$$

Dynamic current force and moment components are expressed as follows,

$$F_{xdyn} = -(a_{yy} - a_{xx})V_c \sin(\alpha - \theta)\dot{\theta} + F_{xd}$$

$$F_{ydyn} = -(a_{yy} - a_{xx})V_c \cos(\alpha - \theta)\dot{\theta} + F_{yd} \quad (4.28)$$

$$F_{\theta dyn} = F_{\theta d}$$

Viscous part of the dynamic load contribution represents the effects of the yaw motion in the relative velocity field and based on the local cross flow principle. According to Wichers, viscous part of the dynamic current load can be approximated as follows,

$$F_{xd} = 0.5(a_{yy} - a_{xx})V_c \sin(\alpha - \theta)\dot{\theta}$$

$$F_{yd} = 0.5\rho TC_{yc}(90^\circ) \int_{AP}^{FP} [(v_c - \dot{\theta}l)|v_c - \dot{\theta}l| - v_c|v_c|]dl \quad (4.29)$$

$$F_{\theta d} = 0.5\rho T \int_{AP}^{FP} [C_{yc}(\alpha_{cr}(l))\{(v_c - \dot{\theta}l)^2 - u_c^2\} - C_{yc}(\alpha_{cr})V_{cr}^2]l dl$$

where $u_c = -u$

$$v_c = -v$$

$$\alpha_{cr}(l) = \arctan((v_c - \dot{\theta}l) / u_c)$$

4.4 SLOWLY VARYING AND MEAN WAVE DRIFT FORCES IN IRREGULAR WAVES

In irregular seas drift forces are time dependent. These low frequency drift forces are small in magnitude but may cause large, low frequency oscillations of the single point moored vessel if the vessel's natural frequency is excited.

In irregular waves the wave elevation on a point is written as

$$\zeta(t) = \sum_{i=1}^N \zeta_i \cos(\omega_i t + \epsilon_i) \quad (4.30)$$

The drift force is related to the square of the wave amplitude and the square of the wave envelope is

$$\zeta^2(t) = \sum_{i=1}^N \sum_{j=1}^N \frac{1}{2} \zeta_i \zeta_j \cos(\omega_i t + \epsilon_i) \cos(\omega_j t + \epsilon_j) \quad (4.31)$$

and the low frequency second order wave drift force is written as follows,

$$F^{(2)}(t) = \sum_{i=1}^N \sum_{j=1}^N \zeta_i \zeta_j P_{ij} \cos\{(\omega_i - \omega_j)t + (\epsilon_i - \epsilon_j)\} \\ + \sum_{i=1}^N \sum_{j=1}^N \zeta_i \zeta_j Q_{ij} \sin\{(\omega_i - \omega_j)t + (\epsilon_i - \epsilon_j)\} \quad (4.32)$$

P and Q represent symmetric and asymmetric matrices respectively:

$$P_{mn} = P_{nm} ; Q_{mn} = -Q_{nm} \quad (4.33)$$

If S_{ζ} is the wave spectrum then, according to Pinkster [4.17], the second order force spectrum is

$$S_F(\omega') = 8 \int_0^{\infty} S_{\zeta}(\omega) S_{\zeta}(\omega' + \omega) \left[\frac{F^{(2)}}{\zeta_1 \zeta_2}(\omega, \omega + \omega') \right]^2 d\omega \quad (4.34)$$

where $F^{(2)}(\omega, \omega + \omega') = \sqrt{P_{ij}^2 + Q_{ij}^2}$

and mean wave drift force is

$$\bar{F} = 2 \int_0^{\infty} S_{\zeta}(\omega) \left[\frac{F^{(2)}}{\zeta_1 \zeta_2}(\omega, \omega) \right] d\omega \quad (4.35)$$

where $F^{(2)}(\omega, \omega)$ is mean wave drift force in regular waves

An approximate method is suggested by Newman [4.18] and Pinkster [4.17], in which the low frequency forces are derived from mean drift forces in regular waves. This method can be used only when wave diffraction effects are dominant because it does not take account of the forces related to the second order horizontal pressure gradient. According to this method,

$$P(\omega_m, \omega_n) \approx P\left(\frac{\omega_m + \omega_n}{2}, \frac{\omega_m + \omega_n}{2}\right) \quad (4.36)$$

$$Q(\omega_m, \omega_n) \approx 0$$

A spectral form of this formula is devised by Pinkster,

$$S_F(\omega') = 8 \int_0^{\infty} S_{\zeta}(\omega) S_{\zeta}(\omega' + \omega) \left[\frac{F^{(2)}}{\zeta_a^2} \left(\omega + \frac{\omega'}{2} \right) \right]^2 d\omega \quad (4.37)$$

where $F^{(2)}(\omega + \frac{\omega'}{2})$ is mean wave drift force in regular waves

Response spectrum of a vessel due to the slowly varying wave forces in irregular waves is given as follows:

$$S_{\omega R}(\omega) = S_F(\omega)Q^2 / k^2 \quad (4.38)$$

where k is the linear stiffness coefficient of a tanker which is moored to a fixed point. A slowly varying force and response spectrum is obtained for the vessel whose main dimensions are given in section 4.2 and plotted in Figs. 4.5 and 4.6.

A time history of slowly varying wave forces in irregular waves could be obtained by using the sum of sines approach with a random phase distribution but this approach leads to a Gaussian distribution of the slowly varying forces. Pinkster [4.5] states that an exponential distribution of slowly varying forces is more realistic. Therefore Pinkster devised a method to generate an exponentially distributed force record [4.19, 4.20]. According to this method,

$$\begin{aligned} F_x^{(2)}(\theta_r, t) &= -F_{xA}^{(2)}(\theta_r)(A + 1) + \bar{F}_x^{(2)}(\theta_r) \\ F_y^{(2)}(\theta_r, t) &= -F_{yA}^{(2)}(\theta_r)(A + 1) + \bar{F}_y^{(2)}(\theta_r) \\ F_\theta^{(2)}(\theta_r, t) &= -F_{\theta A}^{(2)}(\theta_r)A \text{sign}(\text{rnd}(b) - 0.5) + \bar{F}_\theta^{(2)}(\theta_r) \end{aligned} \quad (4.39)$$

where $A = \ln[\text{rnd}(a)]$

$\text{rnd}(a)$, $\text{rnd}(b)$ = uniformly distributed number between 0 and 1

$A = \ln[\text{rnd}(a)]$ has an exponential distribution with average -1 and standard deviation 1. The inclusion of $\text{rnd}(b)$ in the yaw moment assures that $F_\theta^{(2)}(\theta_r, t)$ has a symmetrical distribution, which is coupled to $F_x^{(2)}(\theta_r)$ and $F_y^{(2)}(\theta_r)$ in amplitude but not in phase.

$F_{xA}^{(2)}(\theta_r), F_{yA}^{(2)}(\theta_r)$ and $F_{\theta A}^{(2)}(\theta_r)$ are determined using the derived spectral density $S_F^{(2)}(0)$. The variance of $F_{xA}^{(2)}(\theta_r)$ is given by

$$(\sigma_{F_x^{(2)}(\theta_r)})^2 = E[(F_x^{(2)}(\theta_r))^2] - E^2[F_x^{(2)}(\theta_r)] = (F_{xA}^{(2)}(\theta_r))^2 \quad (4.40)$$

A similar expression can be derived for $F_{yA}^{(2)}(\theta_r)$. Taking a sampling frequency of every ∇t , the maximum frequency in the wave drift force is $\pi / \nabla t$. Applying a random white noise process and assuming that $S_{F_n}^{(2)}$ is frequency independent during the ∇t variance can be written as [4.7]

$$\begin{aligned} (\sigma_{F_x^{(2)}(\theta_r)})^2 &= S_{F_x^{(2)}(0, \theta_r)} \pi / \nabla t = (F_{xA}^{(2)}(\theta_r))^2 \\ (\sigma_{F_y^{(2)}(\theta_r)})^2 &= S_{F_y^{(2)}(0, \theta_r)} \pi / \nabla t = (F_{yA}^{(2)}(\theta_r))^2 \\ (\sigma_{F_\theta^{(2)}(\theta_r)})^2 &= S_{F_\theta^{(2)}(0, \theta_r)} \pi / \nabla t = 2 (F_{\theta A}^{(2)}(\theta_r))^2 \end{aligned} \quad (4.41)$$

An estimate for ∇t could be derived from eq. 4.41. Time histories of the slowly varying forces are derived by using eq. 4.39, 4.40 and 4.41 for the ship and plotted in Fig. 4.7. These block functions are stored in the files and used in the time domain simulations.

Another component of wave drift forces is wave drift damping caused by the low frequency motions of the vessel. Wave drift damping can be evaluated by the gradient method [4.6] as follows:

$$F_{wd}^{(2)} = \frac{\partial F_x^{(2)}}{\partial \dot{x}_x^{(2)}} \dot{x}_x^{(2)} \quad (4.42)$$

Wave drift damping is calculated for different speeds and frequencies and plotted in Fig. 4.8.

4.5 MOTION EQUATIONS OF THE TANKER-BUOY SYSTEM IN TIME AND FREQUENCY DOMAIN

In order to predict the motion response and mooring force values of the coupled buoy and ship system coupled surge, sway and yaw motion equations were formulated in terms of forcing functions which are defined as a function of the relative angle between the direction of forces and the ship's instantaneous position. The ship was modelled as an elliptical cylinder form whose length, draught and volume were equivalent to those of the tanker. This elliptical cylinder form approximation made it possible to formulate wave and motion induced hydrodynamic forces using Mathieu functions. Since the non-linear behaviour of the coupled buoy and ship system was studied using a time domain simulation technique, the reason behind the choice of elliptical cylinder approximation using the Mathieu functions was to obtain a feasible alternative to Green's function techniques to calculate the wave excitation forces with high a degree of accuracy and less computational time.

In formulating the motion equations of the coupled system non-linear stiffness characteristics of the catenary mooring lines and of the hawser were taken into account. The non-linear, coupled motion equations were solved simultaneously in the time-domain using a numerical integration technique. The technique adopted was Adam's variable order variable step differential solver algorithm. In the time domain solutions of the motion equations, variable coefficients on the left hand side of these equations as well as the forcing functions on the right hand-side of equations were re-calculated thus taking into account the displaced positions of the buoy and tanker.

Refs 4.21 and 4.22 summarises the results of some of the numerical predictions carried out using the formulations described in this chapter.

In this section time domain equations which relate the instantaneous values of forces to rigid body motions will be derived. Motion equations are usually written as follows,

$$(m + a(\omega)) \ddot{x} + b(\omega) \dot{x} + c(\omega) x = F_0 \sin(\omega t + \epsilon)$$

As Cummins [4.23], Ogilvie [4.24], Oortmerssen [4.25] and Muga [4.26] pointed out this is not a real equation of motion since the hydrodynamic coefficients depend on the frequency of the motion. Some simplifications, such as linearization of the mooring system, assuming that forcing function is purely sinusoidal or an assumption that hydrodynamic coefficients are constant, are sometimes made to the above equation to retain the model. But these assumptions cannot be justified except in very few cases. In order to relate the instantaneous values of forces to motions Cummins' method [4.23] will be followed.

For any linear system if the response $R(t)$ to a unit impulse is known, then the response of the system to an arbitrary force $F(t)$ is

$$x(t) = \int_{-\infty}^t K(t - \tau) f(\tau) d\tau \quad (4.43)$$

Using the Impulse response function we can write the real time domain equations

$$\sum_{i=1}^5 [(M_{ji} + m_{ji}) \ddot{x}_j + \int_{-\infty}^t K_{ji}(t - \tau) \dot{x}_j(\tau) d\tau + C_{ji} x_j] = F_j(t) \quad (4.44)$$

$$j = 1, \dots, 6$$

where M_{ji} is the mass matrix, m_{ji} is the constant added mass matrix, C_{ji} hydrostatic restoring force coefficients

The impulse response function is

$$K_{ij}(t) = \frac{2}{\pi} \int_0^{\infty} b_{ij}(\omega) \cos \omega t \, d\omega \quad (4.45)$$

$$w_{ij} K_{ij}(t) = \frac{2}{\pi} \int_0^{\infty} b_{ij}(\omega) \cos \omega t \, d\omega \quad \text{frequency independent added mass coefficient}$$

Frequency independent constant added mass coefficient is expressed as follows

$$m_{ij} = a_{ij}(\omega') + \frac{1}{\omega'} \int_0^{\infty} K_{ij}(t) \sin \omega' t \, dt \quad (4.46)$$

where ω' is an arbitrarily chosen value of ω .

Motion Equations of the Tanker-Buoy System in Regular Waves, Steady Wind and Current:

In the tanker-buoy system we will consider surge, sway and yaw motions of the tanker and surge and sway motions of the buoy only (See also Fig. 4.9). Hence 5 degrees of freedom system can be written as follows;

$$(M^B + M_{AVM,x}^B) \ddot{x}_B + \int_{-\infty}^t K_x^B(t-\tau) \dot{x}_B(\tau) \, d\tau + k_x x_B = F_{Ex}^B + F_{Rx} \quad (4.47)$$

$$(M^B + M_{AVM,y}^B) \ddot{y}_B + \int_{-\infty}^t K_y^B(t-\tau) \dot{y}_B(\tau) \, d\tau + k_y y_B = F_{Ey}^B + F_{Ry} \quad (4.48)$$

$$M^S (\ddot{x}_S - \dot{y}_S \dot{\theta}) + M_{AVM,x}^S \ddot{x}_S + \int_{-\infty}^t K_x^S(t-\tau) \dot{x}_S(\tau) \, d\tau = F_{Ex}^S - F_{Rx} \quad (4.49)$$

$$M^S (\ddot{y}_S + \dot{x}_S \dot{\theta}) + M_{AVM,y}^S \ddot{y}_S + \int_{-\infty}^t K_y^S(t-\tau) \dot{y}_S(\tau) \, d\tau = F_{Ey}^S - F_{Ry} \quad (4.50)$$

$$(I^S + I_{AVM,\theta}^S) \ddot{\theta}_S + \int_{-\infty}^t K_{\theta}^S(t-\tau) \dot{\theta}_S(\tau) \, d\tau = F_{E\theta}^S - F_{R\theta} \quad (4.51)$$

where

M^B is the mass of the buoy

M^S is the mass of the ship

I^S is the moment of inertia of mass of the ship in the yaw direction

$M_{AVM,x}^B, M_{AVM,y}^B$: Constant added mass of the buoy in the surge and sway directions respectively.

$M_{AVM,x}^S, M_{AVM,y}^S$: Constant added mass of the tanker in the surge and sway directions respectively.

$I_{AVM,\theta}^S$ is the moment of inertia of added mass of the ship in the yaw direction.

K_x^B, K_y^B : Retardation functions of the buoy in the surge and sway directions respectively

K_x^S, K_y^S, K_θ^S : Retardation functions of the tanker in the surge, sway and yaw directions respectively.

k_x, k_y : Mooring stiffness of the buoy in the surge and sway directions respectively.

F_{Ex}^B, F_{Ey}^B : Wave, wind and current forces acting on the buoy in surge and sway directions respectively.

$F_{Ex}^S, F_{Ey}^S, F_{E\theta}^S$: Wave, wind and current forces acting on the tanker in surge, sway and yaw directions respectively.

$F_{Rx}, F_{Ry}, F_{R\theta}$: Hawser line forces in the surge, sway and yaw directions respectively.

Motion Equations of the Tanker-Buoy System in Irregular Waves, Dynamic Wind and Current:

Wind forces and slowly varying forces in irregular waves have been formulated in the time domain in sections 4.2 and 4.4. First order wave forces can also be formulated in the time domain by applying the sum of sines approach with random phase distribution which was used to obtain the wind velocity time history in sec. 4.2. All these forces obtained in the time domain are used in the time domain simulation of the tanker-buoy system as block functions. Motion equations of the tanker-buoy system in irregular

waves, dynamic wind and current are similar to Eqs. 4.47-4.51 with the exception that environmental forces will include slowly varying wave and wind forces as well.

Motion Equations in Frequency Domain

Motion Equations can be solved in the frequency domain in regular head waves. In this model the stiffness values for the hawser and mooring lines are taken as constant at the value corresponding to the static current and wave drift loading, and the variations in the wave and hydrodynamic induced forces as the system oscillates at the wave frequency are not taken into account. The surge equation of motions describing the behaviour of the system in the frequency domain is given as follows:

$$\begin{bmatrix} M_B & 0 \\ 0 & M_S \end{bmatrix} \begin{bmatrix} \ddot{X}_B \\ \ddot{X}_S \end{bmatrix} + \begin{bmatrix} B_B & 0 \\ 0 & B_S \end{bmatrix} \begin{bmatrix} \dot{X}_B \\ \dot{X}_S \end{bmatrix} + \begin{bmatrix} k_M + k_H & -k_H \\ -k_H & k_H \end{bmatrix} \begin{bmatrix} X_B \\ X_S \end{bmatrix} = \begin{bmatrix} F_B \\ F_S \end{bmatrix} \quad (4.52)$$

where

- B_B : Surge damping of the buoy
- B_S : Surge damping of the ship
- F_B : Wave induced surge forces on the buoy
- F_S : Wave induced surge forces on the ship
- k_M : Mooring stiffness
- k_H : Hawser stiffness
- M_B : Mass and surge added-mass of the buoy
- M_S : Mass and surge added-mass of the barge

The results of time and frequency domain calculations and experimental measurements for the surge motions of the ship are shown in Fig. 4.11. Fig. 4.11 shows that there is good agreement between the time- and frequency domain predictions and that predictions agree well with the measurements. However the correlation between the surge motion predictions of the buoy and the measurements are not so satisfactory as can be seen from Fig. 4.12. This may be attributed to the unstable rigid-body motions of the

buoy observed during the experiments as well as to the linear spring modelling of the hawser. Fig. 4.10 shows the experimental set-up.

Time and frequency domain programs were also run for the configuration shown in Fig. 4.9. Comparisons of surge displacements obtained from frequency and time domain calculations are shown in Figs. 4.13 and 4.14. Whilst the surge motion amplitudes of the ship obtained from frequency and time domain simulations correlate well with each other there are significant differences between the surge motion amplitudes of the buoy as obtained from the frequency and time domain simulations in the wave frequency range between 0.15 and 0.3 rad./sec. This difference may be attributed to the effects of non-linearities in hawser forces.

4.6 NUMERICAL ASPECTS AND RESULTS

In order to calculate the retardation functions given in Eq. 4.45, the frequency dependent damping coefficient should be known up to infinite frequencies. This numerical difficulty could be overcome by making use of the asymptotic behaviour of the damping coefficient in high frequencies. In the high frequencies damping values of surge, sway and yaw motions are approximated by the following equation,

$$b_{ii} = \frac{C_i}{\omega^3} \quad (4.53)$$

This approximation was first suggested by Newman [4.27]. If the damping is known up to a certain value ω_0 , then the C_k value can be calculated from Eq. 4.44 and the retardation function given in Eq. 4.45 can be rewritten as follows,

$$K_{ii}(t) = \frac{2}{\pi} \int_0^{\omega_0} b_{ii}(\omega) \cos \omega t \, d\omega + \frac{2}{\pi} \int_{\omega_0}^{\infty} \frac{C_i}{\omega^3} \cos \omega t \, d\omega \quad (4.54)$$

The second integral in Eq. 4.54 could be evaluated up to very high frequencies. C_k values were calculated for the surge, sway and yaw damping values given in Figs. 3.34,

3.35 and 3.36 and found to be 0.1386, 2.9 and 0.46355 respectively. Retardation functions for surge, sway and yaw motions given in Eq. 4.54 were presented in Figs. 4.15, 4.16 and 4.17. Calculations were carried out for very high frequencies up to 5 rad/sec and the convergence of the functions is quite good for the chosen 25 sec. calculation limit. Retardation functions given in Figs. 4.15-4.17 are approximated by chebyshev polynomials in order to make effective use of them in the time domain simulations. Constant added mass coefficients expressed in Eq. 4.46 were evaluated for 5 different frequencies. Due to approximations made in the calculations the computations did not give exactly the same values. Average values of these calculations, 0.027 for surge, 0.592 for sway and 0.079 for yaw, are in good agreement with Oortmerssen's calculations which are 0.033, 0.505 and 0.045 respectively. Differences between the results could be attributed to the geometrical difference between the tanker and the elliptical cylinder. There is one other way to obtain the constant added mass coefficients, that is to use the limit value of $a_{ij}(\omega)$ as m_{ij} at infinite frequency. Because it is obvious from Eq. 4.46 that when ω approaches infinity, $a_{ij}(\omega)$ takes the value of m_{ij} . Therefore one should like to derive the asymptotic values of $a_{ij}(\omega)$ at infinity. However there is one obstacle, namely that it is very difficult to calculate the Mathieu functions at very high frequencies because of the very large parametric value, q . For instance, for 5 rad/sec the parametric value becomes 38078.56.

In order to solve the differential equations an algorithm written by Gear [4.28] is used. The algorithm which is either a form of the Adams methods or a method for stiff equations has several features such as the automatic selection of step size and order for the method used. In order to avoid shock response of the system due to external forces an exponential ramp function which ensures the gradually increase of the external force for a certain period at the beginning of the simulation is used.

The effect of dynamic wind and irregular waves is shown in Figs. 4.18 and 4.19. It can be easily concluded from the graphs that dynamic environment is causing peak loads on the hawser and slowly varying oscillations of the system.

4.7 CONCLUSIONS

A time-domain simulation procedure to predict the motion response values and mooring forces of a CALM system was described and the results obtained from the time domain simulations were validated by model test measurements. The results of the time domain simulations were also correlated with frequency domain calculations. Whilst the surge motion amplitudes of the ship obtained from the frequency and time domain simulations correlate well with each other and agree with the results of measurements, there are some differences between the surge motion amplitudes of the buoy as obtained from the frequency and time domain simulations and the experimental measurements. These discrepancies may be attributed to the effects of non-linearities in hawser restoring forces and to the unstable behaviour of the buoy model due to its light weight in waves during the experiments.

The results of motion response and mooring force predictions based on non-linear time domain simulations revealed that the unstabilising Munk moment causes unstable large amplitude motions of the buoy and the ship in the horizontal plane yielding mooring line and hawser forces which are about 2-3 times larger than the maximum forces obtained when the effects of Munk moment are not considered.

The results of oblique wave tests revealed that as the current and the wave forces become more orthogonal to each other the magnitude of steady sway and yaw displacements of the ship increases and that the increase in current load, generally yields an increase in the surge, sway and yaw oscillation amplitudes of the ship.

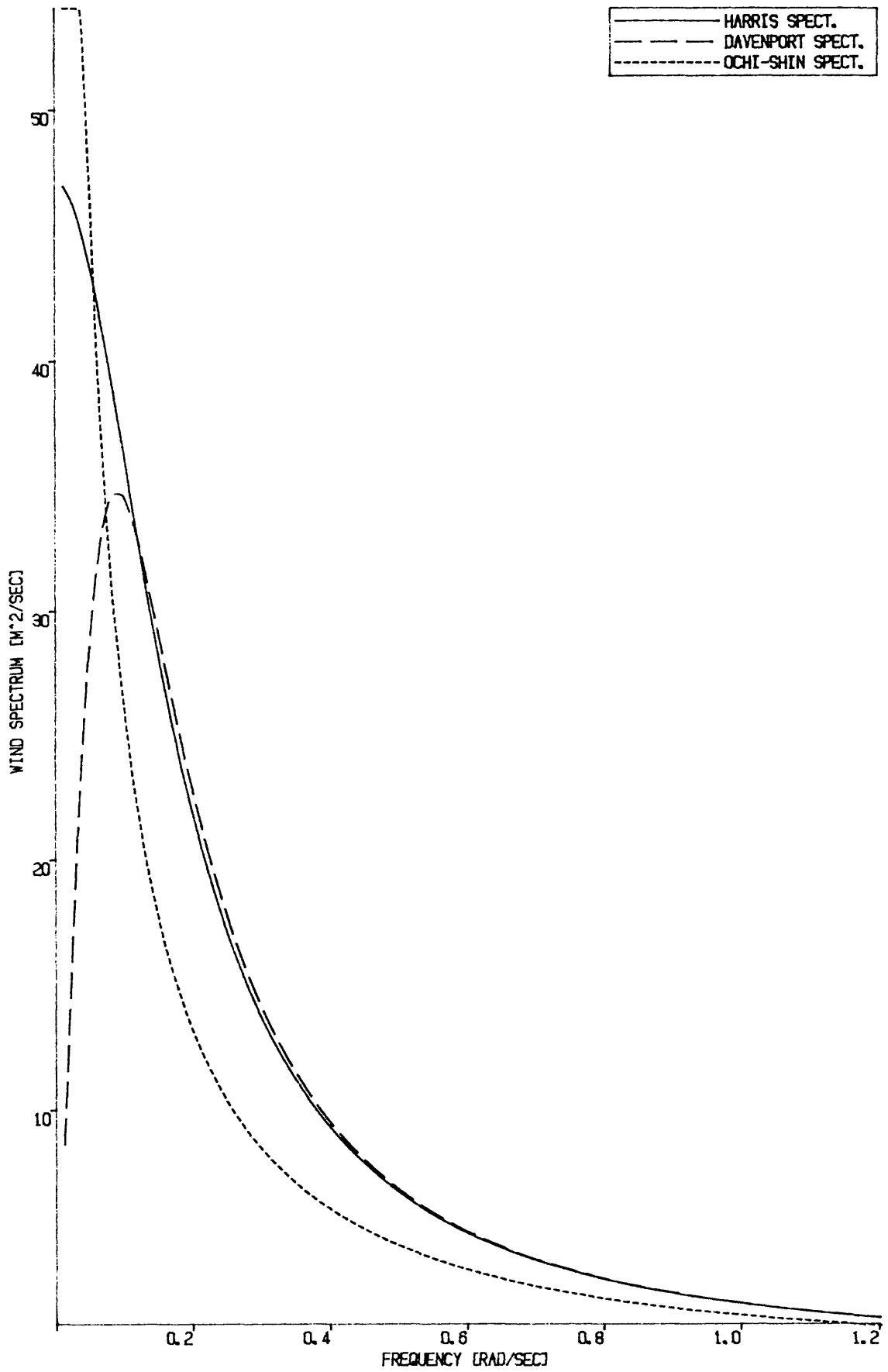


Fig. 4.1 Wind Spectrums
 Mean Wind Speed=22 m/sec

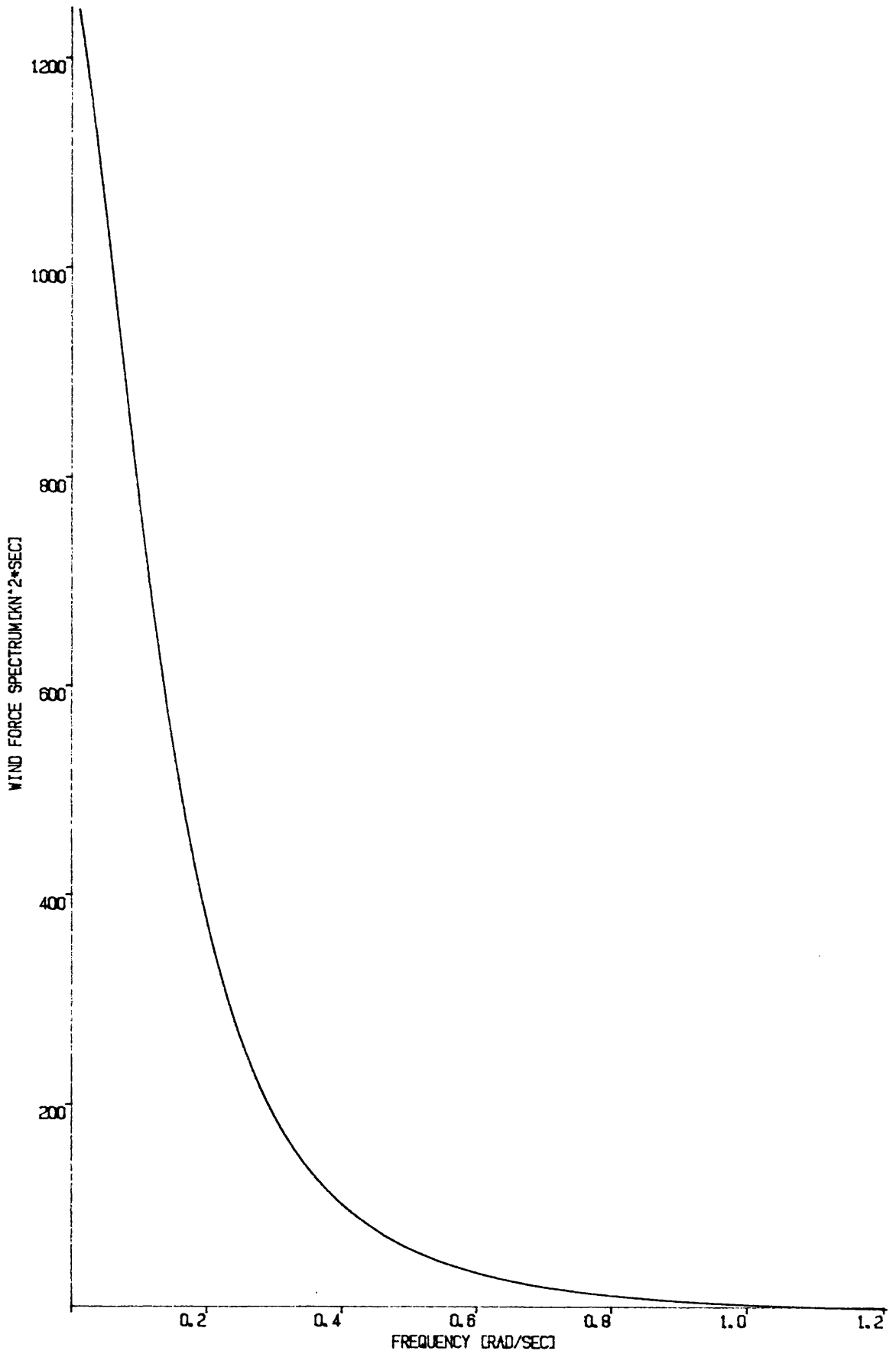


Fig. 4.2 Wind Force Spectrum
Projected Area=472 m²
Mean Wind Speed=22m/sec

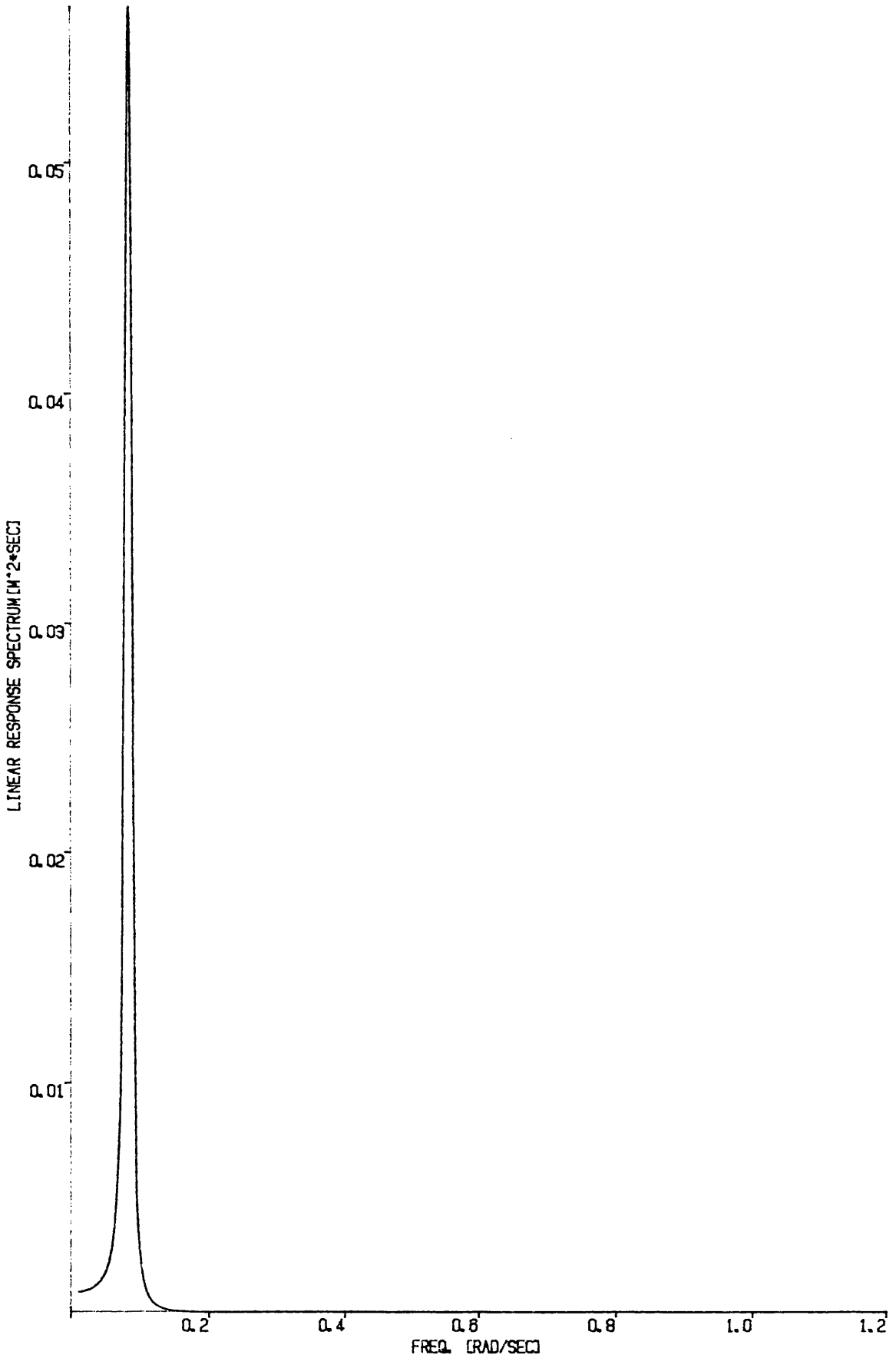


Fig. 4.3 Linear Response Spectrum

Stiffness Coe.=1200 kN/m, Mass+Added Mass=173154 Ton.
Damping Ratio=0.05

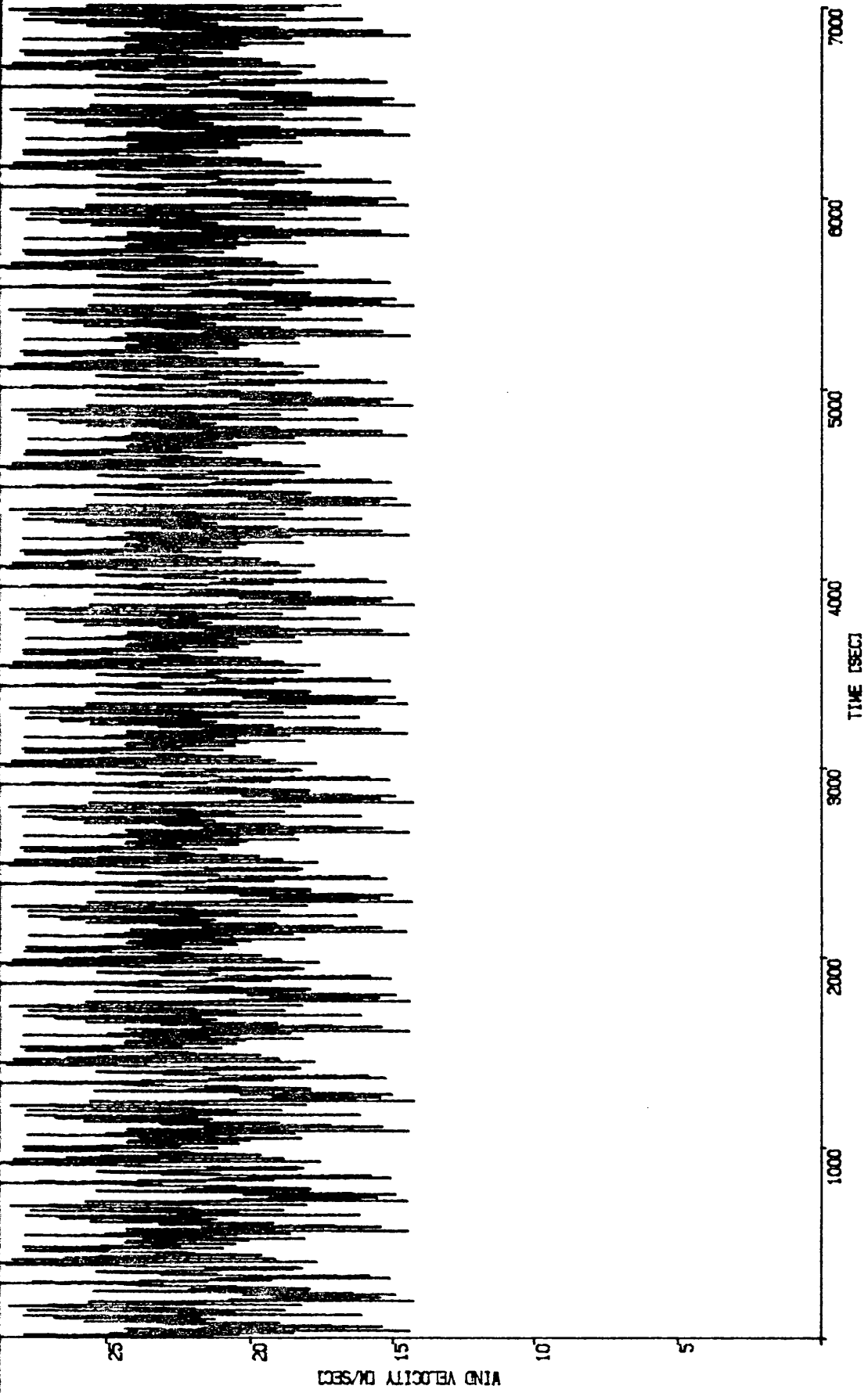


Fig. 4.4 Wind Velocity Time History
Mean Wind Speed=22m/sec

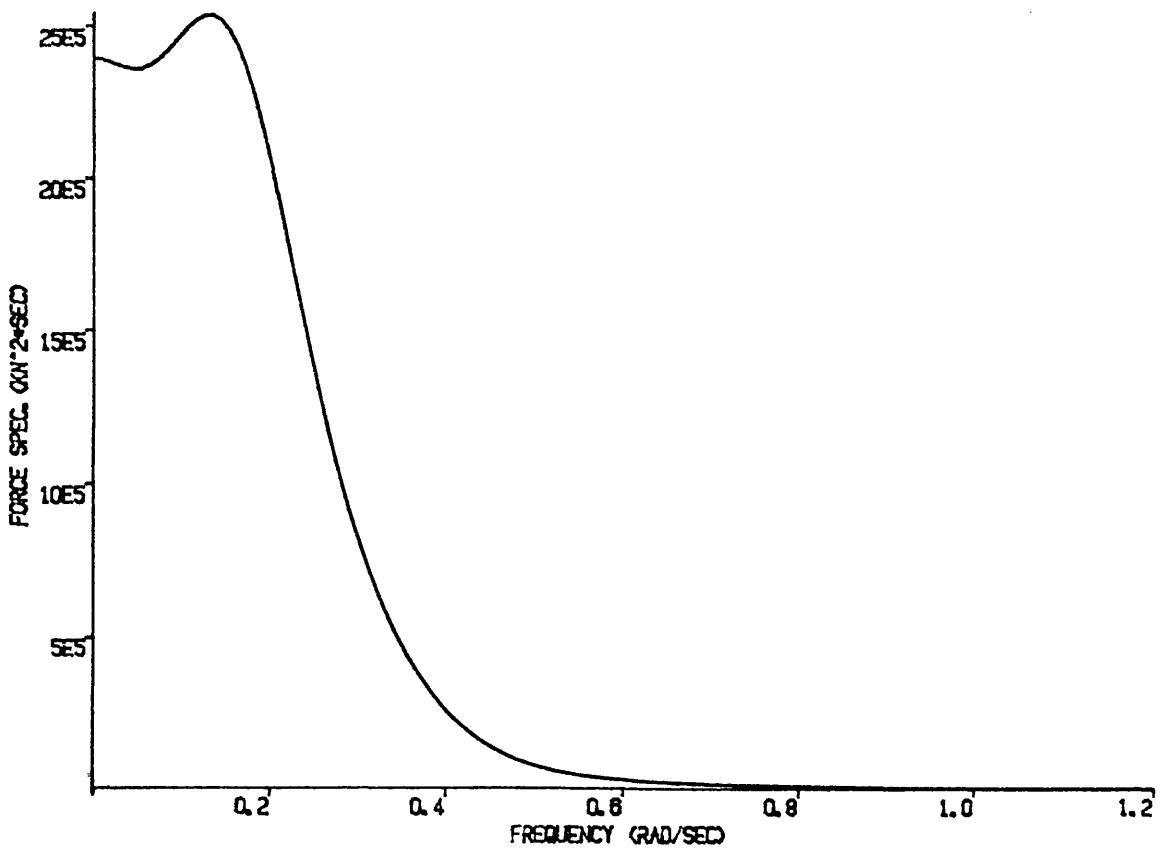
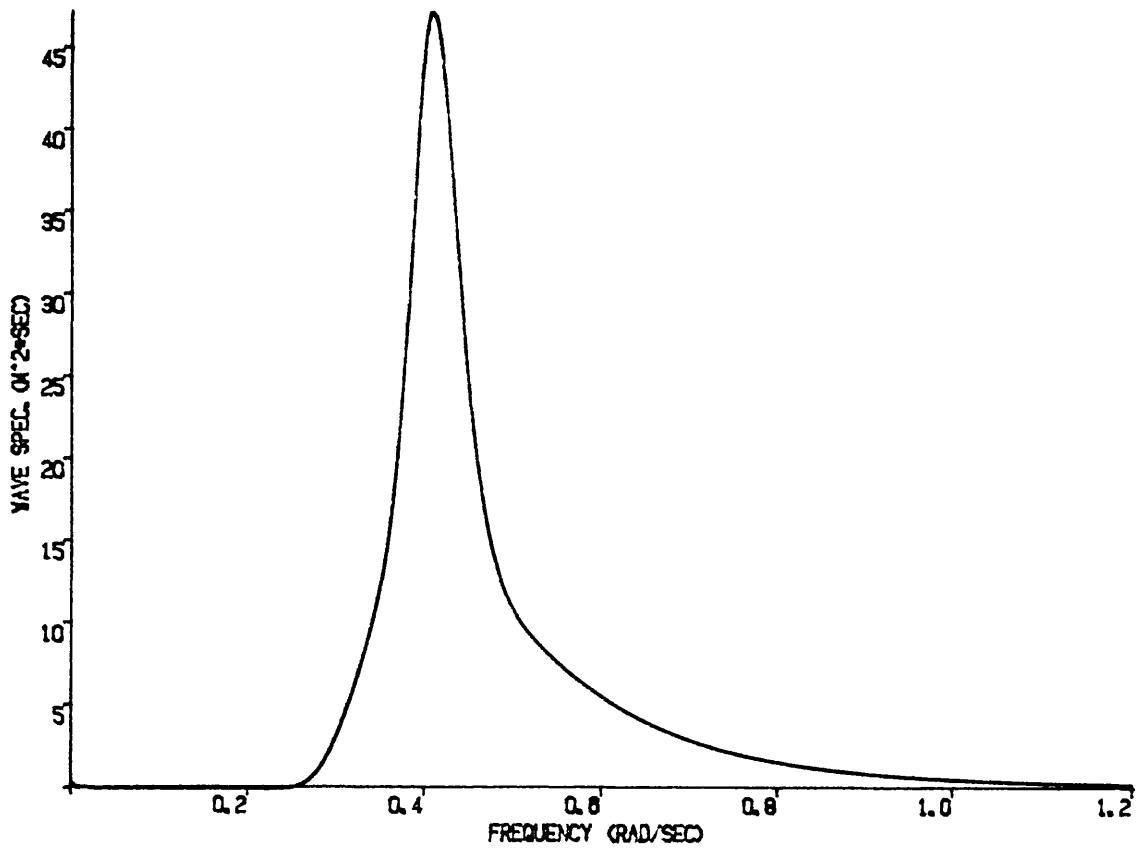


Fig. 4.5 Jonswap Wave Spectrum and Slowly Varying Force Spectrum
 Significant Wave Height=10m, Zero Crossing Period=12sec

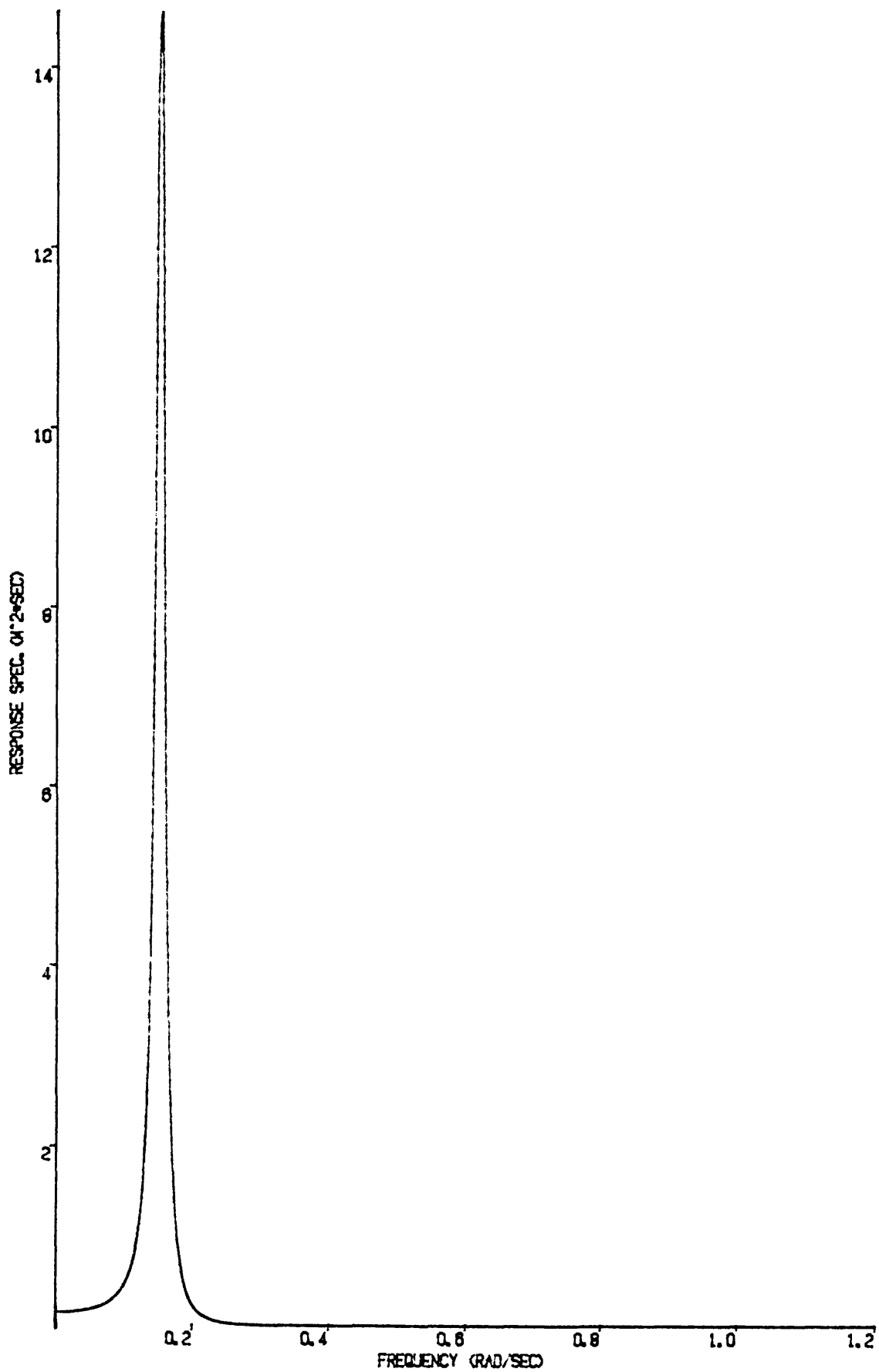


Fig. 4.6 Linear Response Spectrum
Stiffness Coe.=4000 kN/m, Damping Ratio=0.05

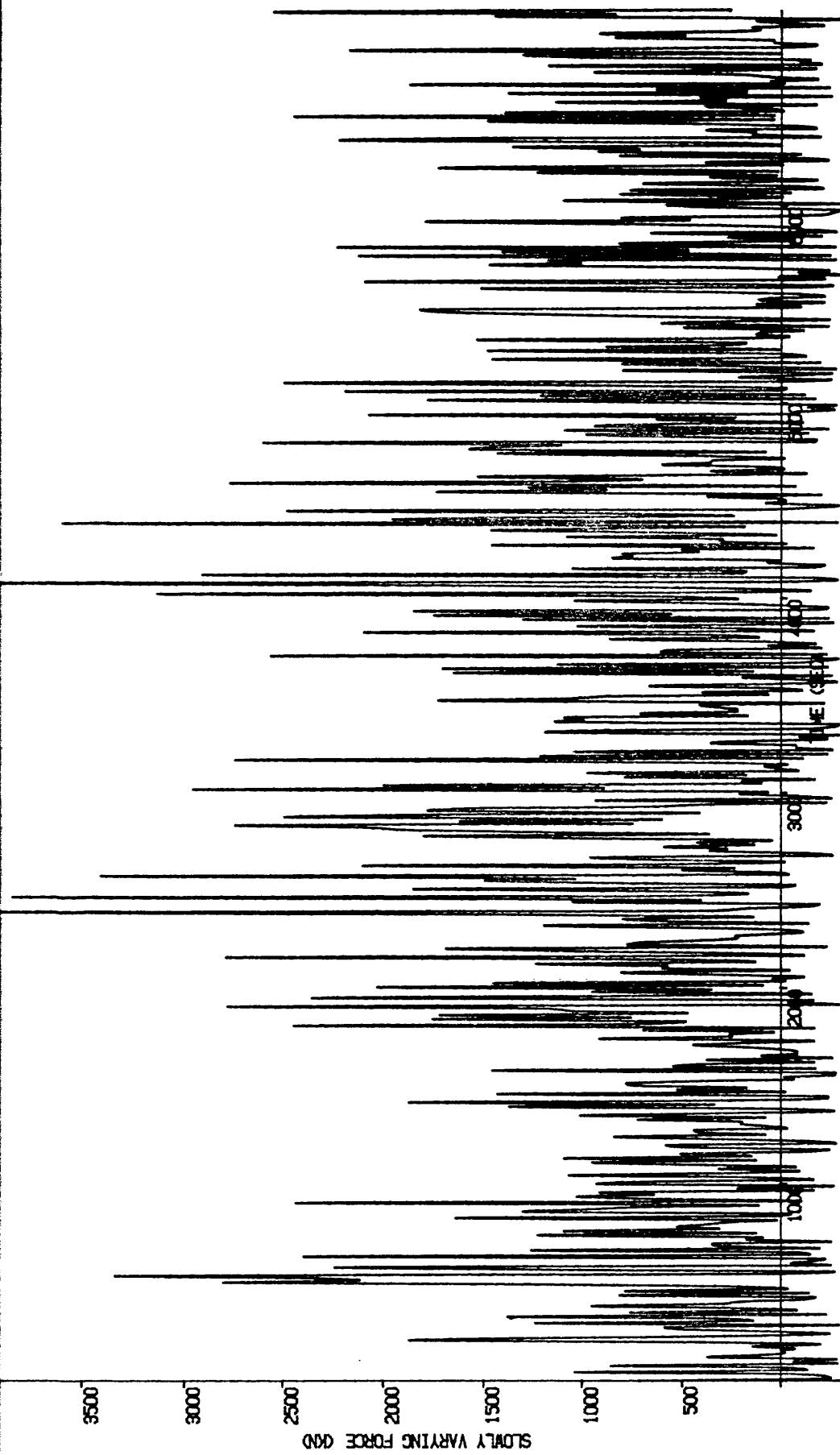


Fig. 4.7 Time History of Wave Forces in Irregular Waves

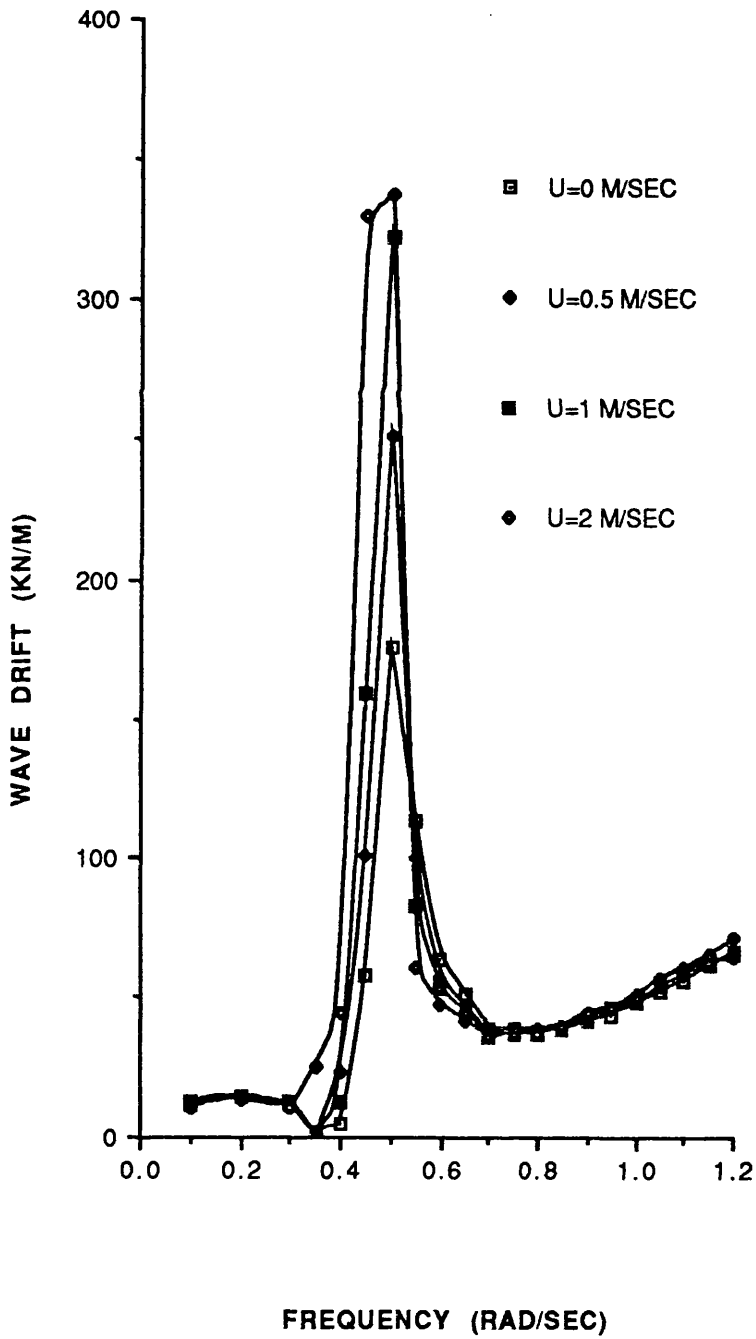
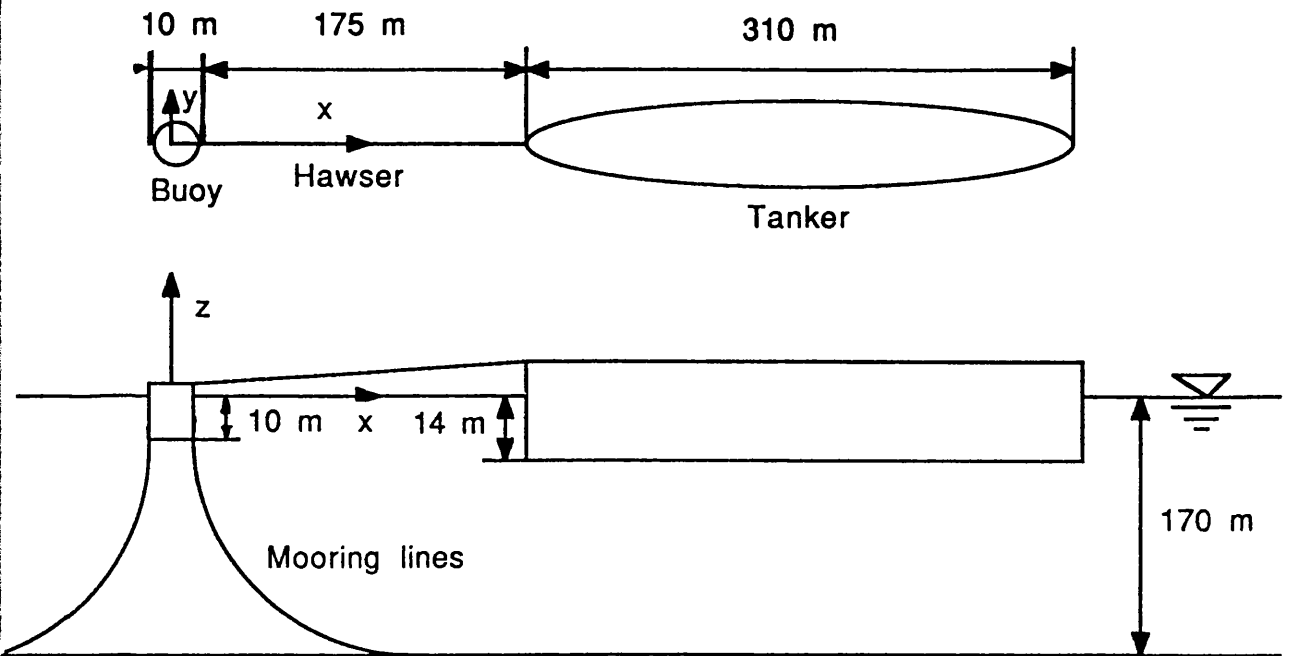


Fig. 4.8 Wave Drift Force for Different Forward Speeds
Angle of Incidence=0 Degree



Tanker-Buoy System used in the parametric study

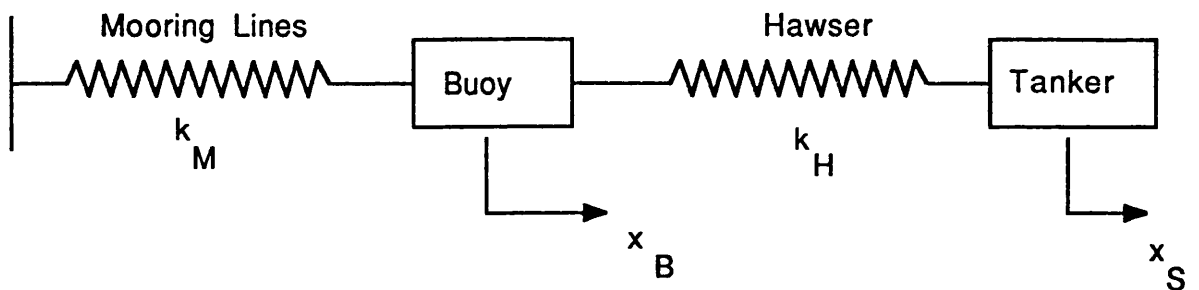


Fig. 4.9 Frequency Domain Modelling of the Tanker-Buoy System

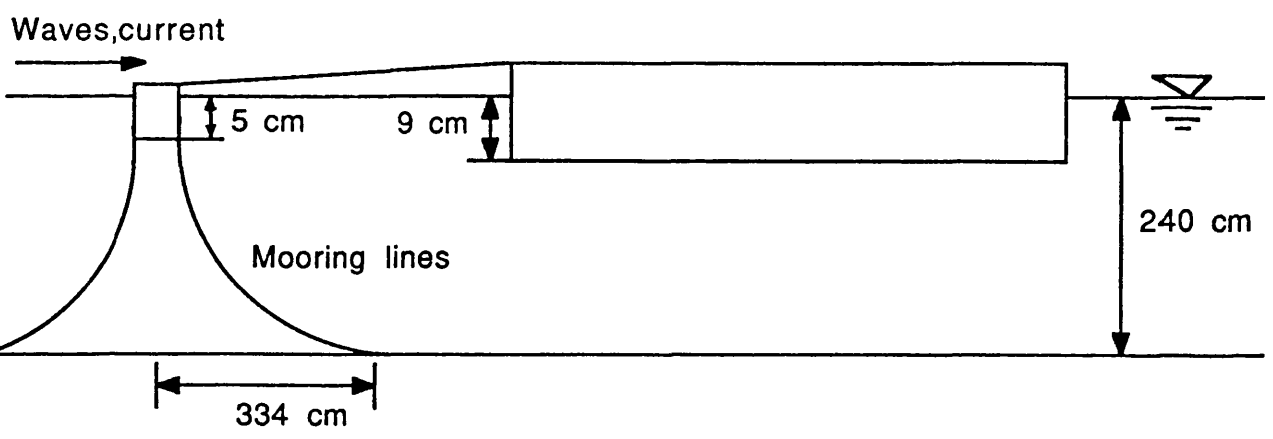
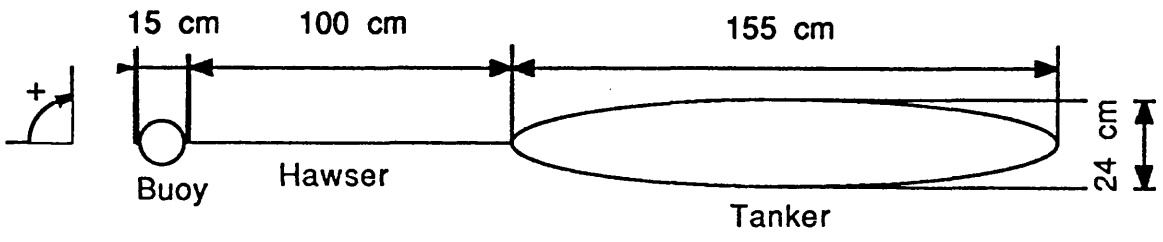


Fig. 4.10 Experiment Set-up of the Tanker-Buoy System
Co-linear Environmental Forces

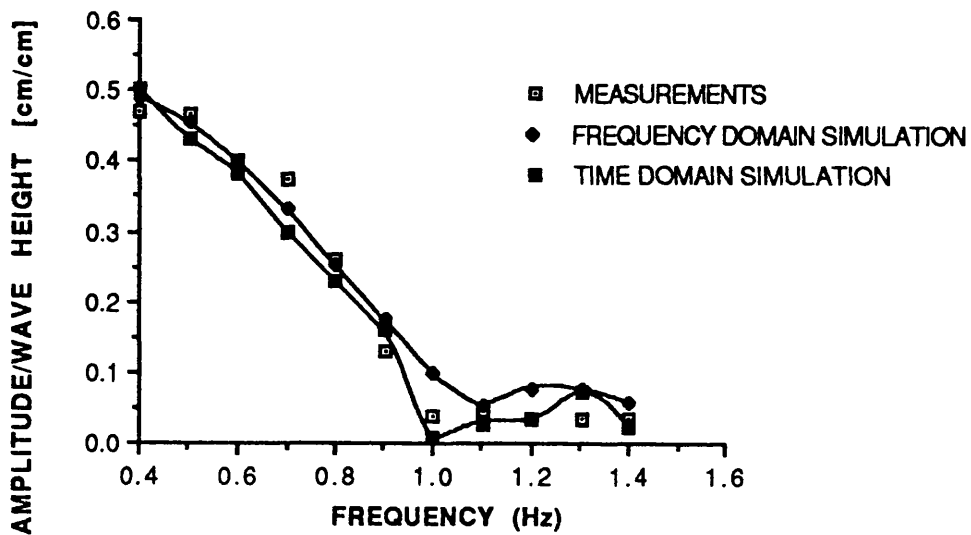


Fig. 4.11 Surge Motion of the Tanker
Co-linear Environmental Forces

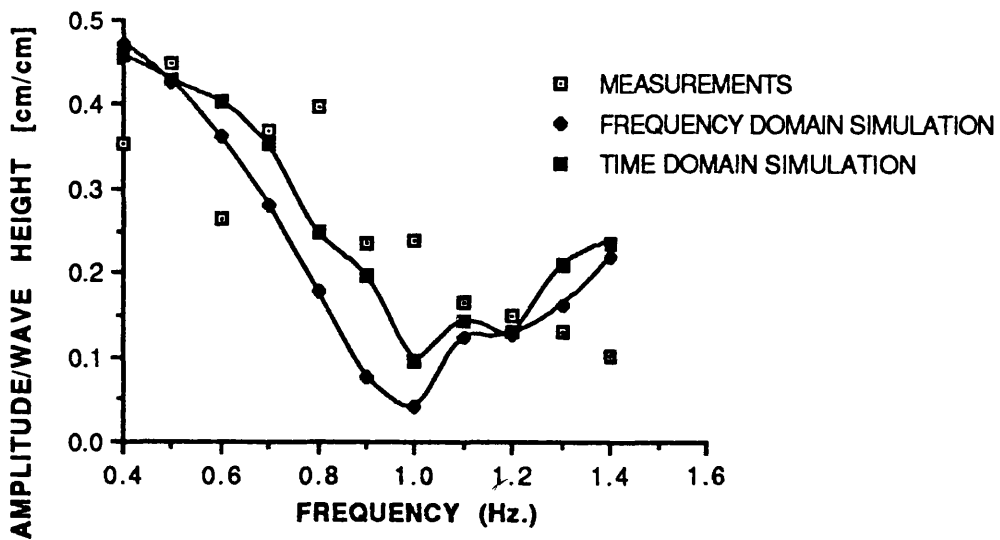


Fig. 4.12 Surge Motion of the Buoy
Co-linear Environmental Forces

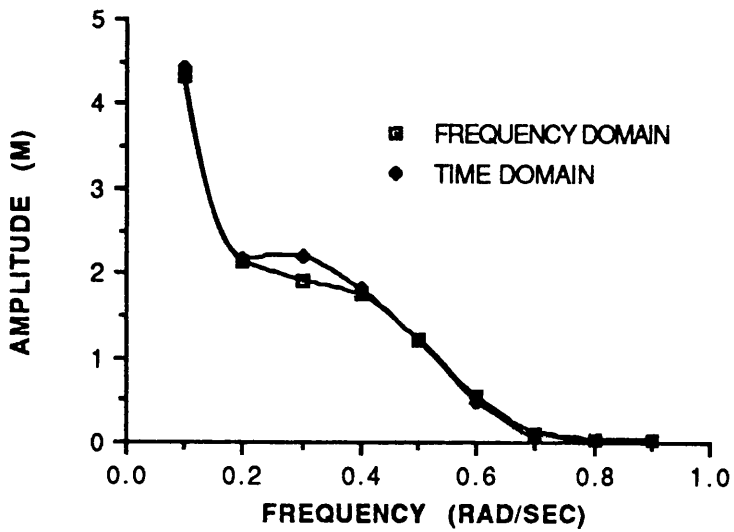


Fig. 4.13 Surge Response of the Tanker
 Wave Height=8 m, Wind Velocity=20 m/sec
 Current Velocity=1.5 m/sec

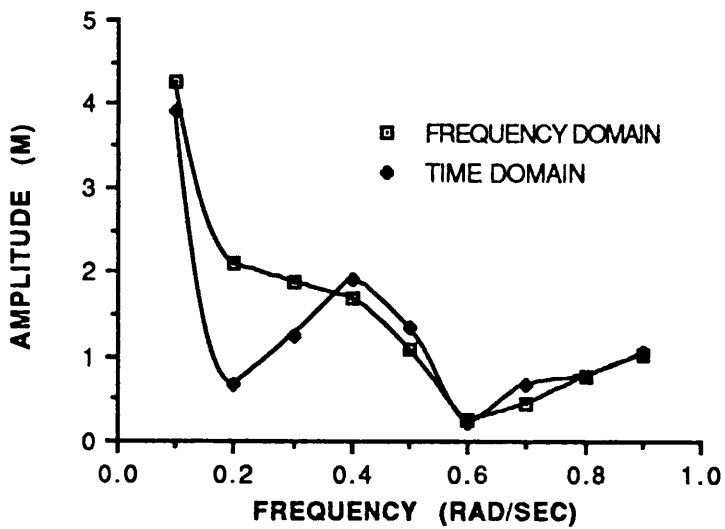


Fig. 4.14 Surge Response of the Buoy
 Wave Height=8 m, Wind Velocity=20 m/sec
 Current Velocity=1.5 m/sec

— ORIGINAL DATA
 - - - - - APPROXIMATION

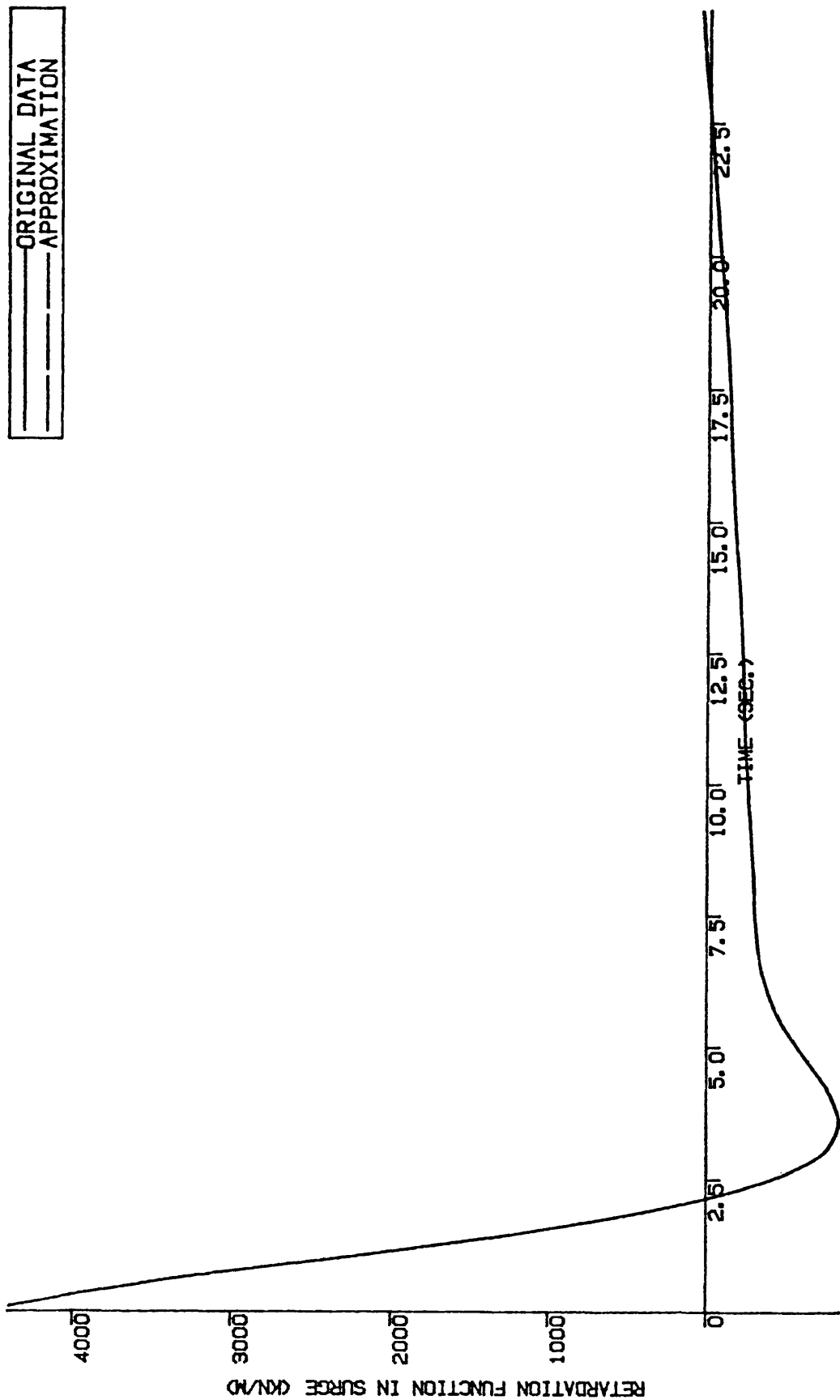


Fig. 4.15 Approximation to the Retardation Function by Chebyshev Polynomials

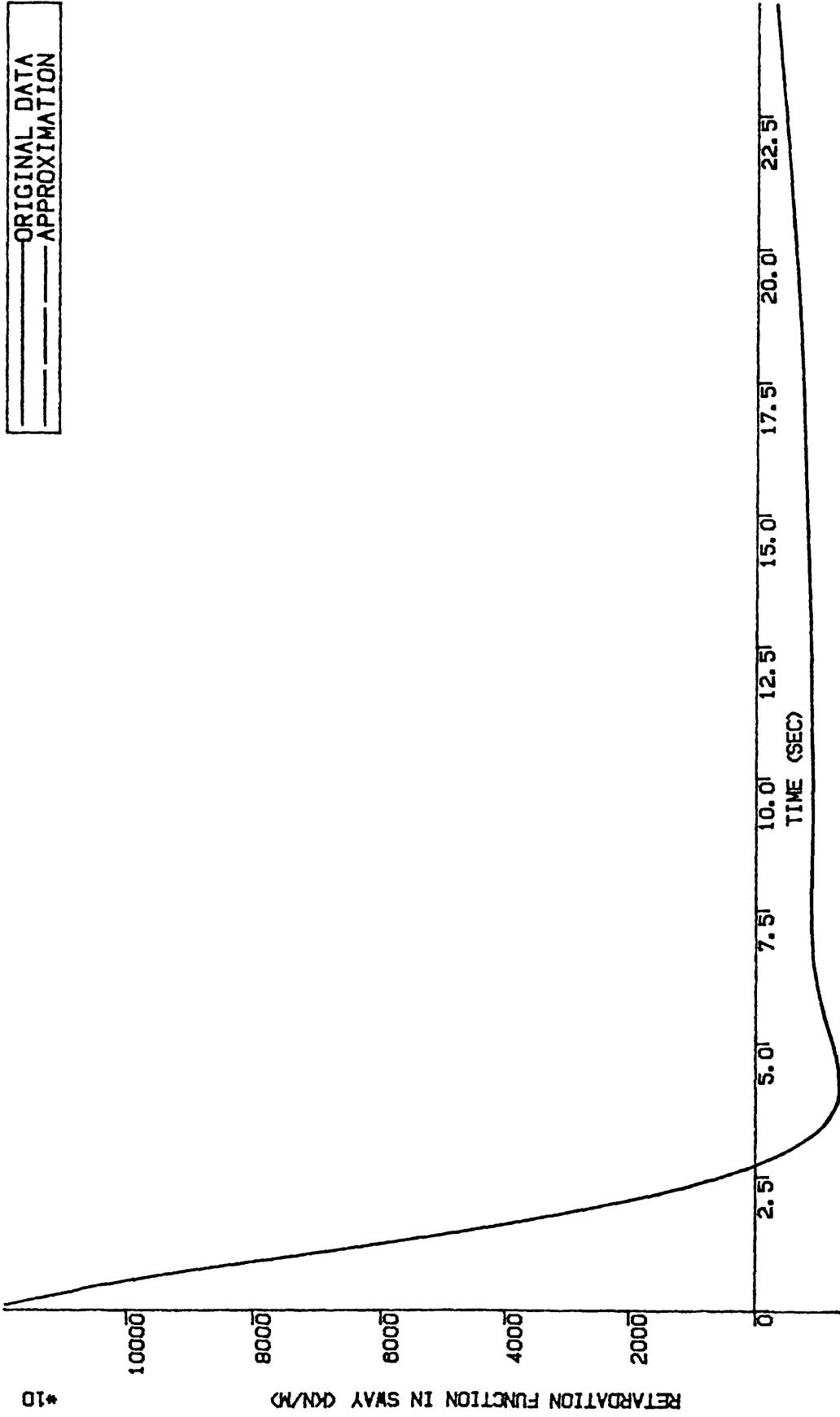


Fig. 4.16 Approximation to the Retardation Function by Chebyshev Polynomials

— ORIGINAL DATA
 - - - - - APPROXIMATION

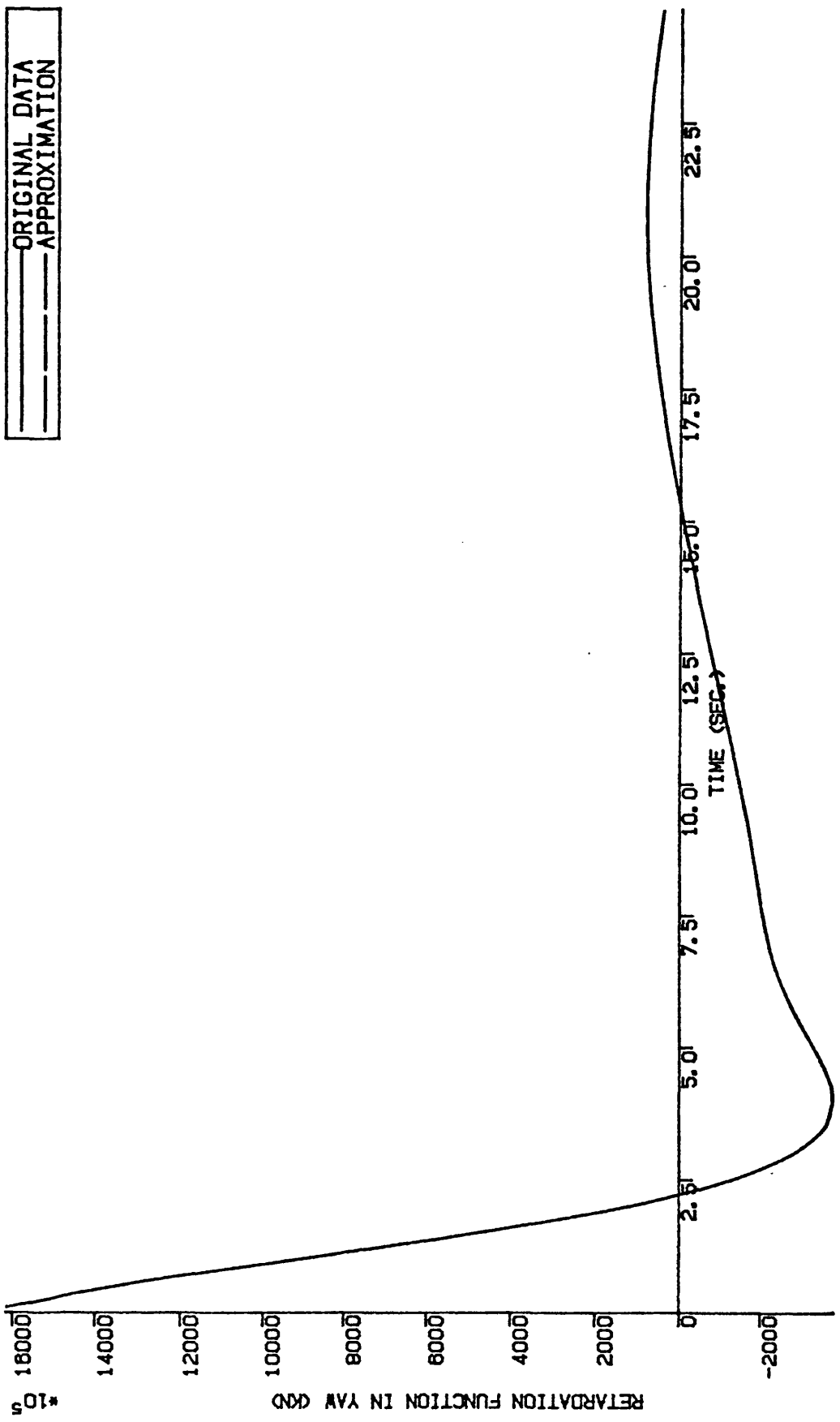


Fig. 4.17 Approximation to the Retardation Function
 by Chebyshev Polynomials

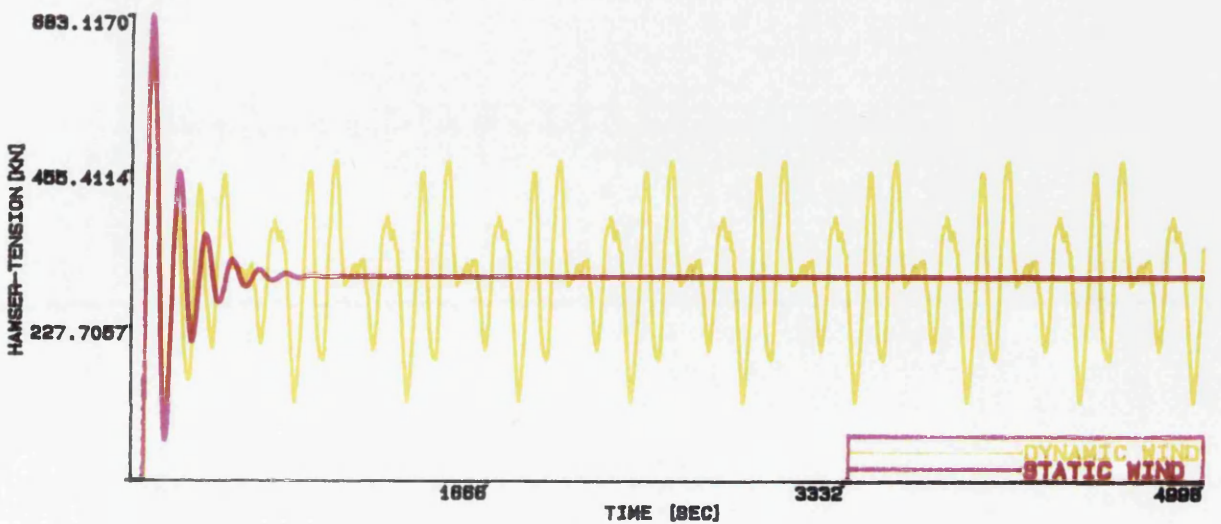
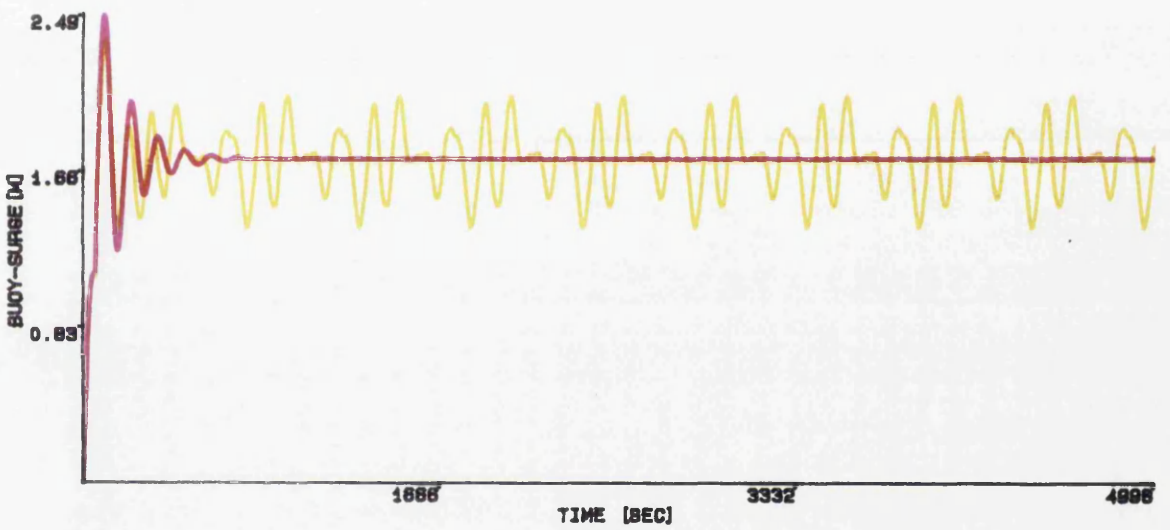
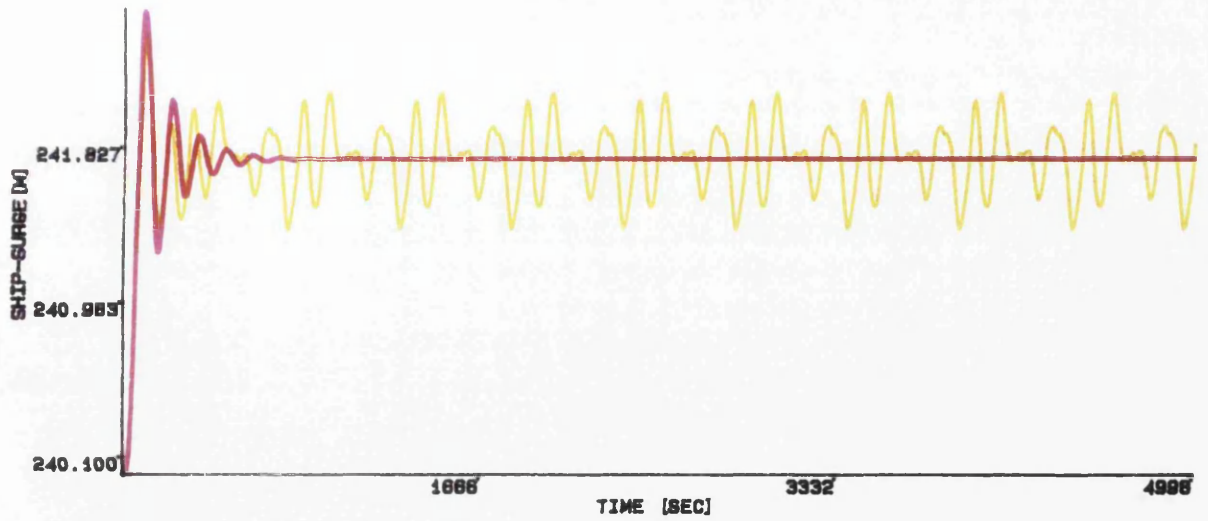


Fig. 4.18 Comparison Between Static and Dynamic Wind
 Mean Wind Speed=22 m/sec, Current Speed=1.5 m/sec
 Co-linear Environmental Forces, OchiShin Wind Spectrum

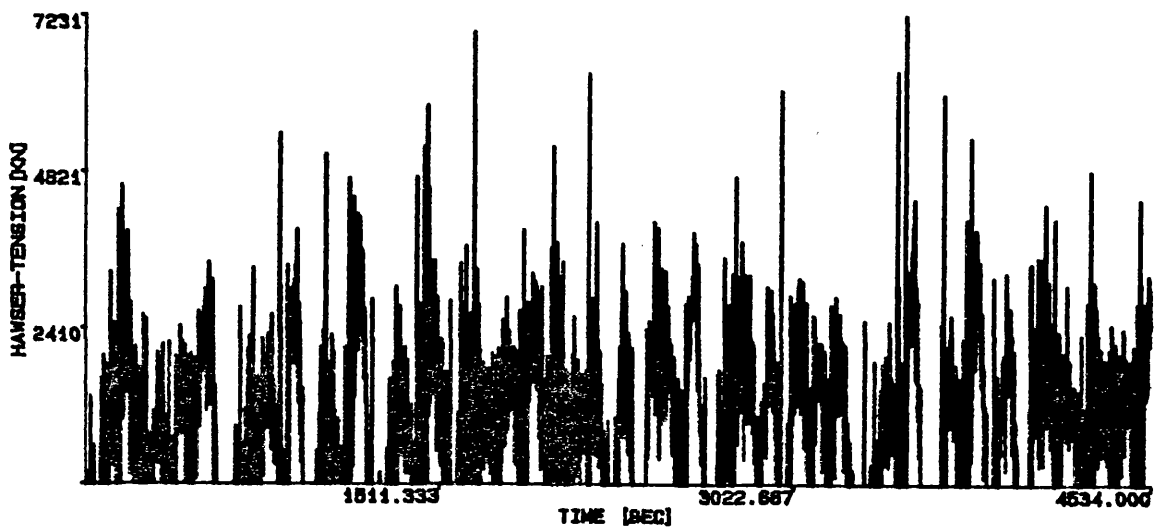
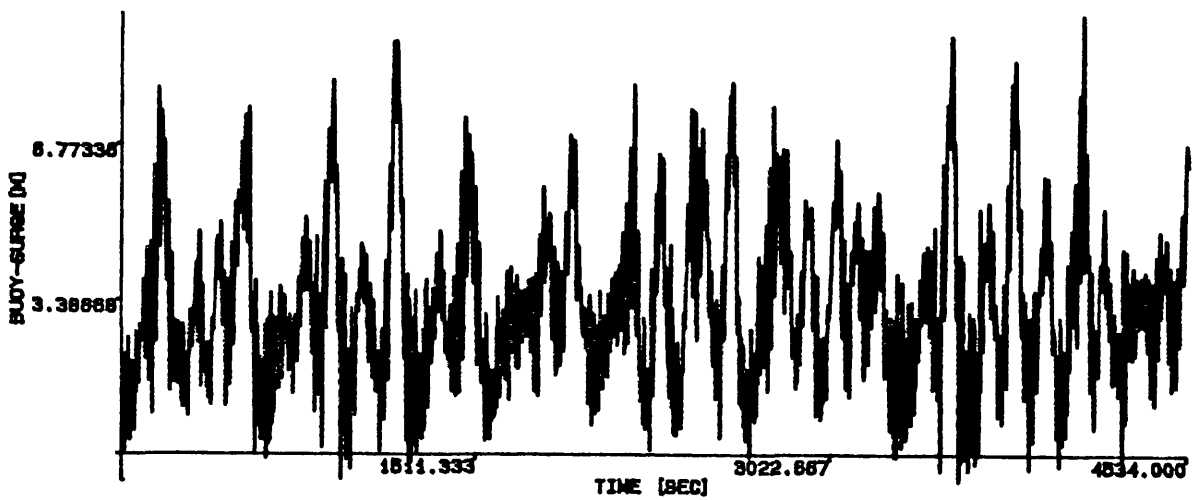
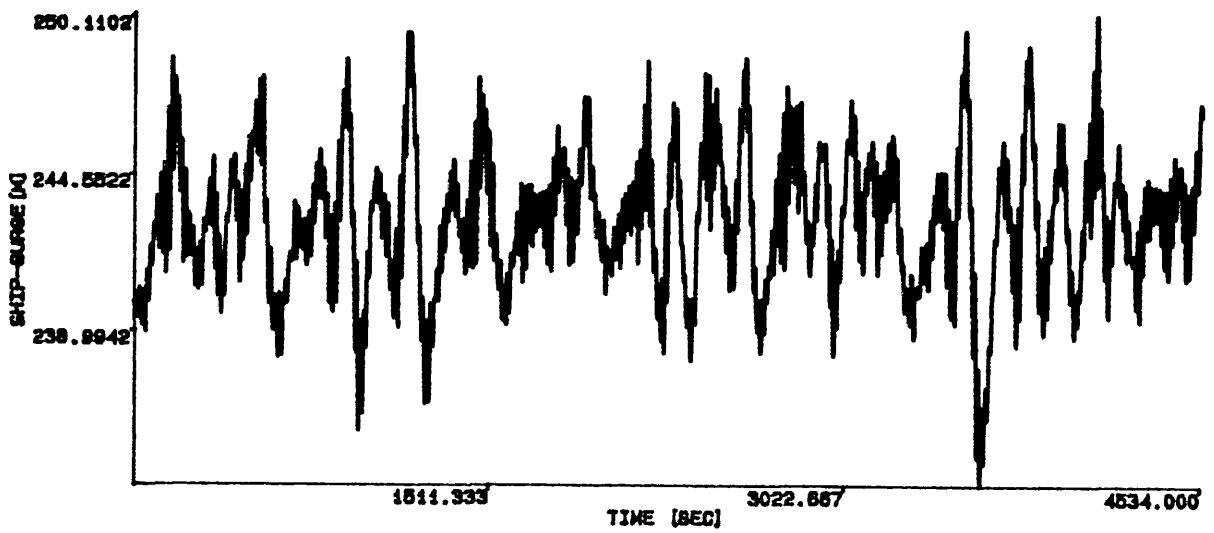


Fig. 4.19 Motion Response and Hawser Tension Predictions
 Mean Wind Speed=22 m/sec, Current Speed=1.5 m/sec
 Significant Wave Height=10 m, OchiShin Wind Spectrum
 Co-linear Environmental Forces

CHAPTER 5

PARAMETRIC STUDIES

5.1 INTRODUCTION

In this chapter the results of a series of parametric studies are presented to illustrate the effects of environmental and geometrical characteristics on the dynamic response and mooring forces of the tanker-buoy system. The parametric studies were carried out considering the tanker-buoy system described in Fig. 4.9. During the parametric studies wave, wind and current angle of attacks, wind and current speed, elasticity of the mooring lines and the hawser line, buoy's geometry, sea state, wind spectrum, the number of mooring lines of the buoy, the hawser length and thruster capacity were varied to study the effect of variations on dynamic response and mooring forces of the system. Numerical aspects of the program, such as; simulation time and integration step are discussed.

5.2 PARAMETRIC STUDIES AND DISCUSSION OF RESULTS

Two sets of parametric studies were carried out. First one investigated the effects of different wave, wind and current force magnitudes and directions on the steady and oscillatory motions and mooring forces of the tanker-buoy system. A second parametric study determined the sensitivity of slowly varying motions and hawser forces to changes in wave and wind spectrums, number of the mooring lines of the buoy, hawser length and thruster capacity. The first parametric study was carried out in regular waves with steady wind and current present while the second one in irregular waves with dynamic wind and current present.

In the first set of parametric studies, six groups of simulation studies were carried out using the non-linear time domain simulation computer program based on the prediction method described in the previous chapters. At the beginning of each simulation the tanker was placed along the x axis with zero yaw angle and the hawser was unstretched. Results of the parametric study are tabulated by using the steady and oscillatory motion responses of the buoy and the tanker, which were obtained through a F.F.T analysis of the time domain simulations. During the first three groups of studies the effects of directionality of wave, wind and current force were investigated and the results of these simulations are given in Tables 5.1-5.3. During the remaining three sets of simulations the effects of variations in wave, wind and current force magnitudes were investigated and the results of these studies are given in Tables 5.4-5.6. The results given in Table 5.1 indicate that maximum steady and oscillatory sway and yaw motions occur when wave and current forces make a 90 degree angle with the wind forces. Similarly maximum sway motions of the buoy occur when wave and current forces make a 90 degree angle with the wind forces. The results given in Table 5.2 indicate that wind direction does not affect the motions significantly. It could be concluded from Table 5.3 that mean sway displacement and yaw angle increase as the current direction changes from 0 to 90 degrees. However maximum oscillatory sway motion of the buoy occurs when wave force direction makes a 0 degree and wind and current directions make a 45 degree angle with the horizontal axis. Maximum steady and oscillatory surge motions of the buoy and ship occur when wave, wind and current forces act co-linearly. Tables 5.4 and 5.5 show that the mean mooring line forces are generally not very sensitive to the changes in current and wind loading since the dominant load on the system is due to wave induced oscillatory and steady forces. Table 5.6 shows that there is no linear relationship between the wave height and the motion response or the mooring force values of the CALM system. This indicates that such systems must be analysed in the time domain using nonlinear analysis tools.

A Second set of parametric studies was carried out to determine the sensitivity of slowly varying motions and hawser forces to changes in the environment, the number of mooring lines of the buoy, hawser length and thruster capacity for the CALM system

illustrated in Fig. 5.1. In the simulations the tanker was given an initial 7.5 deg yaw angle with respect to the current angle, and bow hawser was unstretched and was parallel to the current. During these simulations first order wave forces were neglected.

During the simulations of the tanker-buoy system, the following parameters were varied:

1. Sea state; Pierson Moskowitz spectrum with different wind speeds
2. Wind spectrum formulation; Ochi-Shin, Davenport and Harris.
3. Number of mooring legs of the buoy; 8 and 4 legs.
4. Hawser length: 80 m and 40 m.
5. Thruster capacity (250, 500 and 750 kN)
6. Displaced volume of the buoy (785 and 3534 m³)

Fig. 5.2, 5.3 and 5.4 show the simulations for different sea states with Pierson-Moskowitz spectrum and with mean wind speeds of 10.3, 20.6 and 25.75 m/sec respectively. It can be concluded from the comparison of simulations that an increase in wind speed results in an increase in mean displacements of the system and the mean tension of the hawser. The same trend can also be observed for oscillatory yaw motion of the tanker and sway motion of the buoy. Simulation 1, which is the lowest sea state chosen, gives the biggest motion response values for surge motion of the buoy and sway motion of the tanker. A summary of the results is given in Table 5.7. Frequencies at which the buoy and the tanker oscillate in simulation 1, found through a spectral analysis, are 0.013, 0.025, 0.038 and 0.05 rad/sec. Among these frequencies 0.013 is the dominant frequency for all motions except for the surge motion of the buoy and the tanker whose dominant frequency are 0.025 rad/sec. Dominant frequency for hawser tension oscillations is also 0.025 rad/sec. Dominant frequencies change slightly with increasing wind speed: 0.014 and 0.029 rad/sec for simulation 2 and 0.016 and 0.031 rad/sec for simulation 3.

Simulations with the Ochi-Shin, Davenport and Harris wind spectrums are compared in Figures 5.5, 5.6 and 5.7. Mean wind speed during the simulations was 22

m/sec. Simulation with the Davenport spectrum gives the largest motion response values (0.1-4% higher than the others). Results are summarised at Table 5.8.

Effect of mooring legs on the motion response and hawser tension values is shown in Figures 5.5 and 5.8 and at Table 5.9. As the number of mooring legs is reduced from 8 to 4, dominant (natural) frequencies of the system shift towards lower frequencies taking the values 0.014, 0.028, 0.041 and 0.057 rad/sec compared with the frequencies of 0.015, 0.029, 0.044 and 0.059 rad/sec of the 8 legged system. There is also an increase of 40-145% in the mean and oscillatory motion response values of the tanker and the buoy. This increase in the motions increases the hawser tension by 25%. This is because with fewer mooring legs, the system becomes less stiff, the bow hawser stays slack for a longer time and the sudden acceleration of the buoy and/or the tanker creates larger tensions in the hawser.

A change in hawser length not only changes the motion response values but also the natural frequencies of the system. As it is seen from Figures 5.5 and 5.9 and Table 5.10 that as the hawser length reduces from 80 m to 40 m, 0.019 rad/sec becomes the dominant frequency for sway and yaw motions of the tanker and sway motion of the buoy, 0.038 rad/sec for the surge motion of the buoy and the tanker and the hawser tension. Another conclusion which could be drawn from the simulation is that the motions of the tanker and the buoy are more stable and hawser loads decrease by 6% as the hawser length is reduced (Fig. 5.9).

Slackening of the hawser which is the reason for peak loads is avoided by the use of thrusters. Tanker and buoy motions also become more stable (Fig. 5.5, 5.10, 5.11 and 5.12). But with the use of thrusters the hawser remains stretched with a high mean tension during the simulation, which may not be desirable and the use of thrusters could be expensive. Results are tabulated in Table 5.11.

An increase in displaced volume of the buoy results in more stable motions of tanker and buoy (Figs. 5.5 and 5.13, Table 5.2). This effect is quite similiar to the effect of thrusters.

5.3 NUMERICAL ASPECTS

In order to obtain enough cycles of motion for analysis and to avoid the statistical variance of the results [5.1], simulation time was chosen to be sufficiently long, 7000 seconds. Time step used for the integration of the differential equations was 0.05 seconds, maximum time step which could be used by the algorithm [5.2] for stable solutions was 0.2 seconds and minimum time step was 1.E-07 seconds. Tolerance was chosen to be 10E-03. For higher tolerances the algorithm requires much smaller time steps.

Analysis of the simulations was carried out using Fast Fourier Transformations [5.3]. Results of the F.F.T. analysis ,frequencies and corresponding amplitudes, were tabulated.

Table: 5.1 Effect of Wave Direction

Wave Heading (Deg.)	BUOY MOTIONS			SHIP MOTIONS			MOTIONS			MOORING FORCE (kN)		
	SURGE (M)		SWAY (M)	SURGE (M)		SWAY (M)	YAW(DEG)		MAXIMUM TENSION	MEAN TENSION		
	OSCILL	MEAN	OSCILL	MEAN	OSCILL	MEAN	OSCILL	MEAN				
0	1.02	5.13	0.53	1.89	0.031	331.80	0.007	73.06	0.003	16.70	4979	2585
15	0.98	5.23	0.58	3.08	0.040	312.50	0.012	128.70	0.007	25.10	7003	2802
30	0.95	5.30	0.62	5.09	0.026	283.00	0.027	185.30	0.055	29.72	2660	2617
45	0.97	5.25	0.97	6.75	0.020	254.17	0.029	224.50	0.085	33.85	8009	3874
60	0.99	5.12	0.82	8.75	0.130	219.60	0.028	259.57	0.084	43.50	2652	2518
75	1.24	4.93	0.91	11.04	0.050	183.40	0.124	288.90	0.112	52.33	14130	5571
90	1.39	4.59	1.00	13.25	0.015	146.20	0.265	311.10	0.132	62.30	18838	6522

Wave Height= 8 m, Wave Frequency=0.8 rad/sec, Current Velocity=1.5 m/sec, Wind Velocity=22 m/sec
 Wind direction=0 deg, Current direction=90 deg

Table: 5.2 Effect of Wind Direction

Wind Heading (Deg.)	BUOY MOTIONS			SHIP MOTIONS			MOTIONS			MOORING FORCE (kN)		
	SURGE (M)		SWAY (M)	SURGE (M)		SWAY (M)	YAW(DEG)		MAXIMUM TENSION	MEAN TENSION		
	OSCILL	MEAN	OSCILL	MEAN	OSCILL	MEAN	OSCILL	MEAN				
0	0.12	5.80	1.89	2.41	0.030	323.90	0.022	63.89	0.019	2.24	6851	2838
15	1.08	5.85	2.01	2.98	0.029	320.80	0.023	78.77	0.025	1.76	6139	2947
30	1.17	5.86	2.06	3.42	0.028	317.10	0.023	91.35	0.027	2.31	8253	3039
45	1.17	5.85	2.07	3.74	0.028	314.60	0.025	104.20	0.024	3.91	9504	3099
60	1.07	5.79	2.00	3.59	0.028	315.60	0.025	105.50	0.017	5.59	12240	3036
75	0.95	5.72	1.91	3.35	0.028	317.30	0.023	104.10	0.013	7.07	9676	2953
90	0.79	5.61	1.74	2.74	0.028	322.00	0.022	91.82	0.017	8.36	7400	2783

Wave Height= 8 m, Wave Frequency=0.8 rad/sec, Current Velocity=1.5 m/sec, Wind Velocity=22 m/sec
 Wave direction=0 deg, Current direction=45 deg

Table: 5.3 Effect of Current Direction

Current Heading (Deg.)	BUOY MOTIONS			SHIP MOTIONS			MOORING FORCE (kN)					
	SURGE (M)		SWAY (M)	SURGE (M)		SWAY (M)	MAXIMUM TENSION		MEAN TENSION			
	OSCILL.	MEAN	OSCILL.	MEAN	OSCILL.	MEAN	OSCILL.	MEAN	OSCILL.			
0	0.70	6.49	0.00	0.00	0.038	342.80	0.000	0.00	0.000	0.00	5885	2674
15	0.89	5.83	1.18	0.81	0.022	290.10	0.020	21.69	0.036	2.06	5888	2990
30	1.24	5.91	2.02	1.96	0.030	313.70	0.004	45.98	0.059	1.10	5714	2857
45	0.12	5.80	1.89	2.41	0.030	323.90	0.022	63.89	0.019	2.24	6851	2838
60	0.81	5.52	1.54	2.51	0.026	325.53	0.021	73.11	0.030	7.49	9023	2786
75	0.83	5.26	1.03	2.19	0.028	327.90	0.018	69.73	0.012	12.08	8466	2681
90	1.02	5.13	0.53	1.89	0.031	331.80	0.007	73.06	0.003	16.70	4979	2585

Wave Height= 8 m, Wave Frequency=0.8 rad/sec, Current Velocity=1.5 m/sec, Wind Velocity=22 m/sec
 Wave direction=0 deg, Wind direction=0 deg

Table: 5.4 Effect of Current Velocity

Current Velocity (m/sec)	BUOY MOTIONS			SHIP MOTIONS			MOORING FORCE (kN)					
	SURGE (M)		SWAY (M)	SURGE (M)		SWAY (M)	MAXIMUM TENSION		MEAN TENSION			
	OSCILL.	MEAN	OSCILL.	MEAN	OSCILL.	MEAN	OSCILL.	MEAN	OSCILL.			
0.5	0.93	5.56	0.48	0.92	0.029	334.97	0.004	33.49	0.004	8.24	6299	2540
1.0	0.72	5.55	1.00	1.31	0.026	332.25	0.016	51.09	0.010	10.00	6748	2559
1.5	0.79	5.58	1.74	2.52	0.028	322.03	0.022	84.80	0.017	8.60	8615	2744
2.0	1.54	5.68	2.16	4.68	0.025	300.10	0.024	138.40	0.040	8.98	6169	3296

Wave Height= 8 m, Wave Frequency=0.8 rad/sec, Wind Velocity=22 m/sec
 Wave direction=0 deg, Wind direction=90 deg, Current direction=45 deg

Table: 5.5 Effect of Wind Velocity

Wind Velocity (m/sec)	BUOY MOTIONS				SHIP MOTIONS				MOORING FORCE (KN)	
	SURGE (M)		SWAY (M)		SURGE (M)		SWAY (M)		MAXIMUM TENSION	MEAN TENSION
	OSCILL	MEAN	OSCILL	MEAN	OSCILL	MEAN	OSCILL	MEAN		
10	0.79	5.56	1.73	2.37	0.029	323.50	0.0198	69.70	8144	2723
20	0.80	5.59	1.74	2.60	0.029	322.90	0.022	86.30	8002	2757
30	0.84	5.57	1.77	2.40	0.028	324.20	0.023	75.60	8409	2722
40	1.00	5.61	1.87	2.83	0.025	320.90	0.031	100.00	7337	2796
Wave Height= 8 m, Wave Frequency=0.8 rad/sec, Current Velocity=1.5 m/sec										
Wave direction=0 deg, Wind direction=90 deg, Current direction=45 deg										

Table: 5.6 Effect of Wave Height

Wave Height (m)	BUOY MOTIONS				SHIP MOTIONS				MOORING FORCE (KN)	
	SURGE (M)		SWAY (M)		SURGE (M)		SWAY (M)		MAXIMUM TENSION	MEAN TENSION
	OSCILL	MEAN	OSCILL	MEAN	OSCILL	MEAN	OSCILL	MEAN		
6	0.866	3.440	1.472	3.010	0.020	293.700	0.014	144.700	4097	1894
8	0.790	5.580	1.740	2.520	0.028	322.100	0.022	84.800	8615	2744
10	0.801	8.410	1.681	2.880	0.037	331.500	0.022	66.200	16164	4157
12	1.000	11.810	1.520	2.430	0.044	340.200	0.021	43.900	13542	5788
Wave Frequency=0.8 rad/sec Current Velocity=1.5 m/sec, Wind Velocity=22 m/sec										
Wave direction=0 deg, Wind direction=90 deg, Current direction=45 deg										

Table: 5.7 Effect of Sea State

FREQ. (rad/sec)	BUOY MOTIONS			SHIP MOTIONS			FORCE (KN)			
	SURGE (M)		SWAY (M)	SURGE (M)		SWAY (M)	YAW(DEG)		OSCILL. TENSION	MEAN TENSION
	OSCILL.	MEAN	OSCILL.	MEAN	OSCILL.	MEAN	OSCILL.	MEAN	OSCILL. TENSION	MEAN TENSION
1	0.013	0.72	5.40		9.670		13.300		58	
	0.025	4.85	0.40	0.01	0.140	0.43	0.340	0.07	479	450
	0.038	0.28	2.04		0.490		0.840		34	
	0.05	0.46	0.17						79	
	0.014	2.90	6.33		9.080		13.600		247	
2	0.017		1.42		1.720		2.690			
	0.029	4.28	1.32	0.22	0.420	7.24	0.900	0.44	471	619
	0.031								146	
	0.043	0.36	1.89		0.370		0.630		100	
	0.057	0.25	0.39		0.057		0.089		56	
3	0.016	3.68	7.45		9.360		14.590		343	
	0.02	0.73	0.83						77	
	0.024			0.27		7.80		0.47		746
	0.031	4.45	1.74		0.500		1.070		538	
	0.047	0.69	1.95		0.330		0.570		113	
0.063	0.19	0.43						57		

Current Velocity=1.5 m/sec
 Ochi-Shin Wind Spectrum, Plerson Moskowitz Wave Spectrum
 Simulation1:Mean Wind Speed=10.3 m/s, Simulation2:Mean Wind Speed=20.6 m/s, Simulation3:Mean Wind Speed=25.75 m/s

Table: 5.8 Effect of Wind Spectrum

FREQ (rad/sec)	BUOY MOTIONS				SHIP MOTIONS				FORCE (KN)					
	SURGE (M)		SWAY (M)		SURGE (M)		SWAY (M)		YAW(DEG)		OSCILL TENSION		MEAN TENSION	
	OSCILL	MEAN	OSCILL	MEAN	OSCILL	MEAN	OSCILL	MEAN	OSCILL	MEAN	OSCILL TENSION	MEAN TENSION	OSCILL TENSION	MEAN TENSION
1	0.015	3.30	6.78		8.030		9.390		14.210		284		284	
	0.029	4.54	1.57	0.25	3.300	258.14	0.490	7.41	1.050	0.50	510	651	510	651
	0.044	0.71	1.88		0.280		0.350		0.600		108		108	
	0.059		0.40		0.044		0.060				57		57	
2	0.015	3.46	6.82		8.320		9.430		14.290		297		297	
	0.029	4.65	1.69	0.25	3.410	258.15	0.520	7.61	1.120	0.50	520	652	520	652
	0.044	0.77	1.89		0.320		0.360		0.620		118		118	
	0.059	0.23	0.46		0.059		0.070		0.100		58		58	
3	0.015	3.36	6.81		8.140				14.260		288		288	
	0.029	4.60	1.61	0.25	3.350	258.17	0.500	7.48	1.070	0.50	516	652	516	652
	0.044	0.73	1.93		0.290		0.360		0.620		111		111	
	0.059	0.23	0.42		0.045		0.064		0.094		59		59	

Mean Wind Speed=22 m/sec, Current Velocity=1.5 m/sec

Jonswap Wave Spectrum: Significant Wave Height=8 m, Zero Crossing Period=12 sec

Simulation 1: Ochi Shin Spectrum, Simulation 2 : Davenport Spectrum, Simulation 3 : Harris Spectrum

Table: 5.9 Effect of Mooring Legs

FREQ. (rad/sec)	BUOY MOTIONS						SHIP MOTIONS						FORCE (KN)	
	SURGE (M)		SWAY (M)		SURGE (M)		SWAY (M)		YAW(DEG)		OSCILL TENSION	MEAN TENSION		
	OSCILL	MEAN	OSCILL	MEAN	OSCILL	MEAN	OSCILL	MEAN	OSCILL	MEAN				
1	3.30	15.85	6.78	0.25	8.030	258.14	9.390	7.41	14.210	0.50	284	651		
	4.54		1.57		3.300		0.490		1.050		510			
	0.71		1.88		0.280		0.350		0.600		108			
			0.40		0.044		0.060				57			
2	1.54	24.40	16.63	0.09	3.160	264.01	14.850	2.96	19.480	0.05	114	659		
	6.40		1.52		4.470		0.260		0.560		640			
	0.41		5.02		0.210		0.560		0.910		66			
	0.48		0.49		0.110						102			

Ochi-Shin Wind Spectrum, Mean Wind Speed=22 m/sec, Current Velocity=1.5 m/sec
 Jonswap Wave Spectrum: Significant Wave Height=8 m, Zero Crossing Period=12 sec
 Simulation 1: 8 Legged CALM System, Simulation 2 : 4 Legged CALM System

Table: 5.10 Effect of Hawser Length

FREQ (rad/sec)	BUOY MOTIONS				SHIP MOTIONS				FORCE (KN)					
	SURGE (M)		SWAY (M)		SURGE (M)		SWAY (M)		YAW(DEG)		OSCILL TENSION		MEAN TENSION	
	OSCILL	MEAN	OSCILL	MEAN	OSCILL	MEAN	OSCILL	MEAN	OSCILL	MEAN	OSCILL	TENSION	OSCILL	TENSION
1	0.015	3.30	6.78		8.030		9.390		14.210		284			
	0.029	4.54	1.57	0.25	3.300	258.14	0.490	7.41	1.050	0.50	510			651
	0.044	0.71	1.88		0.280		0.350		0.600		108			
	0.059		0.40		0.044		0.060				57			
	0.012	0.12									44			
2	0.017	0.36			0.880						30			
	0.019		8.71				5.650		12.080					
	0.024			0.01		219.34		0.01		0.02	23			691
	0.031		0.29						0.910					
	0.038	3.56			1.590						482			
	0.05	0.10	0.22											
	0.057	0.16	2.04				0.240		0.410					

Ochi-Shin Wind Spectrum, Mean Wind Speed=22 m/sec, Current Velocity=1.5 m/sec
 Jonswap Wave Spectrum: Significant Wave Height=8 m, Zero Crossing Period=12 sec
 Simulation 1: 80 m Hawser Length, Simulation 2 : 40 m Hawser Length

Table: 5.11 Effect of Thrusters

FREQ (rad/sec)	BUOY MOTIONS			SHIP MOTIONS			YAW(DEG)			FORCE (KN)			
	SURGE (M)		SWAY (M)	SURGE (M)		SWAY (M)	OSCILL		MEAN		OSCILL TENSION		MEAN TENSION
	OSCILL	MEAN	OSCILL	MEAN	OSCILL	MEAN	OSCILL	MEAN	OSCILL	MEAN	OSCILL	MEAN	TENSION
1	0.015	3.30	6.78	0.25	8.030	9.390	14.210	0.50	284	651			
	0.029	4.54	15.85	0.25	3.300	0.490	1.050	0.50	510				
	0.044	0.71	1.88	0.25	0.280	0.350	0.600		108				
	0.059		0.40	0.25	0.044	0.060			57				
	0.0068			0.25		1.020	0.300						
2	0.017	1.12	7.19	0.10	2.310	6.310	12.050	0.16	103	900			
	0.024		18.80	0.10	0.640	0.090	0.180	0.16	39				
	0.035	3.24	0.31	0.10	1.930	0.21	0.33		416				
	0.051		1.3	0.10									
	0.069			0.10					36.13				
3	0.0068		0.10	0.07			0.007			1143			
	0.012	0.37		0.07					38.24				
	0.019	0.75	21.57	0.07	1.690	4.750	10.170	0.09	78				
	0.024			0.07					58				
	0.037	2.29	0.17	0.07	1.230	0.049	0.096		328				
4	0.057		0.76	0.04		0.13	0.18			1388			
	0.0042			0.04			0.230						
	0.012	0.31		0.04					34.9				
	0.02		24.04	0.04	1.290	3.530	8.050	0.03	96				
	0.024	0.80	0.10	0.04	0.160								
0.032			0.04										
0.041	1.37	0.17	0.04	0.71			0.074	218.5					

Ochi-Shin Wind Spectrum, Mean Wind Speed=22 m/sec, Current Velocity=1.5 m/sec
 Jonswap Wave Spectrum: Significant Wave Height=8 m, Zero Crossing Period=12 sec
 Simulation1:No Thruster, Simulation2: 250 kN Propulsion, Simulation3: 500 kN Propulsion, Simulation4: 750 kN Propulsion

Table: 5.12 Effect of Buoy Geometry

FREQ. (rad/sec)	BUOY MOTIONS			SHIP MOTIONS			FORCE (KN)			
	SURGE (M)		SWAY (M)	SURGE (M)		SWAY (M)	YAW(DEG)		OSCILL TENSION	MEAN TENSION
	OSCILL	MEAN	OSCILL	MEAN	OSCILL	MEAN	OSCILL	MEAN	OSCILL TENSION	MEAN TENSION
1	0.015	3.30	6.78	8.030	9.390	14.210	284	651	284	651
	0.029	4.54	15.85	3.300	0.490	1.050	510		510	
	0.044	0.71	1.88	0.280	0.350	0.600	108		108	
	0.059		0.40	0.044	0.060		57		57	
	0.009		0.41			1.370				
2	0.014		3.55		5.940	8.340		633		633
	0.016	0.51	0.50	1.630						
	0.02	0.92		2.020			129		129	
	0.024		28.67	0.02		0.170				
	0.028	2.10		2.510		0.210	326		326	
	0.042	0.12	1.02	0.110	0.200	0.340				
	0.045	0.13		0.120			29		29	
	0.057	0.1	0.12				31		31	

Ochi-Shin Wind Spectrum, Mean Wind Speed=22 m/sec, Current Velocity=1.5 m/sec

Jonswap Wave Spectrum: Significant Wave Height=8 m, Zero Crossing Period=12 sec

Simulation 1 : Displacement of Buoy = 785 m³, Simulation 2 : Displacement of Buoy = 2650 m³

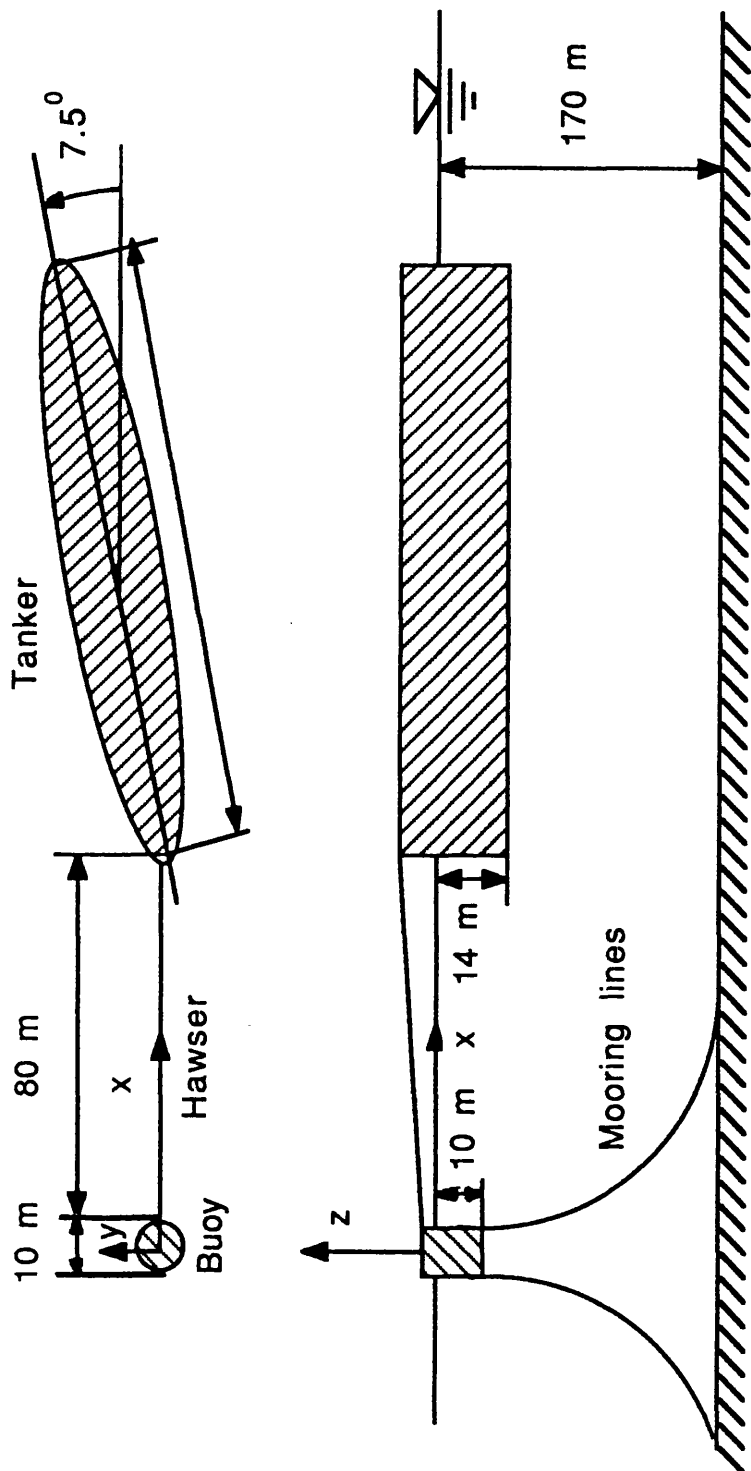


Fig. 5.1 Coupled buoy-ship system

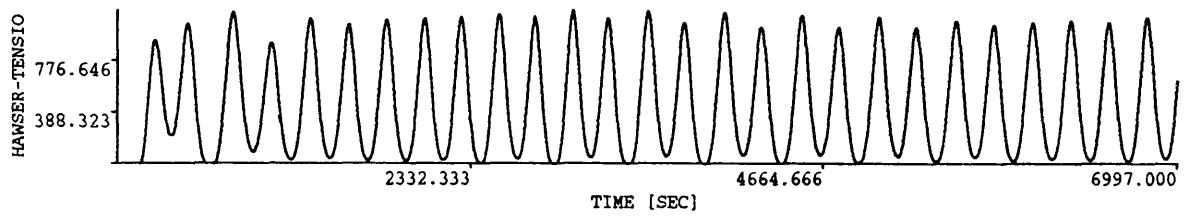
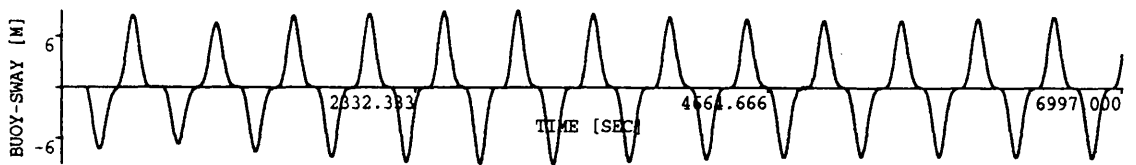
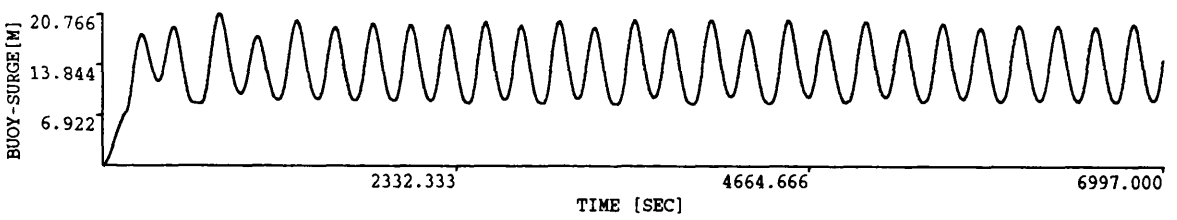
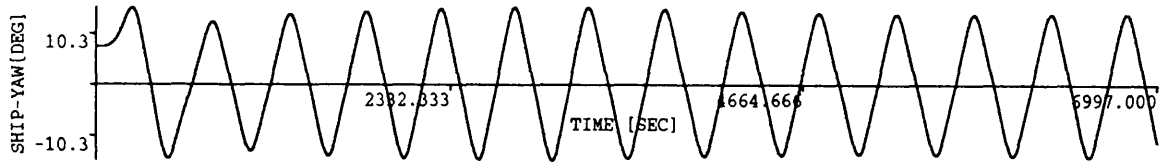
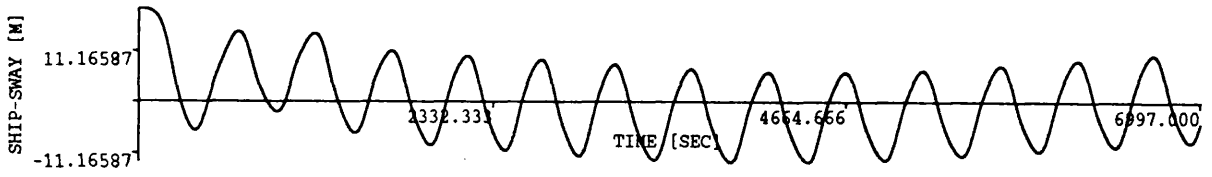
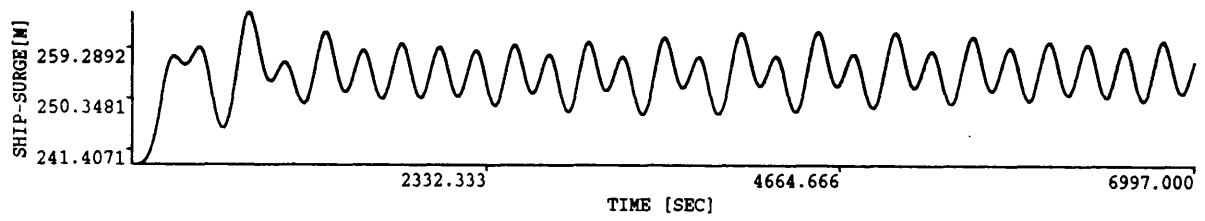


Fig. 5.2 Time Domain Simulation of the Tanker-Buoy System
Pierson Moskowitz Wave Spectrum
Mean Wind Speed=10.3 m/sec

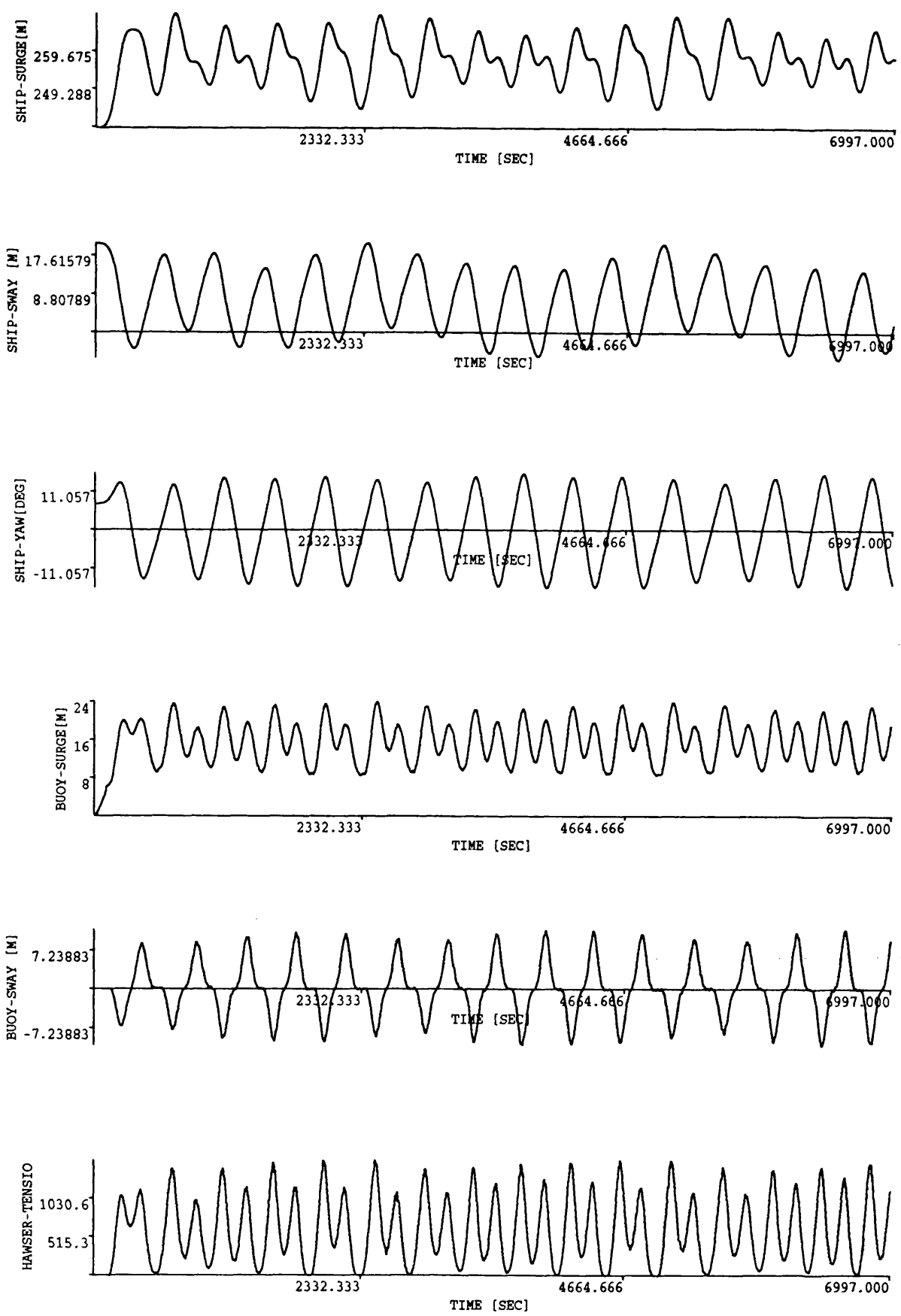


Fig. 5.3 Time Domain Simulation of the Tanker-Buoy System
Pierson Moskowitz Wave Spectrum
Mean Wind Speed=20.6 m/sec

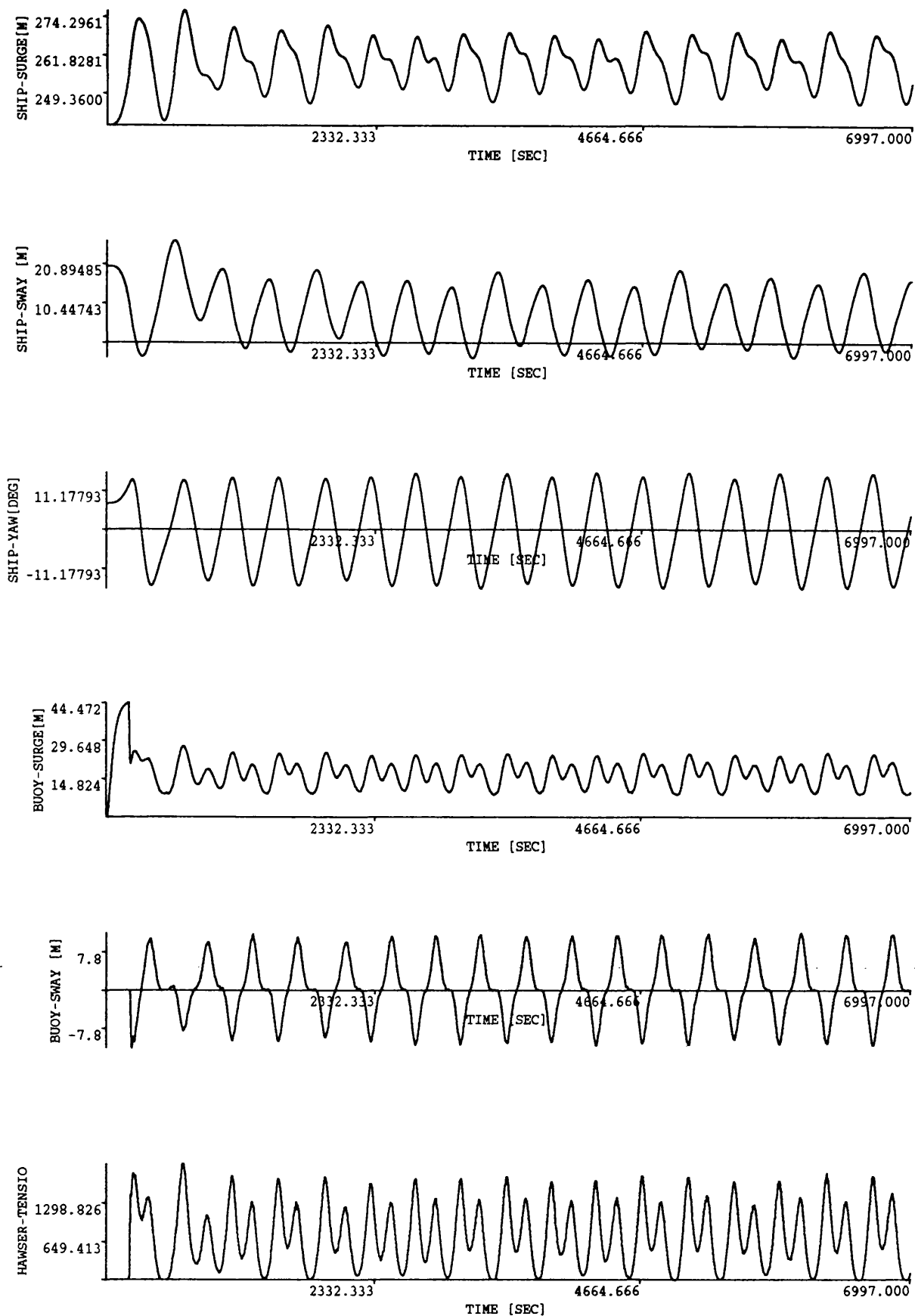
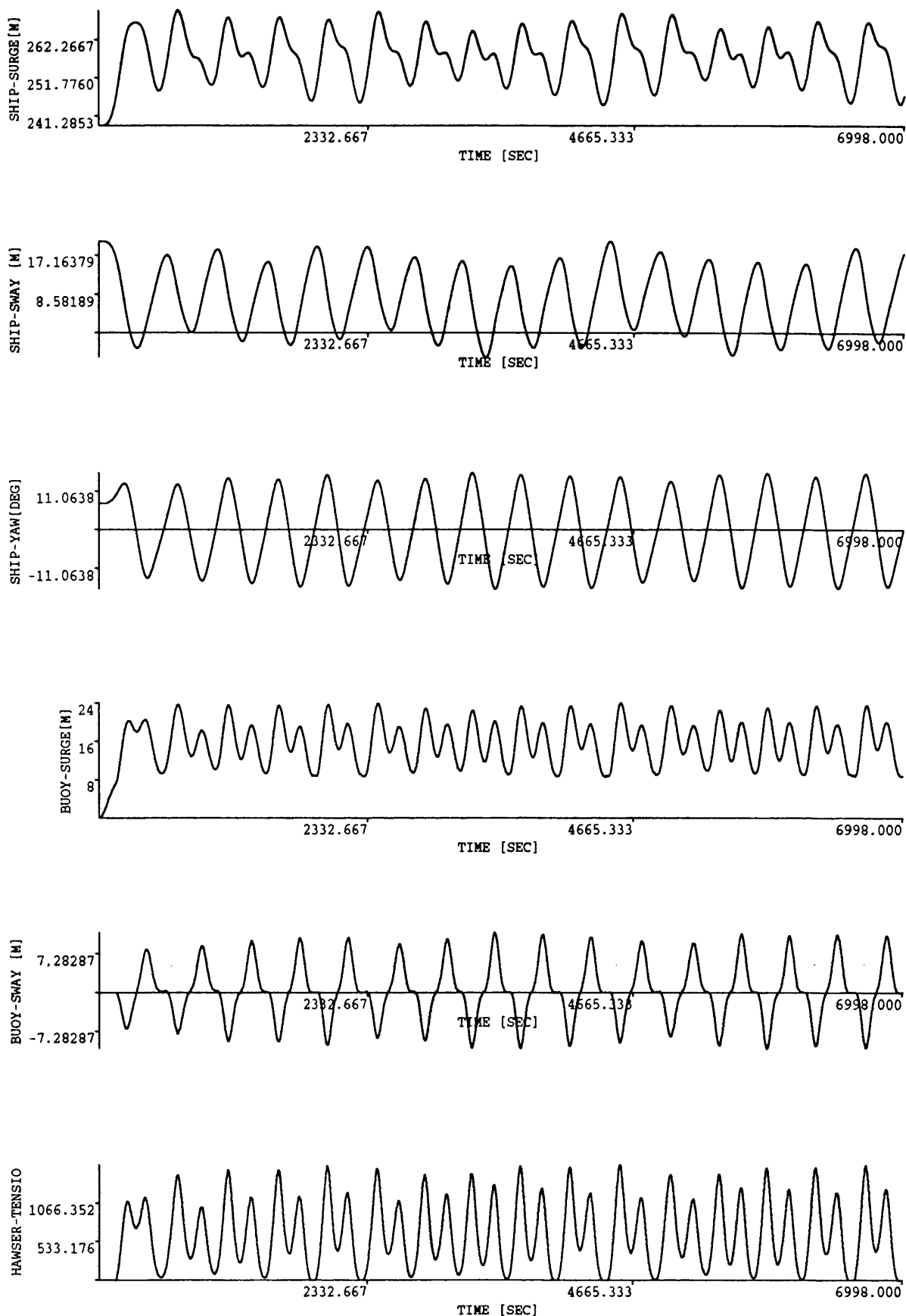
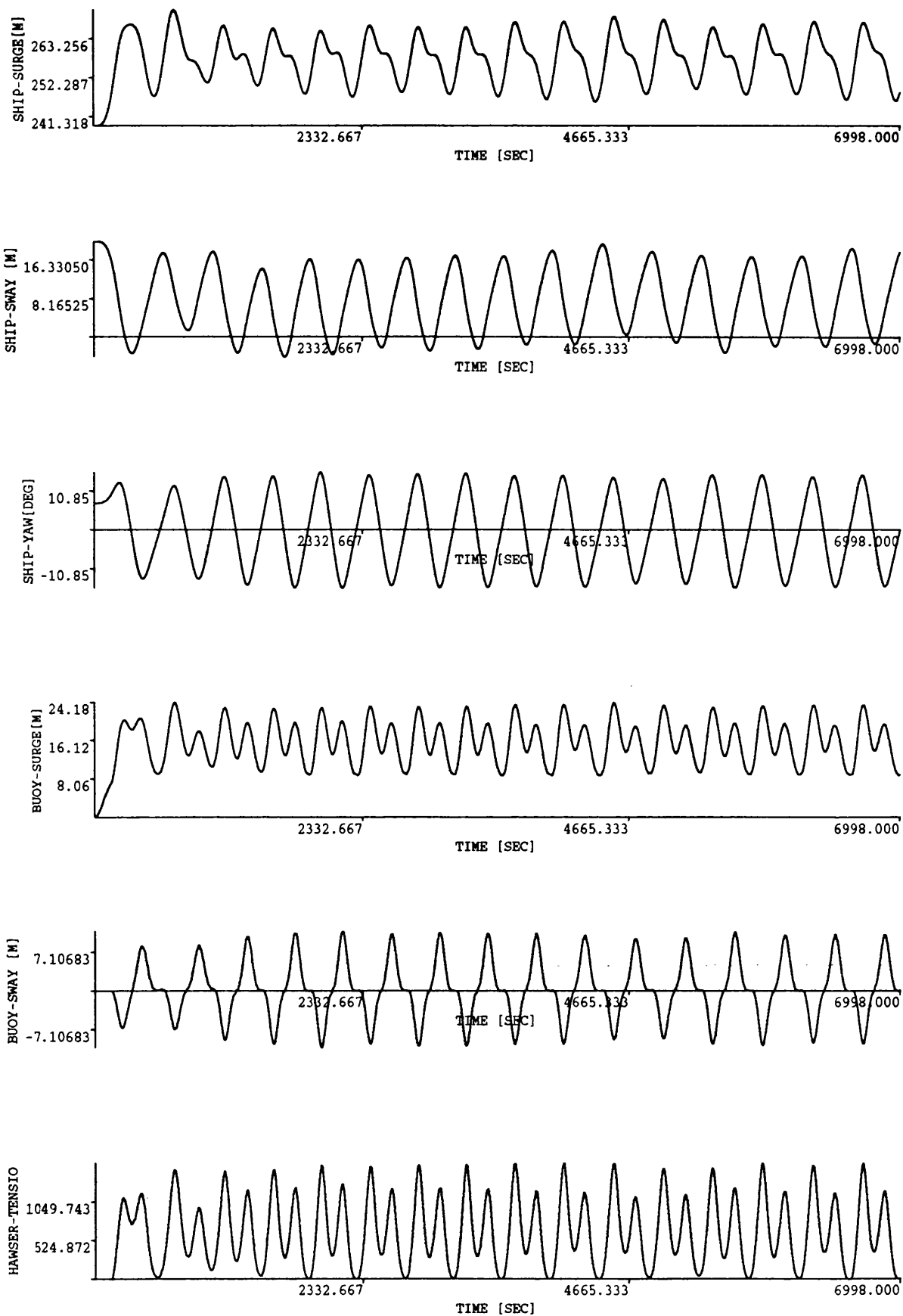


Fig. 5.4 Time Domain Simulation of the Tanker-Buoy System
Pierson Moskowitz Wave Spectrum
Mean Wind Speed=25.8 m/sec



**Fig. 5.5 Time Domain Simulation of the Tanker-Buoy System
Ochi-Shin Wind Spectrum, Mean Wind Speed=22 m/sec**



**Fig. 5.6 Time Domain Simulation of the Tanker-Buoy System
Davenport Wind Spectrum, Mean Wind Speed=22 m/sec**

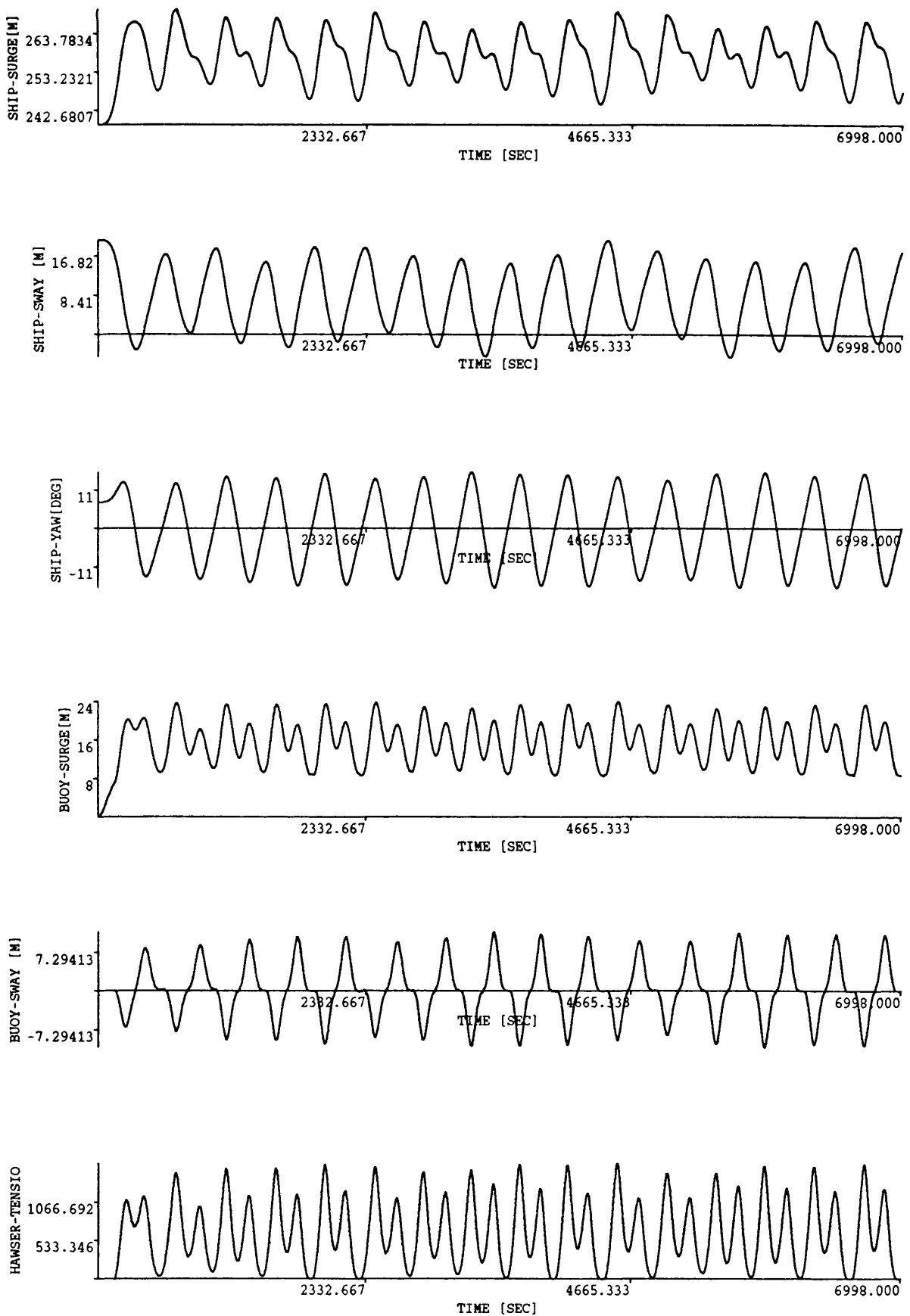


**Fig. 5.7 Time Domain Simulation of the Tanker-Buoy System
Harris Wind Spectrum, Mean Wind Speed=22 m/sec**

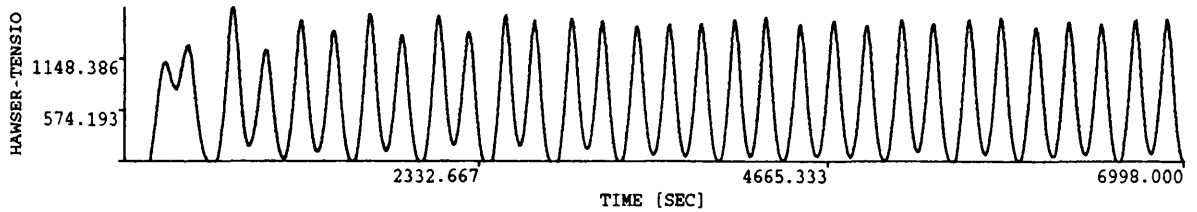
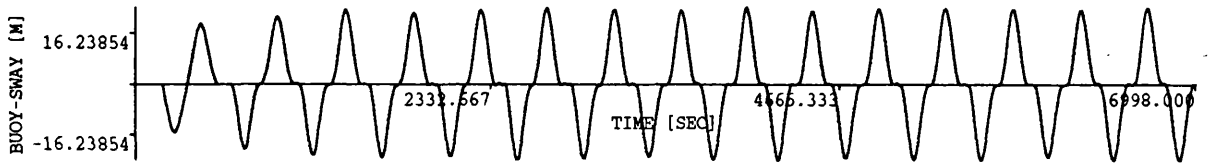
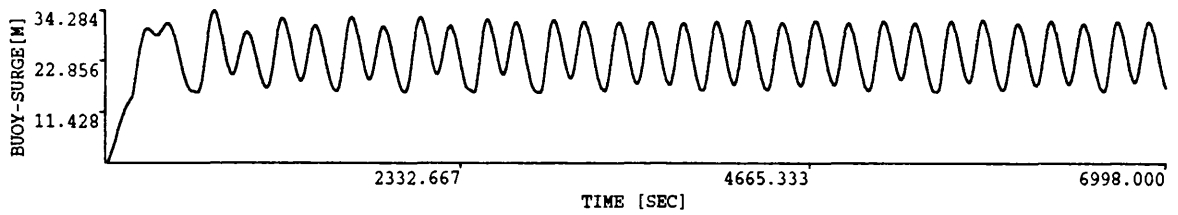
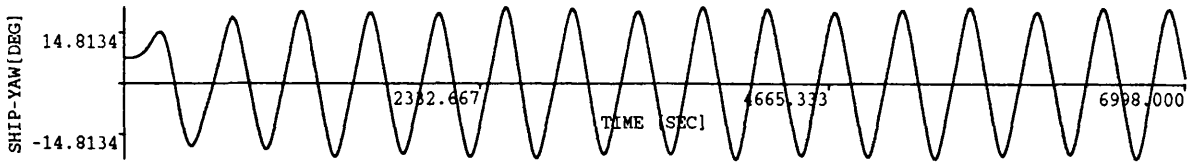
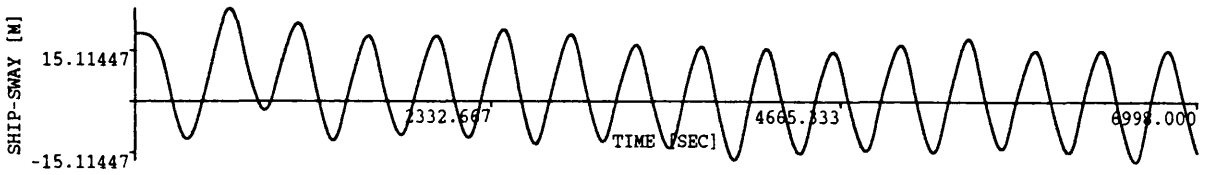
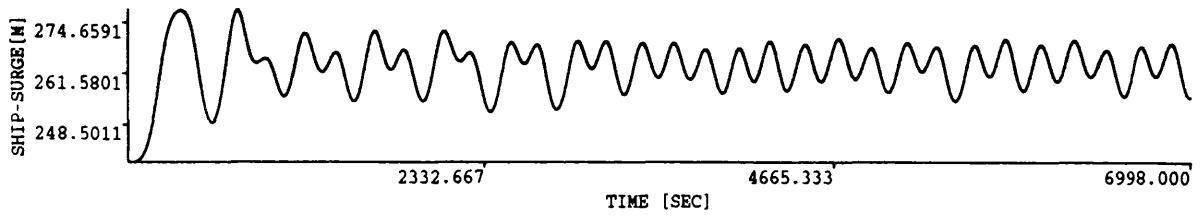


**Fig. 5.8 Time Domain Simulation of the Tanker-Buoy System
4 Legged CALM System**

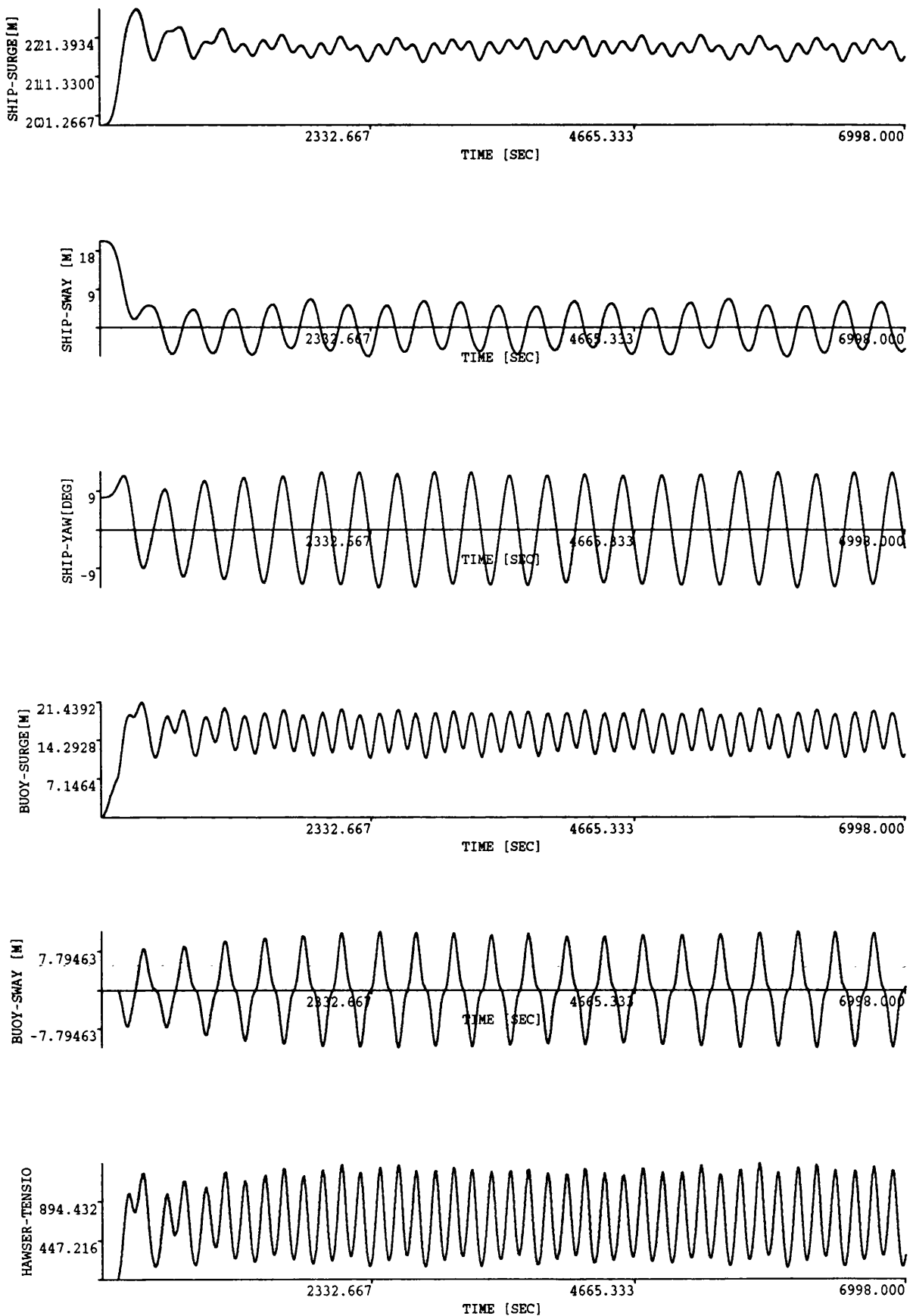


Fig. 5.9 Time Domain Simulation of the Tanker-Buoy System
Hawser Length=40 m

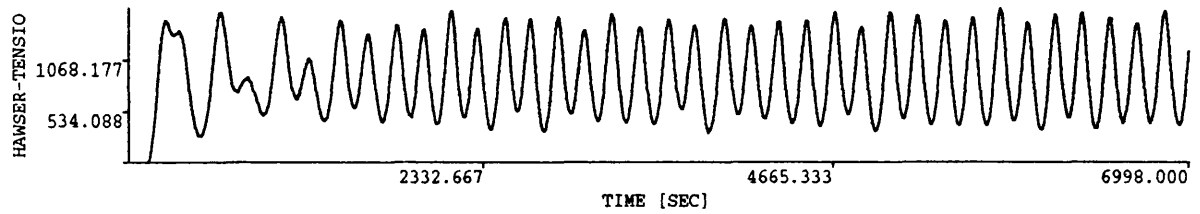
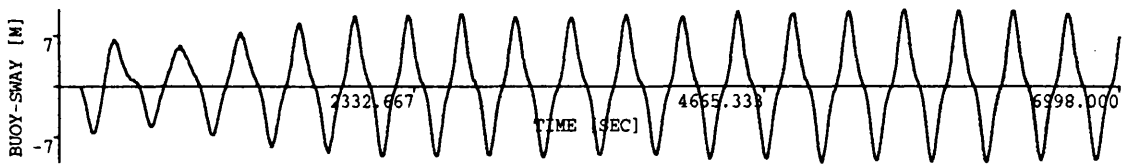
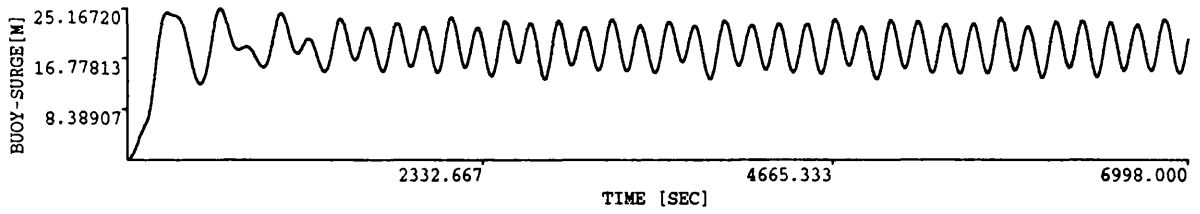
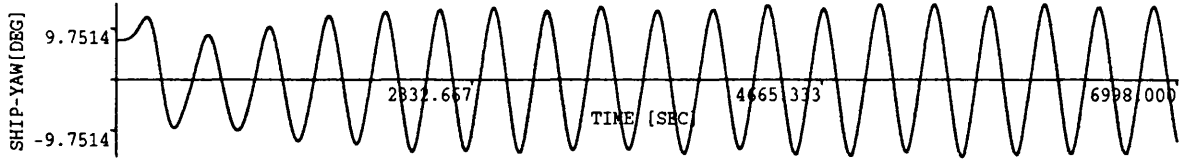
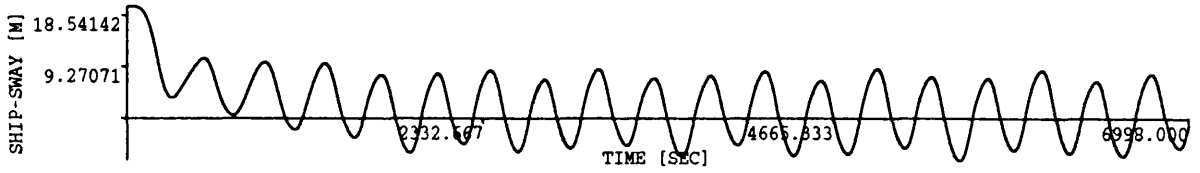
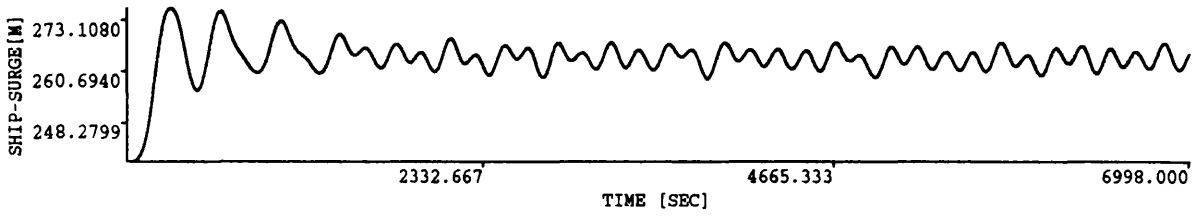


Fig. 5.10 Time Domain Simulation of the Tanker-Buoy System
Thruster Force=250 kN

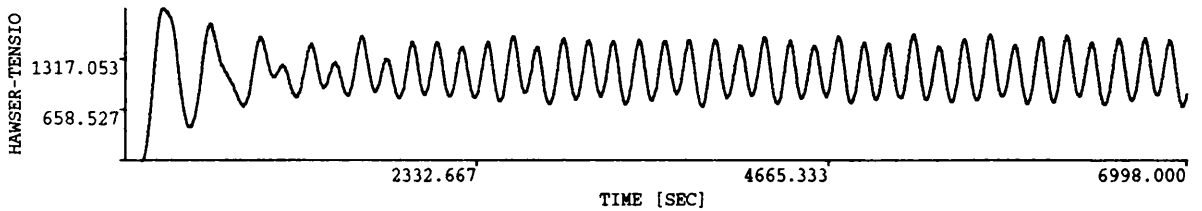
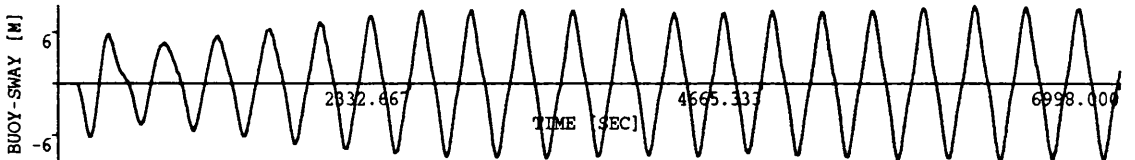
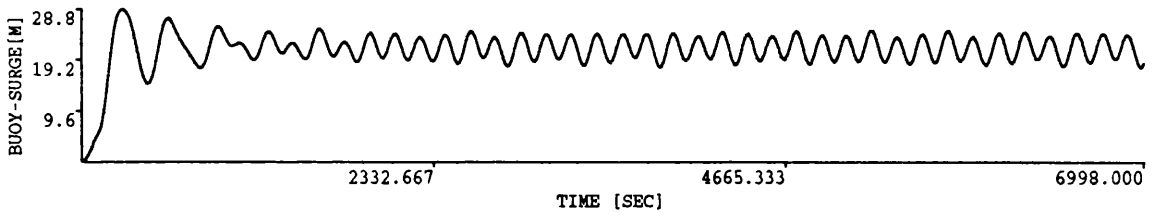
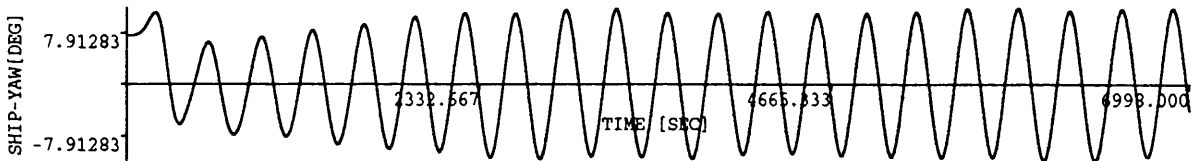
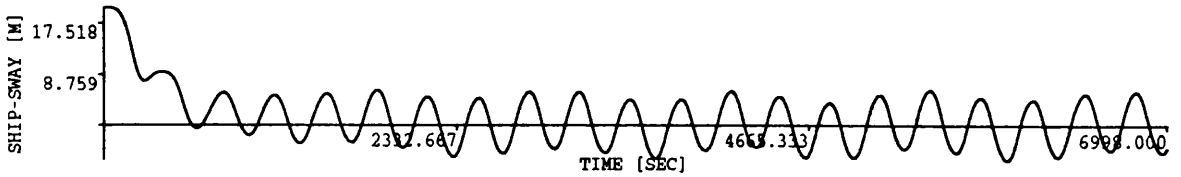
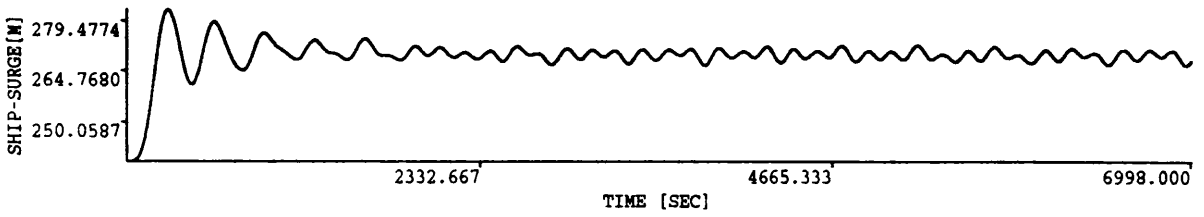
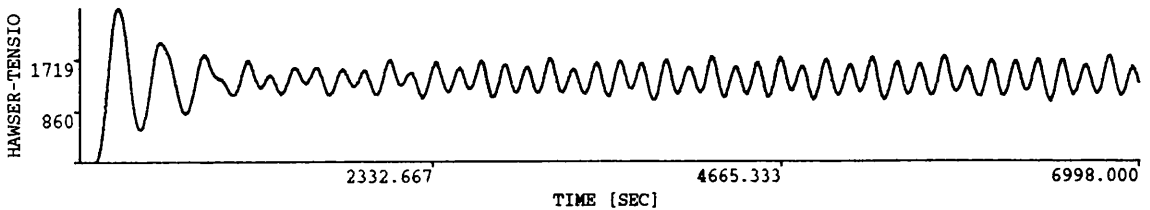
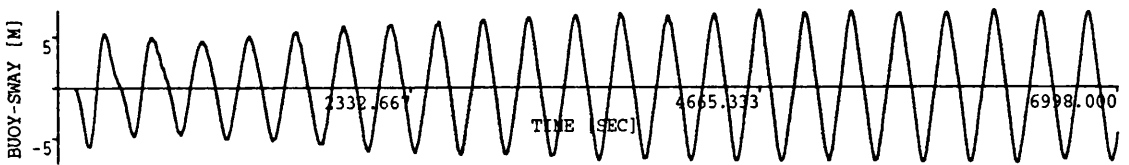
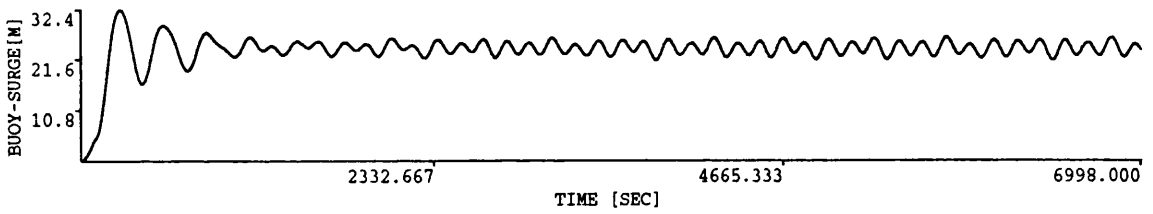
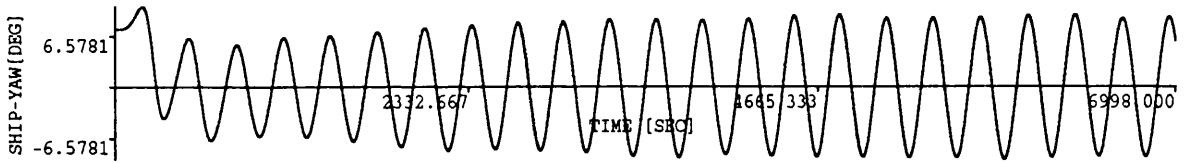
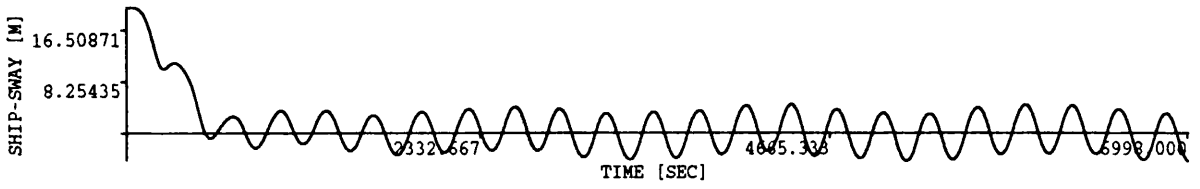
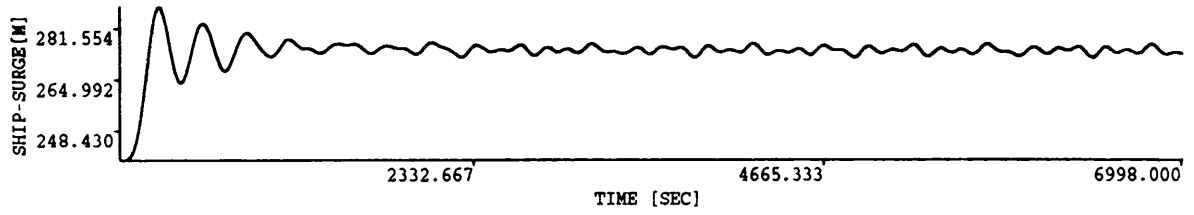


Fig. 5.11 Time Domain Simulation of the Tanker-Buoy System
Thruster Force=500 kN



**Fig. 5.12 Time Domain Simulation of the Tanker-Buoy System
Thruster Force=750 kN**

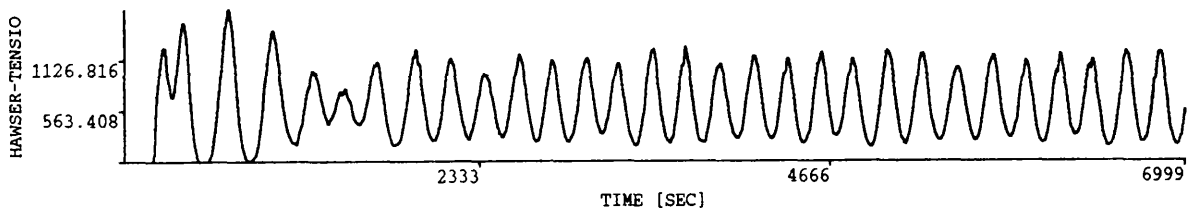
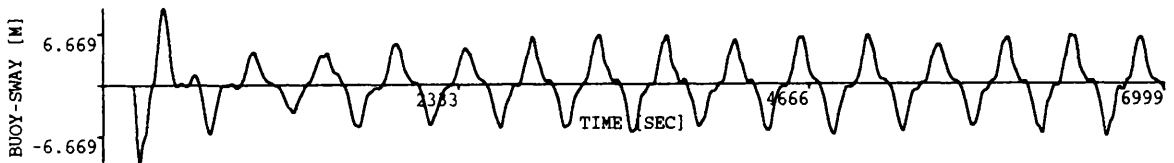
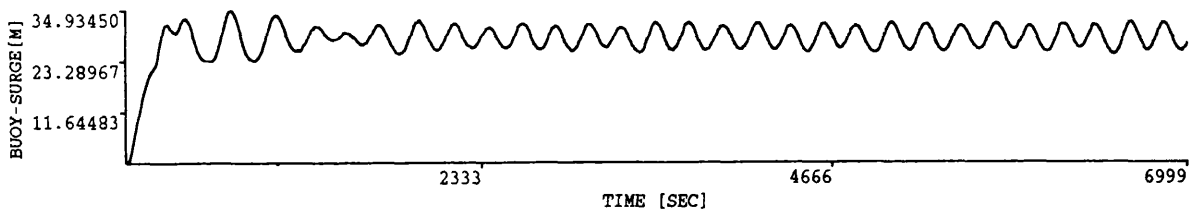
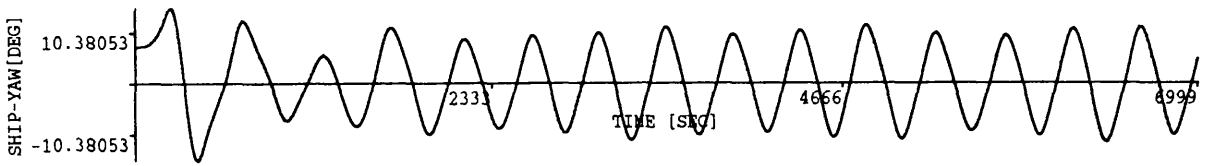
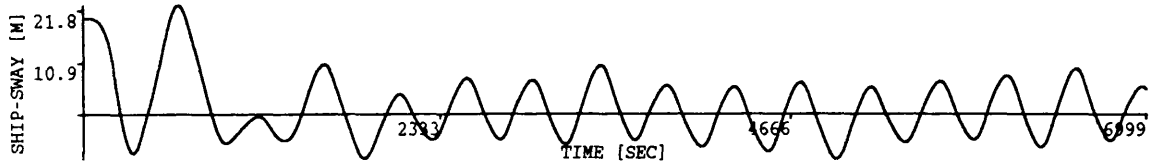
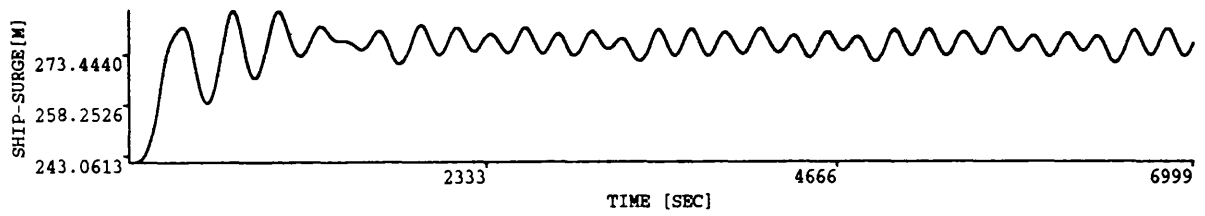


Fig. 5.13 Time Domain Simulation of the Tanker-Buoy System
 Diameter of the Buoy=20 m, Draft of the Buoy=20 m

CHAPTER 6

EXPERIMENTAL WORK

6.1 INTRODUCTION

In this chapter a description of model tests performed in regular waves is presented. Two sets of experiments were conducted, first set of experiments aimed to predict the motion responses of conical and cylindrical buoys, the second was performed to predict the motion responses of the tanker-buoy system and the hawser line forces.

In order to validate the numerical method, which was developed to calculate the motion responses of moored conical and cylindrical buoys, conical and cylindrical buoy models were tested in regular waves over a frequency range of 0.4 to 1.4 Hz at intervals of 0.04, 0.09, 0.18 and a wave height range of 2 to 14 cm (See Fig. 6.1). The sampling of the signals was set at 40 samples per second per channel over a period of 64 seconds for each wave frequency and wave height. The number of channels used was 10 without load cells, 14 with load cells. Three L.E.D.s were used to measure the heave, surge and pitch modes of motion. The signals collected by the L.E.D.s were amplified, digitised and stored in a file in the computer during tests. In order to analyze the experimental data stored in digital form on computer, a program called ATTEMPT was written, which performs Fast Fourier Transformations of experimental data.

The second set of tests was conducted to determine the motion characteristics of a Tanker-Buoy system under wave and current loading. In this system a cylindrical buoy is moored to the tank bottom by means of cables and an elliptical tanker is moored to the buoy by a hawser. Main dimensions of the system are given in Fig. 6.2 and 6.3. The tests were conducted in regular waves over a frequency range of 0.4 to 1.4 Hz at intervals of 0.1 and a wave height range of 4 to 6 cm at the towing/wave tank of the

Hydrodynamics Laboratory at the University of Glasgow, which is 77 m long, 4.6 m wide and 2.7 m deep. The sampling of the signals was set at 100 samples per second per channel over a period of 120 seconds for each wave frequency and wave height. The number of channels used was 16. The signals collected by L.E.D.s and load cell were amplified, digitised and stored in a file in the computer during tests.

During the first part of the second set of experiments a model of a coupled ship-buoy system shown in Fig. 6.4 and 6.5 was tested under co-linear wave and current loading. In the second part the current load was applied at an oblique angle to the direction of waves and the current load was simulated through a weight-pulley mechanism (Fig. 6.6). The ship model which comprised an elliptical cylindrical form was connected to a circular cylindrical buoy by means of a hawser and the buoy was connected to the tank bottom by a series of mooring lines. The stiffness characteristics of the mooring lines and hawser are given in Figs. 6.7 and 6.8 respectively.

The tank has a plunger type wave maker at one end, a wave absorber beach at the other. The regular waves were created by a plunger type wave maker driven by an electronically controlled hydraulic pump. The wave heights were measured by three resistance type wave probes. They were placed between the wave maker and the model. These probes induced an electrical signal whose strength changed as the waves passed the probes.

6.2 MOORED BUOY TESTS IN CALM WATER AND IN REGULAR WAVES

6.2.1 Description of Calibration Procedures

L.E.D.s (Light Emitting Devices) placed on the buoy were calibrated by shifting the camera horizontally for 10 cm and recording the subsequent voltage difference.

All wave probes were calibrated when they were submerged 10 cm into the tank while the water was calm and zero readings on the wave probe amplifiers were taken by marking the pen's position on the chart recorder (All calibration values were also recorded and stored in a computer file). Then wave probes were raised 10 cm and the new position was recorded in the computer as well as on the chart recorder.

6.2.2 Analysis and Comparison of the Measurements

The experiments could be divided into 7 parts:

1. Motion response measurements with the moored conical buoy
2. Motion response measurements with the moored cylindrical buoy
3. Motion response and mooring force measurements with the moored conical buoy.
4. Motion response and mooring force measurements with the moored cylindrical buoy.
5. Surge natural frequency tests in waves with the moored conical buoy
6. Motion response measurements with the moored conical buoy with relatively low initial tension.
7. Natural frequency test of the conical buoy with linear springs

Conical and cylindrical buoys used in the tests are depicted in Fig 6.3. Fig 6.2 shows the experimental set-up.

The first four sets of experiments were performed in order to compare the motion performances of the conical and cylindrical buoys and to validate the computer simulations. Three L.E.D.s were used to measure the heave, surge and pitch modes of motion. First-order, steady and second order motions were measured by applying Fast Fourier Transformations to the experimental data. Some examples of the experimental data and F.F.T analysis are shown in Figs. 6.9, 6.10, 6.11 and 6.12. These measurements are plotted in the frequency domain. First-order heave, surge and pitch measurements with the conical and cylindrical buoys are shown in Figs. 6.13-6.18. Normalized values of the first-order motion measurements are compared with time and frequency domain predictions [6.1]. Fig. 6.19 and 6.20 show that the non-linear time

domain predictions correlate better with measurements than the linear frequency domain predictions. This may be explained by the fact that the non-linear time domain approach models the stiffness characteristics due to hydrostatic and mooring lines more accurately and therefore a significant difference occurs between the results obtained from the two methods in the frequency region where motion responses are controlled by the restoring forces.

Surge response curves (Figs 6.21 and 6.22) show a significant shift at the maximum response values corresponding to the natural surge frequency region. This can be attributed to the different surge stiffness modelling employed in the linear frequency domain formulation as against the non-linear time domain formulation. However both prediction methods yield significantly higher results than experimental measurements. This may be due to the inertia coefficients used in the wave force formulations being higher than they actually should be.

As with the surge responses, predicted pitch response values are higher than the measured experimental pitch responses and the difference may, again, be due to the high wave force coefficients used in the predictions (Figs. 6.23 and 6.24).

Comparisons between the motion performance of the conical buoy and that of the cylindrical buoy indicate that the heave and pitch motions of the conical buoy are significantly less than those of the cylindrical buoy. Although the heave response amplitude values are similar to each other for conical and cylindrical buoy forms since the heave response amplitude curve of the cylindrical buoy has a wider band than that of the conical form spectral analysis gives much more significant motion response values for the cylindrical buoy. It may therefore be concluded that a conical form gives a better motion performance than does a cylindrical buoy.

The second order slowly varying and steady surge responses of the conical and cylindrical buoys are shown in Figs. 6.25, 6.26, 6.27 and 6.28. In order to obtain the horizontal stiffness characteristics of the mooring lines another experimental set-up was

used. In this test the buoy's horizontal displacements against applied horizontal forces were recorded and plotted in Fig. 6.29.

Some measured characteristic values of the conical buoy (in full scale):

Heave natural frequency= 0.448 rad/sec

Surge natural frequency= 0.095 rad/sec

Pitch natural frequency= 0.373 rad/sec

Damping coefficient for heave (γ)= 0.075

Damping coefficient for surge (γ)= 0.098

Damping coefficient for pitch (γ)= 0.134

Metacentric height= 4.784 m

Some characteristic values of the cylindrical buoy (in full scale):

Heave natural frequency = 0.560 rad/sec

Surge natural frequency= 0.141 rad/sec

Pitch natural frequency= 0.410 rad/sec

Damping coefficient for heave (γ)= 0.120

Damping coefficient for surge (γ)= 0.112

Damping coefficient for pitch (γ)= 0.127

Metacentric height= 4.585 m

In the calculation of surge damping coefficients mooring stiffness in surge direction is assumed to be constant (Fig. 6.29).

In the last two sets of experiments the surge natural frequency of the moored conical buoy in waves, the viscous damping of the moored conical buoy in waves and the effect of initial cable tension on the motion behaviour of the buoy were investigated. A surge natural frequency test was performed for two different mooring configurations. The first configuration was the original one (Mooring Configuration A) which was used for the first four sets of experiments (Fig. 6.2), but the result was not very successful. Because of the high initial tension on the cables the amplitude reduced to small values

rather quickly (Fig. 6.30). Then moorings were modified in order to have low initial tension on the cables (Fig. 6.31) (Mooring Configuration B).

Comparisons between the first-order motions of the conical buoy with two different mooring configurations are presented in Figs. 6.32, 6.33 and 6.34. In the case of low initial tension on the cables, a decrease in the first-order surge and pitch motion responses was observed (Figs. 6.32 and 6.34). It was also observed that initial tension on the cables had no significant effect on the heave motion of the conical buoy (Fig. 6.33). The same conclusion was reached after carrying a series of parametric studies performed using the time domain program called HYDCOT (Fig. 6.35). In the case of low initial tension on the cables, an increase in the steady and second-order surge motion responses was observed (Fig. 6.36 and 6.37). Surge natural frequency in waves was measured for two different mooring arrangements; 0.481 rad/sec for the Mooring configuration B (low initial tension on the cables), 1.789 rad/sec for the Mooring configuration A.

The damping coefficients were computed from the examination of the rate of decaying oscillations (Fig. 6.38) [6.2]. The surge signal was numerically filtered with a 2.24 rad/sec (0.2 rad/sec in full scale) low pass filter to isolate the low frequency response of the system. A sample of the data is presented in Fig 6.30. The damping coefficients are plotted in the frequency domain in Fig. 6.39. it may be generally concluded that the damping coefficients increase as wave height increases.

The equation of motion for the damped free oscillation of the conical moored buoy in surge is given by

$$m\ddot{x} + c\dot{x} + kx = 0 \quad (6.1)$$

and natural frequency

$$\omega_n = \sqrt{\frac{k}{m}} \quad (6.2)$$

γ is the damping coefficient and could be found from the logarithmic decrement

$$\log_e \frac{A_1}{A_{n+1}} = \frac{2\gamma n \pi}{\sqrt{1-\gamma^2}} \quad (6.3)$$

A_1 is the amplitude of the oscillation at t_1 and A_{n+1} is the amplitude at t_{n+1} .

Added mass coefficient could be computed from the measured natural frequency, the spring constant and the buoy's mass

$$C_a = \left(\frac{k}{\omega_n^2} - m \right) / m \quad (6.4)$$

In the last set of experiments the conical buoy was moored to the carriage with linear springs which were pretensioned and which never became slack during the experiments (Figs. 6.41, 6.42 and 6.43). Two loadcells were used to measure the forces on the springs and one L.E.D. was used to measure the surge response. As a double check, surge response was also calculated by using the forces on the springs. This method also eliminates the contamination to surge response from other modes of motion. The unstretched length of the springs was 31 cm. Before the experiments they were stretched to 40 cm. Spring coefficients of the springs were measured and were found to be 7.85 kg/m. Damping and added mass coefficients of the conical buoy were calculated using equations (6.3) and (6.4). The added mass coefficient of the conical buoy was found to be 1.734. Damping coefficients for two experimental test set-ups were plotted in Fig. 6.44 and 6.45. It can be concluded from the graphs that the damping coefficient in waves is higher than the damping coefficient in still water. Damping coefficients obtained using test set-up A are higher than the coefficients obtained using test set-up B. This can be attributed to the higher friction in test set-up A, which is caused by the pulley system.

Some difficulties have been encountered during the experiments; In the second set of the experiments at the frequencies of 0.80 and 0.89 Hz yaw motions were observed. In the sixth set of the experiments at the frequency of 1.40 Hz sway motion was observed. This strange phenomenon is believed to be caused by 'wall effect' [6.3].

A parametric study was performed to determine the effect of the current on the motion responses of the moored buoys (Fig. 6.40). It showed that the current increases amplitude of the first-order motions and that the natural frequency region moves towards higher frequencies in the presence of current.

6.3 SINGLE POINT MOORED TANKER-BUOY EXPERIMENTS

6.3.1 Description of Calibration Procedures

Instrumentation of the L.E.D.s, load cells and cameras are shown in Fig. 6.46. Eight L.E.D.s were used to measure the motions of the tanker and the buoy; six on the tanker, two on the buoy. Signals from L.E.D. 1,2,3 and 4 were detected by a camera placed at the top of the carriage and signals from L.E.D.s 5 and 6 were detected by a camera placed at the side of the tank. Another camera was placed at the top of the carriage to detect signals from the L.E.D.s on the buoy. While L.E.D.s nos. 2, 4, 5 and 6 were used for measuring, nos. 1 and 3 were used for calibration purposes only. So L.E.D.s 2 and 4 were calibrated by using 1 and 3 and L.E.D.s 5 and 6 by the use of 2 and 4. the L.E.D. on the buoy was calibrated by shifting the camera horizontally. One load cell was also used to measure the forces on the hawser. All wave probes were calibrated when they were submerged 10 cm into the tank while the water was calm and zero readings on the wave probe amplifiers were taken by marking the pen's position on the chart recorder (All calibration values were also recorded and stored in a computer file). Then wave probes were raised by 10 cm and the new position was recorded in the computer as well as on the chart recorder.

6.3.2 Analysis and Comparison of the Measurements

First, the system was tested in co-linearly acting wave and current loading. Current force was simulated by a single force applied to the system along the x-axis by a pulley system. During the tests wave frequency was varied from 0.4 Hz (2.51 rad/sec) to 1.4 Hz (8.8 rad/sec) and the current force acting on the system was 6 gr (0.059 N). Oscillatory surge motion of the tanker and the buoy were compared with the time and frequency domain simulations in Figs. 6.47 and 6.48. Agreement was very good for the tanker. But there were some discrepancies in the buoy's surge motion. During the experiments it was observed that the buoy's motion was not so stable and it involved some unexpected yaw and sway motion due to the very light buoy model used in the experiments. Some examples of these runs are presented in Figs. 6.49-6.51. Then natural frequency of the system was determined under wave loading and under current loading (single applied force). Under wave loading it was found to be between 0.15 and 0.38 rad/sec (0.024 and 0.060 Hz), under current loading it was between 0.27 and 0.61 rad/sec (0.043 and 0.097 Hz). One example of these tests is given in Figs. 6.52 and 6.53.

In the second set of the tests, the system was tested in oblique angles i.e. current was acting in oblique angles (See Fig. 6.54) and the initial position of the tanker was different from the head-sea tests (See Fig. 6.6). In these tests finer and lighter cables were used to reduce the effect of the cables on the motions. But buoy motions again were not stable due to the very light buoy model. Results of these tests are presented in table 6.1. Wave frequency in the tests was varied from 0.9 Hz to 1.3 Hz. Tests were not performed at the frequencies lower than 0.9 Hz because the wave drift force is almost zero at these frequencies. It is easily seen from the table that with the increase in the current load, an increase in the oscillatory motions of the tanker is obtained. Oblique angle tests are presented in Figures 6.55-6.58. In run 22 (Fig. 6.58) unstable tanker motion was observed.

In order to analyze the experimental data stored in digital form on computer, a program called TIME_EXPE was written, which performs Fast Fourier Transformations of the experimental data.

6.3.3 Observations and Experience from Model Tests

During the experiments it was observed that the tanker-buoy system was too light and so, too sensitive to external loads. The L.E.D. and load cell cables were applying load to the system. This problem was partially solved in the second set of experiments by using fine, lighter cables.

Another problem observed during the experiments was that the L.E.D.s were going out of range of the cameras. This was especially a problem in oblique angle tests because the position of the cameras has to be changed when the current angle of attack or the initial position of the tanker changes.

6.4 CONCLUSIONS

The theoretical work on the motion response predictions of the moored buoys has been validated by experiments. Comparisons between the predictions and the measurements reveal that the predictions are rather conservative in surge and pitch motions but give reasonably good correlations with measurements in all modes of motion.

Another conclusion that could be drawn from the experiments is that the conical buoy performs better than the cylindrical one under wave, wind and current forces.

Second-order surge motions were observed in regular waves. This was quite a surprise since second order motions are originally thought to be caused by irregular waves. One possible reason for this is the non-linearities exhibited by the mooring cables.

The theoretical work on the motion response predictions of the tanker-buoy system has been validated by experiments. Comparisons between predictions and measurements reveal that the predictions agree very well with the measurements for surge motion of the tanker. However the comparison is not so good for surge motion of the buoy. One possible reason for this is the unstable motion of the buoy observed during the experiments.

It can be concluded from oblique angle tests that an increase in the current load usually results in an increase in the oscillatory motions of the tanker and that the system does not always reach a steady state position under wave and current loading (Fig. 6.58).

Run No	Current Direction (Deg.)	Current Force (gr)	Wave Frequency (Hz)	Wave Height (cm)	SHIP MOTIONS					
					SURGE(cm)		SWAY(cm)		YAW(deg)	
					Steady	Oscill.	Steady	Oscill.	Steady	Oscill.
1	213.00	7.00	0.90	4.70	153.90	0.47	-0.60	0.30	-8.27	0.58
2	213.00	7.00	0.90	4.45	157.60	0.44	-1.22	0.23	-9.85	0.40
3	206.50	10.00	0.90	5.32	151.20	0.54	-37.00	0.26	-38.12	1.52
4	212.00	7.00	1.00	4.69	156.50	0.13	2.00	0.13	-8.00	0.62
5	206.50	10.00	1.00	4.31	157.70	0.13	-24.50	0.07	-41.00	0.73
6	207.50	17.00	1.00	4.55	155.00	0.16	-20.00	0.19	-45.00	1.09
7	200.00	20.00	1.00	5.09	147.00	0.17	-32.00	0.24	-45.49	1.58
8	209.00	27.00	1.10	3.50	158.87	0.28	-19.10	0.09	-33.60	0.62
9	213.00	55.00	1.10	4.44	156.20	0.35	-25.00	0.12	-40.00	1.15
10	202.50	65.00	1.10	4.39	146.90	0.41	-40.10	0.12	-60.47	1.72
11	201.00	65.00	1.10	4.36	153.80	0.37	-34.97	0.12	-46.70	1.50
12	200.50	70.00	1.10	5.11	157.70	0.39	-46.42	0.23	-44.31	1.78
13	200.00	80.00	1.10	4.99	149.84	0.39	-51.80	0.23	-46.54	1.84
14	217.00	30.00	1.20	4.47	155.00	0.40	30.60	0.15	-28.70	0.54
15	216.00	37.00	1.20	4.35	157.70	0.41	21.03	0.14	-33.14	0.55
16	208.00	80.00	1.20	4.93	158.60	0.47	-31.60	0.20	-39.05	1.11
17	219.50	47.00	1.30	4.45	156.08	0.18	41.90	0.56	-29.90	0.19
18	219.50	67.00	1.30	3.95	150.22	0.18	29.22	0.37	-33.80	0.08
19	221.00	87.00	1.30	4.75	155.00	0.18	34.00	0.64	-33.49	0.15
20	222.00	97.00	1.30	5.09	148.90	0.19	26.20	0.55	-37.40	0.16
21	215.50	100.00	1.30	4.64	159.40	0.31	-15.02	0.34	33.97	0.83
22	224.50	107.00	1.30	5.09	150.31	0.18	35.50	0.53	-37.42	0.16
23	215.00	120.00	1.30	5.90	148.10	0.40	-12.50	0.31	-26.80	0.81
24	214.00	137.00	1.30	4.61	146.91	0.27	-1.80	0.54	-12.51	0.45
25	213.00	147.00	1.30	5.09	147.10	0.33	-2.43	0.50	-15.68	0.55

Table 6.1 Oblique Wave and Current Loading Test Conditions and Results

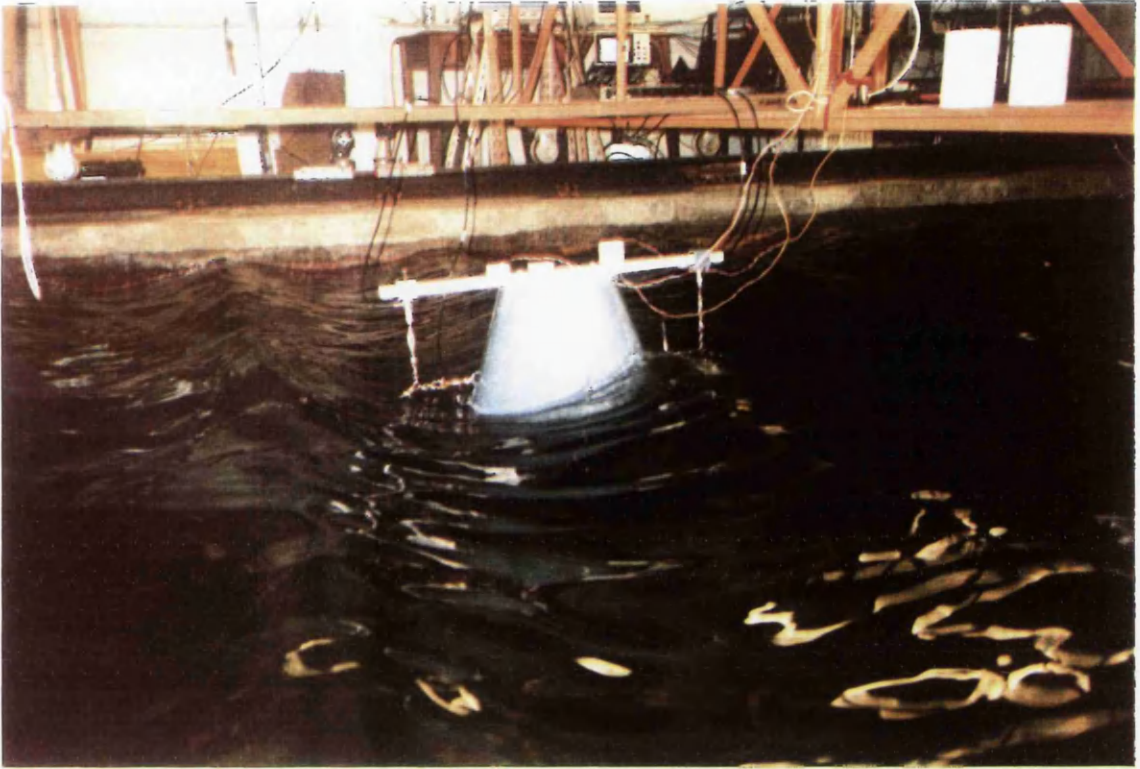


Fig. 6.1 Motion Response and Cable Tension Measurements of the Conical Buoy

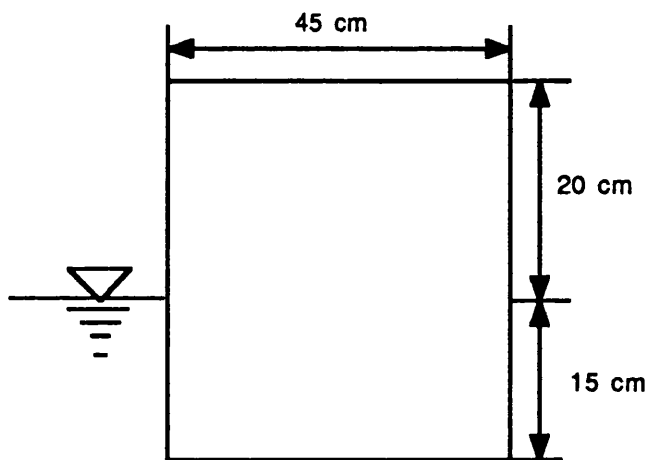
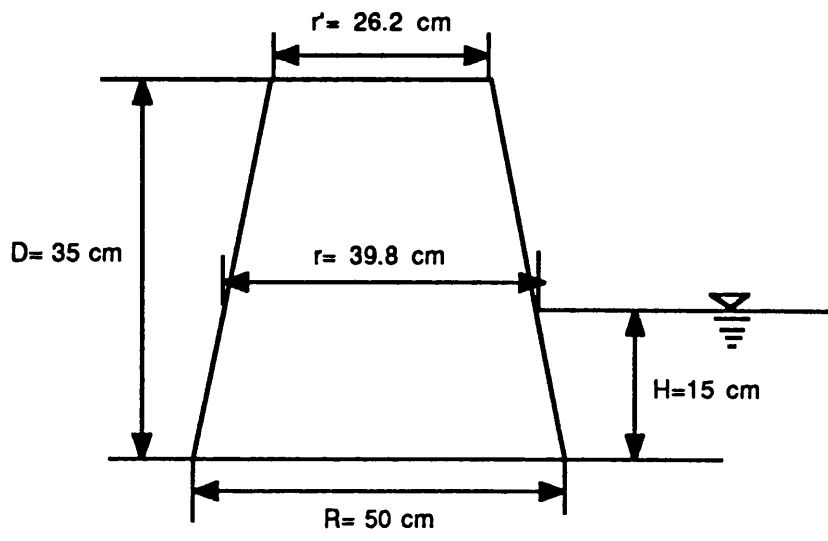


Fig 6.3 Geometrical characteristics of Conical and Cylindrical Buoys

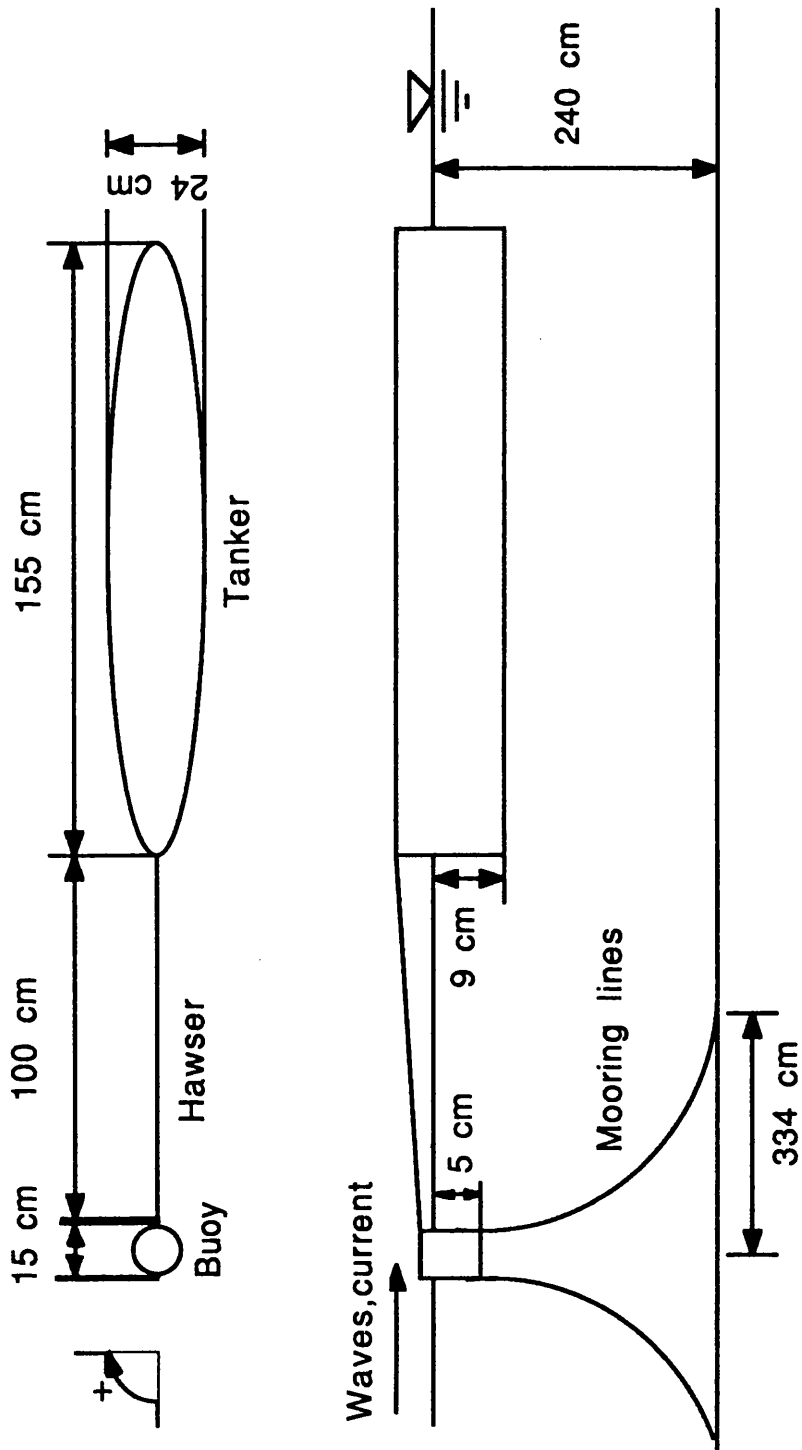


Fig. 6.4 Experimental set-up for the coupled buoy-ship system

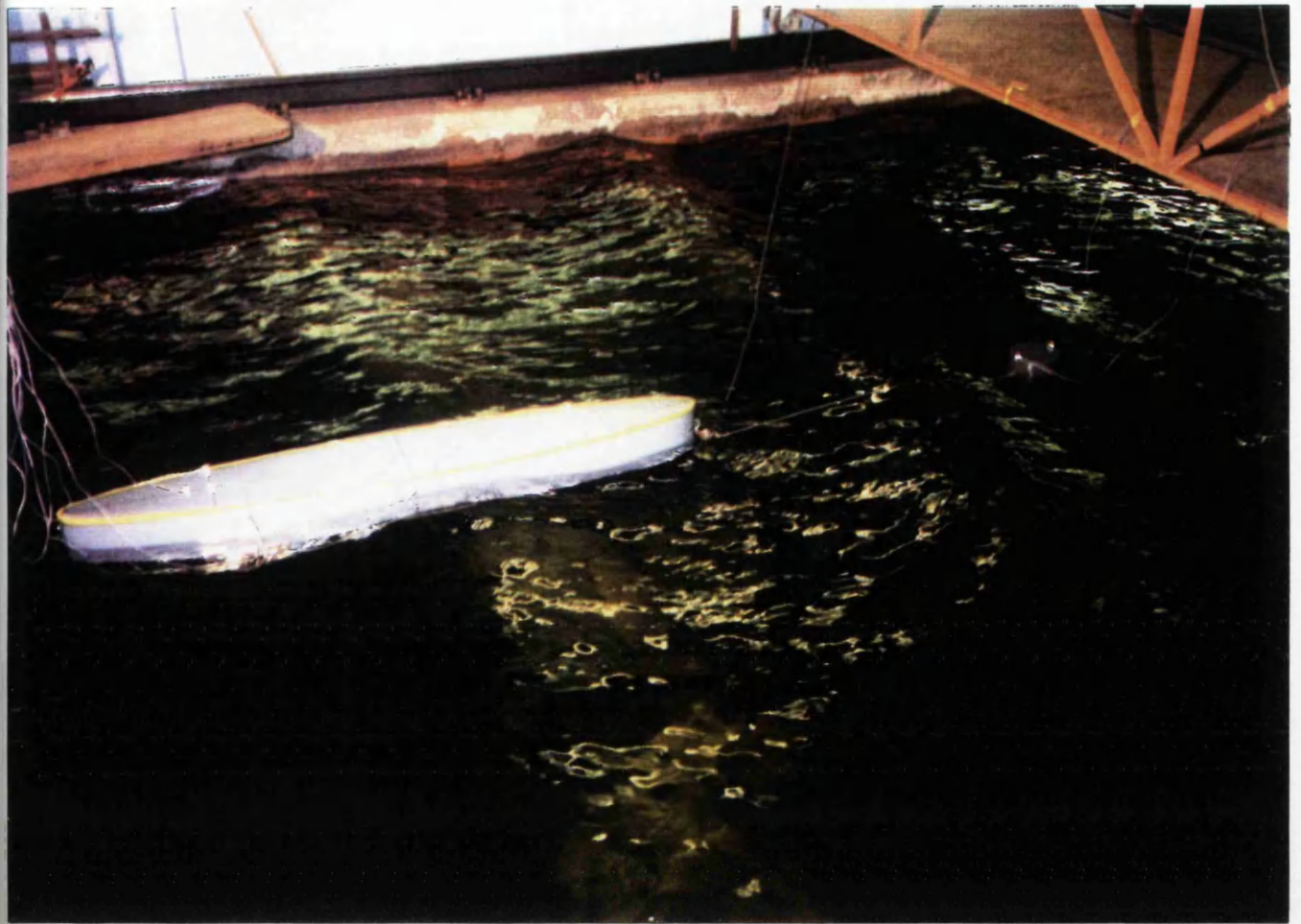


Fig. 6.5 Coupled Tanker-Buoy System

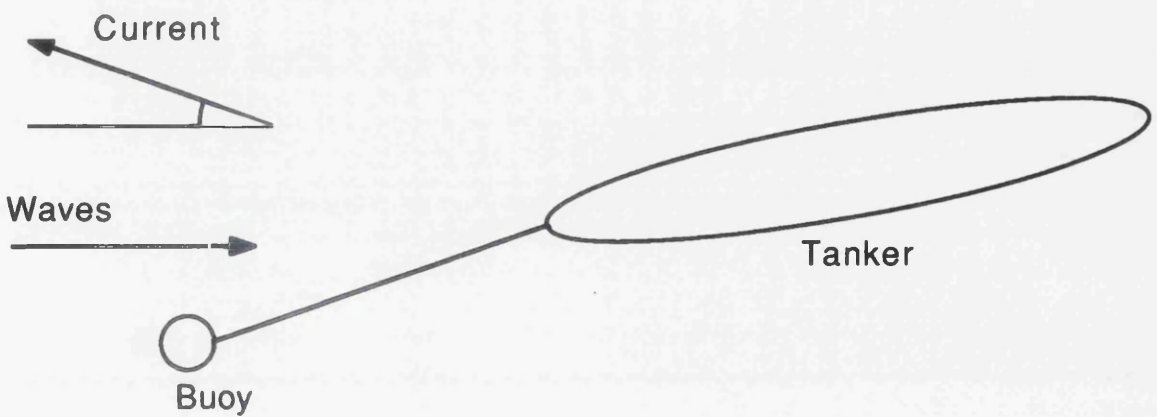


Fig 6.6 Experiment set-up of the Tanker-Buoy system
Wave and current acting in different directions

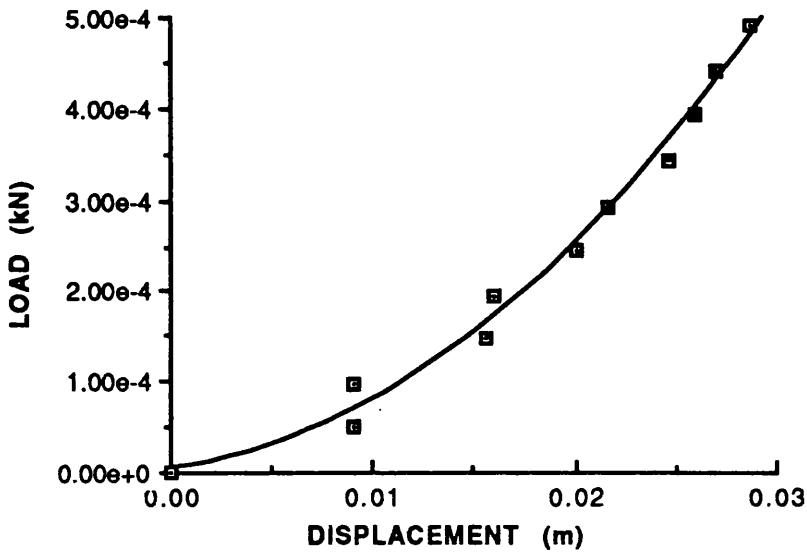


Fig. 6.7 Stiffness Characteristics of Mooring Lines

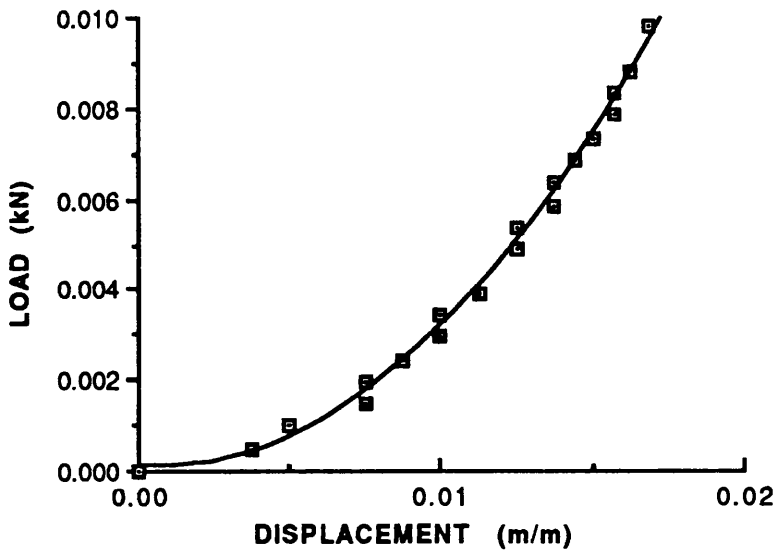


Fig. 6.8 Stiffness Characteristics of Hawser

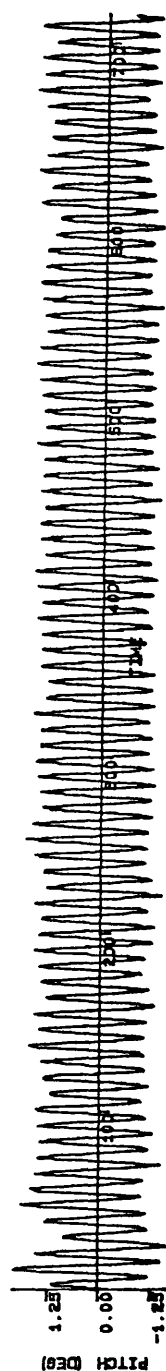
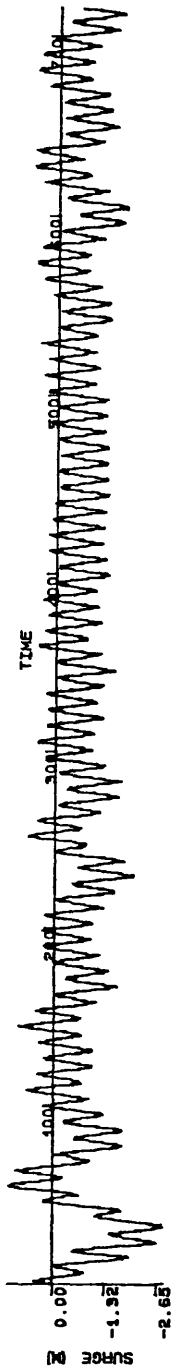
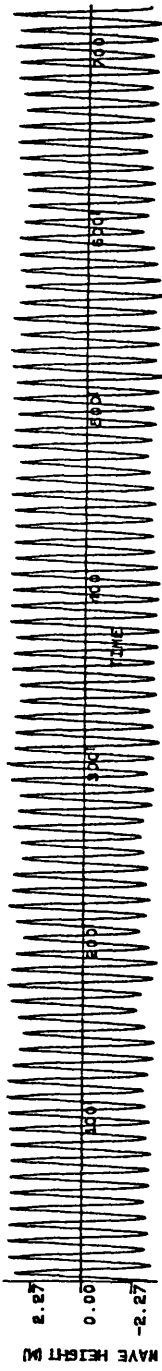


Fig. 6.9 Motion Response Measurements of the Moored Conical Buoy
 Wave Height=6 m, Wave Frequency=0.702 rad/sec
 (All values are in full scale)

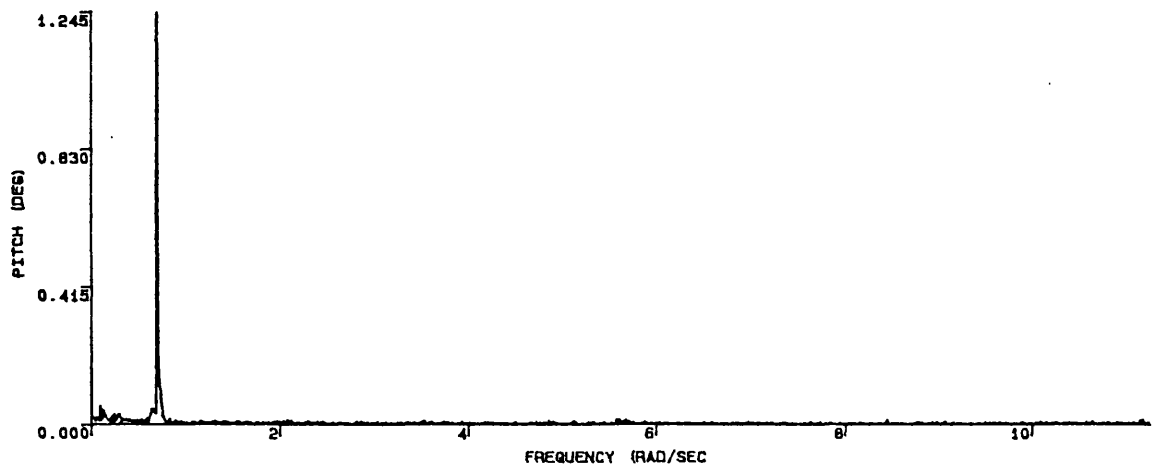
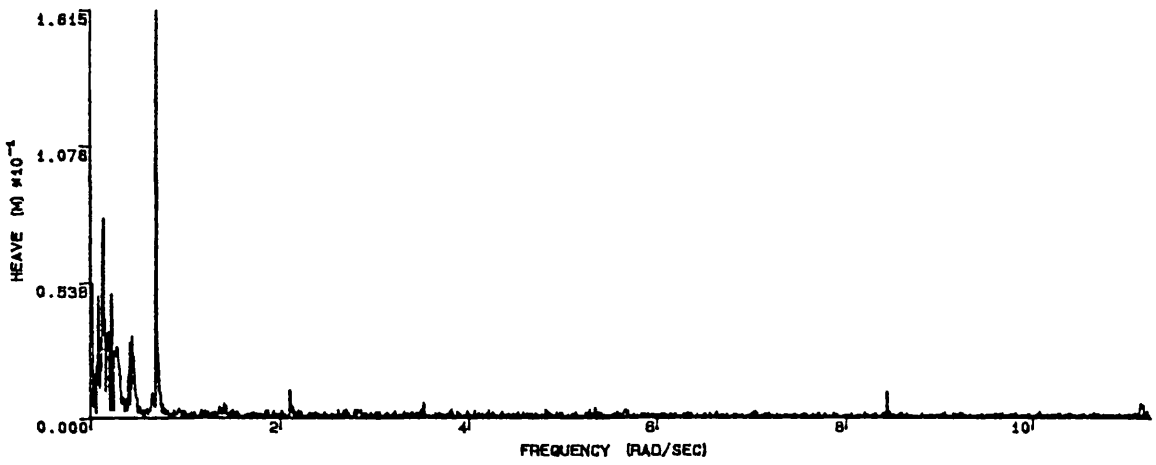
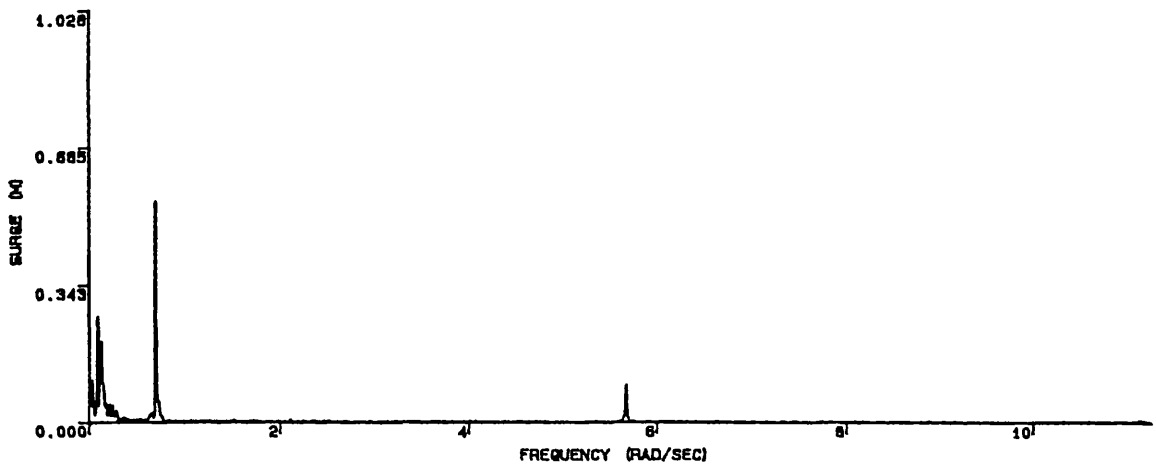


Fig. 6.10 Fast Fourier Transformations of the Time Histories shown in Fig. 6.9

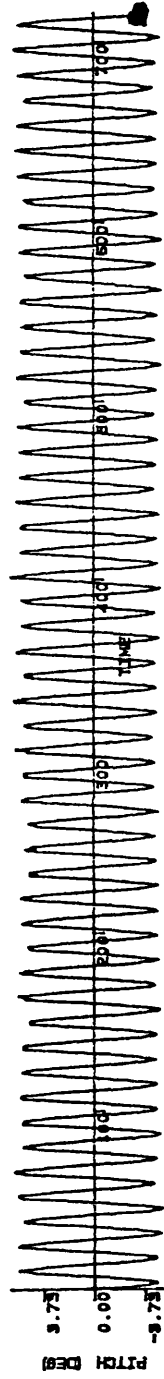
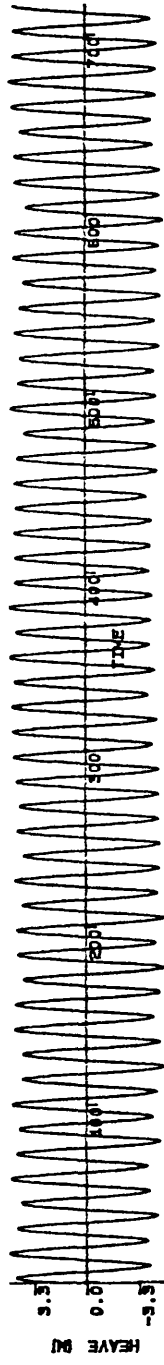
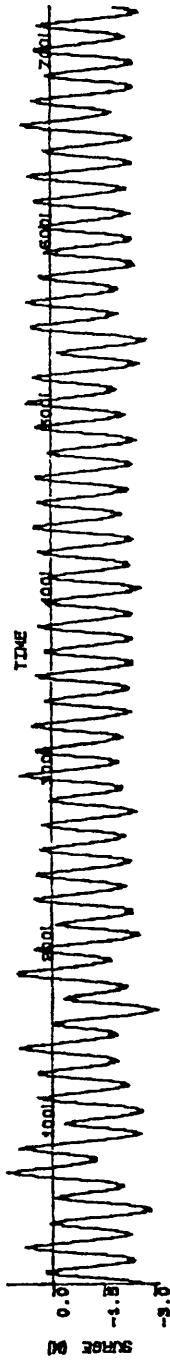
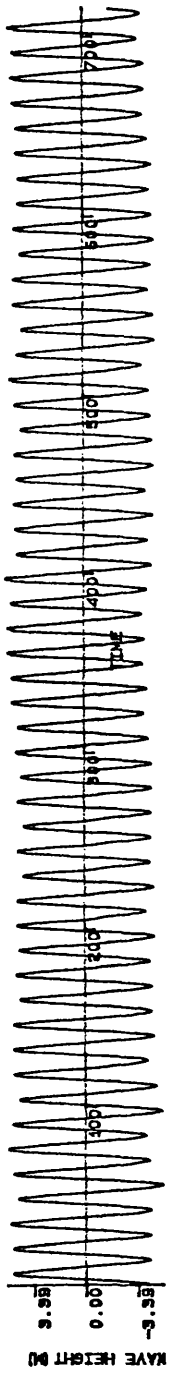


Fig. 6.11 Motion Response Measurements
of the Moored Conical Buoy
Wave Height=8.84 m, Wave Frequency=0.45 rad/sec
(All values are in full scale)

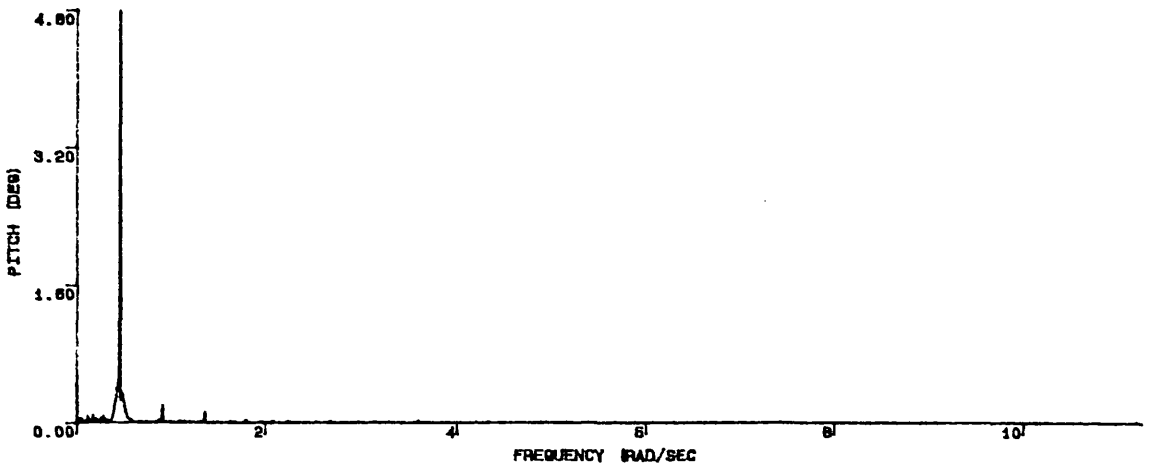
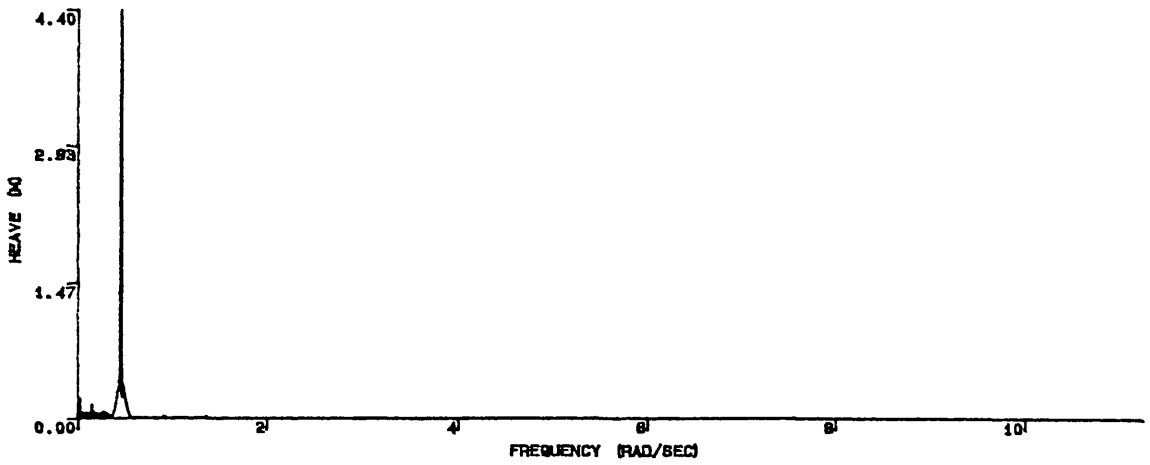


Fig. 6.12 Fast Fourier Transformations of the Time Histories shown in Fig. 6.11

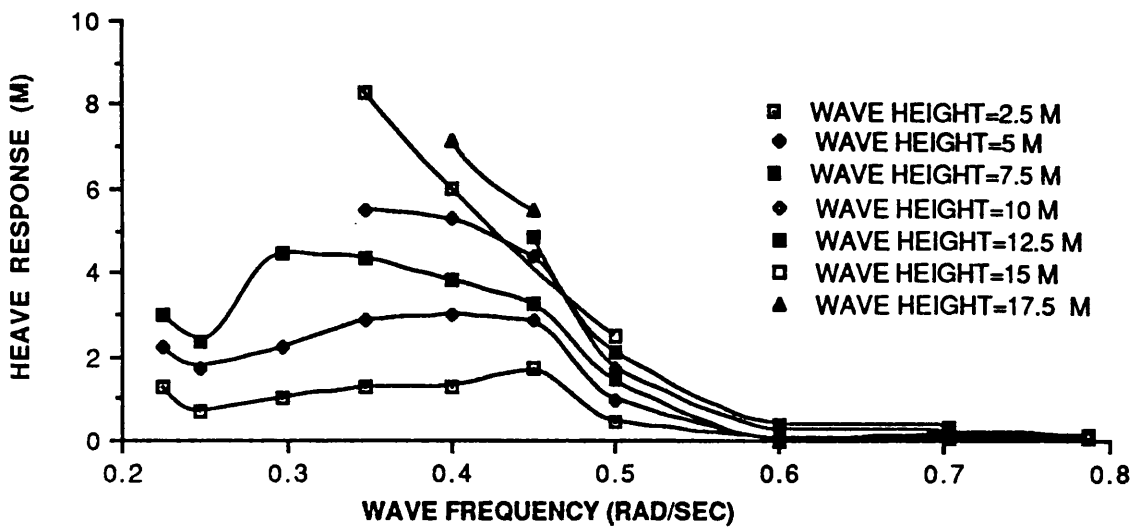


Fig. 6.13 Heave Response Measurements of the Moored Conical Buoy

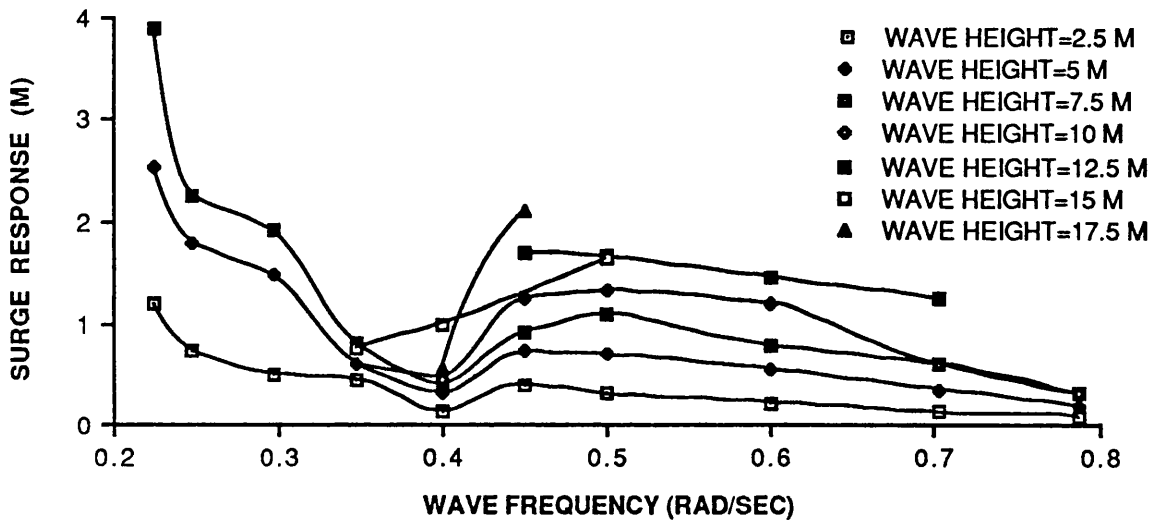


Fig. 6.14 Surge Response Measurements of the Moored Conical Buoy

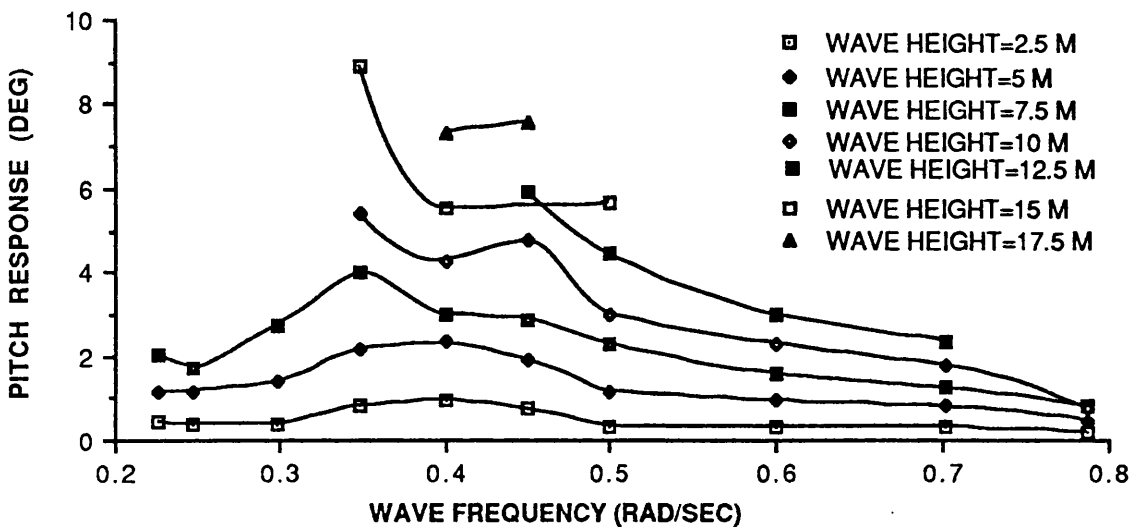


Fig. 6.15 Pitch Response Measurements of the Moored Conical Buoy

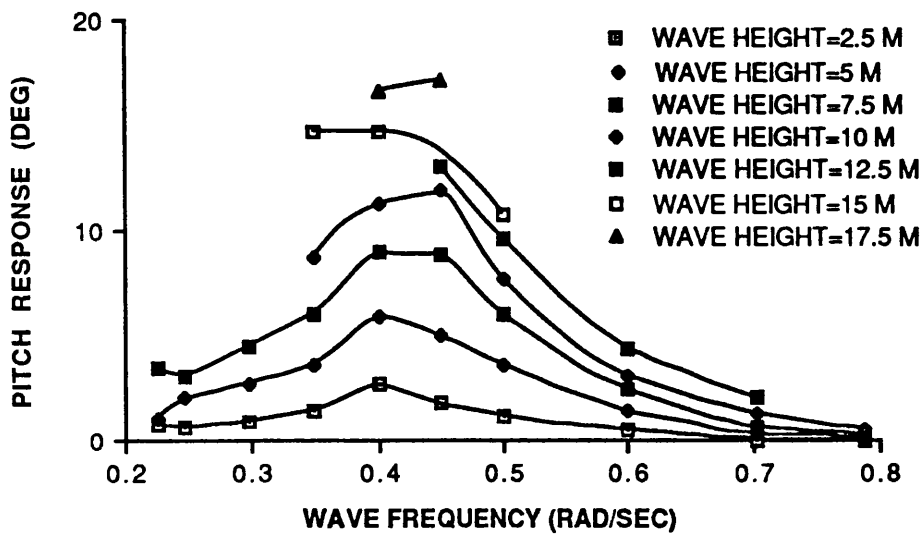


Fig. 6.16 Pitch Response Measurements of the Moored Cylindrical Buoy

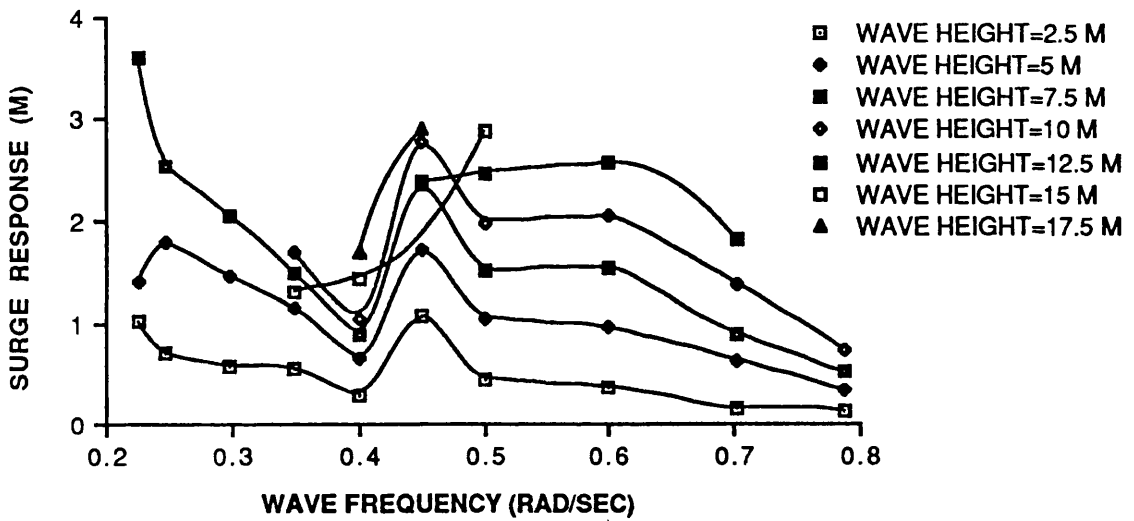


Fig. 6.17 Surge Response Measurements of the Moored Cylindrical Buoy

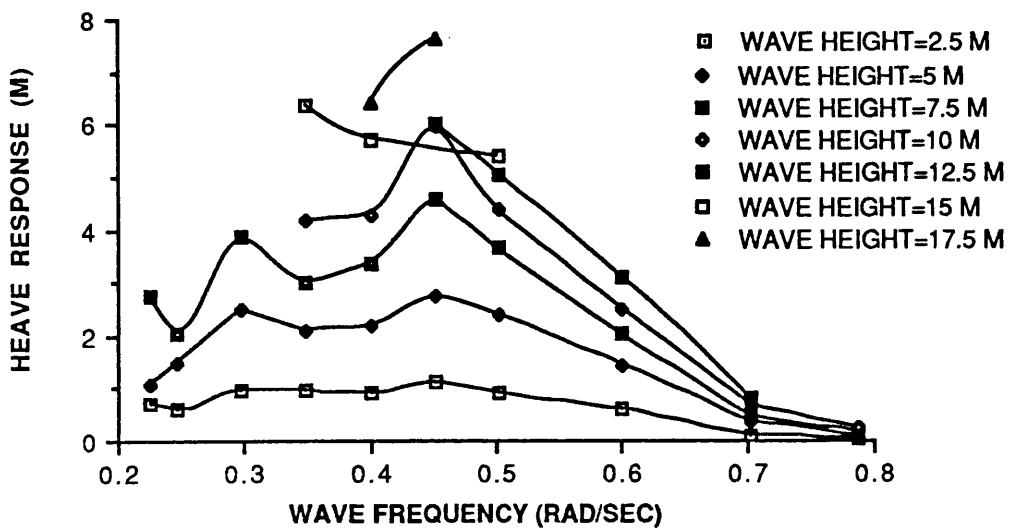


Fig. 6.18 Heave Response Measurements of the Moored Cylindrical Buoy

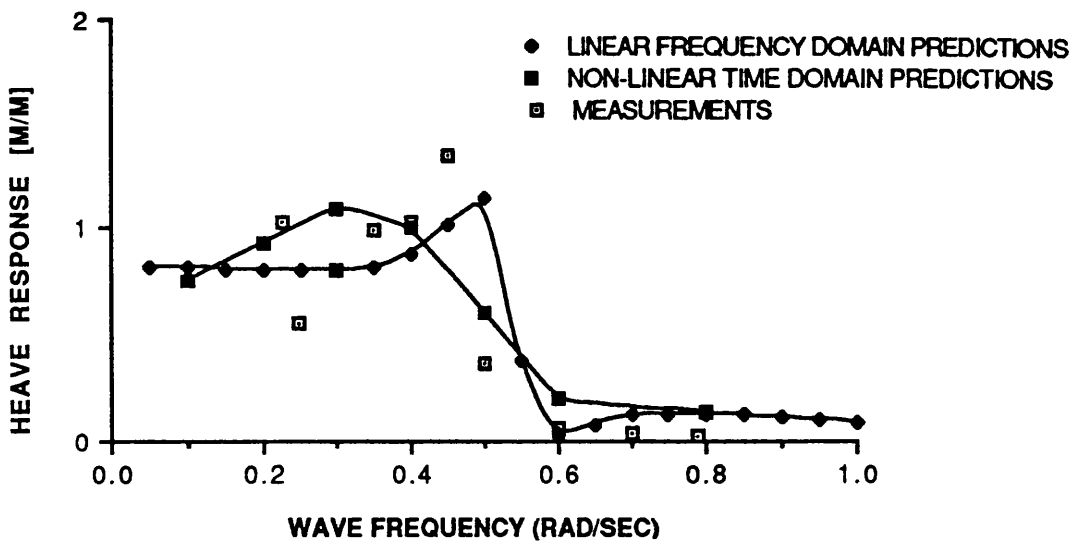


Fig. 6.19 Heave Response Predictions of the Conical Buoy

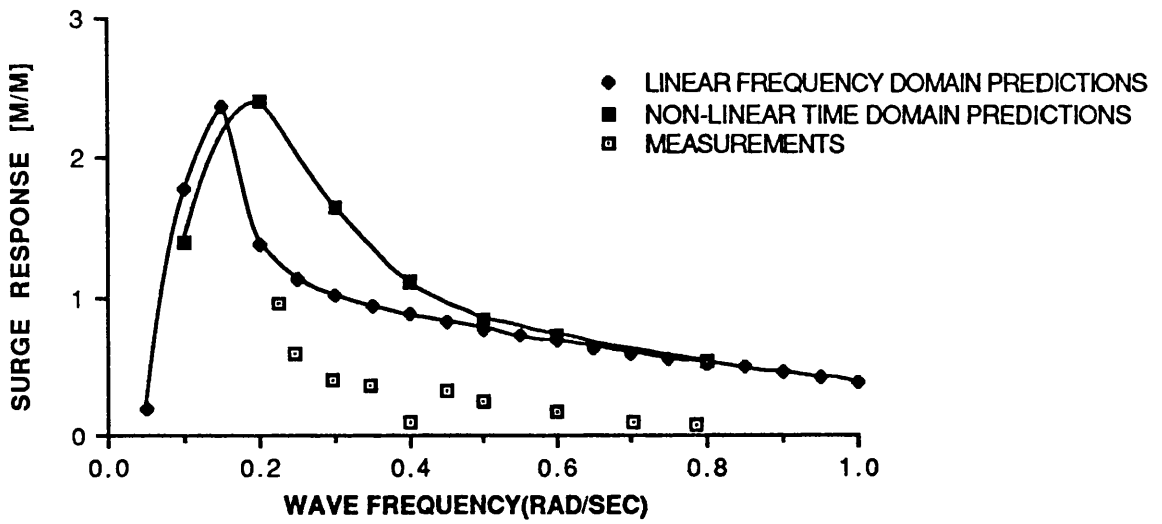


Fig. 6.21 Surge Response Predictions of the Conical Buoy

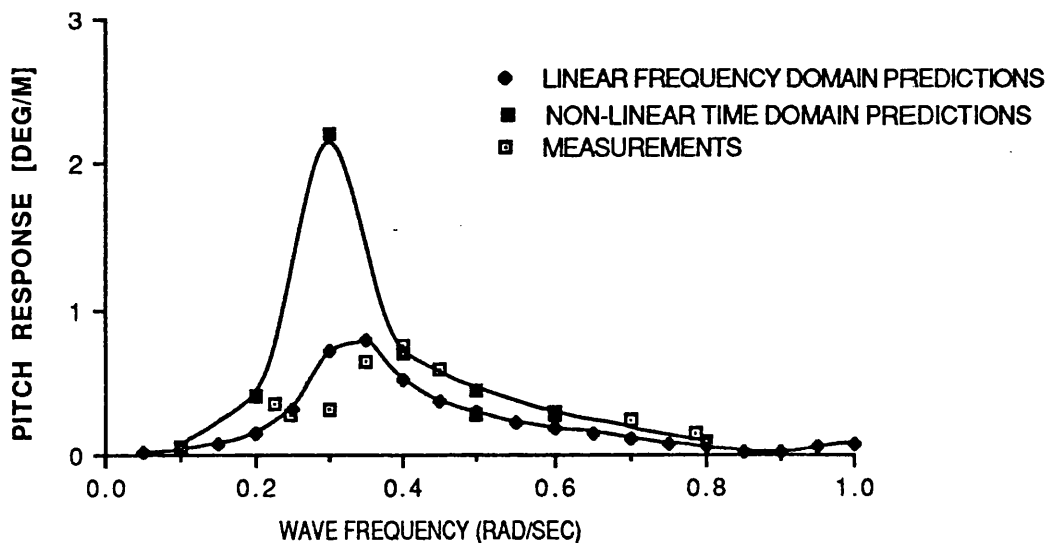


Fig. 6.23 Pitch Response Predictions of the Conical Buoy

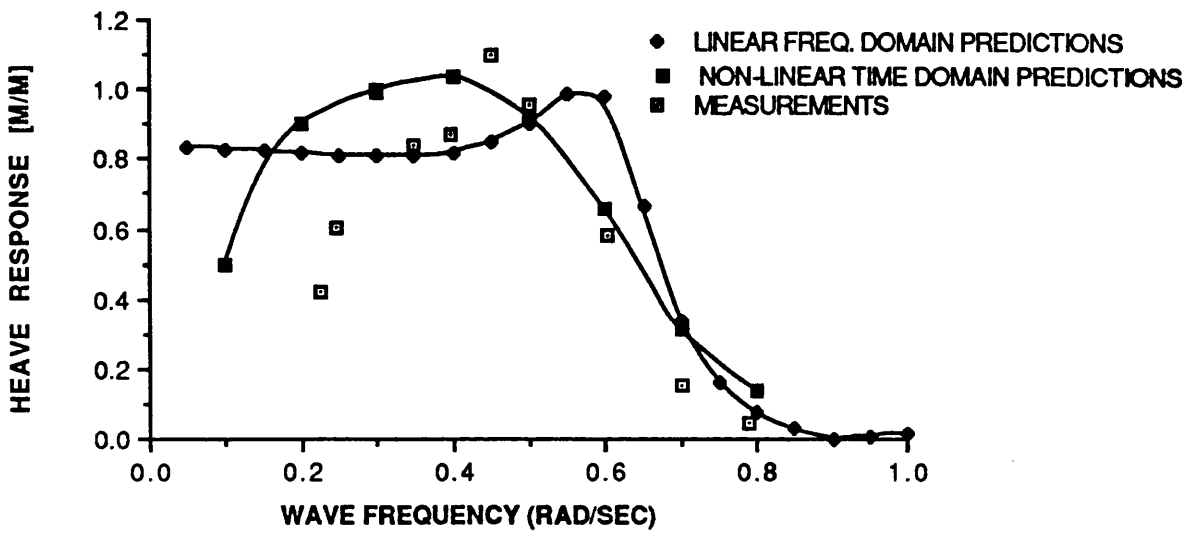


Fig. 6.20 Heave Response Predictions of the Cylindrical Buoy

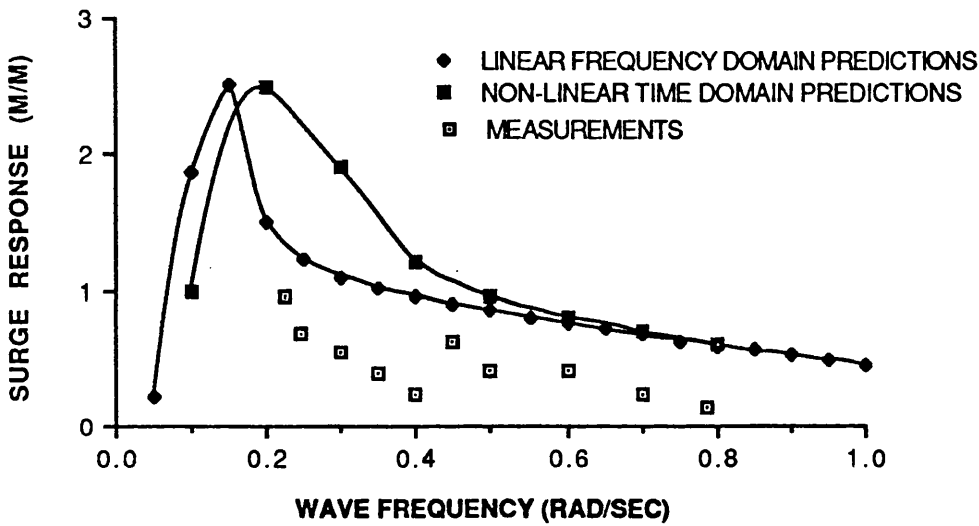


Fig. 6.22 Surge Response Predictions of the Cylindrical Buoy

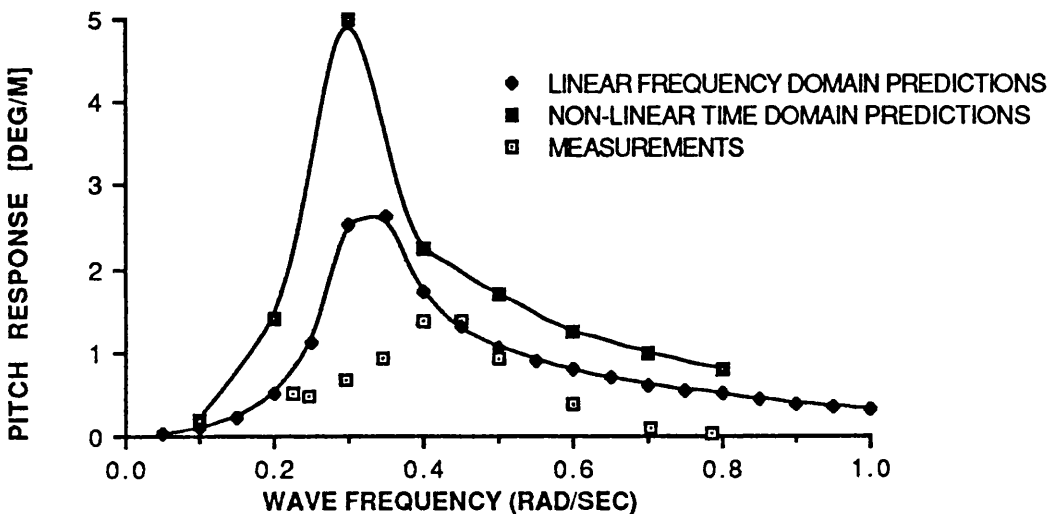


Fig. 6.24 Pitch Response Predictions of the Cylindrical Buoy

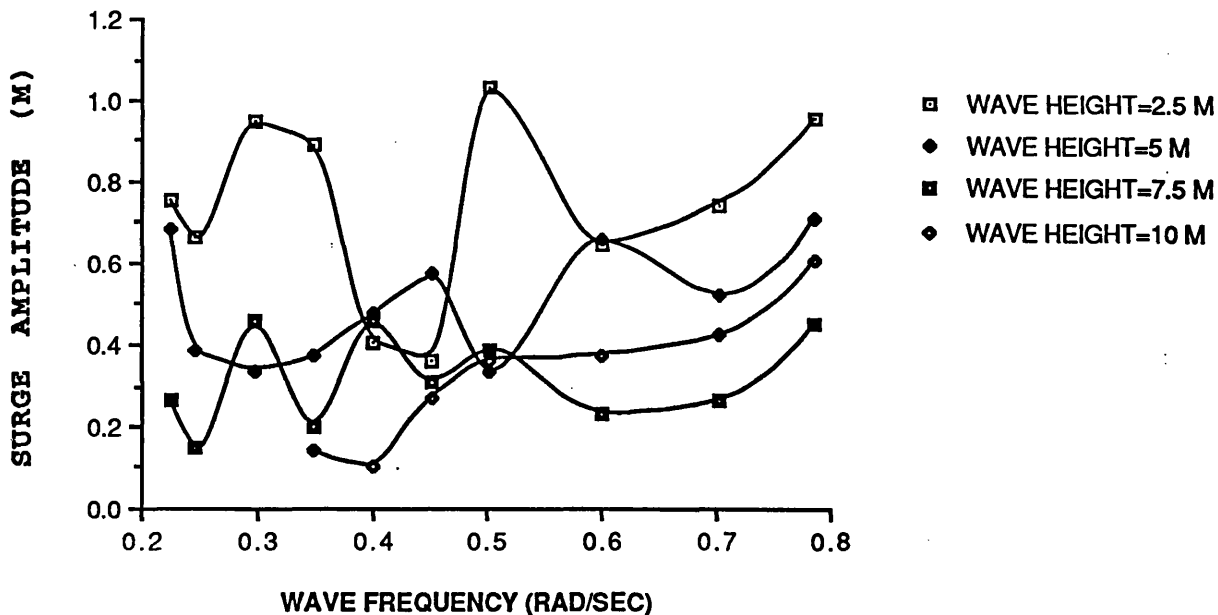


Fig. 6.25 Second-order Surge Response Measurements of the Conical Buoy

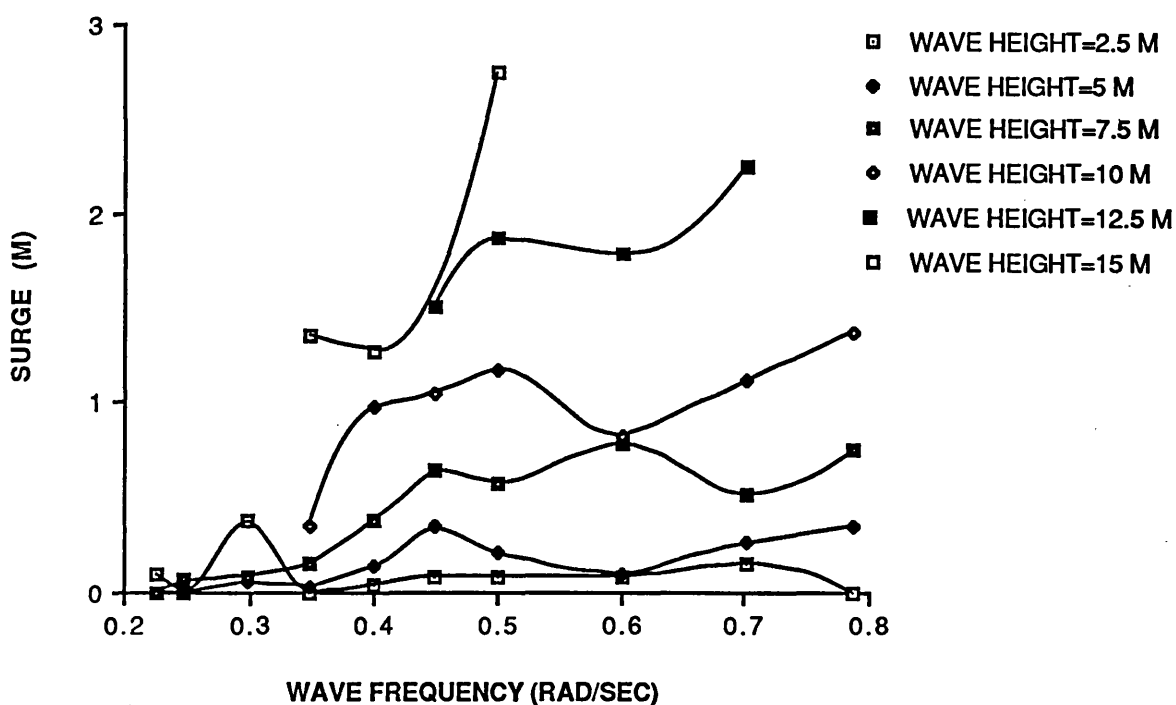


Fig. 6.26 Steady Surge Response Measurements of the Conical Buoy

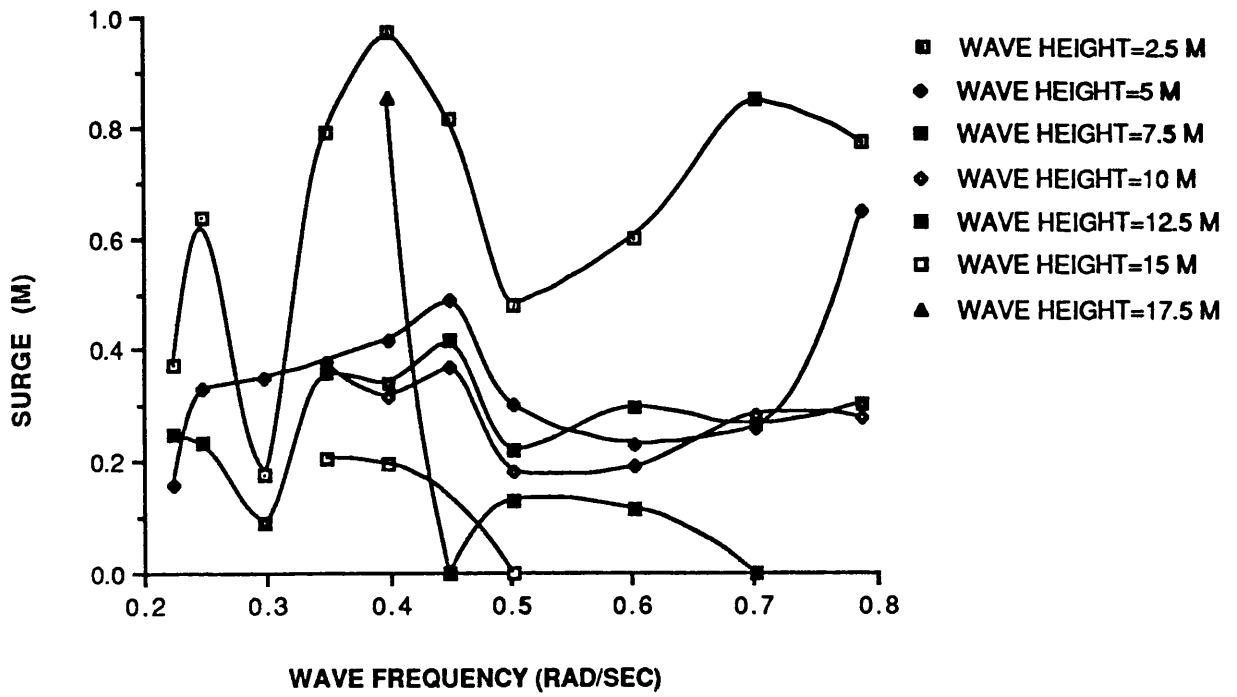


Fig. 6.27 Second-order Surge Response Measurements of the Cylindrical Buoy

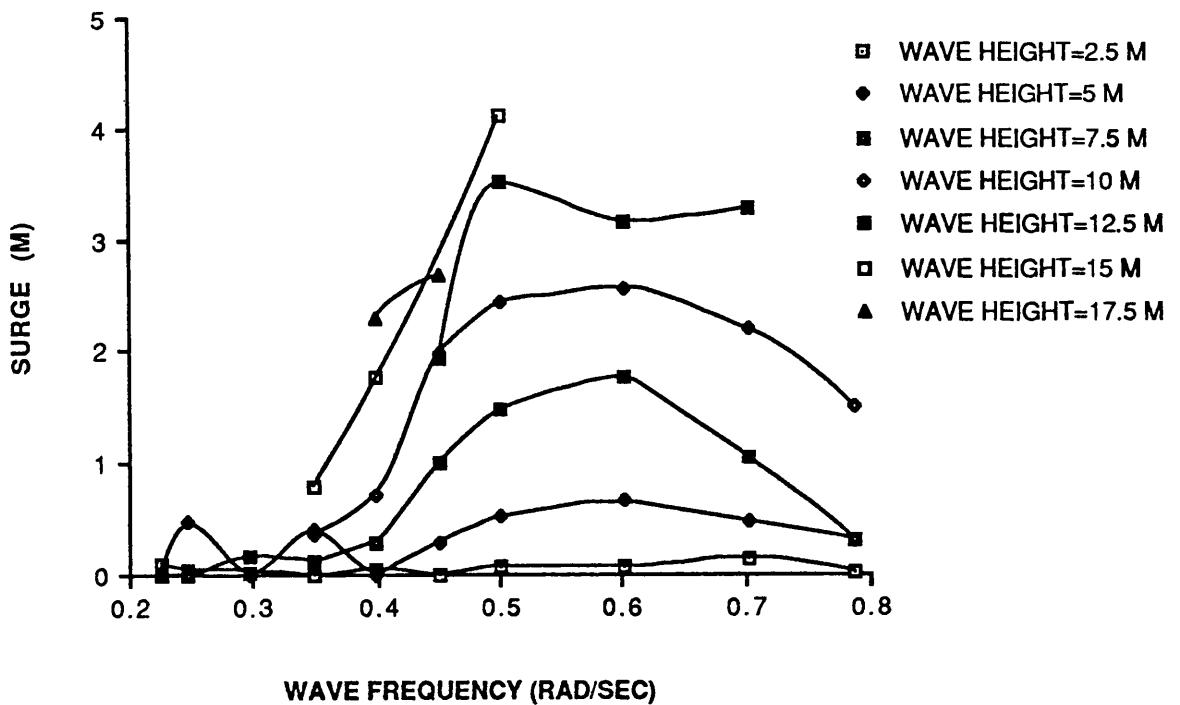


Fig. 6.28 Steady Surge Response Measurements of the Cylindrical Buoy

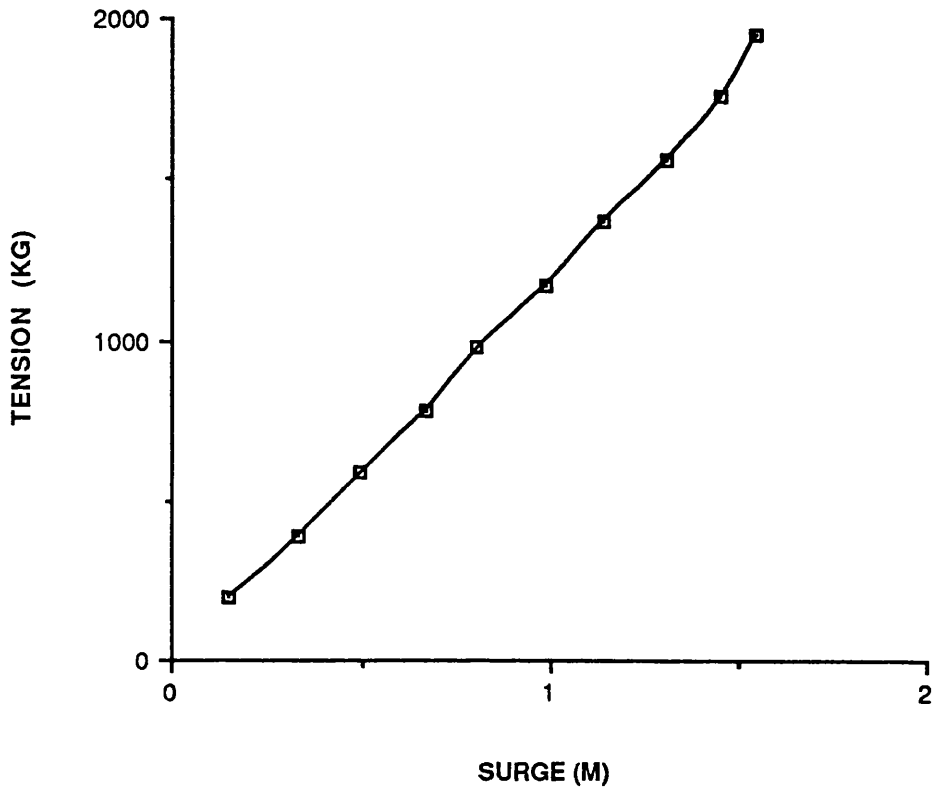


Fig. 6.29 Surge Stiffness of the Cylindrical Buoy due to the Surge Motion

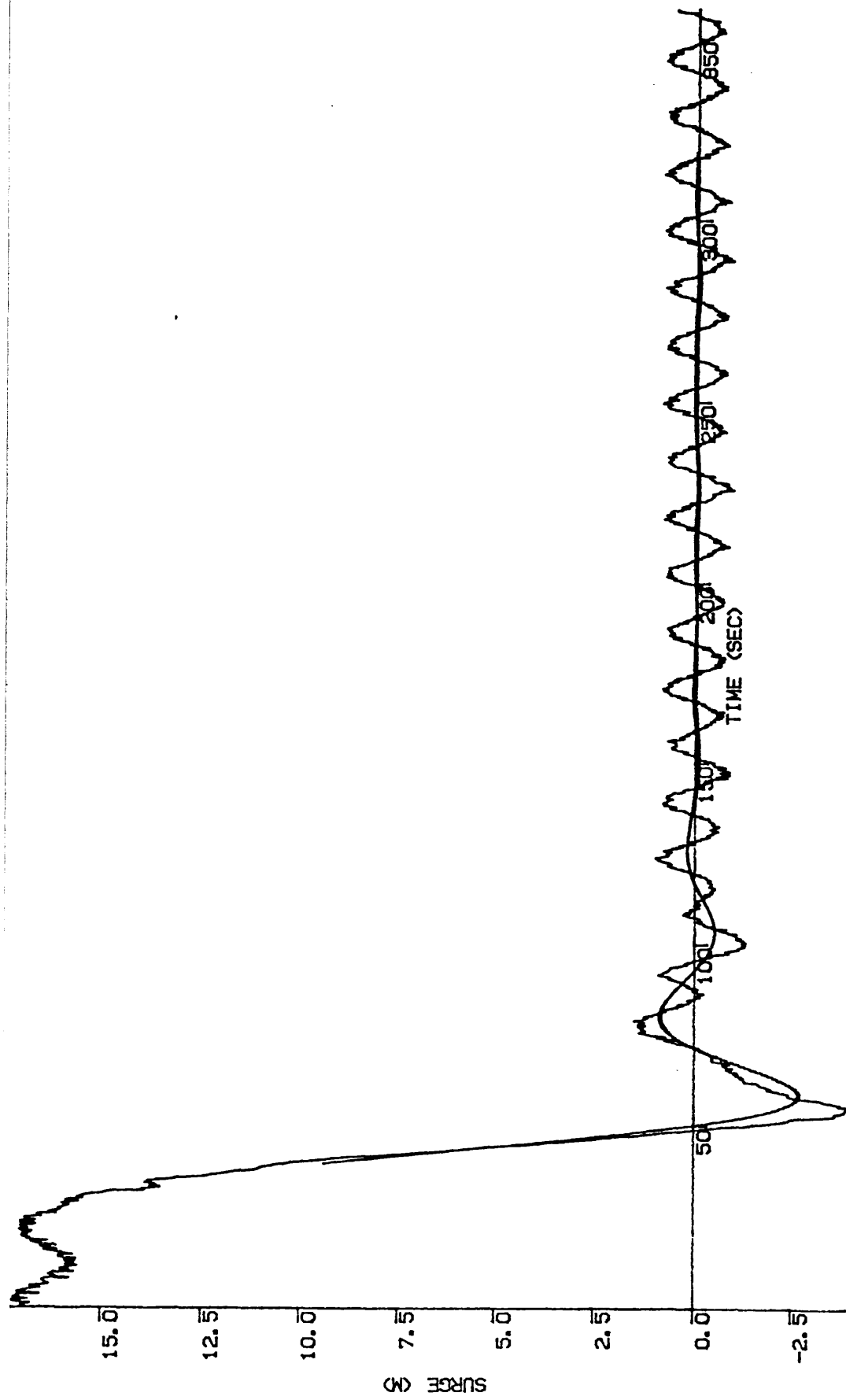


Fig. 6.30 Natural Frequency Test of the Moored Conical Buoy in Waves
 Wave Frequency=0.4 rad/sec, Wave Height=5 m
 (All values are in full scale)

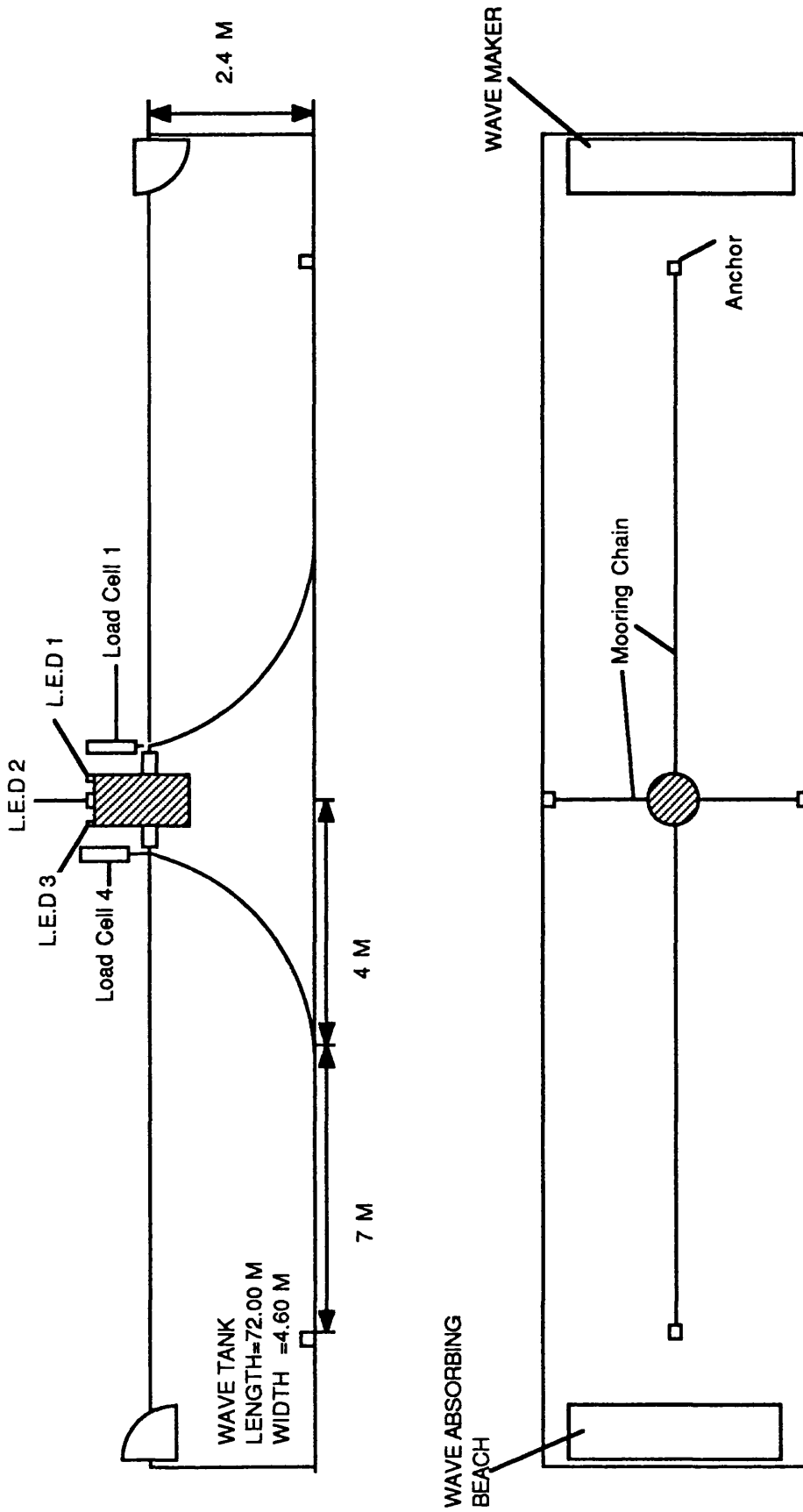


Fig. 6.31 : Experimental Test Set-up
 (Mooring Configuration A)

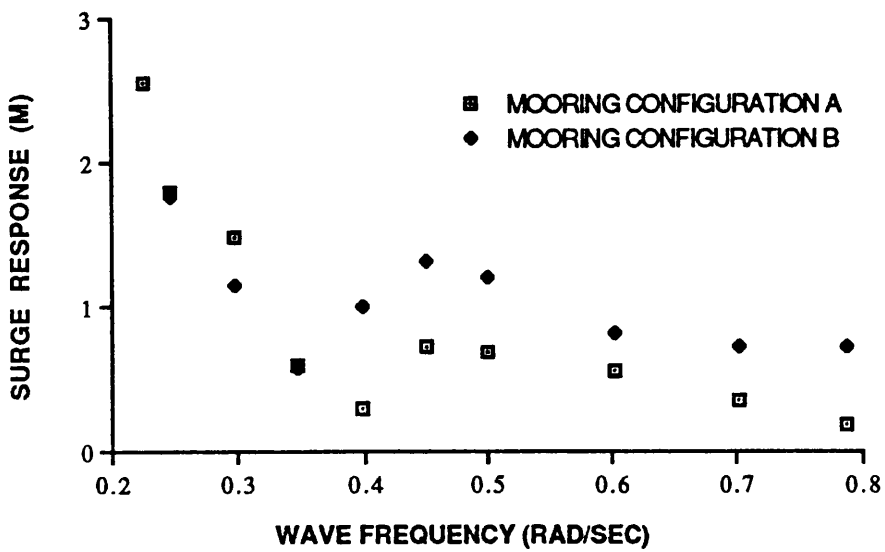


Fig. 6.32 Surge Response Measurements of the Conical Buoy
Wave Height=5 m

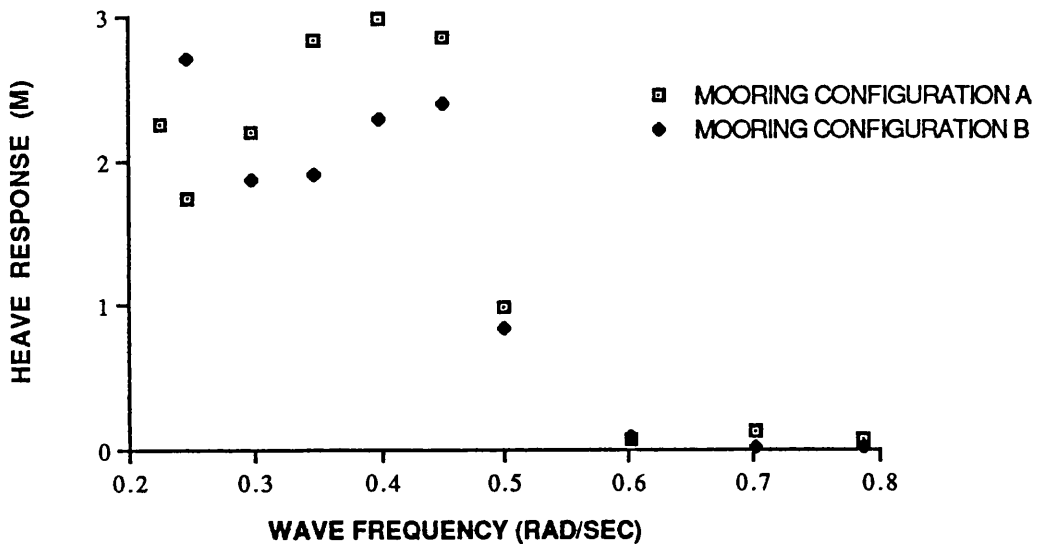


Fig. 6.33 Heave Response Measurements of the Conical Buoy
Wave Height=5 m

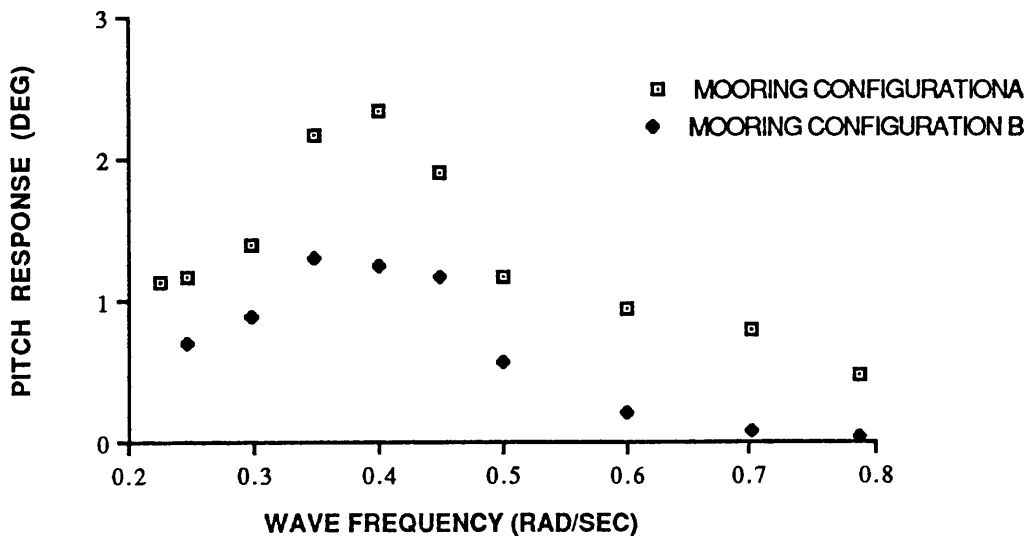


Fig. 6.34 Pitch Response Measurements of the Conical Buoy
Wave Height=5 m

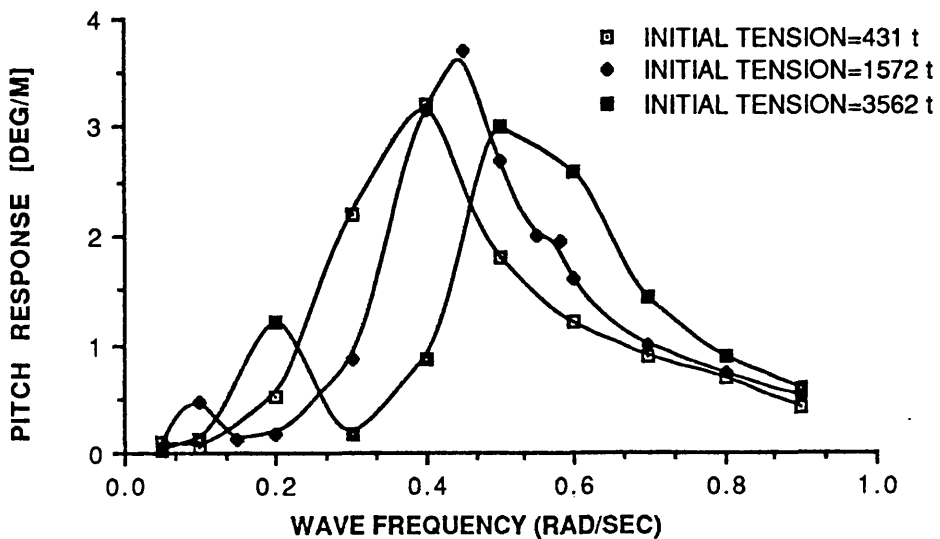
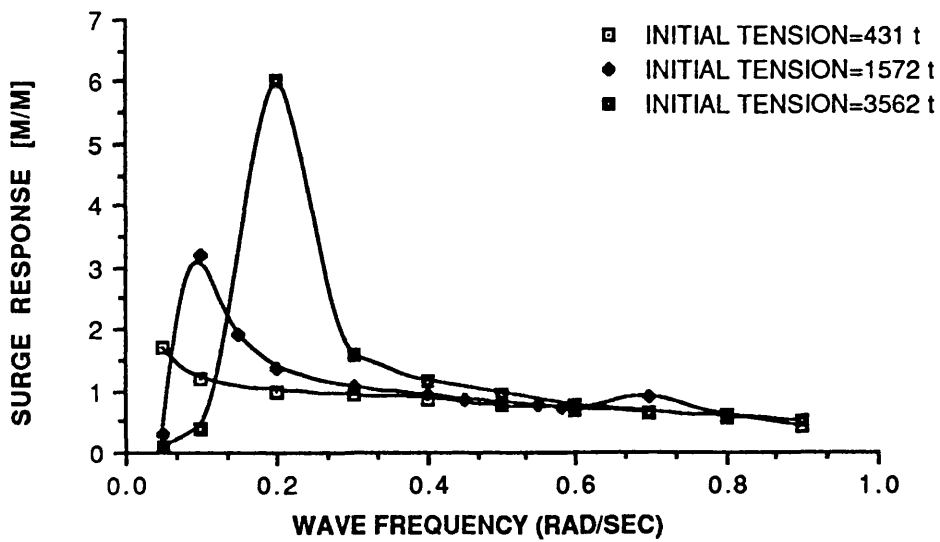
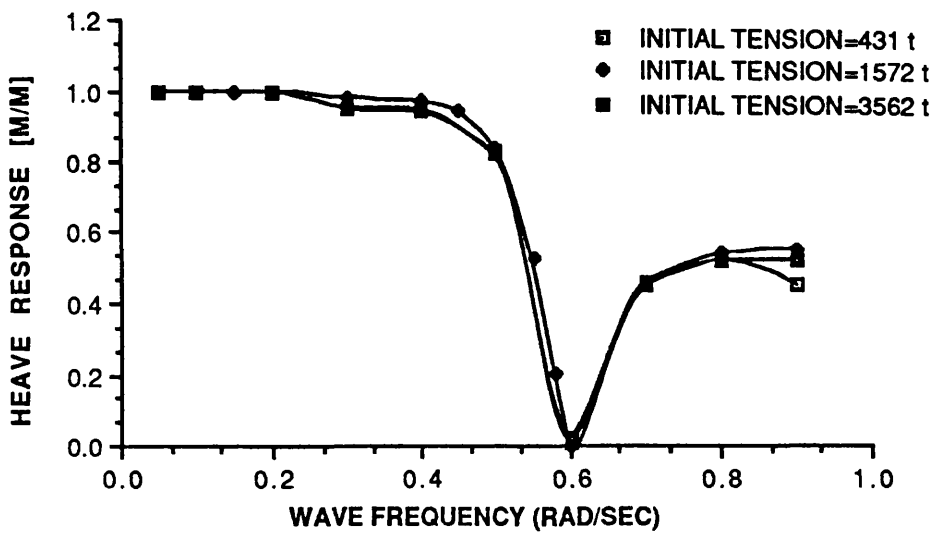


Fig. 6.35 Motion Response Predictions of the Conical Buoy

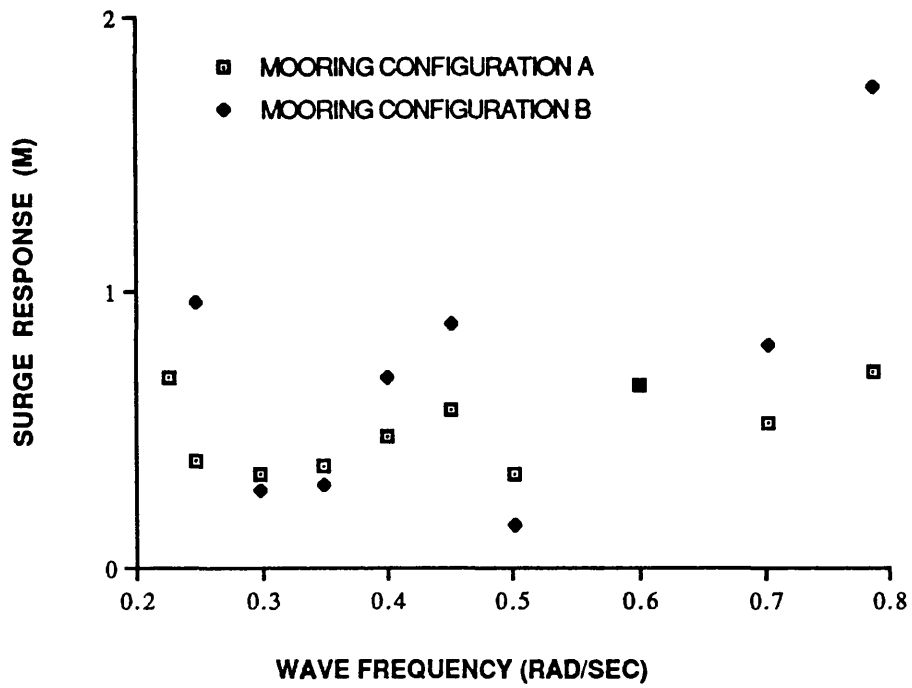


Fig. 6.36 Second-order Surge Measurements of the Conical Buoy
Wave Height=5 m

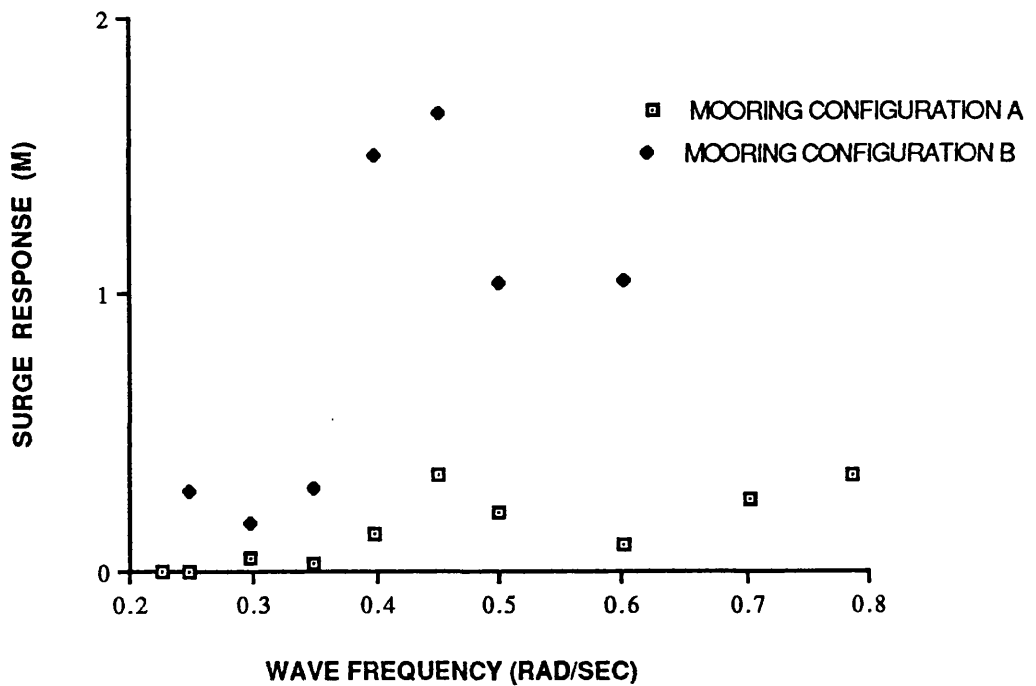


Fig. 6.37 Steady Surge Measurements of the Conical Buoy
Wave Height=5 m

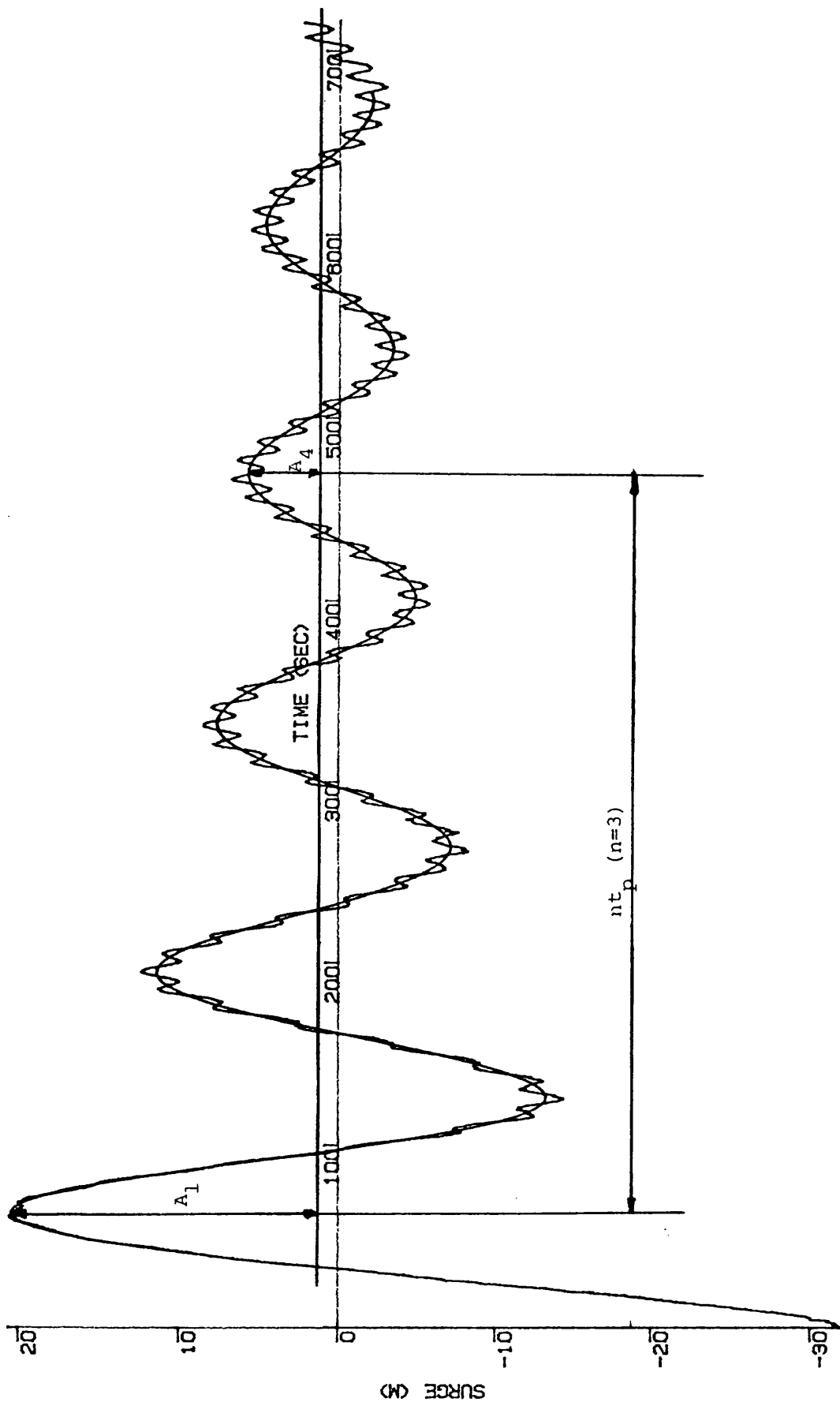


Fig. 6.38 Calculation of the Damping Coefficient from the Rate of Decaying Oscillations

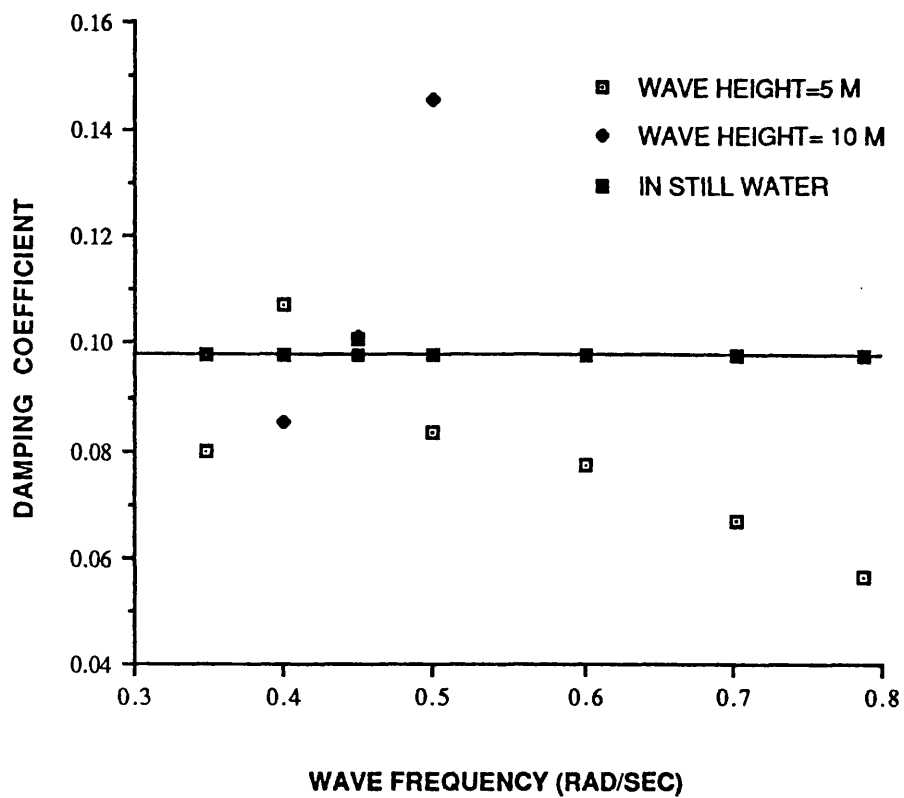


Fig. 6.39 Damping Coefficients of the Conical Buoy (Mooring Configuration B)

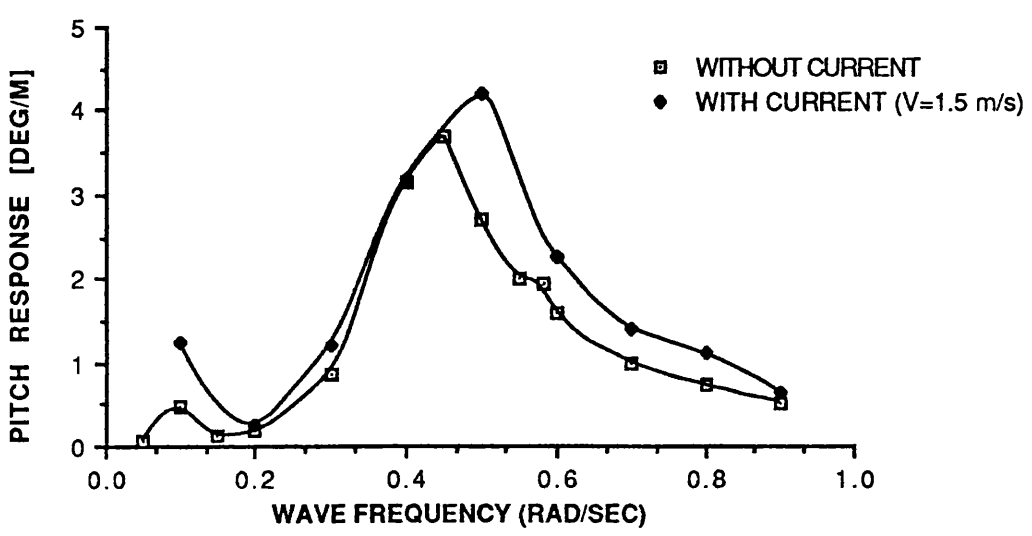
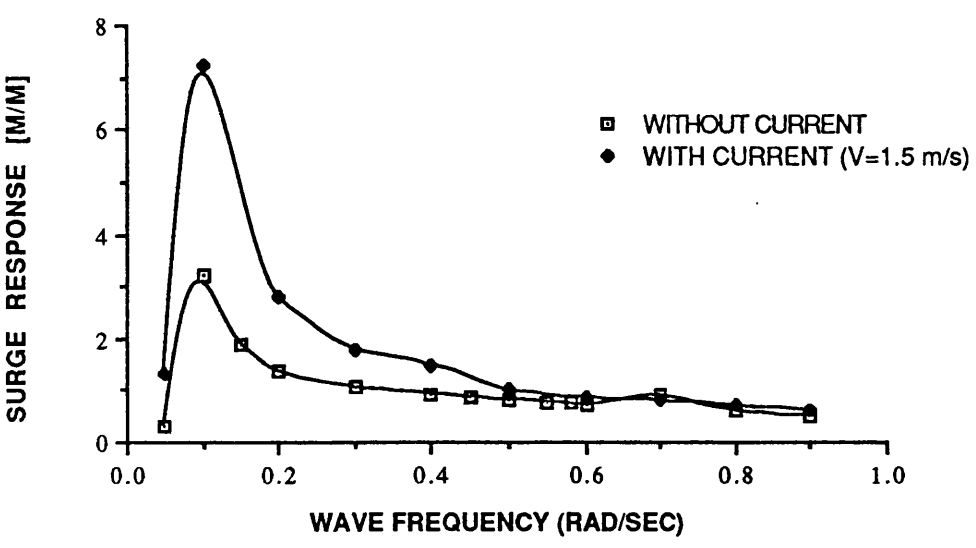
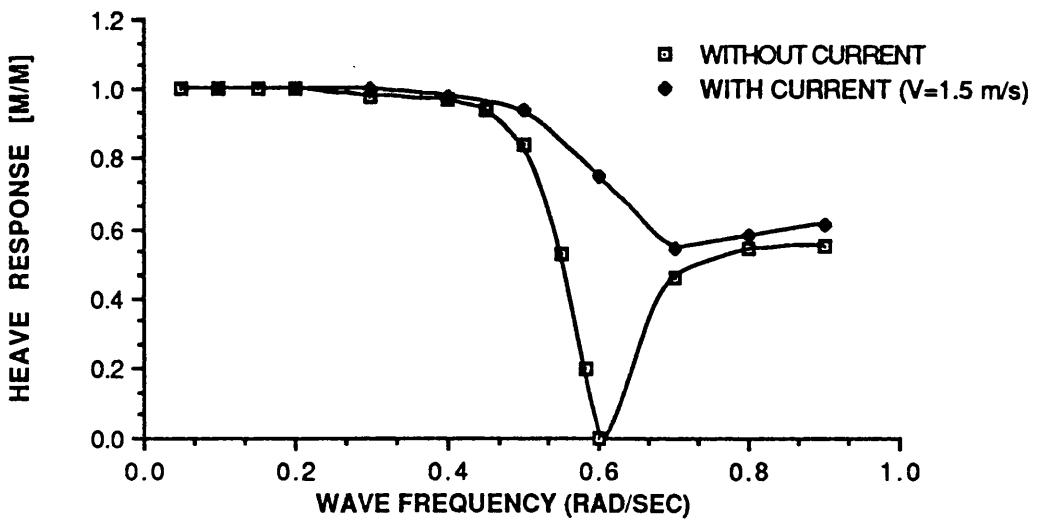


Fig. 6.40 Current effect on the Motion Responses of the Cylindrical Buoy

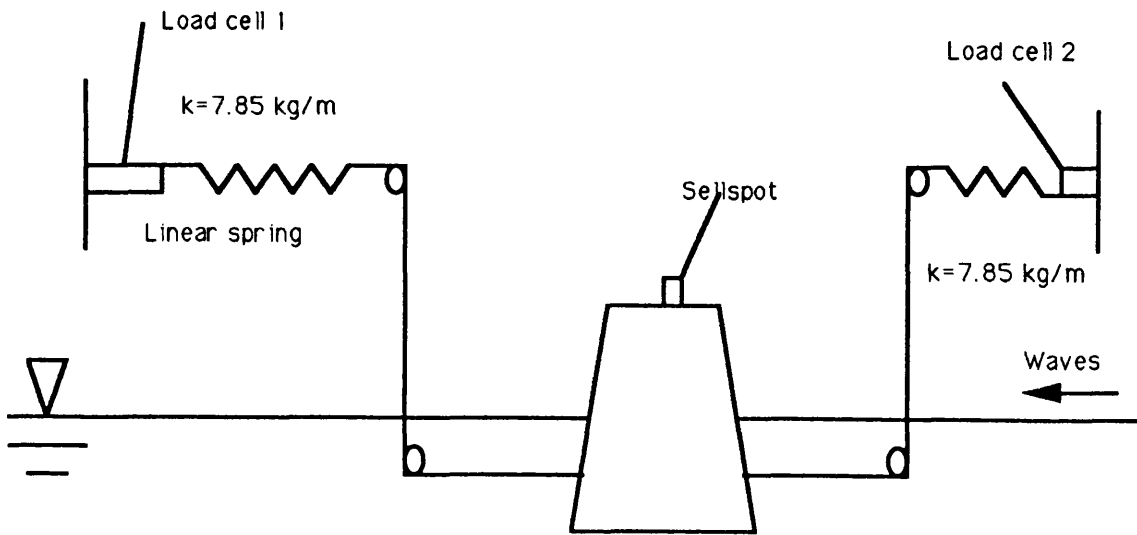


Fig. 6.41 Experimental Test Set-up A

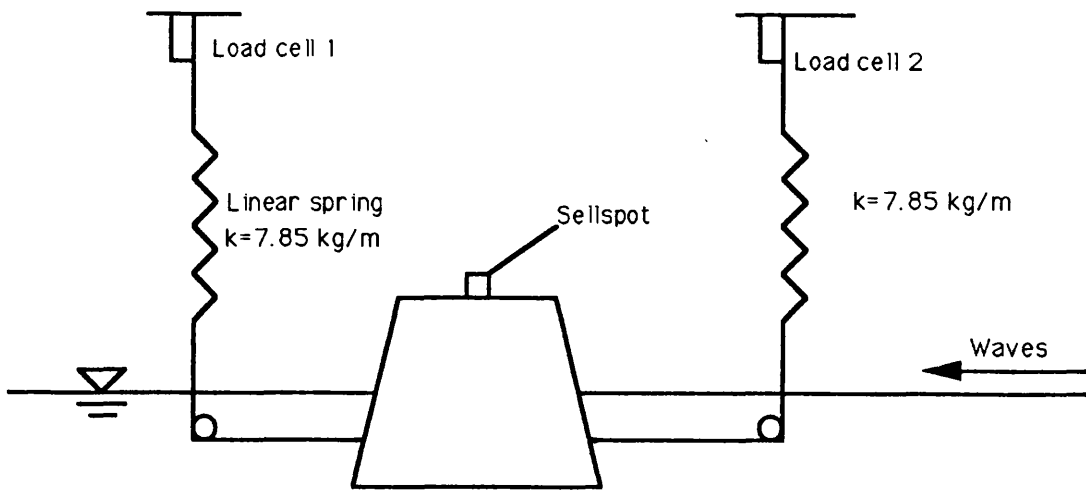


Fig. 6.42 Experimental Test Set-up B

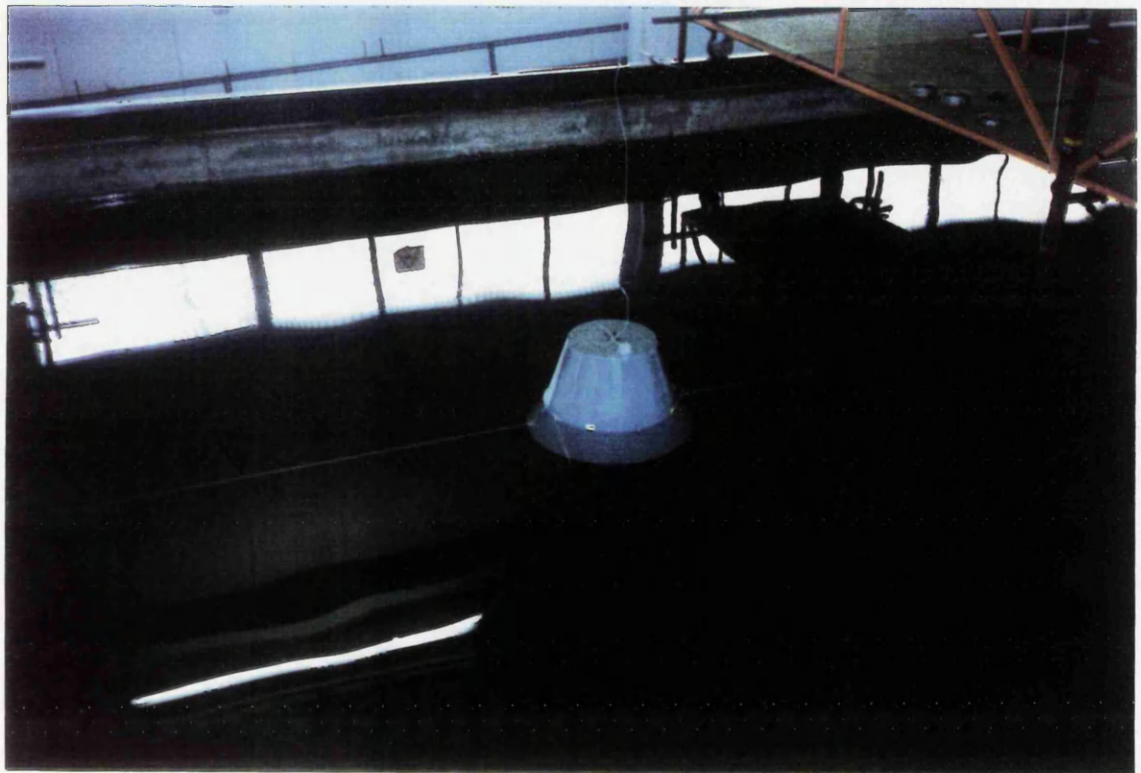
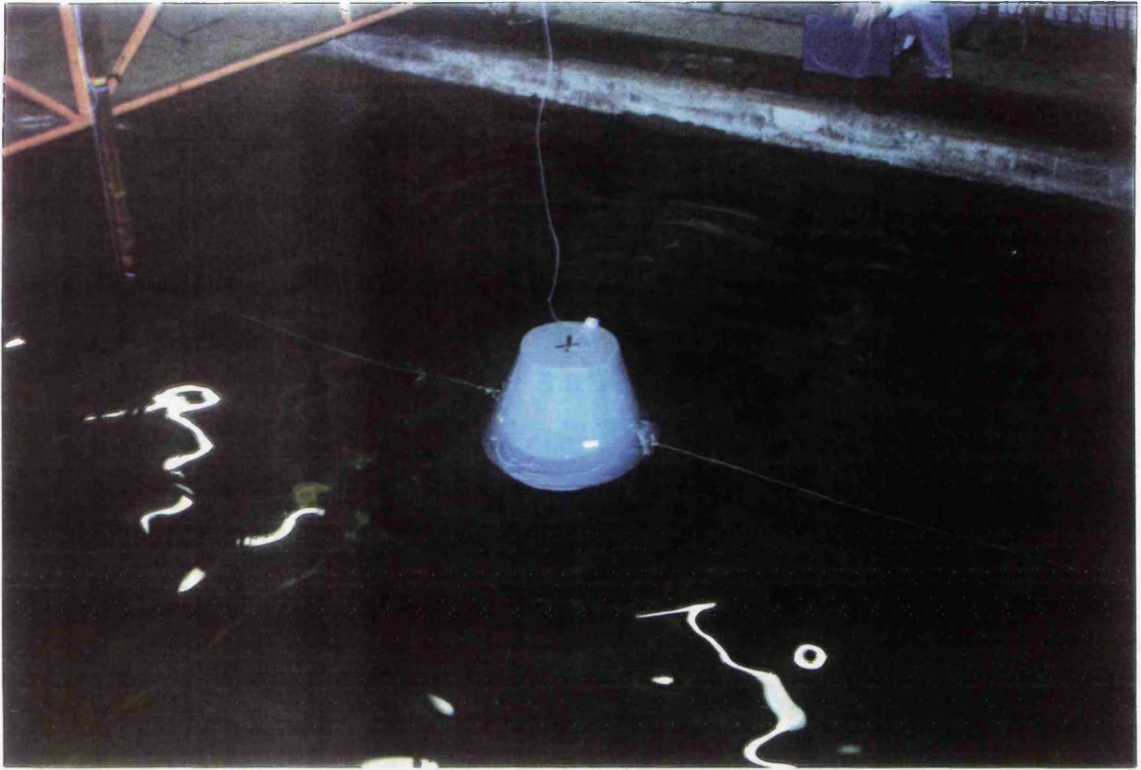


Fig. 6.43 Natural Frequency Test of the
Conical Buoy with Linear Springs

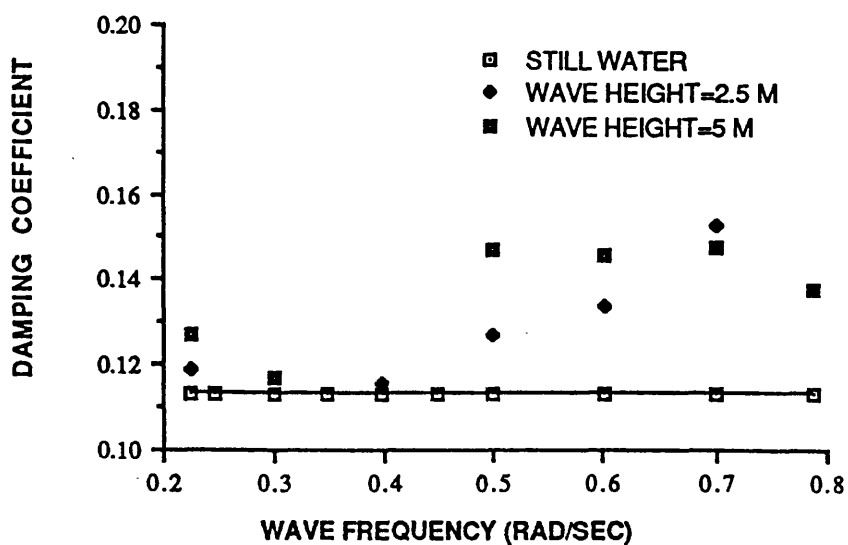


Fig. 6.44 Damping Coefficient of the Conical Buoy (Test Set-up A)

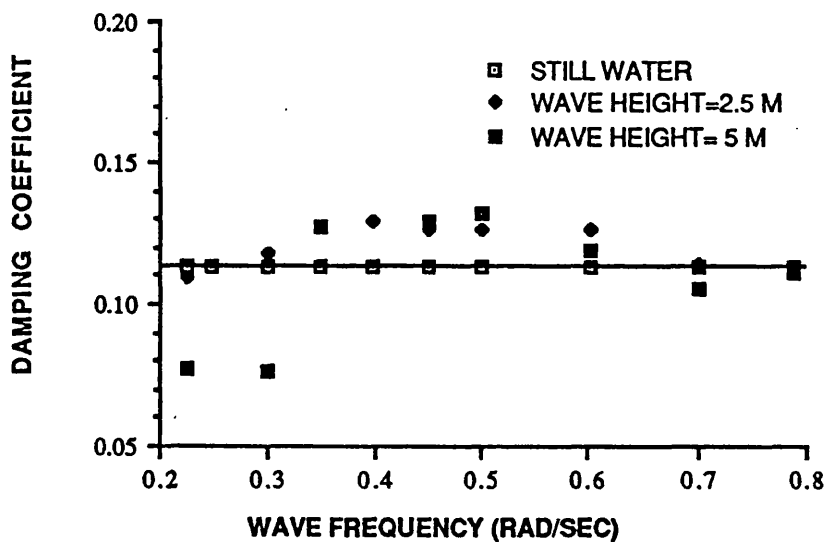


Fig. 6.45 Damping Coefficient of the Conical Buoy (Test Set-up B)

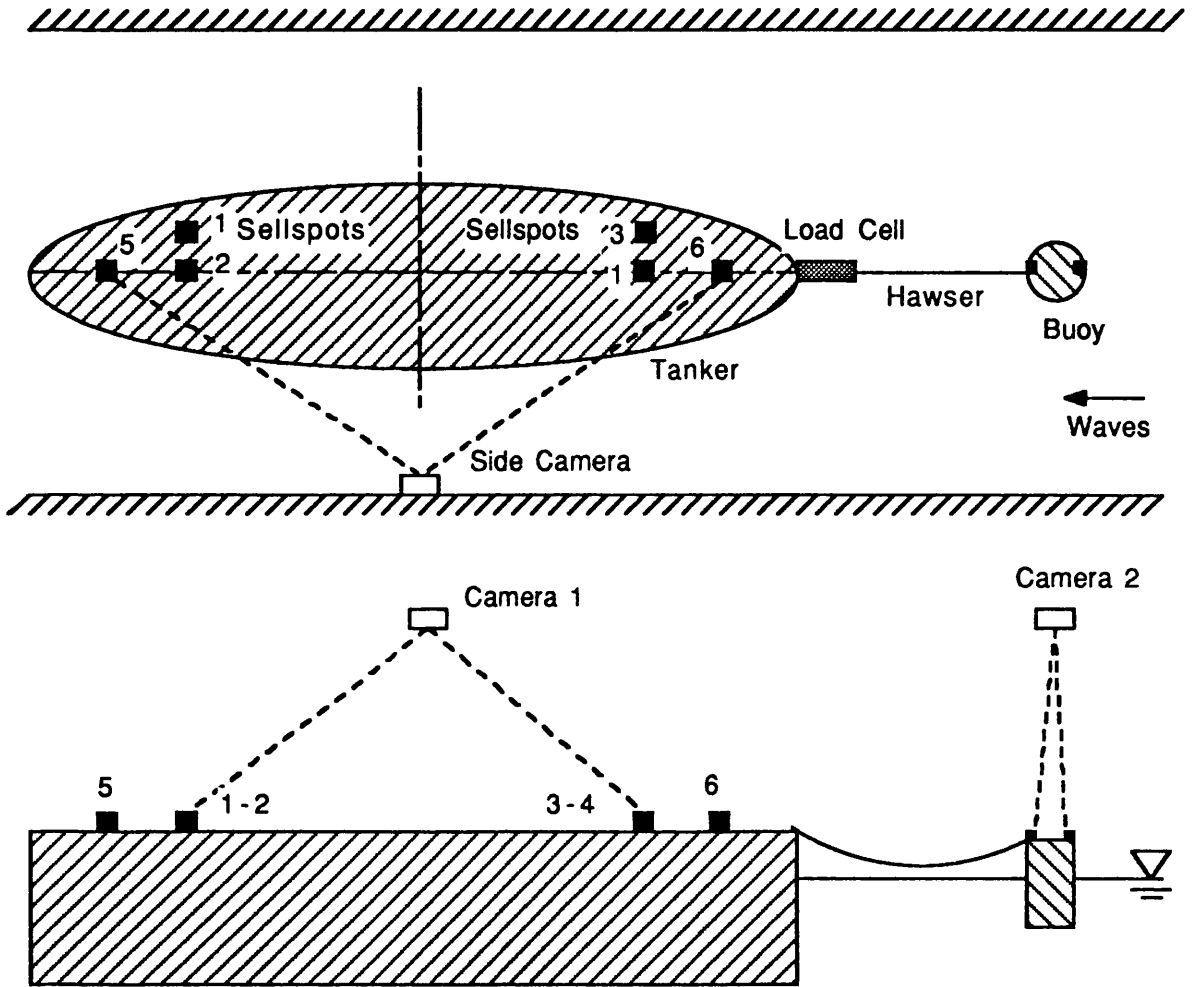


Fig. 6.46 Instrumentation

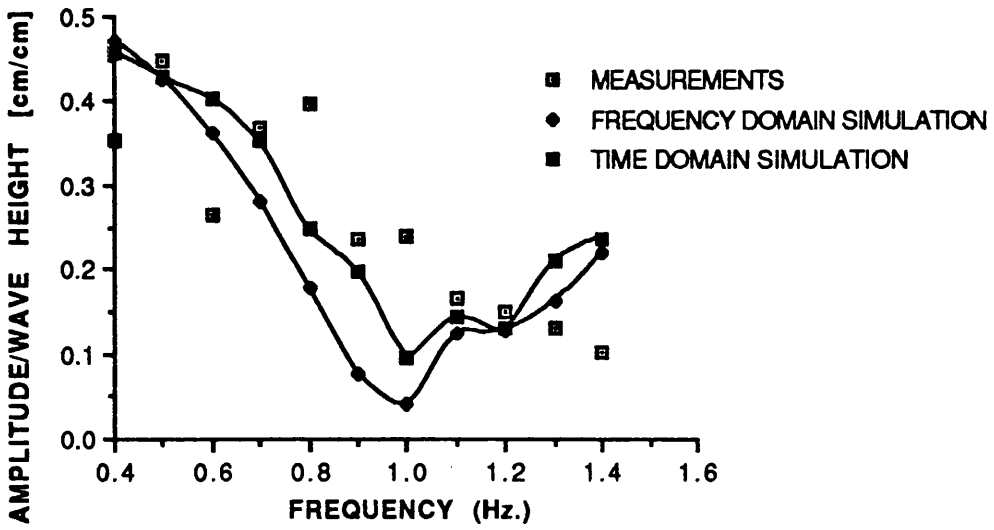


Fig. 6.47 Surge Motion of the Buoy
Co-linear Environmental Forces

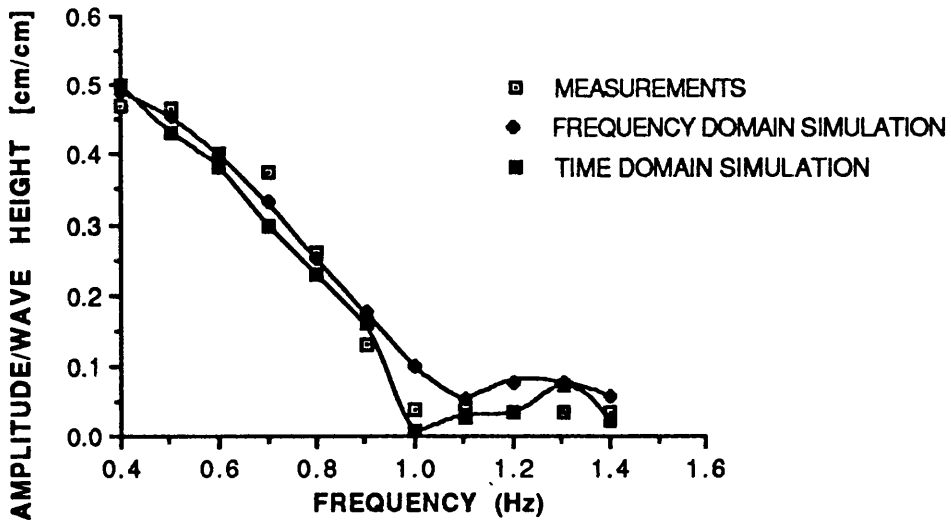


Fig. 6.48 Surge Motion of the Tanker
Co-linear Environmental Forces

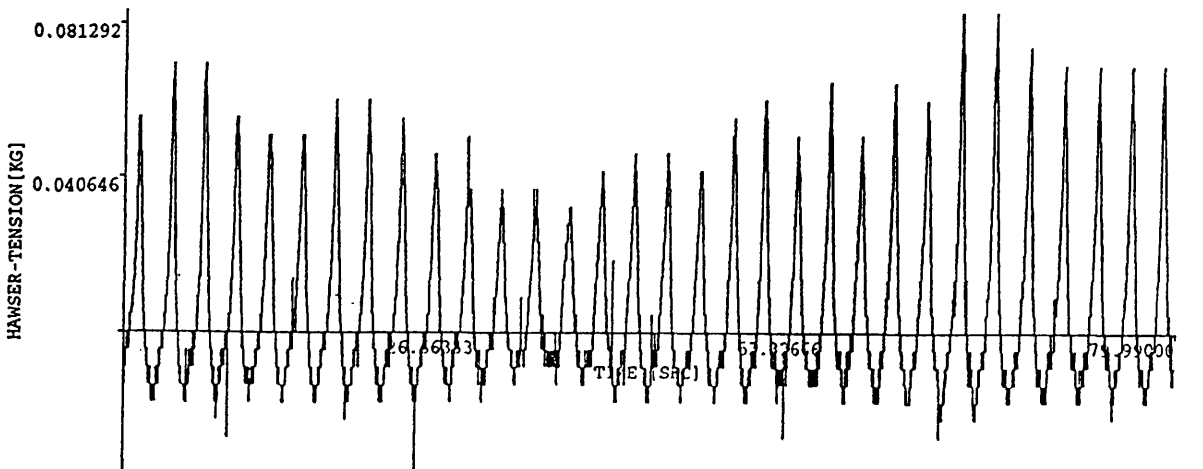
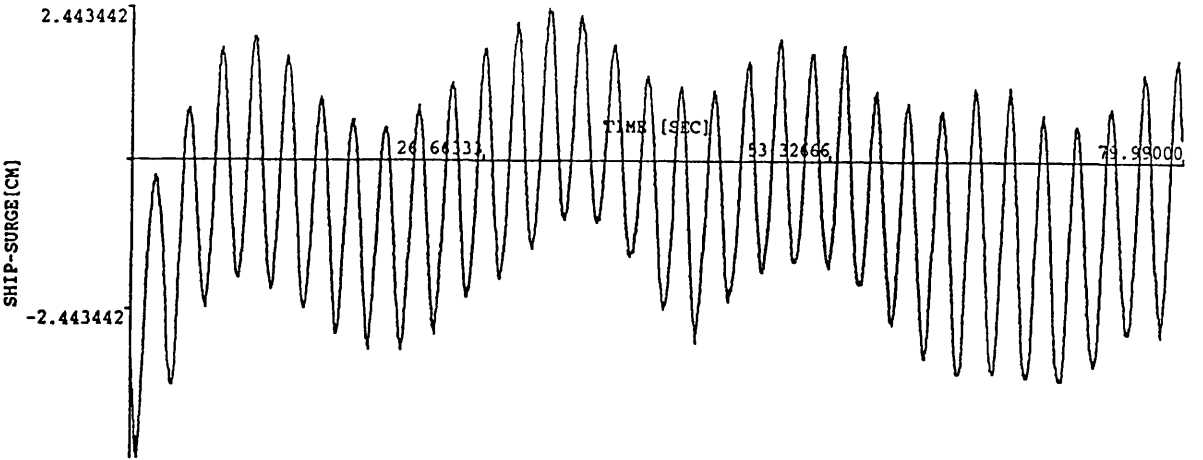
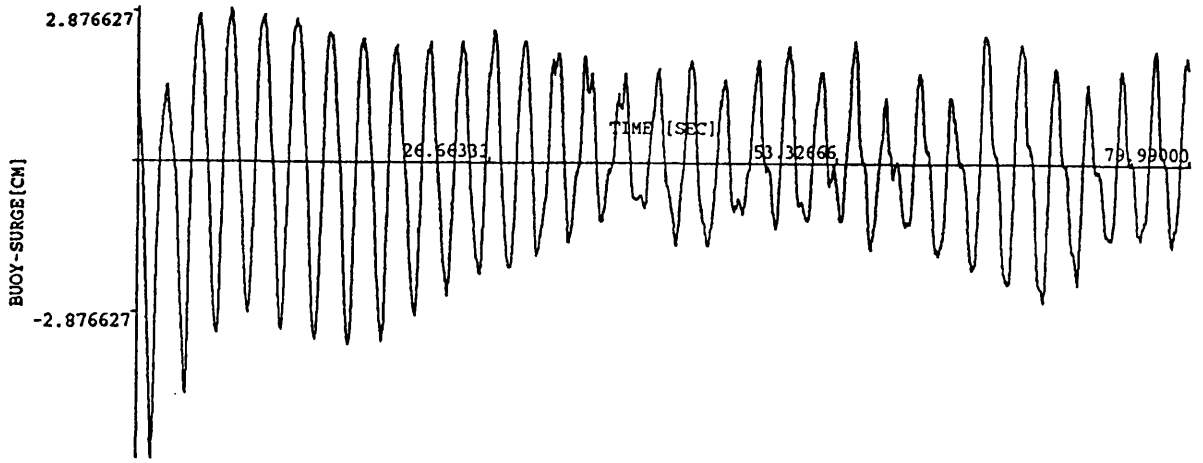


Fig. 6.49 Motion response and Hawser Tension Measurements
 in Co-linear Current and Wave
 Wave Frequency=0.4 Hz, Wave Height=4.10 cm
 Current Force=6 gr

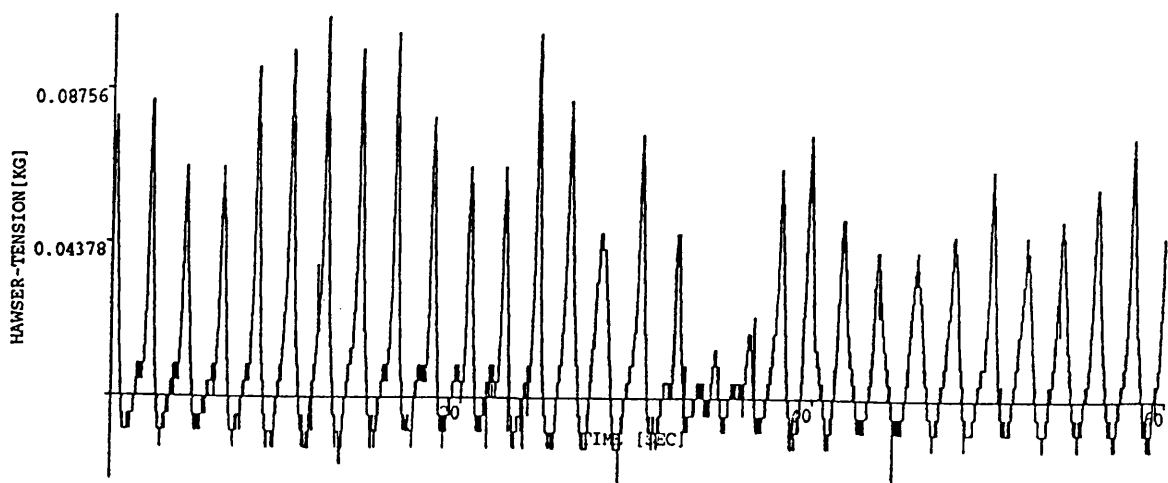
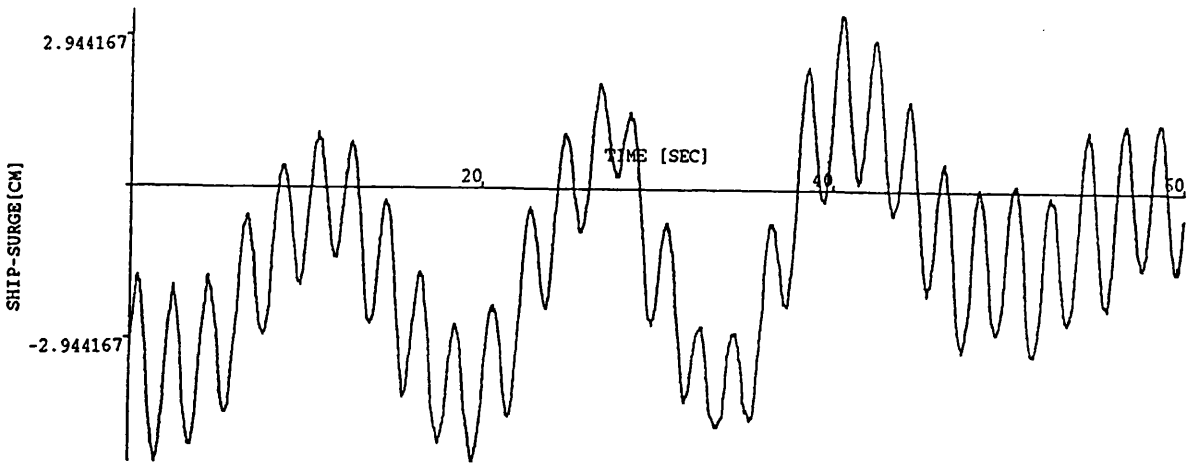
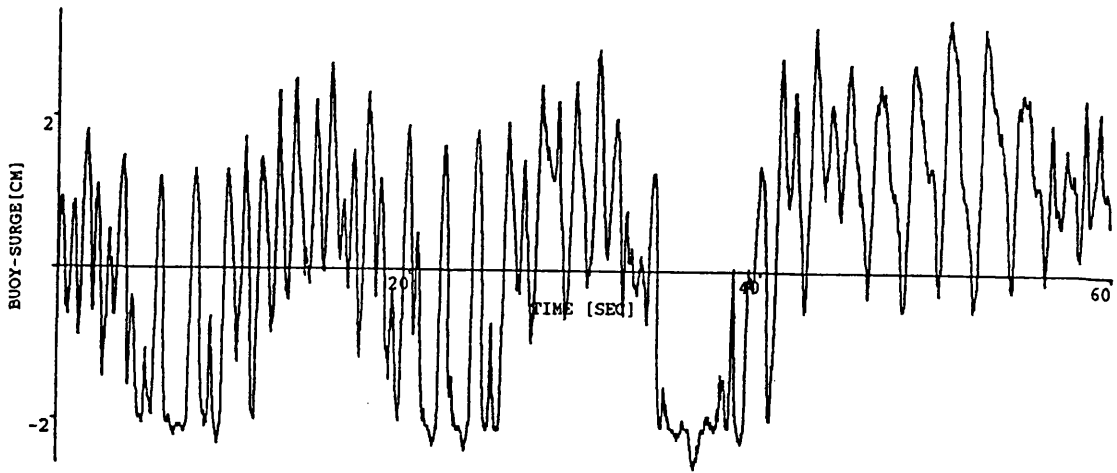


Fig. 6.50 Motion response and Hawser Tension Measurements
 in Co-linear Current and Wave
 Wave Frequency=0.5 Hz, Wave Height=3.70 cm
 Current Force=6 gr

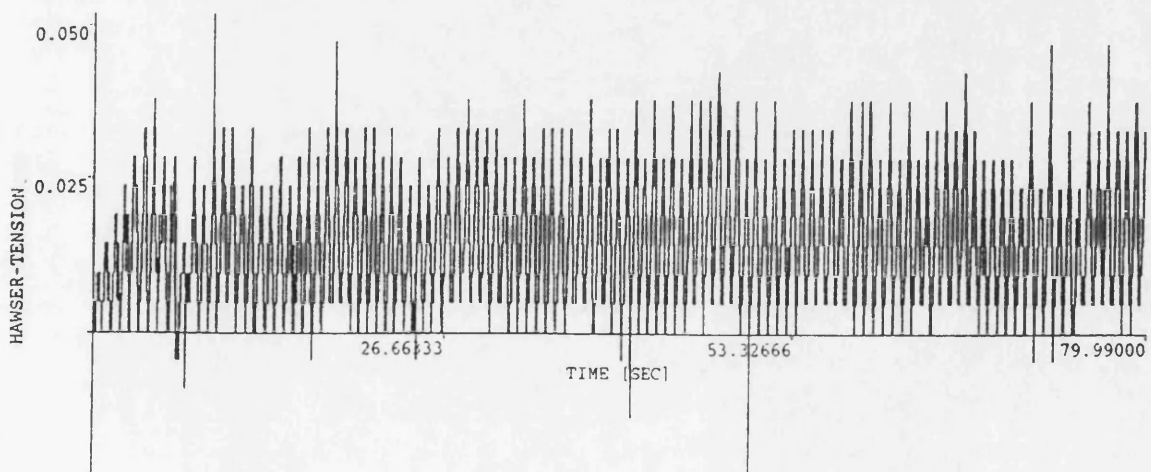
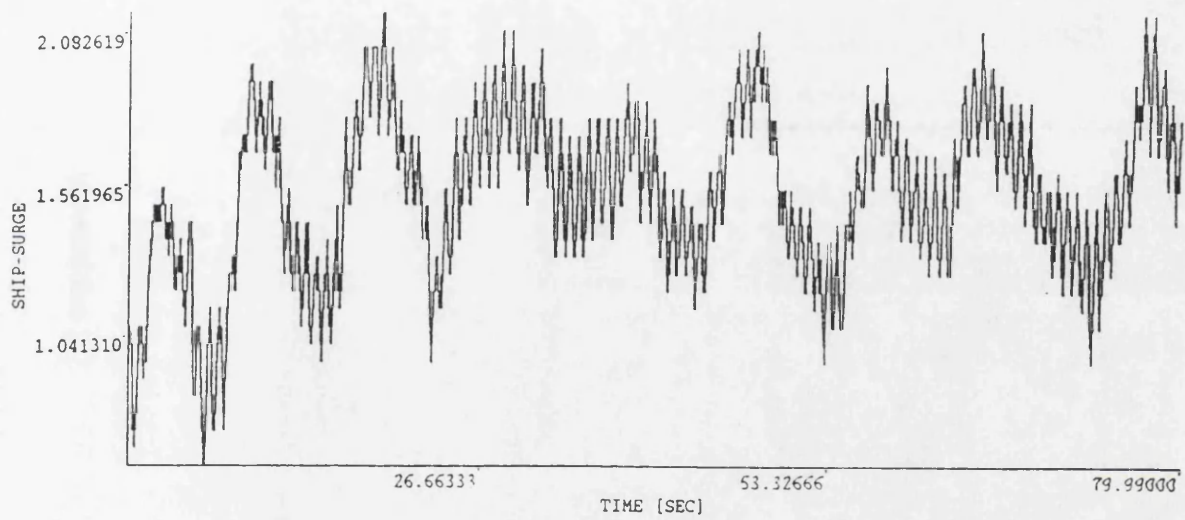
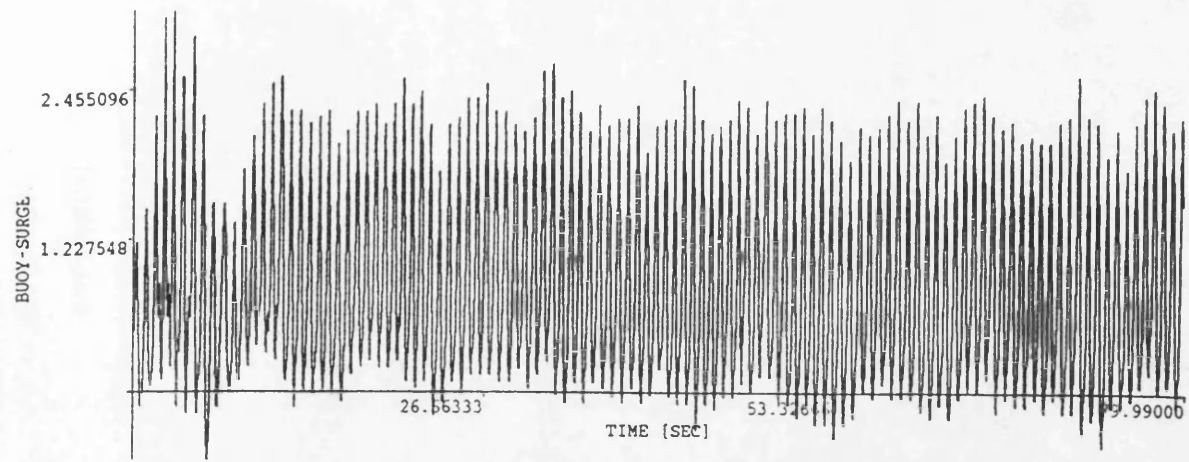


Fig. 6.51 Motion response and Hawser Tension Measurements
 in Co-linear Current and Wave
 Wave Frequency=1.4 Hz, Wave Height=3.50 cm
 Current Force=6 gr

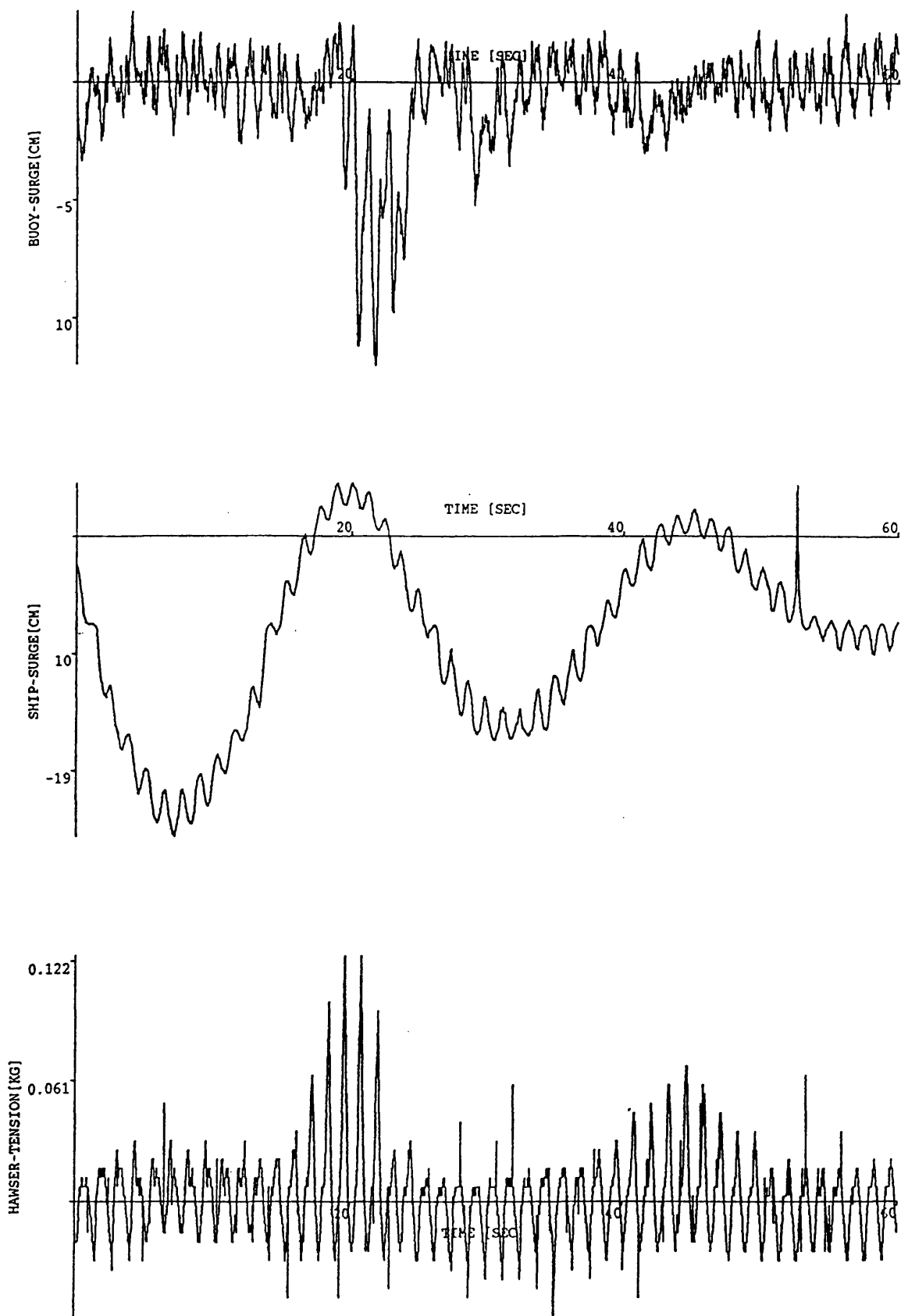


Fig. 6.52 Motion response and Hawser Tension Measurements
in Co-linear Current and Wave
Wave Frequency=0.8 Hz, Wave Height=5.57 cm
Current Force=6 gr

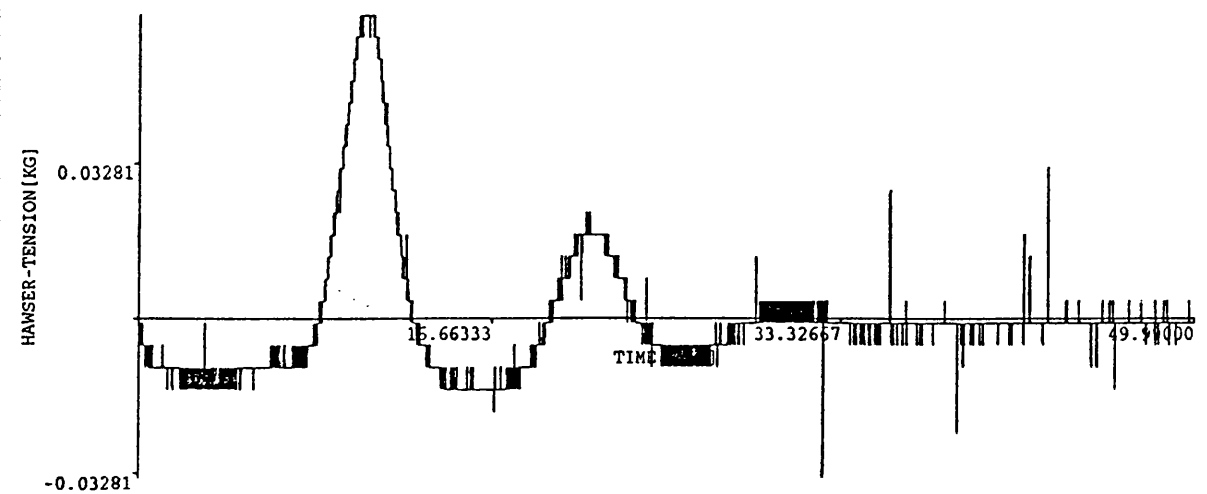
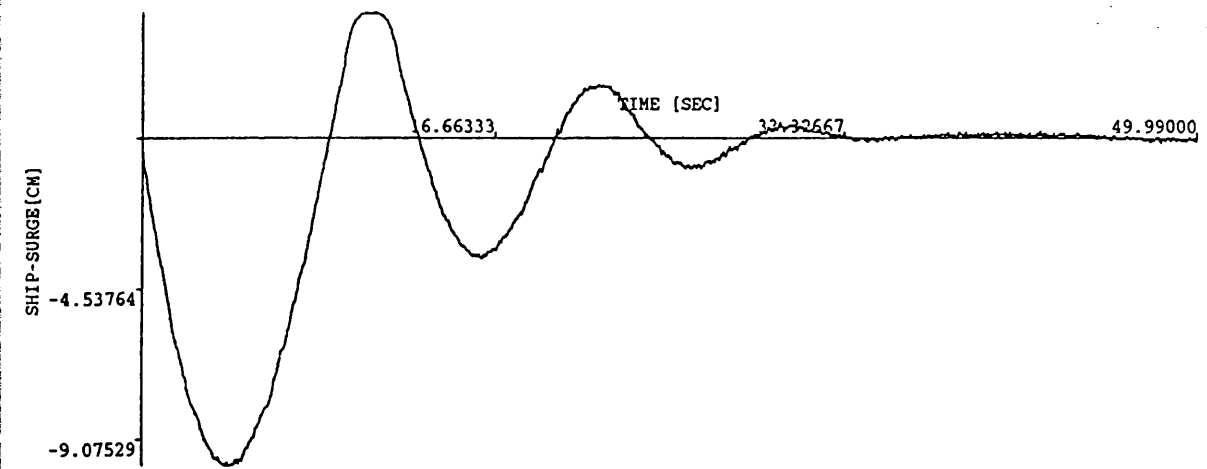
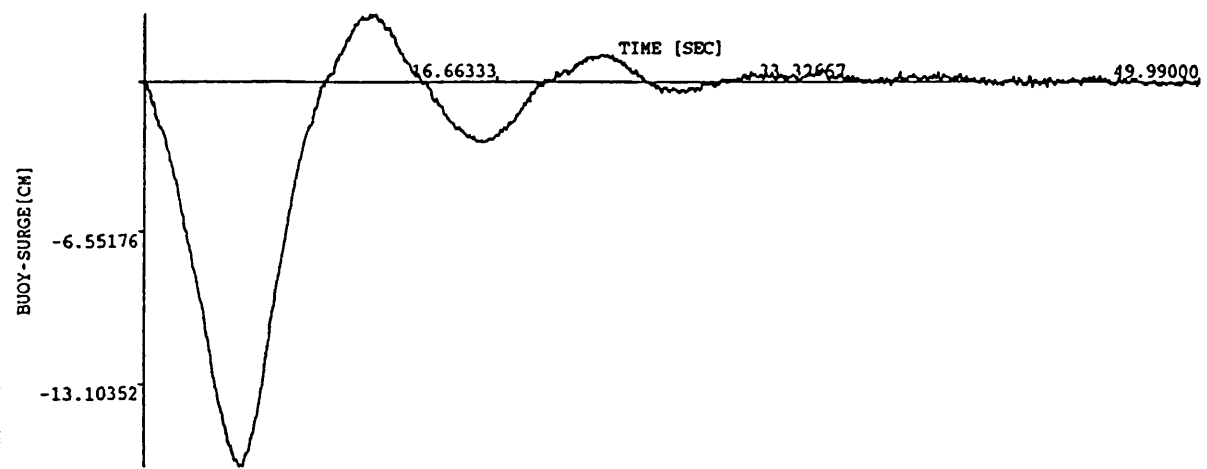


Fig. 6.53 Natural Frequency Test of the Tanker-Buoy System in Current
Current Force=26 gr

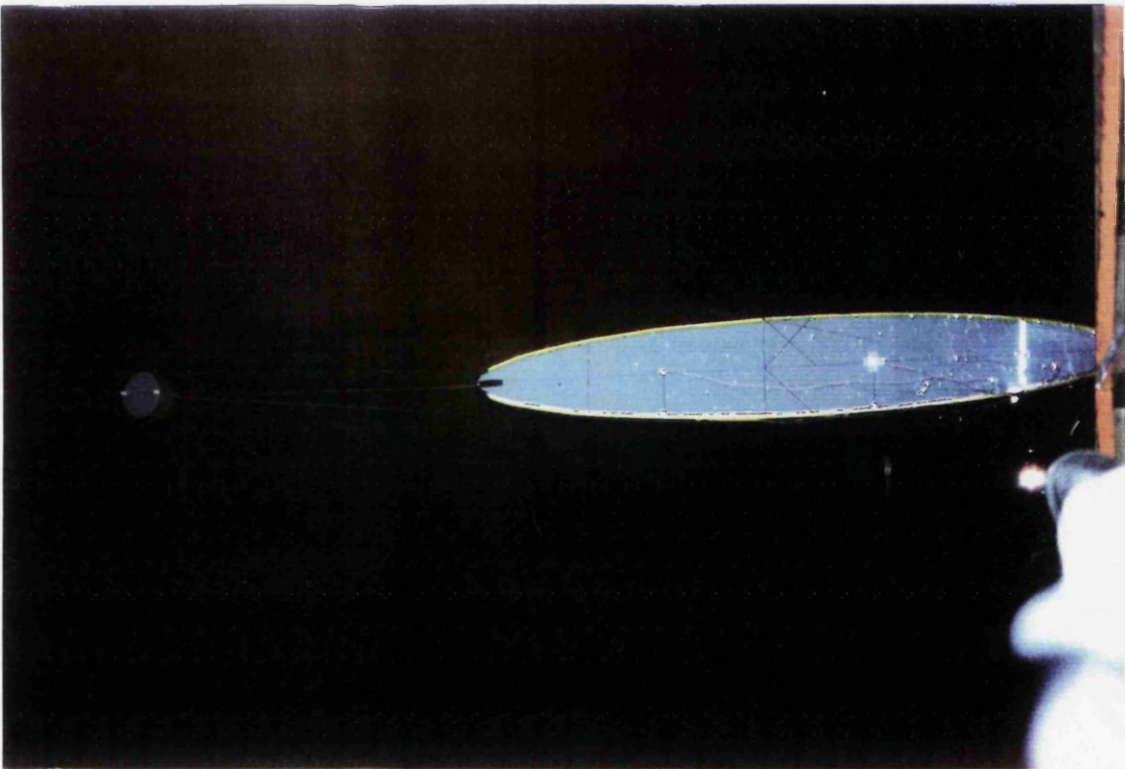
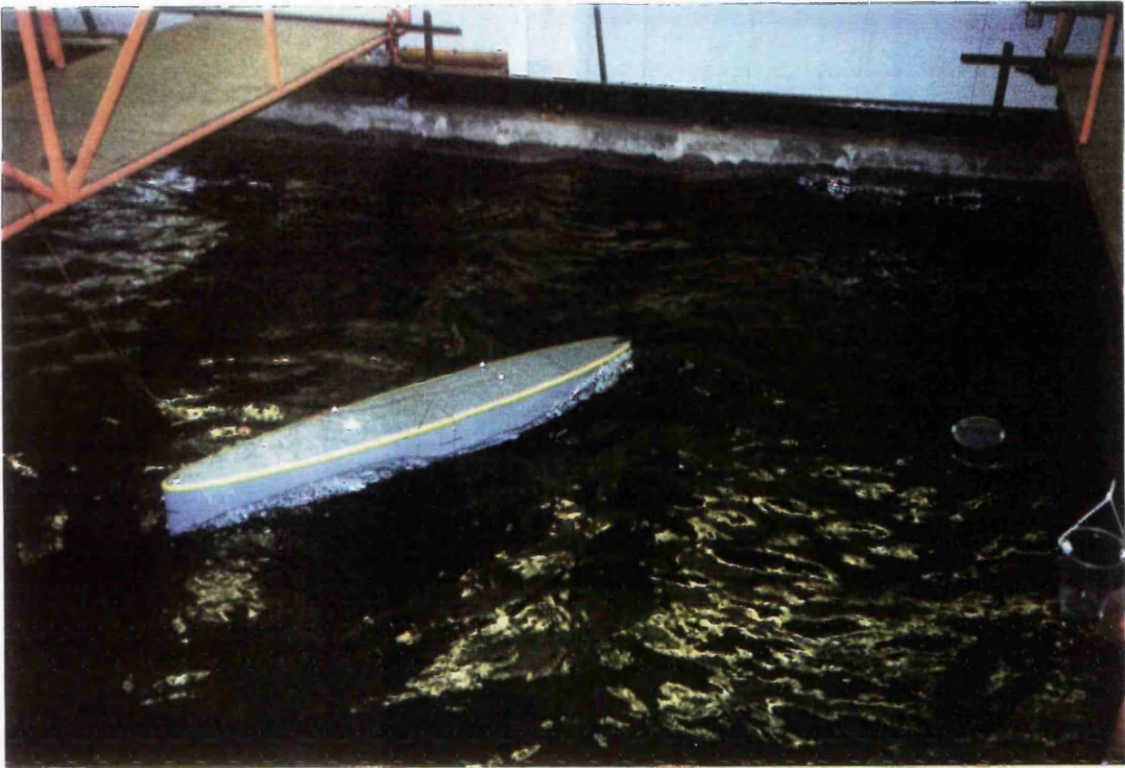


Fig. 6.54 Oblique Angle Tests of the Tanker-Buoy System

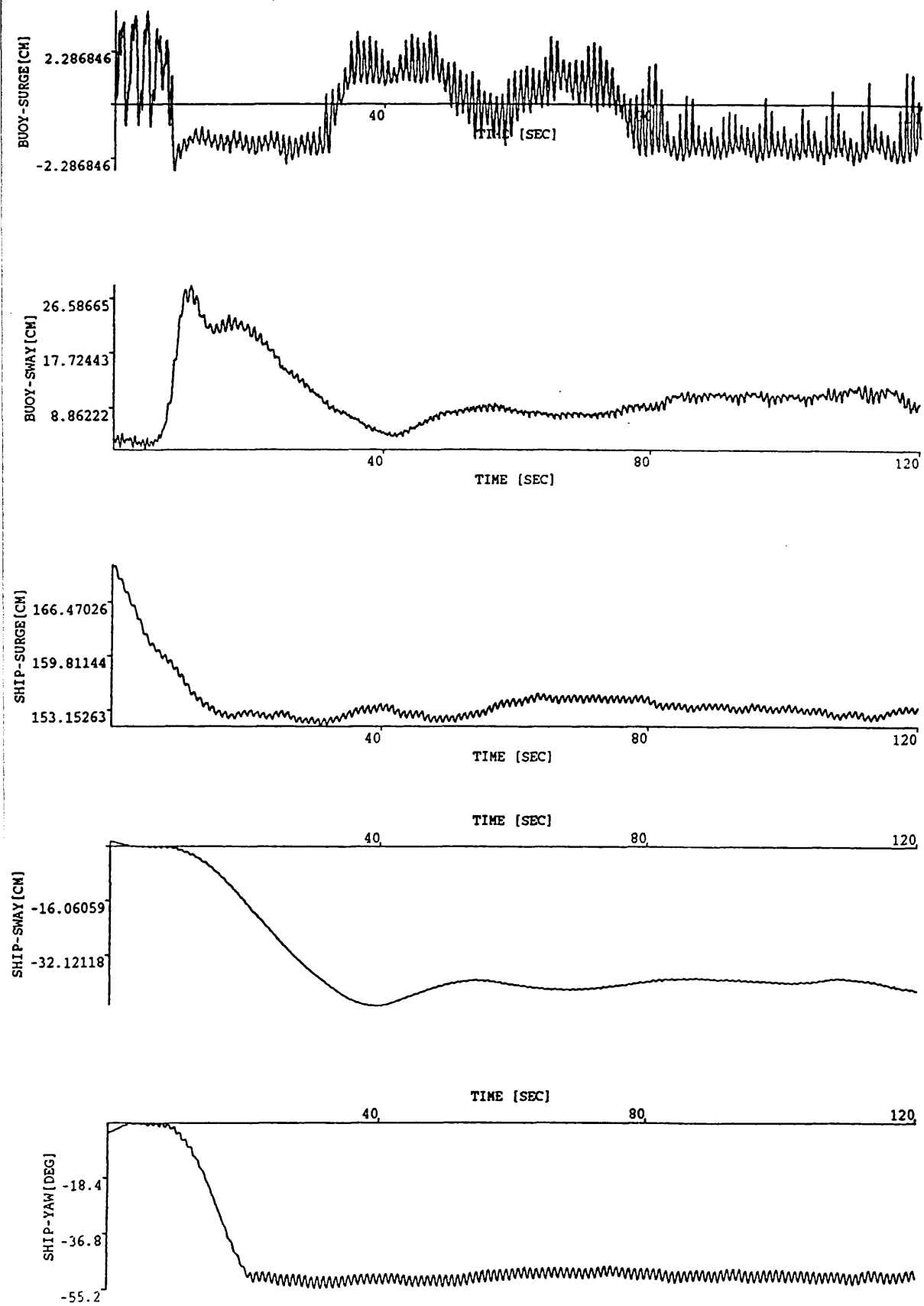


Fig. 6.55 Oblique Angle Test, Run No. 11

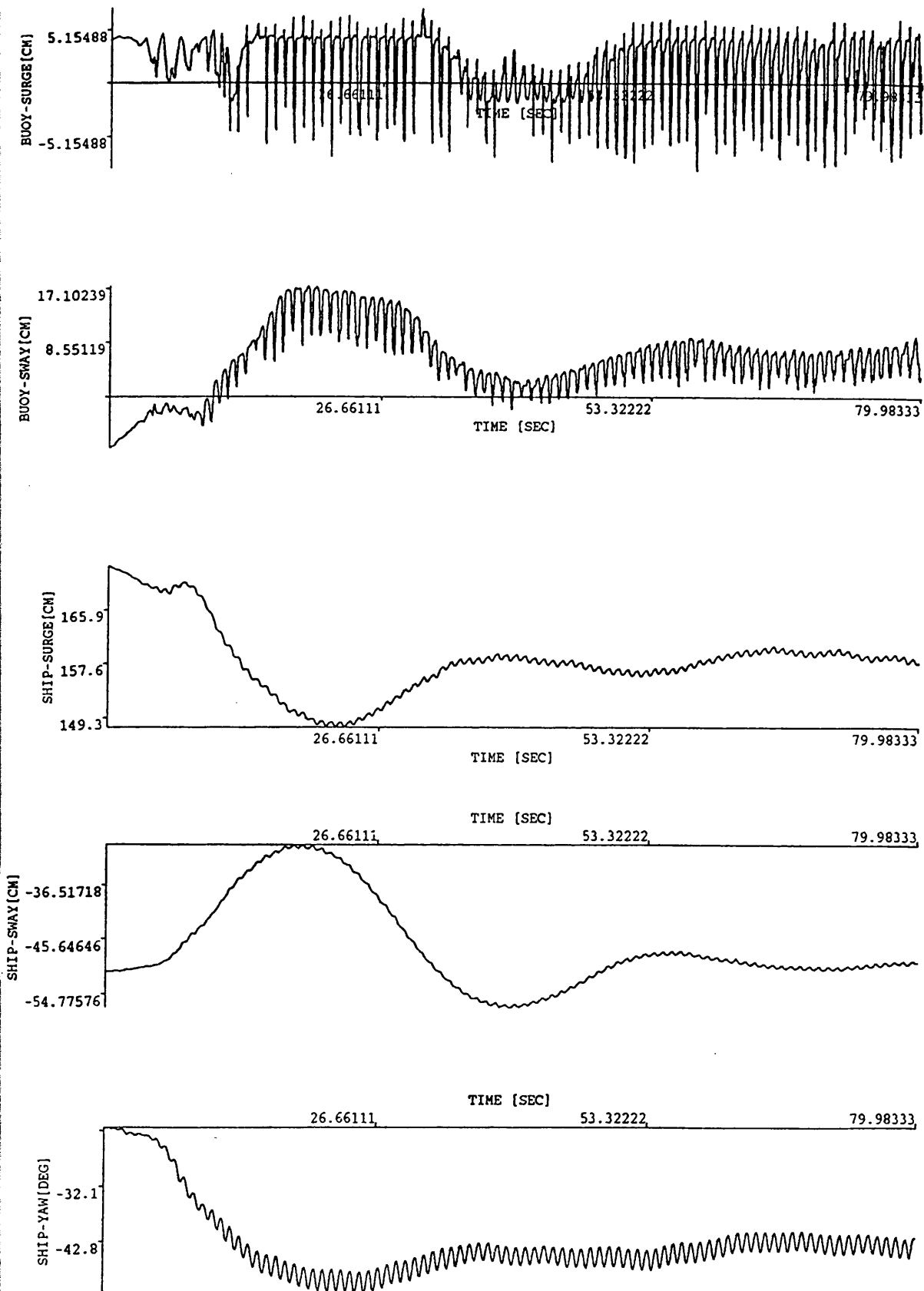


Fig. 6.56 Oblique Angle Test, Run No. 12

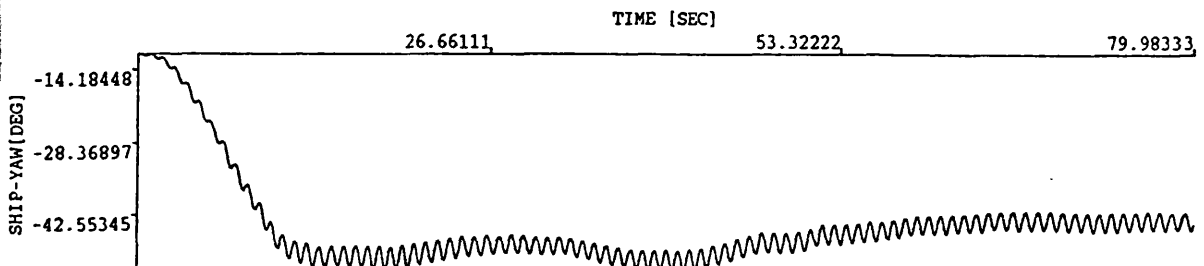
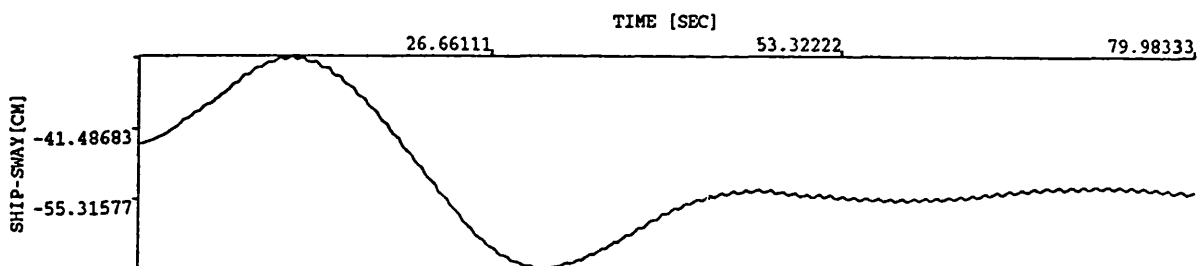
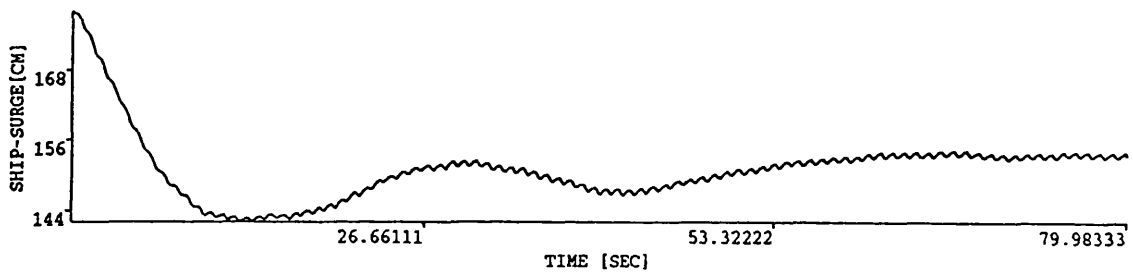
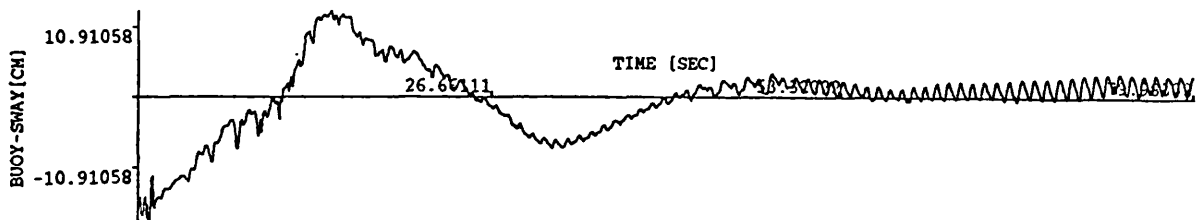
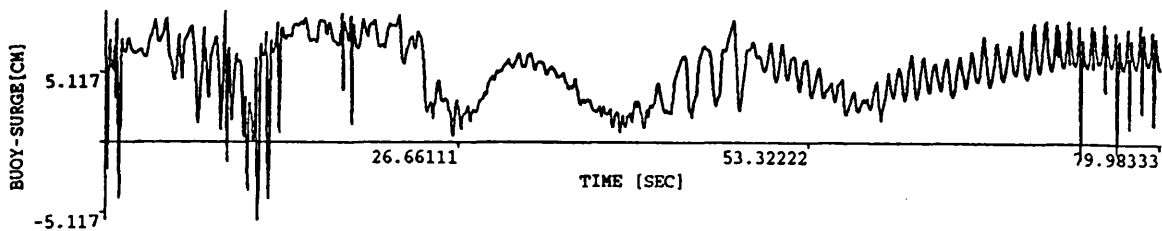


Fig. 6.57 Oblique Angle Test, Run No. 13

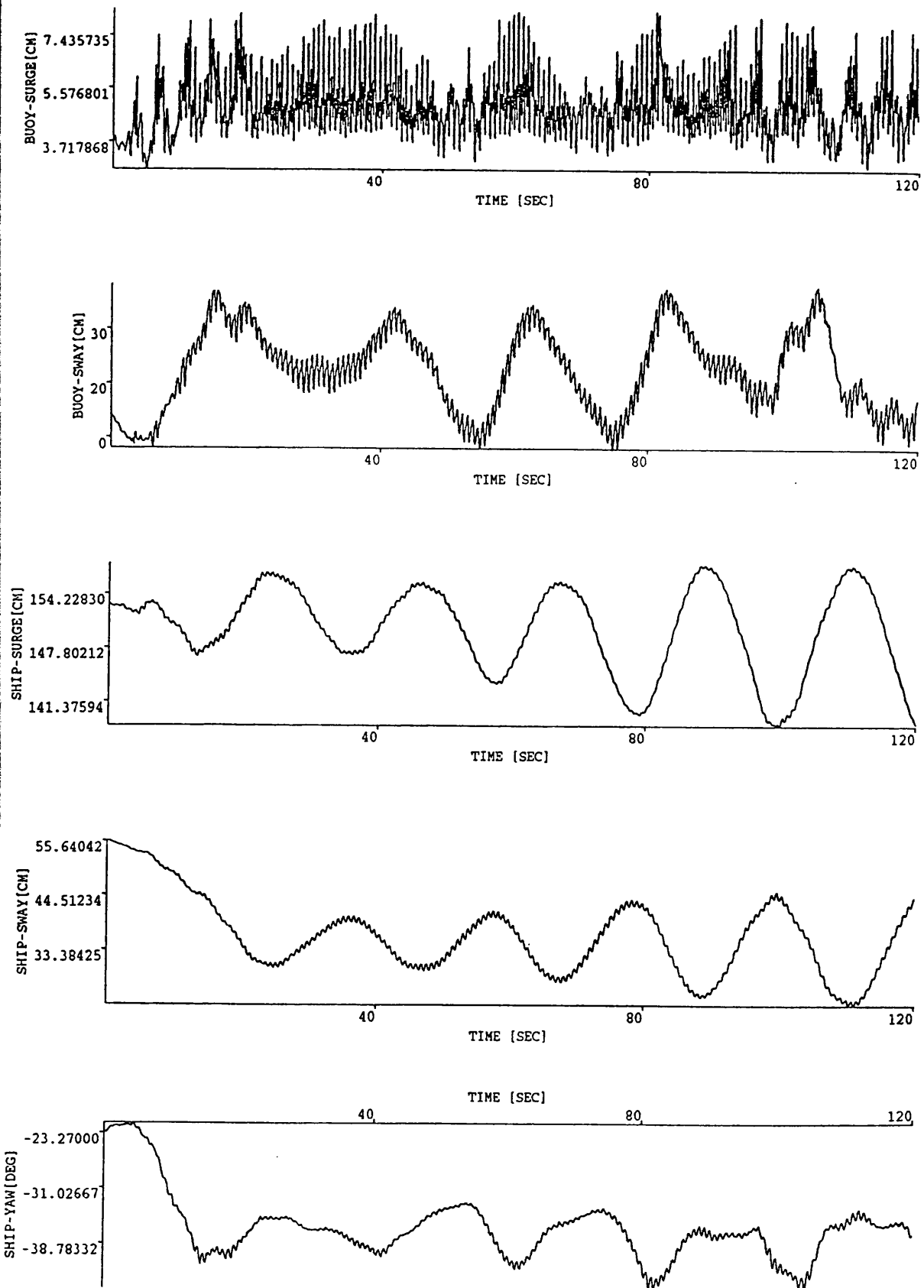


Fig. 6.58 Oblique Angle Test, Run No. 22

CHAPTER 7

CONCLUSIONS

7.1 GENERAL CONCLUSIONS OF THESIS

The aim of this study was to investigate the environmental loading and motion response of moored objects such as moored buoys and Single Point Mooring Systems and to provide the designer with tools that can be used for the analysis of these systems in design. In developing the prediction methods for moored systems particular attention was given to the time domain simulation techniques because the nonlinearities involved in the system, due to the nonlinear mooring forces and the random nature of the environmental forces, can be best treated by time domain prediction techniques. At each stage of the study prediction methods were validated by experiments.

A calculation procedure to predict the non-linear coupled large amplitude motions of a conical or a cylindrical buoy was presented in the second chapter. Comparisons of the motion response predictions with measurements show an acceptable degree of correlation. Comparisons between the motion performance of the conical buoy and that of the cylindrical buoy indicate that the heave and pitch motions of the conical buoy are significantly less than those of the cylindrical buoy (1% reduction in heave and 70% reduction in pitch were predicted). Effects of nonlinear stiffness due to mooring lines and wave height were also investigated. Simulations with nonlinear cable modelling give bigger motion response values than simulation with linear cable modelling. Also the natural frequencies of the buoy shift towards higher frequencies with nonlinear cable modelling. As the wave height increases, the difference in motion responses between the linear and nonlinear cable modellings widens (For an increase in wave height from 4m to 8m, difference in motion responses increase from 5% to 10%). After the F.F.T. analysis of the motion responses obtained from the nonlinear time domain predictions were carried

out, together with the oscillations at wave frequency, some superharmonic motions at twice the wave frequency and subharmonics at fractions of the wave frequency were detected.

The theoretical work on the motion response predictions of the moored buoys was validated by experiments. Comparisons between the predictions and the measurements reveal that the predictions are rather conservative in surge and pitch motions but give reasonably good correlations with measurements in all modes of motion. Second-order surge motions were observed in regular waves. This was quite a surprise since second order motions are generally thought to be caused by irregular waves. One possible reason for this is the non-linearities exhibited by the mooring cables.

The theory to calculate the wave and motion induced forces on tankers described in Chapter 3 provides an alternative method of predicting the wave forces and moments on tankers. CPU time for the calculation of wave forces is about 15 minutes for three angles of wave incidence and for 80 wave frequencies at each wave incidence angle in VAX. It is quite fast compared to the programs which utilize the Green's function method. The combination of reasonable accuracy and low computational cost makes it a good alternative to other numerical methods.

Mean drift forces acting on the elliptical cylinder were compared with a 3-D source distribution program [3.8]. There are large discrepancies between the elliptical cylinder approach and the 3-D program (Figs. 3.51, 3.52 and 3.53). This is because the flow under the cylinder was not modelled in the theory. Results of the elliptical cylinder approach were also compared with the Havelock's method [3.19] for the limiting case of a circular cylinder extending from sea surface to sea bottom and the agreement is quite good (Fig. 3.54).

A time-domain simulation procedure to predict the motion response values and mooring forces of a CALM system was described and the results obtained from the time domain simulations were validated by model test measurements. The results of the time

domain simulations were also correlated with frequency domain calculations. Whilst the surge motion amplitudes of the ship obtained from the frequency and time domain simulations correlate well with each other and agree with the results of measurements, there are some differences between the surge motion amplitudes of the buoy as obtained from the frequency and time domain simulations and the experimental measurements (Figs. 4.11-4.14). These discrepancies may be attributed to the effects of non-linearities in hawser restoring forces and to the unstable behaviour of the buoy model due to its light weight in waves during the experiments.

The theoretical work on the motion response predictions of the tanker-buoy system was validated by experiments. Comparisons between predictions and measurements reveal that the predictions agree very well with the measurements for surge motion of the tanker. However the comparison is not so good for surge motion of the buoy. One possible reason for this is the unstable motion of the buoy observed during the experiments.

The results of oblique wave tests performed for the tanker-buoy system revealed that as the current and the wave forces become more orthogonal to each other the magnitude of steady sway and yaw displacements of the ship increases, and that the increase in current load generally yields an increase in the surge, sway and yaw oscillation amplitudes of the ship.

Two sets of parametric studies were presented in Chapter 6. In the first set, six groups of simulation studies were carried out using the non-linear time domain simulation computer program based on the prediction method described in this thesis. During the first three groups of studies the effects of directionality of wave, wind and current force were investigated. During the remaining three sets of simulations the effects of variations in wave, wind and current force magnitudes were investigated. Results are listed as follows,

1. Maximum steady and oscillatory sway and yaw motions occur when wave and current forces make a 90 degree angle with the wind forces. Similarly maximum sway motions of the buoy occur when wave and current forces make a 90 degree angle with the wind forces.

2. Wind direction does not affect the motions significantly.

3. Mean sway displacement and yaw angle increase as the current direction changes from 0 to 90 degrees. However maximum oscillatory sway motion of the buoy occurs when wave force direction makes a 0 degree and wind and current directions make a 45 degree angle with the horizontal axis. Maximum steady and oscillatory surge motions of the buoy and ship occur when wave, wind and current forces act co-linearly.

4. Mean mooring line forces are generally not very sensitive to the changes in current and wind loading since the dominant load on the system is due to wave induced oscillatory and steady forces.

5. There is no linear relationship between the wave height and the motion response or the mooring force values of the CALM system. This indicates that such systems must be analysed in the time domain using nonlinear analysis tools.

A second set of parametric studies was carried out to determine the sensitivity of slowly varying motions and hawser forces to changes in the environment, the number of mooring lines of the buoy, hawser length and thruster capacity for the CALM system. Results of the parametric studies are as follows,

1. An increase in wind speed (sea state) results in an increase in mean displacements of the system and the mean tension of the hawser (Table 5.7). The same trend can also be observed for oscillatory yaw motion of the tanker and sway motion of the buoy. Simulation 1, which is the lowest sea state chosen, gives the biggest motion response values for surge motion of the buoy and sway motion of the tanker. Frequencies at which

the buoy and the tanker oscillate in simulation 1 ,found through a spectral analysis, are 0.013, 0.025, 0.038 and 0.05 rad/sec. Among these frequencies 0.013 is the dominant frequency for all motions except for the surge motion of the buoy and the tanker whose dominant frequency are 0.025 rad/sec. Dominant frequency for hawser tension oscillations is also 0.025 rad/sec. Dominant frequencies change slightly with increasing wind speed: 0.014 and 0.029 rad/sec for simulation 2 and 0.016 and 0.031 rad/sec for simulation 3.

2. Simulation with the Davenport spectrum gives the largest motion response values (0.1-4% higher than the others). (Table 5.8)

3. As the number of mooring legs is reduced from 8 to 4, dominant (natural) frequencies of the system shift towards lower frequencies taking the values 0.014, 0.028, 0.041 and 0.057 rad/sec compared with the frequencies of 0.015, 0.029, 0.044 and 0.059 rad/sec of the 8 legged system (Table 5.9). There is also an increase of 40-145% in oscillatory motion response values of the tanker and the buoy. This increase in the motions increases the hawser tension by 25%. This is because with fewer mooring legs, the system becomes less stiff, the bow hawser stays slack for a longer time and the sudden acceleration of the buoy and/or the tanker creates larger tensions in the hawser.

4. A change in hawser length not only changes the motion response values but also the natural frequencies of the system. As the hawser length reduces from 80 m to 40 m, 0.019 rad/sec becomes the dominant frequency for sway and yaw motions of the tanker and sway motion of the buoy, 0.038 rad/sec for the surge motion of the buoy and the tanker and the hawser tension (Table 5.10). Another conclusion which could be drawn from the simulation is that the motions of the tanker and the buoy are more stable and hawser load at the dominant frequency decrease by 6% as the hawser length is reduced.

5. Slackening of the hawser which is the reason for peak loads is avoided by the use of thrusters. Tanker and buoy motions also become more stable (Table 5.11). But with

the use of thrusters the hawser remains stretched with a high mean tension during the simulation, which may not be desirable and the use of thrusters could be expensive.

6. An increase in displaced volume of the buoy results in more stable motions of tanker and buoy (Table 5.12). This effect is quite similar to the effect of thrusters.

7.2 RECOMMENDATIONS FOR FUTURE WORK

1. The diffraction problem of the vertical ellipse with finite draft could be solved in six degrees of freedom and then, mean drift forces acting on the cylinder can be obtained following the method described in Chapter 3.

2. Current and wind forces acting on tankers are usually calculated using semi empirical formulas together with experimental data. More experimental and theoretical investigation of this topic is needed to improve the present formulations.

3. Motion stability of the tanker-buoy system can be investigated under wave, wind and current loading by using the linearized equations of motion.

APPENDIX A
EVALUATION OF MOORING FORCES

Solution Algorithm due to the horizontal excursion of the upper end of the cable

In the following an algorithm is given to determine cable forces due to the horizontal displacements of the upper end of the cable. (See Fig. A-1)

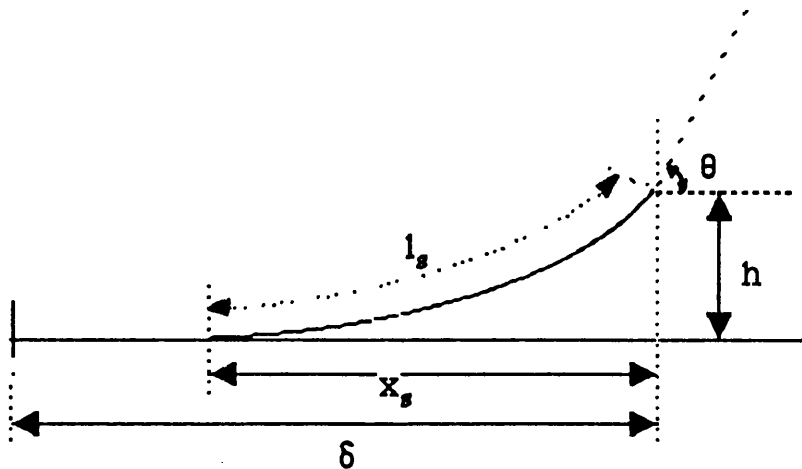


Fig. A-1 Definition of Cable Parameters

Input data:

w is the submerged unit weight of the cable element.

h is the water depth.

l is the total cable length.

θ_e is the angle of the upper end of the cable with the horizontal at the beginning of the motion.

$T_{0\max}$ is the maximum tension of the cable.

N is the number of cables.

The calculation steps:

1. Assume an initial value of T_0

2. Calculate θ

a. x_s from (2.32) $x_s = \frac{T_0}{w} \cosh^{-1}\left(\frac{hw}{T_0} + 1\right)$

b. l_s from (2.31) $l_s = \frac{T_0}{w} \sinh\left(\frac{wx_s}{T_0}\right)$

c. $\delta = 1 - l_s + x_s$ (A-1)

d. θ from (2.30) $\theta = \tan^{-1}\left(\sinh\left(\frac{wx_s}{T_0}\right)\right)$

3. Compare θ with θ_e

$$\frac{|\theta - \theta_e|}{\theta} \leq 0.001 \quad (\text{A-2})$$

4. If Step3 is not satisfied and $T_0 \geq T_{0\max}$, stop solution.

5. If Step3 is not satisfied and $T_0 < T_{0\max}$, increment T_0 and goto step(2)

6. When Step3 is satisfied;

$$l_{sc} = l_s \quad ; \quad x_{sc} = x_s \quad ; \quad d_e = d$$

7. Assume an initial value of T_0

$$8. \quad x_s = \frac{T_0}{w} \cosh^{-1} \left(\frac{hw}{T_0} + 1 \right)$$

$$l_s = \frac{T_0}{w} \sinh \left(\frac{wx_s}{T_0} \right)$$

$$\delta = l - l_s + x_s$$

$$\theta = \tan^{-1} \left(\sinh \left(\frac{wx_s}{T_0} \right) \right)$$

$$q_v = T_0 \tan \theta \tag{A-3}$$

$$\psi = \tan^{-1} \left(\frac{\delta - \delta_e}{h} \right) \tag{A-4}$$

$$x_b = h \tan \psi \tag{A-5}$$

9. If $T_0 > T_{0\max}$, stop solution.

10. If $T_0 \leq T_{0\max}$, increment T_0 and goto step(8)

11. Plot $X_b - T_0$; find the interpolation function

12. Plot $X_b - q_v$; find the interpolation function

These single cable results are used to calculate the total loads q_x and q_z for N cables in a symmetric array , Where each cable has a twin diametrically opposite. The procedure for computing q_x and q_z is as follows:

1. Assume an initial value of $Y = 0$

$$2. \quad q_x(v) = \sum_{n=0}^I [q_h(vC_N) - q_h(-vC_N)] C_N, \quad (q_h = T_0) \quad (\text{A-6})$$

$$q_z(v) = \sum_{n=0}^I [q_v(vC_N) + q_v(-vC_N)] \quad (\text{A-7})$$

$v = h \tan Y$ (horizontal displacement at the point of cable attachment)

$$C_N = |\cos(\beta_n)| \text{ and } B_0 = 0, \quad I = (N - 2) / 2 \quad (\text{A-8})$$

3. If $Y \geq Y_{\max}$, table is complete

4. If $Y < Y_{\max}$, increment Y and return to step 2

5. Plot $v - q_x(v)$

6. Plot $v - q_z(v)$

7. Change the water depth to take into account the influence of heave motion on the horizontal cable stiffness, return to step 7 in which we calculate the single cable horizontal stiffness.

Solution Algorithm due to the vertical motion of the upper end of the cable

The procedure to find the initial geometric conditions of the cable is the same as in the first solution algorithm (first 6 steps).

1. Calculate the initial unsupported weight of the cable. We had calculated the l_{se} , the initial unsupported length of the cable. wl_{se} gives us the initial unsupported weight.

$$T_{zi} = wl_{se}$$

2. $T_0 = T_{zi} / \tan(\theta_e)$ (A-9)

3. Enter an initial value of x_s

4. Find the x_s from the below equation by iteration.

$$\delta_e = \frac{T_0}{w} \sinh\left(\frac{wx_s}{T_0}\right) - l_s + x_s$$

5. Calculate the vertical displacement.

$$y = \frac{T_0}{w} \left(\cosh\left(\frac{wx_s}{T_0}\right) - 1 \right) - H$$
 (A-10)

6. $\theta = \tan^{-1}\left(\sinh\left(\frac{wx_s}{T_0}\right)\right)$

7. Calculate the vertical tension of the cable

$$T_z = 4(lw - T_{zi})$$
 (A-11)

8. If y is less than 10 m , increment T_0 return to step 3.

9. Plot y versus T_z , find the interpolation function.

10. Plot y versus T_0 , find the interpolation function.

APPENDIX B
ELLIPTICAL COORDINATE SYSTEM

Coordinate transformations between the rectangular and elliptic coordinates (See Fig. 3.2) are written as follows:

$$x = h \cosh \zeta \cos \eta \quad y = h \sinh \zeta \sin \eta \quad (\text{B-1})$$

At the extremities of the major and minor axes of any confocal ellipse, we find the following relations:

$$a = h \cosh \zeta \quad b = h \sinh \zeta$$

$$h^2 = a^2 - b^2 \quad (\text{B-2})$$

The line element along the ellipse is as follows:

$$ds_2 = l_1 d\eta$$

$$l_1 = h[\cosh^2 \zeta \sin^2 \eta + \sinh^2 \zeta \cos^2 \eta]^{\frac{1}{2}} = \frac{h}{\sqrt{2}}(\cosh 2\zeta - \cos 2\eta)^{\frac{1}{2}} \quad (\text{B-3})$$

The distance of any point from the origin is,

$$r = (x^2 + y^2)^{\frac{1}{2}} = h[\cosh^2 \zeta \cos^2 \eta + \sinh^2 \zeta \sin^2 \eta]^{\frac{1}{2}} \quad (\text{B-4})$$

APPENDIX C
SOME PROPERTIES OF MATHIEU FUNCTIONS

Fourier expansions for the even periodic Mathieu function is as follows:

$$ce_r(z, q) = \sum_{k=0}^{\infty} A_{2k+p} \cos(2k+p)z \quad (C-1)$$

associated with $a_r(q)$ and the odd periodic solution is,

$$se_r(z, q) = \sum_{k=0}^{\infty} B_{2k+p} \sin(2k+p)z \quad (C-2)$$

associated with $b_r(q)$. The order, r , is of the form $2n+p$. The n is a nonnegative integer while $p=0$ or 1 indicates the solution is of period π or 2π .

Radial Mathieu function associated with $a_r(q)$ and $b_r(q)$ are as follows:

$$Mc_r^{(j)}(z, q) = \sum_{k=0}^{\infty} (-1)^{n+k} A_{2k+p} [F_k + G_k] / A_{2s+p} \epsilon_{2s+p} \quad (C-3)$$

$$Ms_r^{(j)}(z, q) = \sum_{k=0}^{\infty} (-1)^{n+k} B_{2k+p} [F_k - G_k] / B_{2s+p} \quad (C-4)$$

if $m \neq 0$, $\epsilon_m = 1$ but $\epsilon_0 = 2$. Coefficients A and B can be generated from a derived set of recursion relationships in Eqs. 3.16 and 3.17.

Orthogonality of Mathieu functions:

$$\int_0^{2\pi} \text{ce}_{2m+\alpha}(z, q) \text{ce}_{2n+\beta}(z, q) dz = \pi \delta_{mn} \delta_{\alpha\beta} \quad (\text{C-5})$$

$$\int_0^{2\pi} \text{ce}_{2m+\alpha}(z, q) \text{ce}_{2n+1+\beta}(z, q) dz = 0 \quad (\text{C-6})$$

$$\int_0^{2\pi} \text{se}_{2m+1+\alpha}(z, q) \text{ce}_{2n+1+\beta}(z, q) dz = \pi \delta_{mn} \delta_{\alpha\beta} \quad (\text{C-7})$$

Some integrations appear in the study are as follows:

$$\int_0^{2\pi} \text{ce}_{2n}(\eta, q) \cos \eta d\eta = \int_0^{2\pi} \text{se}_m(\eta, q) \cos \eta d\eta = 0 \quad (\text{C-8})$$

$$\int_0^{2\pi} \text{ce}_{2n+1}(\eta, q) \cos \eta d\eta = \pi A_1^{(2n+1)} \quad (\text{C-9})$$

$$\int_0^{2\pi} \text{ce}_m(\eta, q) \sin \eta d\eta = \int_0^{2\pi} \text{se}_{2n+2}(\eta, q) \sin \eta d\eta = 0 \quad (\text{C-10})$$

$$\int_0^{2\pi} \text{se}_{2n+1}(\eta, q) \sin \eta d\eta = \pi B_1^{(2n+1)} \quad (\text{C-11})$$

$$\int_0^{2\pi} ce_m(\eta, q) \sin\eta \cos\eta \, d\eta = \int_0^{2\pi} se_{2n+1}(\eta, q) \sin\eta \cos\eta \, d\eta = 0 \quad (\text{C-12})$$

$$\int_0^{2\pi} se_{2n+2}(\eta, q) \sin\eta \cos\eta \, d\eta = \pi B_2^{(2n+2)} \quad (\text{C-13})$$

APPENDIX D
DERIVATION OF THE INCIDENT WAVE POTENTIAL FOR THE
ELLIPTICAL CYLINDER

If we assume that

$$\cos[z \cos(\theta - \alpha)] =$$

$$\sum_{m=0}^{\infty} [C_{2m}(\eta) Ce_{2m}(\zeta) ce_{2m}(\theta) + S_{2m+2}(\eta) Se_{2m+2}(\zeta) se_{2m+2}(\theta)] \quad (D-1)$$

If both sides are multiplied by $se_{2n}(\theta)$, integrate from 0 to 2π and use the orthogonality we obtain,

$$C_{2n}(\eta) = 2 ce_{2n}(\eta) / p_{2n} \quad (D-2)$$

If both sides of (D-1) are multiplied by $se_{2n+2}(\theta)$ we have,

$$S_{2n+2}(\eta) = 2 se_{2n+2}(\eta) / s_{2n+2} \quad (D-3)$$

Substituting (D-3) and (D-2) into (D-1) gives the expansion,

$$\cos[2k(\cosh \zeta \cos \eta \cos \theta + \sinh \zeta \sin \eta \sin \theta)] =$$

$$2 \sum_{n=0}^{\infty} \left[\frac{Ce_{2n}(\zeta) ce_{2n}(\eta) ce_{2n}(\theta)}{P_{2n}} + \frac{Se_{2n+2}(\zeta) se_{2n+2}(\eta) se_{2n+2}(\theta)}{s_{2n+2}} \right] \quad (D-4)$$

Similarly we find that

$$\sin [2k(\cosh \zeta \cos \eta \cos \theta + \sinh \zeta \sin \eta \sin \theta) =$$

$$2 \sum_{n=0}^{\infty} \left[\frac{\text{Ce}_{2n+1}(\zeta) \text{ce}_{2n+1}(\eta) \text{ce}_{2n+1}(\theta)}{p_{2n+1}} + \frac{\text{Se}_{2n+1}(\zeta) \text{se}_{2n+1}(\eta) \text{se}_{2n+1}(\theta)}{s_{2n+1}} \right]$$

and we obtain the incident wave potential

$$e^{iz \cos(\theta-\alpha)} = e^{ik(x \cos \theta + y \sin \theta)} =$$

$$\cos[k(x \cos \theta + y \sin \theta)] + i \sin [k(x \cos \theta + y \sin \theta)] =$$

$$2 \sum_{n=0}^{\infty} \left[\frac{1}{p_{2n}} \text{Ce}_{2n}(\zeta) \text{ce}_{2n}(\eta) \text{ce}_{2n}(\theta) + \right.$$

$$\left. \frac{1}{s_{2n+2}} \text{Se}_{2n+2}(\zeta) \text{se}_{2n+2}(\eta) \text{ce}_{2n+2}(\theta) + \right.$$

$$\left. i \left\{ \frac{1}{p_{2n+1}} \text{Ce}_{2n+1}(\zeta) \text{ce}_{2n+1}(\eta) \text{ce}_{2n+1}(\theta) + \right. \right.$$

$$\left. \left. \frac{1}{s_{2n+1}} \text{Se}_{2n+1}(\zeta) \text{se}_{2n+1}(\eta) \text{ce}_{2n+1}(\theta) \right\} \right] \quad (\text{D-5})$$

Coefficients p_n and s_n are given by McLachlan [3.1]

$$p_{2n} = \text{ce}(0, q) \text{ce}_{2n}(\pi/2, q) / A_0^{(2n)} \quad (\text{D-6})$$

$$p_{2n+1} = -\text{ce}_{2n+1}(0, q) \text{ce}'_{2n+1}(\pi/2, q) / kA_1^{(2n+1)} \quad (\text{D-7})$$

$$s_{2n+1} = \text{se}'_{2n+1}(0, q) \text{se}_{2n+1}(\pi/2, q) / kB_1^{(2n+1)} \quad (\text{D-8})$$

$$s_{2n+2} = se'_{2n+2}(0, q) se'_{2n+2}(\pi/2, q) / k^2 B_2^{(2n+2)} \quad (D-9)$$

APPENDIX E

BLANCH'S DEFINITION FOR RADIAL FUNCTIONS

The radial solutions given by Blanch are $Mc_m^{(i)}(z, q)$ and $Ms_m^{(i)}(z, q)$ $i=1,2,3,4$ and correspond to $Ce_m(z, q)$ and $Se_m(z, q)$, $Fey_m(z, q)$ and $Gey_m(z, q)$ and $Me_m^{(i)}(z, q)$ and $Ne_m^{(i)}(z, q)$, $i=1,2$. This notation is used because the computer program, which is used in evaluating the Mathieu functions uses this notation. The relationships are [3.20],

$$Ce_{2r}(z, q) = \frac{ce_{2r}(\frac{\pi}{2}, q) ce_{2r}(0, q)}{(-1)^r A_0^{2r}} Mc_{2r}^{(1)}(z, q) \quad (E-1)$$

$$Ce_{2r+1}(z, q) = \frac{ce'_{2r+1}(\frac{\pi}{2}, q) ce_{2r+1}(0, q)}{(-1)^{r+1} \sqrt{q} A_1^{2r+1}} Mc_{2r+1}^{(1)}(z, q) \quad (E-2)$$

$$Se_{2r}(z, q) = \frac{se'_{2r}(0, q) se'_{2r}(\frac{\pi}{2}, q)}{(-1)^r q B_2^{2r}} Ms_{2r}^{(1)}(z, q) \quad (E-3)$$

$$Se_{2r+1}(z, q) = \frac{se'_{2r+1}(0, q) se_{2r+1}(\frac{\pi}{2}, q)}{(-1)^r \sqrt{q} B_1^{2r+1}} Ms_{2r+1}^{(1)}(z, q) \quad (E-4)$$

$$Fey_{2r}(z, q) = \frac{ce_{2r}(\frac{\pi}{2}, q) ce_{2r}(0, q)}{(-1)^r A_0^{2r}} Mc_{2r}^{(2)}(z, q) \quad (E-5)$$

$$\text{Fey}_{2r+1}(z, q) = \frac{ce'_{2r+1}(\frac{\pi}{2}, q) ce_{2r+1}(0, q)}{(-1)^{r+1} \sqrt{q} A_1^{2r+1}} \text{Mc}_{2r+1}^{(2)}(z, q) \quad (\text{E-6})$$

$$\text{Gey}_{2r}(z, q) = \frac{se'_{2r}(0, q) se'_{2r}(\frac{\pi}{2}, q)}{(-1)^r q B_2^{2r}} \text{Ms}_{2r}^{(2)}(z, q) \quad (\text{E-7})$$

$$\text{Gey}_{2r+1}(z, q) = \frac{se'_{2r+1}(0, q) se_{2r+1}(\frac{\pi}{2}, q)}{(-1)^r \sqrt{q} B_1^{2r+1}} \text{Ms}_{2r+1}^{(2)}(z, q) \quad (\text{E-8})$$

and

$$M_r^{(3)}(z, q) = M_r^{(1)}(z, q) + iM_r^{(2)}(z, q)$$

$$M_r^{(4)}(z, q) = M_r^{(1)}(z, q) - iM_r^{(2)}(z, q)$$

$$M_r^{(j)}(z, q) = \text{Mc}_r^{(j)} \text{ or } \text{Ms}_r^{(j)}$$

REFERENCES OF CHAPTER 1

- 1.1 Haring, R.E. ' Single-Point Tanker Mooring Measurements in the North Sea', *Proceedings of Offshore Technology Conference*, Paper No. 2711, Houston, 1976.
- 1.2 Wichers, J.E.W. ' On the Slow Motions of Tankers Moored to Single Point Mooring Systems', *Proceedings of Offshore Technology Conference*, Paper No. 2548, Houston, 1976.
- 1.3 Owen, D.G. and Linfoot, B.T. ' The Development of Mathematical Models Of Single-Point Mooring Installations', *Proceedings of Offshore Technology Conference*, Paper No. 2490, Houston, 1976.
- 1.4 Owen, D.G. and Linfoot, B.T. ' Theoretical Analysis of Single Point Mooring Behaviour', *The Society of Naval Architects and Marine Engineers*, 1977.
- 1.5 Muga, B.J. and Freeman, M.A. ' Computer Simulation of Single Point Moorings', *Proceedings of Offshore Technology Conference*, Paper No. 2829, Houston, 1977.
- 1.6 Wichers, J.E.W. ' Slowly Oscillating Mooring Forces in Single Point Mooring Systems', *Second International Conference on Behaviour of Offshore Structures*, Paper No. 27, London, 1979.
- 1.7 Oortmerssen, I.G.V. ' The Motions of a Moored Ship in Waves', Publication No. 510, Netherlands Ship Model Basin, Wageningen, The Netherlands, 1976.
- 1.8 Faltinsen, O.M. , Kjaerland, O. , Liapis, N. and Walderhaug, H. ' Hydrodynamic Analysis of Tankers at Single Point Mooring Systems', *Second International Conference on Behaviour of Offshore Structures*, No. 59, London, 1979.

- 1.9 Liapis, N. ' Wave Loads and Motion Stability of Tankers at Single Point Mooring Systems', Department of Marine Technology, University of Trondheim, Report No. UR-85-44, 1987.
- 1.10 Ractliffe, A.T. and Clarke, D. ' Development of a Comprehensive Model of a Single Point Mooring System', *The Royal Institution of Naval Architects*, Spring Meetings, Paper No. 9, 1980.
- 1.11 Bliault, A.E. and Stewart, W.P. ' Single Point Mooring Terminals: A Summary of Selection and Design Methods', *The Royal Institution of Naval Architects*, Spring Meetings, Paper No. 8, 1980.
- 1.12 Sørheim, H.R. ' Analysis of Motion in Single Point Mooring Systems', *Modelling, Identification and Control*, No. 3, Vol. 1, 1980.
- 1.13 Molin, B. and Bureau, G. ' A Simulation Model for the Dynamic Behaviour of Tankers Moored to Single Point Moorings', *International Symposium on Ocean Engineering and Ship Handling*, Gothenburg, Sweden, 1980.
- 1.14 Wichers, J.E.W. ' On the Low-Frequency Surge Motions of Vessels Moored in High Seas', *Proceedings of Offshore Technology Conference*, Paper No. 4437, Houston, 1982.
- 1.15 Wichers, J.E.W. and van den Boom H.J.J. ' Simulation of the Behaviour of SPM-moored Vessels in Irregular Waves, Wind and Current', *Proceedings of the 2nd International Conference and Exhibition on Deep Offshore Technology*, Valletta, Malta, 1983.

- 1.16 Gerritsma, J., Beukelman, W. and Glansdorp, C.C. ' The Effect of Beam on the Hydromechanic Characteristics of Ship Hulls', *Proceedings of Symposium on Naval Hydrodynamics*, Boston, 1974.
- 1.17 Oltmann, P. and Sharma, S.D. ' Simulation of Combined Engine and Rudder Manoeuvres Using an Improved Model of Hull-Propeller-Rudder Interactions', *Proceedings of 15th Symposium on Naval Hydrodynamics*, Hamburg, pp. 83-108, 1984.
- 1.18 Jiang, T. , Schellin, T.E. and Sharma S.D. ' Maneuvering Simulation of a Tanker Moored in a Steady Current Including Hydrodynamic Memory Effects and Stability Analysis', *Proceedings of the International Conference on Ship Maneuvrability*, RINA, Paper No. 25, Vol. 1, London, 1987.
- 1.19 Sharma, S.D. , Jiang, T. and Schellin, T.E. ' Dynamic Instability and Chaotic Motions of a Single-Point-Moored Tanker', *Proceedings of the 17th ONR Symposium on Naval Hydrodynamics*, The Hague, 1988.
- 1.20 Schellin, T.E. and Jiang, T. ' Motion Simulation and Dynamic Stability of an Anchored Tanker Subject to Current, Wind and Waves', *Schiffstechnik*, Vol. 37, 1990.
- 1.21 Jiang, T. and Schellin, T.E. ' Motion Prediction of a Single-Point Moored Tanker Subjected to Current, Wind and Waves', *Journal of Offshore Mechanics and Arctic Engineering*, Vol. 112, Feb. 1990.
- 1.22 Papoulias, F.A. ' Dynamic Analysis of Mooring Systems', Ph. D. Thesis, University of Michigan, 1987.
- 1.23 Bernitsas, M.M. and Papoulias, F.A. ' Stability of Single Point Mooring Systems', *Applied Ocean Research*, Vol. 8, No. 1, 1986.

- 1.24 Papoulias, F.,A. and Bernitsas, M.,M. ' Autonomous Oscillations, Bifurcations, and Chaotic Response of Moored Vessels ', *Journal of Ship Research*, Vol. 32, No. 3, pp. 220-228, Sept. 1988.
- 1.25 Wichers, J.E.W. ' Progress in Computer Simulations of SPM Moored Vessels', *Proceedings of Offshore Technology Conference*, Paper No. 5175, Houston, 1986.
- 1.26 Wichers, J.E.W. ' The Prediction of the Behaviour of Single Point Moored Tankers', *Proceedings of a Workshop on Floating Structures and Off-shore Operations*, Wageningen, The Netherlands, pp. 125-142, 1987.
- 1.27 Obokata, J. ' Mathematical Approximation of the Slow Oscillation of a Ship Moored to Single Point Moorings', *Marintec Offshore China Conference*, Shanghai, October, 1983.
- 1.28 Wichers, J.E.W. ' A Simulation Model for a Single Point Moored Tanker', Publication No. 797, Netherlands Ship Model Basin, Wageningen, The Netherlands, 1988.
- 1.29 Aghamohammadi, F. and Thompson, J.M.T. ' An Experimental Study of the Large Amplitude Fish-Tailing Instabilities of a Tanker at a Single Point Mooring', *Applied Ocean Research*, Vol. 12, No. 1, 1990.
- 1.30 de Kat, J.O. and Wichers, J.E.W., ' Behaviour of a Moored Ship in Unsteady Current Wind and Waves', *Marine Technology*, Vol.28, No.5, September, 1991.
- 1.31 Cummins, W.E. ' The Impulse Response Function and Ship Motions', *Schiffstechnik*, Vol. 9, No. 47, 1962.

REFERENCES OF CHAPTER 2

- 2.1 Berteaux, H.O. *Buoy Engineering*, Wiley-Interscience Publications', 1976.
- 2.2 Remery, G.F.M. and Kokkeel, R. ' On the Origin of Wave Induced Motions of Mooring Buoys', *Proceedings of Offshore Technology Conference*, Paper No. 2468, 1976.
- 2.3 Arai, S. , Nekado, Y. and Takagi, M. ' Study on the Motion of a Moored Vessel among the Irregular Waves', *Naval Architecture and Ocean Engineering*, Vol.17, The Society of Naval Architecture and Ocean Engineering, 1976.
- 2.4 Koterayama, W. ' Motions of Moored Floating Body and Dynamic Tension of Mooring Lines in Regular Waves', *Transactions of the West-Japan Society of Naval Architects*, No. 53, 1977.
- 2.5 Harichandran, R.S. and Irvine, H.M. ' A Static Analysis Technique for Multi-leg Cable-buoy Systems', Project No. R/0-5, M.I.T., 1982.
- 2.6 Tsinipizoglou, S. ' Dynamics of Moored Buoys', Ph.D. Thesis, Department of Naval Architecture and Ocean Engineering, Glasgow University, 1982.
- 2.7 Nakajima, T. ' Time-Domain Simulations of Coupled Responses of the Moored Buoy and the Mooring Lines in Deep-Sea ', *International Symposium on Developments in Deeper Waters*, Paper No. 13, 6-7 Oct. 1986.
- 2.8 Morison, J.R., O'Brien, M.P., Johnson, J.W. and Schaaf, S.A. ' The Force Exerted by Surface Waves on Piles', *Petroleum Transactions*, AIME, Vol. 189, pp. 149-154, 1950.

2.9 Incecik, A. ' Design Aspects of the Hydrodynamic and Structural Loading on Floating Offshore Platforms Under Wave Excitation', Ph.D. Thesis, University of Glasgow, 1982.

2.10 Orgill, G. , Wilson, J.F. and Schmertmann, G.R. ' Static Design of Cable Mooring Arrays for Off-shore Guyed Towers', *Applied Ocean Research*, Vol. 7, No. 3, 1985.

2.11 Hooft, J.P. *Advanced Dynamics of Marine Structures*, Wiley-Interscience Publication, 1982.

2.12 The NAG Fortran Library Manual-Mark 12, Published by the Numerical Algorithms Group Ltd, 1987.

2.13 Sincock, P. ' Nonlinear Compliant Systems in Irregular Seas', Ph.D. Thesis, Dept. of Mechanical Engineering, University College London, 1990.

REFERENCES OF CHAPTER 3

- 3.1 McLachlan, N.W. *Theory and Application of Mathieu Functions*, Dover Publications, 1951.
- 3.2 Goda, Y. and Yoshimura, T. 'Wave Force on a Vessel Tied at Offshore Dolphins', *Proc. 13th Coastal Engineering Conference*, Vol. 3, pp. 1723-1741, 1972.
- 3.3 Muga, B.J. and Fong, H. 'Wave Forces Induced on Very Large Crude Carriers', *Proceedings of Offshore Technology Conference*, Paper No. 2535, 1976.
- 3.4 Chen, H. S. and Mei, C. C. 'Wave Forces on a Stationary Platform of Elliptical Shape', *Journal of Ship Research*, Vol.17, No.2, pp.66-71, 1973.
- 3.5 Mathieu, É. 'Mémoire sur le mouvement vibratoire d'une membrane de forme elliptique', *Jour. de Math. Pures et Appliquées* (Jour. de Liouville), Vol. 13, No.137, 1868.
- 3.6 Clemm, D.S. 'Algorithm 352, Characteristic Values Associated Solutions of Mathieu's Differential Equation', *Communications of the Association for the Computing Machinery*, Vol. 12, No. 7, July 1969.
- 3.7 Oortmerssen, I.G.V. 'The Motions of a Moored Ship in Waves', Publication No. 510, Netherlands Ship Model Basin, Wageningen, The Netherlands, 1976.
- 3.8 Chan, H.S. 'A Three-Dimensional Technique for Predicting First- and Second-Order Hydrodynamic Forces on a Marine Vehicle Advancing in Waves', Ph. D. Thesis, Department of Naval Architecture and Ocean Engineering, University of Glasgow, Aug. 1990.

- 3.9 Maruo, H. ' The Drift of a Body Floating on Waves', *Journal of Ship Research*, vol. 4, 1960.
- 3.10 Pinkster, J. A. ' Low Frequency Second Order Wave Exciting Forces on Floating Structures ', MARIN Publication No. 600, Wageningen, 1980.
- 3.11 Newman, J.N. ' The Drift Force and Moment on Ships in Waves', *Journal of Ship Research*, March 1967.
- 3.12 Yilmaz, O. ' Calculation of Wave Forces on a Tanker', Department of Naval Architecture and Ocean Engineering, Report No. NAOE-90-22, University of Glasgow, Dec. 1990.
- 3.13 Krokstad, J.R. ' Drift Forces, Moment and Wave Drift Damping in Multidirectional Seas. A Theoretical and Experimental Study', *International Symposium on Dynamics of Marine Vehicles and Structures in Waves*, London, 1990.
- 3.14 Ince, E.L. ' Tables of the elliptic cylinder functions', *Proc. Roy. Soc. Edinburgh*, Vol. 52, Part 4, 1931-32.
- 3.15 Blanch, G. and Clemm, D.S. ' *Tables Relating to the Radial Mathieu Functions*', Vol. 2, US Govt. Print. Off., Washington, D.C., 1967.
- 3.16 Garrett, C.J.R. ' Wave Forces on a Circular Dock', *Journal of Fluid Mechanics*, vol. 46, part 1, pp. 129-139, 1971.
- 3.17 Black, J.L., Mei, C.C. and Bray, M.C.G. ' Radiation and Scattering of Water Waves by rigid bodies', *Journal of Fluid Mechanics*, vol. 46, part 1, pp.151-164,1971.

3.18 Incecik, A. ' Design Aspects of the Hydrodynamics and Structural Loading on Floating Offshore Platforms under Wave Excitation', Ph.D. thesis, Dept. of Naval Architecture and Ocean Engineering, Glasgow University, 1982.

3.19 Havelock, T.H. ' The Pressure of Water Waves on a Fixed Obstacle', *Proc. Roy. Soc.*, London, Vol. A175, pp 409-421, 1940.

3.20 Abramowitz, M. and Stegun, I.A. *Handbook of Mathematical Functions with Formulas, Graphs and Mathematical Tables*, Dover Publications, 1970.

RERERENCES OF CHAPTER 4

- 4.1 Korvin-Kroukovsky, B.V. and Jacobs, W.R. ' Pitching and Heaving Motions of a Ship in Regular Waves ', *Transactions of the Society of Naval Architects and Marine Engineers*, New York, 1957.
- 4.2 Newman, J.N. *Marine Hydrodynamics*, The M.I.T. Press, 1978.
- 4.3 Hooft, J.P. ' Hydrodynamic Aspects of Semi-Submersible Platforms', MARIN Publication No. 400, Wageningen, 1972.
- 4.4 Remery, G.F.M. and Hermans, A.J. ' The Slow Drift Oscillations of a Moored Object in Random Seas', *Proceedings of Offshore Technology Conference*, Paper No. 1500, Houston, May 1971.
- 4.5 Pinkster, J. A. ' Low Frequency Second Order Wave Exciting Forces on Floating Structures ', MARIN Publication No. 600, Wageningen, 1980.
- 4.6 Wichers, J.E.W. ' A Simulation Model for a Single Point Moored Tanker ', MARIN Publication No. 797, Wageningen, 1988.
- 4.7 de Kat, J.O. and Wichers, J.E.W., ' Behaviour of a Moored Ship in Unsteady Current Wind and Waves', *Marine Technology*, Vol.28, No.5, September, 1991.
- 4.8 Yilmaz, O. ' Non-linear Dynamic Interaction Between Mooring Systems and a Floating Structure Under Environmental Forces', Annual Report, The University of Glasgow, Naval Architecture and Ocean Engineering Department, 1989.

- 4.9 Singh, S. ' Uncertainties in the Estimation of Fluid Loading on Offshore Structures with Special Emphasis on Wind Forces, *Trans. of Institute of Marine Engineers*, Vol 101, pp 269-287, 1989.
- 4.10 Davenport, A.G. ' Gust Loading Factors', *Journal of the Structural Division*, ASCE, Vol. 93, No. ST3, pp11-34, 1967.
- 4.11 Harris, R.I. ' The Nature of the Wind, The Modern Design of Wind-Sensitive Structures', Construction Industry Research & Information Association, London, pp. 29-55, 1971.
- 4.12 Davenport, A.G. ' The Spectrum of Horizontal Gustiness Near the Ground in High Winds', *Quarterly Journal of Royal Meteorological Society*, Vol. 87, pp. 194-211, 1961.
- 4.13 Ochi, M.K. and Shin, Y.S. ' Wind Turbulent Spectra for Design Consideration of Offshore Structures', *Proceedings of Offshore Technology Conference*, Paper No. 5736, pp. 461-467, Houston, 1988.
- 4.14 Faltinsen, O.M. , Kjaerland, O. , Liapis, N. and Walderhaug, H. ' Hydrodynamic Analysis of Tankers at Single Point Mooring Systems', *Second International Conference on Behaviour of Offshore Structures*, No. 59, London, 1979.
- 4.15 Molin, B. and Bureau, G. ' A Simulation Model for the Dynamic Behaviour of Tankers Moored to Single Point Moorings', *International Symposium on Ocean Engineering and Ship Handling*, Gothenburg, Sweden, 1980.
- 4.16 Norbinn, N.H. ' Theory and Observation on the Use of a Mathematical Model for Ship Manoeuvring in Deep and Confined Water.', Publication No. 68, SSPA, Gothenburg, 1971.

- 4.17 Pinkster, J.A. ' Low Frequency Phenomena Associated with Vessels Moored at Sea', *Society of Petr. Engrs. AIME*, paper no. SPE4837, 1974.
- 4.18 Newman, J.N. ' Second Order Slowly Varying Forces on Vessels in Irregular Waves', *Proceedings of Symposium on Dynamic Marine Vehicles Structures in Waves*, pp. 182-186, London, 1974.
- 4.19 Nienhuis, U. ' Simulation of Low Frequency Motions of Dynamically Positioned Offshore Structures', *Royal Institution of Naval Architects Spring Meeting*, London, 1986.
- 4.20 Wichers, J.E.W. ' The Behaviour of Dredging Equipment Operating in Waves', Vol. 3, *Chapter 37 of Handbook of Coastal and Ocean Engineering*, 1990.
- 4.21 Yilmaz, O. and Incecik, A., ' Non-linear Dynamic Interaction Between Mooring Systems and A Floating Structure under Environmental Forces', *Proceedings of the Offshore Mechanics and Arctic Engineering Conference*, Houston, Feb. 1990.
- 4.22 Yilmaz, O. and Incecik, A., ' Non-linear Dynamic Time Domain Simulation of Moored Floating Systems', *Proceedings of the Offshore Mechanics and Arctic Engineering Conference*, Stavanger, June. 1991.
- 4.23 Cummins, W.E. ' The Impulse Response Function and Ship Motions', *Schiffstechnik*, Vol. 9, No. 47, 1962.
- 4.24 Ogilvie, T.F. ' Recent Progress Toward the Understanding and Prediction of Ship Motions', *5th Symposium on Naval Hydrodynamics*, pp. 3-80, Bergen, 1964.
- 4.25 Oortmerssen, I.G.V. ' The Motions of a Moored Ship in Waves', Publication No. 510, Netherlands Ship Model Basin, Wageningen, The Netherlands, 1976.

4.26 Muga, B.J. and Freeman, M.A. ' Computer Simulation of Single Point Moorings', *Proceedings of Offshore Technology Conference*, Paper No. 2829, Houston, 1977.

4.27 Newman, J.N. ' The Exciting Forces on Fixed Bodies in Waves', *Journal of Ship Research*, Vol. 6, No. 3, 1962.

4.28 Gear, C.W. ' The Automatic Integration of Ordinary Differential Equations', *Communications of the ACM*, Vol. 14, No. 3, 1971.

REFERENCES OF CHAPTER 5

5.1 Pinkster, J.A. and Wichers, J.E.W. ' The Statistical Properties of Low-Frequency Motions of Nonlinearly Moored Tankers', *Proceedings of Offshore Technology Conference*, Vol. 3, Paper No. 5457, Houston, 1987.

5.2 Gear, C.W. ' The Automatic Integration of Ordinary Differential Equations', *Communications of the ACM*, Vol. 14, No. 3, 1971.

5.3 The NAG Fortran Library Manual-Mark 12, Published by the Numerical Algorithms Group Ltd, 1987.

REFERENCES OF CHAPTER 6

- 6.1 Yılmaz, O. and Incecik, A. ' Non-linear Dynamic Interaction between Mooring Systems and a Floating Structure under Environmental Forces', *Proceedings of the Offshore Mechanics and Arctic Engineering Conference*, Vol. 1B, Houston, 1990.
- 6.2 Chakrabarti, S.K. and Cotter, D.C. ' Damping Coefficient of a Moored Semisubmersible in Waves and Current', *Proceedings of the Offshore Mechanics and Arctic Engineering Conference*, Vol. 1A, Houston, 1990.

